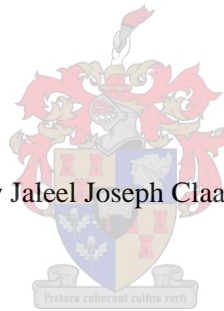


# **Experimental testing and numerical modelling of a large-scale modular cellular structural steel and composite sandwich decking flooring system in fire**

by **Jaleel Joseph Claasen**



Dissertation presented for the Degree of Doctor of Philosophy

in the Faculty of Engineering, at Stellenbosch University

Supervisor: Professor Richard S. Walls

Co-supervisor: Dr Antonio Cicione

April 2022

## **Declaration**

By submitting this dissertation electronically, I declare that the entirety of the work contained therein is my own original work, that I am the authorship owner thereof (unless to the extent explicitly otherwise stated) and that I have not previously in its entirety or in part submitted it for obtaining any qualification.

Date: April 2022

Copyright © 2022 Stellenbosch University

All rights reserved

## Abstract

The Southern African Institute of Steel Construction (SAISC) has determined that the current office building market segment within the South African construction industry does not satisfy the performance requirements of the public, developers, and tenants. Through consultation with industry leaders, the SAISC were able to establish the specific performance criteria required for the design, construction, and operation of future office buildings. With the established performance requirements in mind, the SAISC have developed a cellular beam modular access floor office building system (CBS system) which is able to satisfy all criteria. The system consists of two interdependent components: (1) the building system's structural components, which include horizontal cellular beam sections and vertical columns; and (2) the profiled steel sandwiched decking flooring system (SD system), which is attached to the bottoms of the horizontal structural members. The system involves no wet work, with the intention of having a building system that could be assembled in modules off-site, transported on a truck, and erected quickly and safely on-site in a multitude of possible configurations to allow for architectural freedom while standardizing the modules. However, the lightweight nature of the system and flooring system implemented in the CBS design has put the fire resistance of the system in question.

This dissertation forms part of a larger study conducted to experimentally and numerically quantify the fire rating for the CBS system. An extensive experimental programme was carried out as part of this work, ranging from small-scale materials tests to medium-scale four point bending tests of the flooring system and large-scale standard fire tests. The main experimental test performed was a large-scale standard fire test of an experimental frame (spanning 5.66 m and 3.64 m wide) built according to the design aspects of the CBS system. The results from the test were positive as the structure was able to maintain load bearing capacity throughout the entire duration of the test, with no major structural failure occurring. Furthermore, the horizontal structural elements deflections were well within the specified limits for fire design, and the flooring system nearly achieving the required 1 hour fire rating with regards to the insulation fire limit state criteria.

Using the data obtained from the experimental programme, and through the use of the Finite Element Method, numerous experimental models were developed to analyse the thermomechanical response of the CBS system, and the flexural and thermal performance of the flooring system to be implemented in the CBS design. The numerical models were able to successfully predict the thermal behaviour of the flooring system and the thermal-stress performance of the horizontal structural elements of the experimental frame tested in the large-scale standard fire test.

## Opsomming

Die Suid-Afrikaanse Instituut vir Staalkonstruksie (SAISC) het vasgestel dat die huidige marksegment binne die Suid-Afrikaanse konstruksiebedryf nie aan die prestasievereistes van die publiek, ontwikkelaars en huurders voldoen nie, veral wat kantoorstrukture betref. Deur oorlegpleging met bedryfsleiers kon die SAISC die spesifieke prestasiekriteria bepaal wat vir die ontwerp, konstruksie en bedryf van toekomstige kantoorgeboue vereis word. Met die gevestigde prestasievereistes in gedagte, het die SAISC 'n sellulêre balk modulêre toegangsvloer-kantoorgeboustelsel (CBS-stelsel) ontwikkel wat aan alle kriteria kan voldoen. Die stelsel bestaan uit twee dele wat in sinergie werk: (1) die strukturele komponente van die boustelsel, wat bestaan uit horisontale sellulêre balkgedeeltes en vertikale kolomme (2) die geprofileerde staaldekvloerstelsel (SD-stelsel) wat aan geheg is die onderkant van die horisontale strukturele lede. Die stelsel behels geen nat werk nie, met die bedoeling om 'n boustelsel te hê wat in modules buite die perseel saamgestel kan word, op 'n vragmotor vervoer kan word en vinnig en veilig op die perseel opgerig kan word in 'n menigte moontlike konfigurasies om argitektoniese vryheid toe te laat, terwyl standaardisering van die modules. Die liggewig aard en vloerstelsel wat in die CBS-ontwerp geïmplementeer is, het egter die brandweerstand van die betrokke stelsel geplaas.

Hierdie proefskrif vorm deel van 'n menigte studies wat uitgevoer is om die brandgradering vir die CBS-stelsel eksperimenteel en numeries te kwantifiseer. 'n Uitgebreide eksperimentele program is as deel van hierdie werk uitgevoer, wat wissel van kleinskaalse materiaaltoetse tot mediumskaalse vierpuntbuigtoetse van die vloerstelsel en grootskaalse standaardbrandtoetse. Die hoof eksperimentele toets wat uitgevoer is, was 'n grootskaalse standaardbrandtoets van 'n eksperimentele raam (wat strek oor 5,66 m en 3,64 m breed) wat volgens die ontwerpaspekte van die CBS-stelsel gebou is. Die resultate van die toets was positief aangesien die struktuur in staat was om lasdravermoë deur die hele duur van die toets te handhaaf, met geen groot strukturele mislukking wat plaasgevind het nie. Verder was die horisontale strukturele elemente defleksies goed binne die gespesifiseerde perke vir brandontwerp, en die vloerstelsel het amper die vereiste brandgradering behaal met betrekking tot die isolasiebrandgrenstoestandkriteria

Met behulp van die data verkry uit die eksperimentele program, en deur die gebruik van die Eindige Element Metode, is talle eksperimentele modelle ontwikkel om die termomeganiese reaksie van die CBS-stelsel, en die buig- en termiese werkverrigting van die vloerstelsel wat in die CBS geïmplementeer moet word, te ondersoek ontwerp. Die numeriese modelle was in staat om die termiese gedrag van die vloerstelsel en die termiese spanning prestasie van die horisontale strukturele elemente van die eksperimentele raam wat in die grootskaalse standaard brandtoets getoets is, suksesvol te voorspel.

## Acknowledgements

I would like to thank the following people for the significant contributions made towards this work:

- My supervisor, Professor Richard S. Walls, for the life-changing opportunity to work with him and for his unwavering patience throughout this process. Richard is without a doubt one of the kindest people I've ever met and would go to lengths for me as a student under him that most supervisors would not. He was truly instrumental in the creation of this work, and for that I am eternally grateful. I cannot speak enough about his character, work ethic, and leadership qualities, which have served as a great source of motivation throughout this entire process. I can only hope that we will remain friends in the future, and that I will be able to repay him in some way for everything he has done for me.
- My co-supervisor, Dr Cicione, for the sound technical advice and leadership throughout this journey. I got to experience my first taste of full-scale fire testing as part of his project and many more after that.
- Mr Dirk Streicher and Mr Johan Swart, for being crazy enough to build a testing furnace large enough to conduct one of the largest standard fire tests in Africa. It was a pleasure working under Mr Streicher and Mr Swarts when conducting my large-scale experimental tests. Mr Streicher always knew how to keep the atmosphere around the work site fun and exciting with his endless jokes. He was also an amazing source of technical advice, with a deep understanding of the behaviour of material under fire conditions.
- Mrs. Zara Sander for the help she provided during my experimental testing. She was instrumental in keeping me on track during most of my experimental testing, by providing valuable administrative help, working on logistics, and data capturing.
- Mr. Johan van der Merwe, for the help he provided me with in the Stellenbosch University structures laboratory. Mr van der Merwe was nearing retirement when I first started working in the structures laboratory, and I was lucky enough to get to learn from him before he left the university. He taught me how to use most of the machinery in the laboratory among other valuable skills.
- Mr Gerhard Swart who was working for the Etex group South Africa and Mr Andries Botha from Voidcom South Africa, for the endless supply of materials which have made the experimental tests conducted in this work possible. Both Mr Swart and Mr Botha would always go great lengths to make sure I received my materials on time, sometimes even at their own expense.
- MacSteel South Africa, for the supply of roughly a ton of steel, from which I was able to construct the experimental frame tested in this work.
- My colleagues in the Department of Civil Engineering.
- To my entire immediate family for the major sacrifices that had to be made for me to be able to study for this long, the patience throughout this journey, unending love, and motivation.

# Table of Contents

Abstract .....	iii
Opsomming .....	iv
Acknowledgements .....	v
List of Figures .....	xi
List of Tables .....	xvii
List of abbreviations .....	xviii
List of Symbols .....	xix
Chapter 1 Introduction.....	1
1.1 Background.....	1
1.1.1 Key attributes of the CBS system.....	3
1.2 Problem statement .....	4
1.3 Project goals and objectives .....	5
1.4 Project scope and limitations .....	5
1.5 Dissertation outline.....	7
Chapter 2 Literature review.....	9
2.1 Introduction .....	9
2.2 General background on fire safety.....	9
2.3 Standard Fire Testing .....	10
2.3.1 Prescriptive design approach .....	11
2.4 Performance-based design.....	12
2.4.1 Eurocode parametric fire curves.....	12
2.5 Fire behaviour.....	14
2.5.1 What fire really is .....	14
2.5.2 Heat transfer mechanisms.....	15
2.6 Steel structures exposed to fire.....	18
2.6.1 Steel design in fire .....	19

2.6.2 Protective systems for steel structures.....	19
2.6.3 Thermal and mechanical properties of steel at elevated temperatures .....	20
2.6.4 Testing of cellular beams in fire .....	25
2.7 Profiled steel sheet dry board composite flooring systems .....	28
2.7.1 Components, material properties, and modelling considerations.....	29
2.8 Advanced calculation methods.....	36
2.8.1 Thermal response analysis.....	38
2.8.2 Mechanical response analysis.....	40
2.9 summary .....	41
Chapter 3 Cellular beam structure and sandwich decking system background and specifications .....	42
3.1 Introduction .....	42
3.2 Originally proposed Cellular Beam Structural System .....	42
3.3 Previous research conducted and findings.....	45
3.3.1 Research conducted by Marx (2018).....	45
3.3.2 Research conducted by Kloos (2017).....	49
3.4 Design of experimental CBS frame.....	56
3.5 Development of SD specifications to be investigated in this work.....	58
3.6 Conclusion.....	60
Chapter 4 Small-scale and medium-scale experimental setups and results.....	61
4.1 Introduction .....	61
4.2 Small-scale material tests conducted and results.....	61
4.2.1 Structural and Voidcon VP profiled decking steel tensile tests and results.....	62
4.2.2 Fibre cement and calcium silicate boards materials tests and results .....	63
4.3 SD system four-point bending tests and results.....	66
4.3.1 Test specimens setup .....	67
4.3.2 Universal testing machine setup (Instron).....	71
4.3.3 Decking only tests – VP50-IO5 and VP115-ISO sample results .....	72
4.3.4 VP50 and VP115 sample results .....	74
4.4 Conclusion.....	83

Chapter 5 Large-scale experimental setups and results .....	86
5.1 Introduction .....	86
5.2 Large-scale test 1 (LST-1) setup and results .....	86
5.2.1 Ceiling only experimental setup .....	87
5.2.2 Instrumentation.....	90
5.2.3 Experimental results and discussion.....	92
5.3 Large-scale test 2 (LST-2) setup and results .....	97
5.3.1 Experimental setup .....	97
5.3.2 Instrumentation.....	102
5.3.3 Experimental results and discussion.....	106
5.4 Conclusion.....	117
Chapter 6 Sandwich decking (SD) system mechanical performance finite element modelling.....	119
6.1 Introduction to modelling chapters.....	119
6.2 Introduction to the modelling of the SD system at ambient temperature .....	120
6.2.1 Considerations regarding model development and focus .....	120
6.2.2 Considerations of joints and limitations on analysis .....	121
6.3 Model development and specifications .....	121
6.3.1 Parts and components .....	121
6.3.2 Mesh specifications .....	122
6.3.3 Material properties of components .....	123
6.3.4 Connectors.....	125
6.3.5 Step and contact/interactions .....	126
6.3.6 Load application and boundary conditions.....	127
6.4 Results .....	128
6.5 Conclusion.....	132
Chapter 7 Sandwich decking (SD) system thermal performance finite element modelling (VP50-9).....	134
7.1 Introduction .....	134
7.2 Heat transfer model configuration.....	135
7.2.1 Overview .....	135

7.2.2 Model parameters and setup.....	136
7.2.3 Mesh and mesh interactions .....	137
7.3 Material thermal properties .....	140
7.4 Results and analysis.....	141
7.5 Conclusions .....	144
Chapter 8 Structural models of the experimental steel frame (LST-2) .....	145
8.1 Introduction .....	145
8.2 Common modelling parameters.....	146
8.2.1 General solution procedure.....	146
8.2.2 Material properties.....	146
8.2.3 Structural loading .....	147
8.2.4 Final temperatures measured in LST-2 .....	149
8.3 Single element models.....	149
8.3.1 Geometry and mesh.....	150
8.3.2 Structural loading and boundary conditions .....	153
8.3.3 Thermal loading.....	155
8.4 Global structure model .....	157
8.4.1 Geometry and mesh.....	157
8.4.2 Structural loading and boundary conditions .....	158
8.4.3 Interactions .....	159
8.4.4 Thermal loading.....	160
8.5 Results .....	160
8.5.1 Data overview and naming convention .....	161
8.5.2 Parallel flange channel support beams (PC) results .....	163
8.5.3 Main cellular support beam (CB) results.....	168
8.5.4 Comparison between single beam and full analysis models, and interconnectional behaviour .....	173
8.6 Conclusion.....	180
Chapter 9 Conclusions.....	182
9.1 Overview .....	182

9.2 Overview of chapters.....	183
9.2.1 Introductory chapters – Chapters 1 to 3.....	183
9.2.2 Experimental programme – Chapter 4 to 5 .....	183
9.3 Main findings.....	184
9.3.1 Medium-scale four point bending tests .....	184
9.3.2 Large-scale standard fire tests .....	185
9.4 Recommendations and future research.....	189
9.4.1 Proposed details for the CBS and SD for the future.....	189
9.4.2 Recommendations for future research.....	191
Chapter 10 References.....	193

## List of Figures

Figure 1-1 The modular cellular beam structural system (CBS) showing both a single sub-structure (i.e., three interconnected modules) and an entire building .....	3
Figure 1-2 Cross-sectional view of access flooring components and incorporated SD system. (Image not to scale).....	3
Figure 2-1 Time-temperature curves of the standard, external and hydrocarbon fire curves.....	10
Figure 2-2 Fire triangle. (Drawn using AutoCad by author).....	15
Figure 2-3 Thermal conductivity of carbon steel as a function of the temperature (BSI, 2005). .....	21
Figure 2-4 Specific heat of carbon steel as a function of temperature (BSI, 2005).....	22
Figure 2-5 Relative thermal elongation of carbon steel as a function of the temperature (BSI, 2005). .....	23
Figure 2-6 Stress-strain relationship for carbon steel at elevated temperatures (BSI, 2005). .....	24
Figure 2-7 Reduction factors for the stress-strain relationship of carbon steel at elevated temperatures (BSI, 2005).....	25
Figure 2-8 Temperature-dependent thermal conductivity values of Calcium Silicate Boards reported by various authors. ....	31
Figure 2-9 Specific heat capacity of Calcium Silicate Board.....	33
Figure 2-10 Modified specific heat capacity of Fibre cement board.....	35
Figure 2-11 Simplified load-slip behaviour of a composite section.....	36
Figure 2-12 Stages of analysis when considering structures is fire.....	37
Figure 2-13 boundary conditions and governing equations for a generic structural element exposed to a fire.	39
Figure 3-1 Isometric view to illustrate terminology and the configuration of a single sub-structure of the CBS system.....	43
Figure 3-2 Prototype of the CBS showing the system without the ceiling or false floor in place.....	44
Figure 3-3 Cross-sectional configuration of the initial access flooring components of the CBS system. (Note: Image not drawn to scale).....	45
Figure 3-4 The respective Flute and Trough areas of the VP 50 profiled steel sheeting (Top-Right), the configuration of each of the test samples (Left), and a schematic of the test furnace setup (Bottom-Right). (Marx, 2018).....	46
Figure 3-5 FE model configuration of each of the main horizontal structural members, including the ISD system. (Marx, 2018).....	47
Figure 3-6 A 2-hour parametric fire curve for the CBS system and standard fire curve (Marx, 2018). .....	48
Figure 3-7 Fixed-fixed (FF) J-beam experiencing lateral deflection of the bottom flange caused by restrained thermal expansion. The total deflection is shown in (m). (Kloos, 2017) .....	50
Figure 3-8 P-Beam single element model under ambient temperatures (Left) and standard fire (Right) conditions. (Kloos, 2017) .....	51

Figure 3-9 Terminology used for global structural components (Left) and diagram of the three fire cases and the corresponding structural element that experience elevated temperatures (Right). (Kloos, 2017).....	52
Figure 3-10 Initial connection detail of the J-Beams to the P-Beams (Kloos, 2017), which was modified to reduce torsional effects.....	53
Figure 3-11 Initial buckling behaviour of the P-Beams in opposite directions away from the structure (Top) and the eventual buckling of both P-beams in a single direction (Bottom). (Kloos, 2017) .....	54
Figure 3-12 Fire case 3 (FS3) – global model at 38 (Top) and 120 (Bottom) minutes in a parametric fire analysis. (Kloos, 2017).....	55
Figure 3-13 Diagram of the experimental frame layout and structural components terminology.....	57
Figure 3-14 Proposed and tested variations of the SD system and their components. ....	59
Figure 4-1 Dimensions of tensile test samples (mm). ....	62
Figure 4-2 Stress-strain graphs of the structural steel (Left) and profiled steel sheeting (Right).....	63
Figure 4-3 Materials in three-point bending (Left) and compression (Right) tests setups. ....	64
Figure 4-4 Fibre cement board bending tests results. ....	65
Figure 4-5 Fibre cement board crushing tests results. ....	65
Figure 4-6 Calcium silicate board bending tests results. ....	65
Figure 4-7 Calcium silicate board crushing tests results. ....	65
Figure 4-8 VP50-9 and VP50-12 cross-sectional view. ....	68
Figure 4-9 VP115-12 and VP115-20 cross-sectional view .....	68
Figure 4-10 CSB (a) and FCB (b) fixities arrangement for a given VP115-12 sample, and Sample VP115-20-T2 Stiffeners (c).....	70
Figure 4-11 Top view of the fixities arrangement for each composite test conducted.....	70
Figure 4-12 Experimental setup (Left) and schematic (Right) of VP50 and VP115-20 samples tested. ....	71
Figure 4-13 Experimental setup (Left) and schematic (Right) of VP115-ISO and VP115-12 samples tested..	72
Figure 4-14 VP50-ISO load-deflection curve. ....	72
Figure 4-15 VP115-ISO load-deflection curve. ....	72
Figure 4-16 VP50-ISO and VP115-ISO Experimental and theoretical results. ....	74
Figure 4-17 Local buckling of steel of VP50-9-T1 (Left) and warping/buckling of steel between the points of fixities of VP115-20-T4 (Right). ....	76
Figure 4-18 VP50-9 and VP50-12 samples load-deflection curves. ....	76
Figure 4-19 VP115-12 and VP115-20 samples load-deflection curves. ....	77
Figure 4-20 Original section (Top) and the transformed section (Bottom) with representative elastic stress gradient.....	79
Figure 4-21 Theoretical and experimental ultimate load capacities for all floor tests conducted. ....	80
Figure 4-22 Relationship between the flexural rigidity and length using the deflection formula for a uniformly distributed beam. ....	82

Figure 5-1 LST-1 CSB ceiling system (Left) and FCB (Right) configurations and fixities arrangements. (All units in mm). Colours used: CSB strips – blue; CSB strip fixing screws – green; CSB joints/edge – red; top FCB joints – magenta; top FCB screws – red. ....	88
Figure 5-2 LST-1 experimental setup top view. ....	89
Figure 5-3 Section A-A view of LST-1 setup (Top) and Section B-B view of LST-1 setup. ....	90
Figure 5-4 LST-1 Thermocouple groups layout (Right) and top view of each group thermocouple layout (Left). ....	91
Figure 5-5 Section A-A (Left) and Section B-B (Right) of thermocouple groups. ....	91
Figure 5-6 Final test setup prior to testing. ....	91
Figure 5-7 LST-1 Average furnace temperature VS the Standard Fire curve. ....	92
Figure 5-8 LST-2 Group 2 Time-Temperature curves. ....	93
Figure 5-9 LST-1 Group 6 Time-Temperature curves. ....	93
Figure 5-10 LST-1 Average Time-temperature curves for all groups (G1-G6). ....	93
Figure 5-11 Failure of SD system at the South-West corner. ....	94
Figure 5-12 LST-1 Unexposed surface average time-temperature curves on top of the FCB above the flutes (F-FC) and troughs (FC-T) of the decking. ....	96
Figure 5-13 Steel plates used to support the decking of the SD system showing (a) a view from the bottom with the decking on top of the plate, (b) counter-sunk connectors which are used to hang plates from beams above, and (c) a top view of a channel with hangers connected through it. ....	98
Figure 5-14 Uniformly distributed load on structure applied using sandbags in the plenum. FCB boards were placed over the bags upon completion to simulate the false floor. ....	99
Figure 5-15 CSB ceiling system (Left) and FCB (Right) configuration and fixities arrangements. The CSB system covered the side walls of the furnace, whereas the FCB fitted within the steel beams, hence the difference in size. ....	100
Figure 5-16 Experimental setup top view. ....	101
Figure 5-17 Section A-A (top) and Section B-B (bottom) of LST-1 top view. ....	101
Figure 5-18 Enlarged view of decking system C1 and D1. ....	102
Figure 5-19 LST-2 Decking thermocouple groups layout. ....	103
Figure 5-20 LST-2 Decking thermocouple layout for each group. ....	103
Figure 5-21 Horizontal steel frame thermocouple group locations (Top-left), thermocouple locations per group along the height of beam sections (Top-right) and thermocouple group locations along beams section (Bottom). ....	104
Figure 5-22 LST-2 LVDT locations (Left) and image of attached LVDT to truss system (Right). ....	105
Figure 5-23 Outside (top) and inside (bottom) images of the final test setup prior to testing. ....	105
Figure 5-24 LST-2 Average furnace temperature versus the Standard Fire curve. ....	106
Figure 5-25 LST-2 Group 2 time-temperature curves. ....	107
Figure 5-26 LST-2 Group 6 time-temperature curves. ....	107

Figure 5-27 LST-2 groups average time-temperature curves.....	107
Figure 5-28 Unexposed surface average Time-Temperature curves.....	109
Figure 5-29 All unexposed surface temperatures vs Single point insulation limit for FLS. ....	110
Figure 5-30 Ceiling system (Left) and FCB (Right) after completion of the experiment. ....	111
Figure 5-31 Vertical deflection data for steel beams for LST-2.....	112
Figure 5-32 CB 1 time-temperature curves showing (T)op, (M)idle and (B)ottom steel temperatures at positions B1, D1 and F1 along the beam length. ....	113
Figure 5-33 PC 1 time-temperature curves showing (T)op, (M)idle and (B)ottom steel temperatures at positions C2, C3 and C4 along the beam length. ....	113
Figure 5-34 PB 1 time-temperature curves showing (T)op, (M)idle and (B)ottom steel temperatures at positions A2, A3 and A4 along the beam length. ....	114
Figure 5-35 Group B1 average temperatures vs average deflection of LVDT 3 and 6 (CB 1)).....	115
Figure 6-1 Geometry of VP115-20 SD system model (Top) and implementation of CBS strips in the numerical model (Bottom). ....	123
Figure 6-2 Stress-strain curves of materials. ....	124
Figure 6-3 Idealized stress profile of the VP115-20 SD system under bending load.....	124
Figure 6-4 Connector elements implemented in numerical model.....	126
Figure 6-5 Model boundary conditions and applied loading.....	128
Figure 6-6 Comparison of numerical and experimental results.....	129
Figure 6-7 Final Stress distribution of FEM-200 spacing-3695 N/mm numerical model, and the stress distribution of each the individual parts. (Stress values are in MPa) .....	131
Figure 6-8 Horizontal longitudinal shear forces for each of the connector element of the Fibre Cement board (Right) and the Calcium Silicate board (Left). (Force in N) .....	132
Figure 7-1: Schematic of various heat transfer mechanisms considered in FE model. ....	136
Figure 7-2 Geometry and dimensions (mm) of the VP50-9 SD system model.....	137
Figure 7-3 Defined cavities (Top) and mesh densities (Bottom) in FE model.....	138
Figure 7-4 Nodes used to save the average time-temperature histories of the respective cavities .....	140
Figure 7-5 Node locations used to obtain final predicated temperatures and final predicated temperature profile. ....	141
Figure 7-6 Finite Element Model results compared to the experimental average group temperatures from the same thermocouple locations .....	142
Figure 8-1 Yield stress of steel at elevated temperatures .....	147
Figure 8-2 LST-2 experimental frame structural load path.....	148
Figure 8-3 Geometry and mesh density of Parallel Channel beam model. ....	151
Figure 8-4 Geometry and mesh density of the Cellular beam model. ....	152
Figure 8-5 Parallel channel beam model loads and boundary conditions .....	153
Figure 8-6 Cellular beam model loads and boundary conditions. ....	155

Figure 8-7 Sections used to apply thermal loading to the parallel channel beam (Top) and cellular beam (Bottom-Right) models. Segments used to apply the temperatures along the beam height in each section as shown by example for the PC beams (Bottom-Left) .....	156
Figure 8-8 Implementation of connection parts in global structural model. ....	158
Figure 8-9 Geometry, loading and boundary conditions of the global structural model.....	159
Figure 8-10 Connection of interconnected structural elements in global model.....	159
Figure 8-11 Comparison of the global structural model and experimental data. ....	162
Figure 8-12 Final deformed shape and stress distribution of global structural model. (Deformation magnification factor = 3) .....	162
Figure 8-13 Numerical and experimental deflection data of PC 1. ....	163
Figure 8-14 Deflected shape, stress and temperature distribution of PC 1 at the end of the single element model analysis. (Deformation magnification factor = 3). NT11 provides the elemental temperature in °C at the end of the analysis. ....	164
Figure 8-15 Lateral deflections of PC 1 from the single element and global structural model in comparison to the average temperatures recorded at C3-Series.....	164
Figure 8-16 Numerical and experimental deflection data of PC 2. ....	166
Figure 8-17 Deflected shape, stress and temperature distribution of PC 2 at the end of the single element model analysis. (Deformation magnification factor=3). NT11 provides the elemental temperature in °C at the end of the analysis. ....	167
Figure 8-18 Lateral deflections of PC 2 from the single element and global structural model in comparison to the average temperatures recorded along the bottom flange of PC 2. ....	168
Figure 8-19 Numerical and experimental deflection data of CB 1.....	169
Figure 8-20 Deflected shape, stress and temperature distribution of CB 1 at the end of the single element model analysis. (Deformation magnification factor = 2 ). ....	170
Figure 8-21 Numerical and experimental deflection data of CB 2.....	171
Figure 8-22 Deflected shape, stress and temperature distribution of CB 2 at the end of the single element model analysis. (Deformation magnification factor = 2). . ....	172
Figure 8-23 Final deflected shape and stress distribution at the end of the global model analysis. (Deformation magnification factor = 3 ) .....	173
Figure 8-24 Longitudinal expansion of Parallel Channel beams (a). (Deformation magnification = 3), Close-up of induced torsional twisting in CB 1 beam by the PC beams (b). (Deformation magnification = 3). ....	175
Figure 8-25 Lateral deflections of CB 1 from the single element and global models, and the longitudinal thermal expansion of the PC beams from the single element and global models.....	175
Figure 8-26 Axial force components as measured along three intervals along the PC beam lengths for both the single element and global models at 66 minutes. ....	177
Figure 8-27 Average axial forces induced in the PC beams, for both the single element and global models. ....	177

Figure 8-28 Axial force components as measured along three intervals along the CB beam lengths for both the single element and global models at 66 minutes. .... 178

Figure 8-29 Average axial forces induced in the CB beams, for both the single element and global models. 178

Figure 8-30 Longitudinal expansion of the cellular beams in both the global and single element models. .... 179

Figure 9-1 Design implementation to further reduce thermal exposure of primary and tertiary beams by making the FCB continuous under the beams. .... 190

Figure 9-2 Design implementation to allow for the SD system to be situated underneath all the horizontal structural elements. .... 190

## List of Tables

Table 2-1 General equation used to produce the general stress-strain curve as defined in EN 1993-1-2 (BSI, 2005).....	24
Table 2-2 Selected literature on the design and testing of cellular beams in fire.....	28
Table 4-1 Mechanical properties of structural and VP profiled decking steel.....	63
Table 4-2 MOR and MOE properties of the FCB and CSB.....	66
Table 4-3 FCB and CSB average crushing strength properties.....	66
Table 4-4 Complete list of samples tested under four-point bending.....	67
Table 4-5 VP50-ISO and VP115-ISO ULS and theoretical load capacities.....	73
Table 4-6 Failure modes of all composite samples tested.....	75
Table 4-7 ULS and SLS experimental results for all tested samples.....	78
Table 5-1 LST-1 Thermocouple legend.....	90
Table 5-2 LST-2 Thermocouple legend.....	102
Table 6-1 Material properties of model components.....	123
Table 7-1 Resultant emissivity's for defined cavities.....	139
Table 7-2 Material properties of insulation materials in FE model.....	141
Table 8-1 Loads used to calculate the applied loads in the models.....	148
Table 8-2 Experimental temperature at 66 minutes. (N/A refers to thermocouples that malfunctioned during the experiment).....	149
Table 8-3 Percentage differences between the single element and global models, and the error differences between the single element models and the global model to that of the experimental data for all recorded vertical deflections at the 60-minute mark.....	174

## List of abbreviations

CBS	Cellular Beam Structural
CSB	Calcium silicate board
DOF	Degrees of freedom
EN	European Standard (Europäische Norm)
FCB	Fibre cement board
FE	Finite element
FEM	Finite element model/Finite element method
FF	Fixed-Fixed
FLS	Fire limit state
FR	Fixed-Roller
ISO	International Organisation for Standardisation
GB	Gypsum board
ISD	Initial sandwich decking
LST	Large scale test
LVDT	Linear variable differential transducer
MOE	Modulus of elasticity
MOR	Modulus of rupture
PB	Primary beam
PC	Parallel channel
PP	Pinned-Pinned
PR	Pinned-Roller
SAISC	Southern African Institute of Steel Construction
SANS	South African National Standard
SD	Sandwich decking
SLS	Serviceability limit state
UK	United Kingdom
ULS	Ultimate limit state

## List of Symbols

### **Roman**

$a$	Parameter 1 for calculation of EN 3-1-2 stress-strain curve of steelwork
$A$	Cross-sectional area
$A_v$	Area of the ventilation openings
$A_{st}$	Area of the steel
$A_t$	Total area
$b$	Parameter 2 for calculation of EN 3-1-2 stress-strain curve of steelwork
$B$	Breadth
$c$	Parameter 3 for calculation of EN 3-1-2 stress-strain curve of steelwork
$c$	Material specific heat capacity
$c_a$	Specific heat of steelwork
$DC_p$	Additional average specific heat
$E$	Young's modulus
$E_\theta$	Young's modulus at temperature $\theta$
$EI$	Bending stiffness
$EI_{eff}$	Effective bending stiffness
$f_s$	Yield stress
$f_y$	Yield stress of steel work
$h$	Convective heat transfer coefficient
$h_{eq}$	Weighted average height of the openings
$I$	Second moment of area
$I_{cmp}$	Effective second moment of area of composite section
$I_{fcb}$	Effective second moment of area of a fibre cement board
$I_{st}$	Second moment of area of a steel
$q_{Con}$	Conductive rate of heat flow per unit area
$q_{Conv}$	Convective heat flux generated
$q_{rad}$	Resultant radiative heat flow from the emitting surface to the receiving surface
$t$	Time
$t_{max}$	Time at which peak temperature occurs
$T$	Temperature.
$T$	Thickness
$T_e$	Temperature of emitting surface
$T_r$	Temperature of receiving surface
$\Delta T$	Change in temperature.
$u$	moisture content expressed as a fraction by weight
$y_{st}$	Neutral axis of steel
$y_{cmp}$	Neutral axis of composite section

**Greek**

$\varepsilon$	Material emissivity
$\varepsilon_{ress}$	Resultant emissivity
$\varepsilon_e$	Emissivity of emitting surface
$\varepsilon_r$	Emissivity of receiving surface
$\varepsilon_c$	Cracking strain
$\varepsilon_r$	Tensile rupture strain
$\varepsilon_y$	Yield strain
$\theta_a$	Temperature of steelwork
$\theta_g$	Gas temperature
$\theta_{max}$	Peak temperature
$\lambda_a$	Thermal conductivity of steelwork
$\lambda$	Material thermal conductivity
$\rho$	Material density
$\sigma$	Stephan-Boltzmann constant
$\sigma_{(st)}$	Maximum allowable stress of steel
$\sigma_{(FCB)}$	Maximum allowable stress of fibre cement board
$\varphi$	Configuration factor
$\Lambda$	Correction factor

# Chapter 1 Introduction

## 1.1 Background

When considering low and medium rise buildings in South Africa, reinforced concrete has been the most dominant form of construction method used (Drennan, 2017). The reason for this is partially unknown, as South Africa is one of the largest producers of steel on the African continent, with the material being readily available (World Steel Association, 2020). According to a research study conducted by Drennan (2017), a common self-perpetuating perception has been developed in the South African construction industry that reinforced concrete structures are more economical to build compared to their equivalent steel structures. This stems from the lack of steel structures constructed in South Africa, leading to few comparisons being developed between steel and reinforced concrete buildings in terms of their cost-effectiveness to build. Consequently, this also caused a decline in the overall knowledge of structural steel design and construction within the South African industry. Hence, it is difficult for designers to properly consider steel structures as a viable construction method, due to the lack of knowledge and experience in the industry, and the evidence of the cost-effectiveness that it may provide (Drennan, 2017). Furthermore, Drennan (2017) compared typical steel structures to equivalent reinforced concrete structures and concluded that steel structures used in typical low-rise office buildings could potentially be more cost-effective to build when all aspects are considered, especially when considering speed of construction and associated additional rental income.

The Southern African Institute of Steel Construction (SAISC) have carried out an investigation into the office building development market of South Africa. They have found that there is a large migration of the global labour work force into the service sector, and thus, into office buildings. Secondly, the current market segment is not responding adequately to the various performance requirements of the public, developers, and tenants (Gebremeskel, 2013). Such findings are likely to be applicable in many countries around the world. Based on extensive consultation with leaders in the South African building construction industry, four performance requirements have been developed for the design, construction and operation of future office buildings and are as listed below:

1. Architecturally expressive and economical;
2. Flexible to reconfiguration and space optimization;
3. Consumers of significantly reduced energy and materials; and
4. Fast and safe to build and fit for occupancy.

The SAISC found that satisfying all the above-mentioned criteria using current traditional construction methods proves to be difficult. With this backdrop in mind, the SAISC have conceived a solution to satisfy all criteria with the development of a modular access floor office building system. The building system is comprised of a two-part system that works in synergy: 1) the structural framing that consists of horizontal cellular beam sections and vertical columns, and 2) the access flooring, that consists of a unique sandwiched decking (SD) system attached to the bottom of the beams and a raised false floor placed on top to form the access flooring. In the interest of simplicity, the entire building system, including the structural frame and all flooring components, will be referred to as the Cellular Beam Structural (CBS) system.

After extensive testing conducted by the SAISC on typical design aspects of the CBS system, the final stage of testing has involved investigating the thermal performance of the structural system at elevated temperatures. More specifically, it is necessary to ensure a fire resistance for the CBS system, which is specified according to SANS 10400 Part T (SABS, 2011a) of the national building codes. These requirements are almost identical to many other countries around the world, and hence the research will be broadly applicable. Hence, the final major hurdle to the introduction of the system to industry is quantifying its fire performance.

The research conducted in this study serves as a continuation of two previous research studies conducted on the CBS system, which has formed the preliminary work to quantify the performance of the system at elevated temperatures. The first study (Marx, 2018; Marx and Walls, 2019) investigated the thermal behaviour of the CBS system, and the other (Kloos, 2017; Kloos and Walls, 2019) focused on the structural behaviour of the CBS system in fire. Small-scale experiments were conducted by Marx (2018) on the SD system (i.e. only the sandwich system without steel beams) to investigate the heat transfer through the various layers of the flooring components. The study used the experimental results to develop and benchmark thermal response models of the SD system, which, in turn, was used to develop numerical models that can predict the temperature evolutions of the horizontal steel members. Kloos (2017) used the numerical data produced by Marx (2018) to develop numerical thermal-stress models of the CBS structural members. The numerical models produced by the aforementioned research studies culminated in a fully de-coupled thermomechanical analysis of the CBS system. Significant progress was made by these research studies in the understanding of the CBS system at elevated temperatures. However, the studies highlighted shortcomings, and lacked large-scale experimental data.

Furthermore, it has been identified through this research that the SD system, which forms the bottom part of the access flooring of the CBS system, is not limited in its application to only the CBS system. The versatility of the SD system allows it to be potentially used as a trafficable, quick-assembly, fire-rated, stand-alone flooring system in other structural building designs, such as housing or educational buildings. However, this addition has brought about a new set of challenges, which are also described in Section 1.2 below. The CBS and SD systems are briefly described below, and in depth in Chapter 3.

### 1.1.1 Key attributes of the CBS system

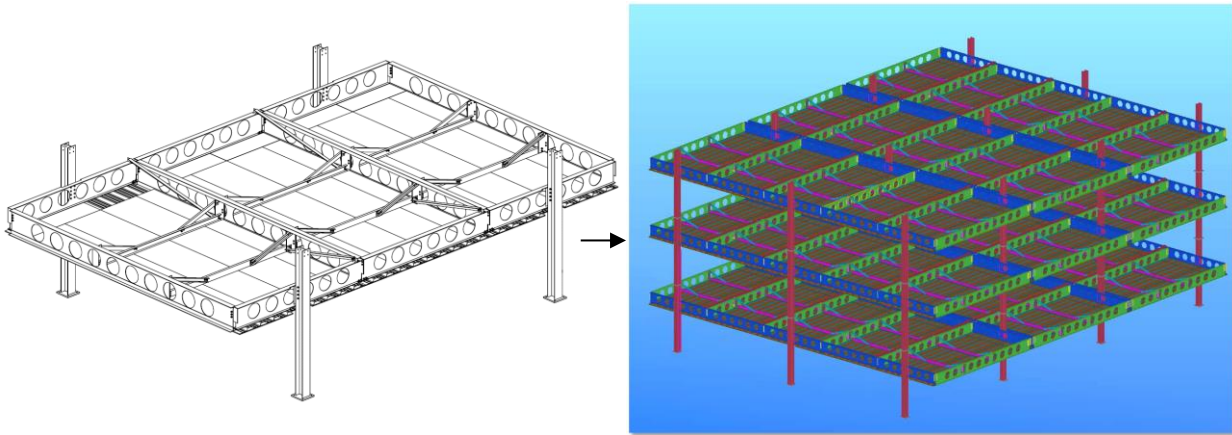


**Figure 1-1 The modular cellular beam structural system (CBS) showing both a single sub-structure (i.e., three interconnected modules) and an entire building.**

The CBS system configuration is depicted above in Figure 1-1. The core intention of the CBS system is to have a building system that could be assembled in modules off-site, transported on a truck, and erected quickly and safely on-site in a multitude of possible configurations to allow for architectural freedom while standardizing the modules. The system is also designed according to the conventional 8 m × 8 m column grid utilized in typical low-rise office buildings in South Africa to accommodate automobile parking underneath (Gebremeskel, 2013). Furthermore, the access flooring of the system was designed as such to house all horizontal structural components and services, making it a critical component of the CBS system design as discussed in section 1.2 below.

The incorporated SD system of the access flooring comprises VP50/115 Voidcon profiled steel sheeting sandwiched between an inner Fibre Cement Board (FCB) on top (acting as the inner floor of the access flooring) and a Calcium Silicate Board (CSB) on the bottom (acting as the ceiling for the floors below). With the SD system attached to the bottom of the horizontal structural components, pedestals are placed on top of the inner FCB and followed with a top FCB (acting as the flooring for the floor above) to form the access floor plenum.

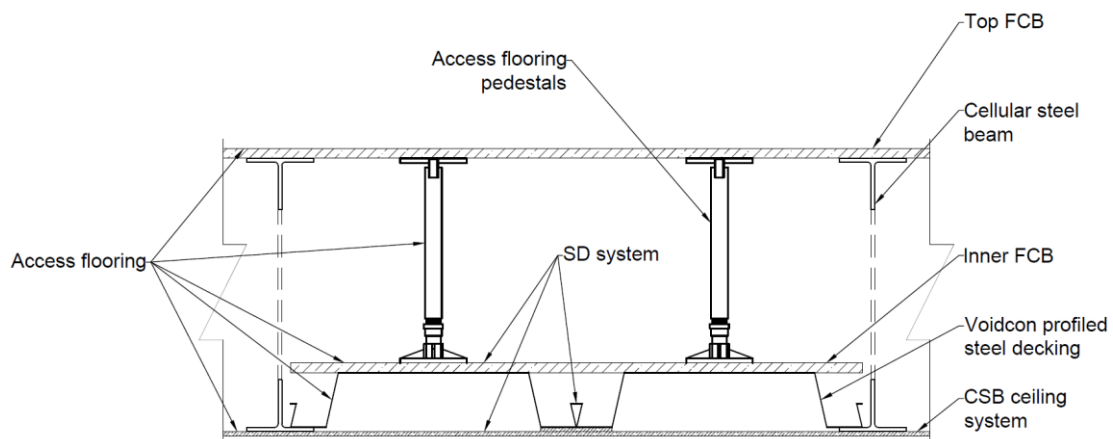


**Figure 1-2 Cross-sectional view of access flooring components and incorporated SD system. (Image not to scale)**

Below are some of the key characteristics of the CBS system:

- No wet trade is involved: as the access flooring only consists of steel sheeting sandwiched between inner fibre cement and calcium silicate boards with a raised false floor on top (Figure 1.2).
- The horizontal structural framing system is placed inside the access floor plenum to save on floor-to-floor height.
- The system can be disassembled and reused for other purposes due to its modularity and no wet trade involved.
- The use of cellular beams and access flooring allows for all electrical, mechanical, and plumbing services to be installed within the access flooring and maintained with ease.
- Utilizes girder continuity over columns to facilitate erection stability and reduce beam weights.

## 1.2 Problem statement

There is certainly a great deal of novelty in this system, however, departure from common and well-known construction methods will come with some implications (Gebremeskel, 2013). The light-weight nature and modularity of the CBS systems access flooring comes with a multitude of advantages. However, deviating from typical concrete flooring systems, which tend to behave well in unwanted fires, has put the fire resistance of the CBS system in question. More specifically, the fire resistance of the SD system is unknown, which is intended to act as the fire barrier between each of the respective floors and fire protection for the housed structural components and services.

Furthermore, there is a lack of literature to assess the unconventional configuration of the CBS system's access flooring fire resistance (Marx, 2018). In addition, resorting to standard prescriptive methods without any further analysis and experimental testing would not suffice, as it tends to lead to over-conservative and costly designs (Kloos, 2017). It is for these very reasons that Marx (2018) carried out the small-scale standard fire tests of the SD system.

However, through the research conducted by Marx (2018) and Kloos (2017), using the data gained from the small-scale experimental tests and extensive Finite Element (FE) analyses, further shortcomings have been identified that need to be addressed. Firstly, the temperature evolutions of the horizontal structural steel members were entirely predicted through numerical modelling without any experimental data or validation studies to compare to, and secondly, the small-scale experiments conducted did not fully capture the thermal and mechanical response of the SD system.

Next, the parameters of some of the elements tested (e.g. the decking) and the proposed configuration of the SD system components have changed, as detailed in Chapter 3, to the current proposed configuration. Consequently, the flexural performance of the newly proposed SD system as a stand-alone flooring system is unknown. Again, using standard analysis procedures to predict the flexural performance without any further experimental testing will not suffice, due to the lack of literature or robust analysis methods available.

### 1.3 Project goals and objectives

The goal of this research project is to experimentally and numerically quantify the fire rating for the CBS system, addressing both the structural steelwork members and the SD system. To successfully meet this goal, the following objectives have been outlined and summarized below:

- To undertake large-scale standard fire tests of the CBS and SD system.
- To develop detailed numerical models of the SD and CBS systems by means of Finite Element Models (FEM) that are capable of simulating the behaviour of the SD and CBS systems under fire conditions.
- To perform and benchmark detailed numerical analyses of the SD and CBS systems against the experiments, and gain a better understanding of the behaviour of the structural system at elevated temperatures.
- To establish if the CBS system has a sufficient fire resistance required for office building use in the industry.
- To undertake experimental and numerical work on the SD system and gain insight to the flexural performance of the system for industry use.
- To propose modifications to enhance the structural and fire performance of the CBS system.

### 1.4 Project scope and limitations

The work performed by Marx and Kloos, laid the groundwork for a full-scale real fire experiment of a built prototype of the CBS system by the SAISC. This would prove to be the ultimate test of the CBS systems fire resistance. However, due to the high costs and limited resources, two large-scale standard fire furnace tests were conducted as part of this project, one of which only included the isolated SD system and the other on a scaled-down structural frame (spanning 5.66 m and 3.64 m wide) based on the CBS system's design, with the SD system attached to the bottom of the beams. The tests were conducted with the use of a newly build standard fire furnace with a floor size of 6 m × 4 m. Standard fire tests do not fully represent real fire behaviour in typical structural fires, nonetheless, it has been a long-standing international benchmark to assess the performance of structural components and systems in fire.

Similar to the work performed by Marx (2018) and Kloos (2017), this dissertation will primarily focus on the thermal behaviour and structural response of the CBS system in fire. Utilizing the more comprehensive experimental data gained in the large-scale standard fire tests, numerous FE models have been developed to further investigate the heat transfer through the various layers of the SD system and structural response of the CBS system. The FE analyses performed in this research also culminate in a fully decoupled thermomechanical analysis of the CBS system. Specific attention is paid to the thermal performance of the SD system as this is the main component to act as the fire barrier in the CBS system.

There is a limited amount of literature with large- or full-scale fire testing experimental data available. Hence, the experimental data gained in this work will add to the empirical evidence in literature for quantifying global structural performance. Furthermore, the findings in this research will assist in extending the fire engineering approach in the area of structural performance and fire safety design for non-composite steel structures, and for the SD system.

However, in the interest of keeping the project scope realistic, the following limitations have been set out as listed below.

- I. The influence of the CBS system's columns at elevated temperatures have been excluded from all analyses as it has been assumed that the columns will be fire protected using standard prescriptive methods.
- II. The thermal properties of the components used in the SD system vary from one supplier and manufacturer to the other. Thus, the temperatures obtained from the FE heat transfer analyses are only applicable to the thermal properties implemented into the material properties models of this dissertation. The thermal properties of the boards and steel decking used in the SD system are based on thermal properties found in literature and calibrated according to the experimental data.
- III. The scale of the models will only extend to the size of the actual scaled-down experimental structural frame tested in this work (i.e., analysis of the CBS system with multiple floors and compartments will not be considered).

The secondary focus of this dissertation is the determination of the flexural performance of the SD system as a stand-alone flooring system to be used in the CBS system design and potentially used in other structural designs. Multiple medium-scale four-point bending tests are carried out on two variations of the SD system, namely, the VP50 and VP115 versions of the SD system, in combination with different board thicknesses and fixity arrangements. Again, the scope is limited to only the flexural performance of the SD system, i.e., the vertical stiffness of the SD system. Thus, no investigations have been carried out on the damping this system may provide, which is crucial if vibration induced discomfort to the occupants is to be avoided. Similarly, no investigations into the acoustics that the system may provide have been carried out in this work. Furthermore, only single span simply supported variations of the system have been considered in this work. Hence, the flexural performance of the SD system variations has not been tested or quantified in multi-span experimental setups. Finally, the flexural performance of the SD system variations at elevated temperatures have also not been considered in this dissertation.

## 1.5 Dissertation outline

To successfully achieve the project goals and objectives listed in Section 1.3, the following process was followed, forming the synopsis of this dissertation.

*Chapter 2* provides a literature overview of general concepts in structural fire engineering, the behaviour of steel and cellular beams in fire, and important concepts related to fire engineering. Topics related to general fire behaviour will also be covered.

*Chapter 3* serves as a thorough introduction to the CBS and SD systems and the findings of previous research conducted on the systems. Specific details of the design and layout of the CBS system and of the experimental frame tested in the standard fire furnace will be presented. The final proposed design of the SD system tested is also presented, highlighting the design changes that have been made as a result of the findings in the previous research conducted.

*Chapter 4* details the small-scale material tests and the medium-scale four-point bending tests conducted throughout this research and the results thereof, highlighting the general observations made during testing and the failure modes that occurred. Details of the experimental setup of each test conducted are outlined. The SD system capacity results according to SANS 10162-1 (SABS, 2011b) ultimate and serviceability limit states are also presented.

*Chapter 5* describes the findings of two large-scale standard fire tests carried out in this study, highlighting general observations made during the tests as well as the failure modes that occurred. Each test's experimental setups will be fully described. The data from the two large-scale fire tests, which includes the time-temperature and deflection curves will be presented.

*Chapter 6* details the development of the experimental model to predict the deflection behaviour of the VP115-20 SD system variation tested in the four-point bending tests at ambient temperature. Results of the numerical analysis will also be presented.

*Chapter 7* details the thermal response model developed to predict the temperature evolution of the SD system tested in the second large-scale standard fire test, which includes the experimental frame as mentioned above. Results of the numerical analysis will also be presented.

*Chapter 8* details the development of the thermal-stress models to predict the thermal-stress response of the experimental frame tested in the second large-scale standard fire test, which includes multiple single element models and a single global structural model. The results of each of the models will also be presented.

*Chapter 9* presents the most important findings of the research and compliance of the CBS and SD system with the national building codes, which is done such that the findings can be internationally applicable. Shortcomings of the structural system are detailed along with the necessary design changes made to give a final design methodology for the system to be used in commercial production of the system.

## Chapter 2 Literature review

### 2.1 Introduction

The aim of this chapter is to provide insight to the current literature available related to structural fire engineering. First, a brief discussion on the general background on fire safety and structural fire engineering is presented. Following that, a discussion on standard and performance-based fire testing will be presented. Thereafter, a review of the science of fire and its heat transfer mechanisms is presented. Next, a discussion on steel structures exposed to fire, protective systems, mechanical and thermal properties, and cellular beams in fire is given. The following section presents a discussion on profiled steel sheet dry board systems (PSSDB). Finally, we will look at advanced calculation methods and the complexities that must be considered when doing fire design.

### 2.2 General background on fire safety

Since its discovery, fire has had a profound impact on the manner of life of all people on the planet. However, with this amazing discovery came a huge potential for calamity, as fire can be a destructive force to be reckoned with. There have been a number of memorable fires during the past centuries across the world, destroying homes and killing people in the thousands, leaving cities and communities in ruin (Walls, 2016). The great Chicago fire of 1871, which displaced about 90,000 people and killed an estimated 300 people, is a well-known example (Woody, 1947). More recently, the Campfire in California in November 2018 destroyed over 18,000 structures and killed 85 people, making it the state's deadliest and most destructive fire event in recent history (CAL FIRE, 2019a, 2019b). Throughout literature, there are numerous relevant fire disasters, proving that it still remains a significant problem in our society that needs to be addressed.

In the wake of every fire disaster, progress was gradually made over time to develop stricter construction rules and methods to prevent future fires. As in the time after the great Chicago fire, the new mayor Joseph Medill (1823-99) was elected after promising to enforce stricter building and fire codes, a pledge that may have won him the office. He led the Fireproof-Reform party who proposed legislation to ban wooden construction frame buildings in city limits. Legislation was also passed to give government officials authority to regulate building materials and review construction plans (Dilworth, 2011; Grossman, 2016; History.com Editors, 2010). This history forms part of the growth over time in the field of fire and structural fire engineering. The reader is referred to Law and Bisby (2020) for an interesting read on the historical development of fire testing. Structural fire engineering is essentially a combination of two older disciplines, structural engineering, and fire engineering (Lennon, 2011). The primary aim of such research is to reduce to an acceptable level, loss of life, property and environmental damaged suffered during an unwanted fire.

## 2.3 Standard Fire Testing

In the wake of the Baltimore and San Francisco fires at the turn of the 20<sup>th</sup> century, standard fire testing emerged as an assessment for comparative performance testing of different building materials and systems in the most severe fire possible (Gales *et al.*, 2012). Single element or isolated structural assemblies are tested in testing furnaces, where they are mechanically loaded and subjected to a time-temperature fire curve to induce the thermomechanical stresses in each element as if they were in place of the actual structure. The fire curve typically used in fire resistance tests is called the standard fire curve (Purkiss, 2007). The standard fire curve estimates the increase of temperature over time according to a logarithmic relationship, it assumes that the temperature in a compartment fire is uniform and that it increases indefinitely with time (Wang *et al.*, 2012). This testing methodology has been incorporated into several design standards world-wide since then and developed further to include various other structural elements and standard fire curves, namely the external and hydrocarbon fire curves. The Eurocodes, which have also been drawn from in the study, are considered the most technically advanced with regards to fire design. Below we have the nominal temperature-time curves (BSI, 2002) and as depicted in Figure 2-1.

Standard temperature-time curve with the gas temperature  $\theta_g$ , at a given time  $t$ :

$$\theta_g = 20 + 354 \log_{10}(8t + 1) \quad (2.1)$$

Hydrocarbon temperature-time curve is given by:

$$\theta_g = 1080(1 - 0.325e^{-0.167t} - 0.675e^{-2.5t}) + 20 \quad (2.2)$$

External temperature-time curve is given by:

$$\theta_g = 660(1 - 0.687e^{-0.32t} - 0.313e^{-3.8t}) + 20 \quad (2.3)$$

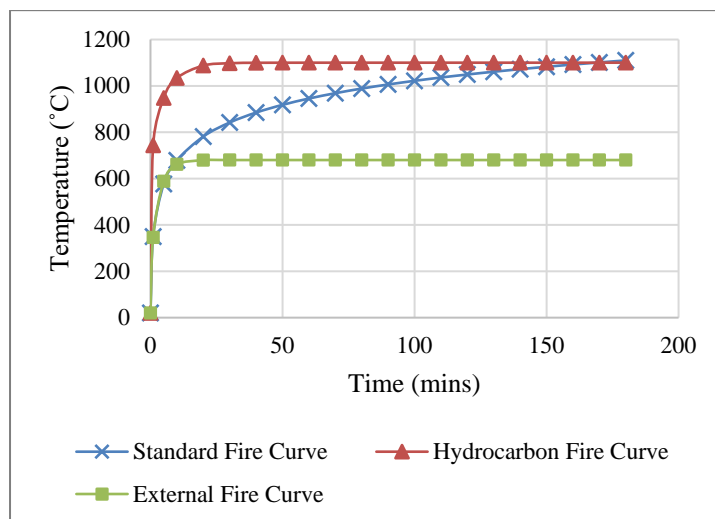


**Figure 2-1 Time-temperature curves of the standard, external and hydrocarbon fire curves.**

It was argued by many that standard fire testing serves as a good benchmark since it could be easily repeated in a controlled environment (Bisby *et al.*, 2013). Although there are some legitimate benefits, there are also significant drawbacks that must be considered. The lack of a cooling branch and the absence of physical parameters that govern fire behaviour, such as fuel load and available ventilation, are notable drawbacks (Wang *et al.*, 2012). Furthermore, the size of test furnaces is limited, making more realistic multi-span beam testing difficult. This also contributes to the fact that most specimens can only be tested using idealized end conditions (Purkiss, 2007).

### 2.3.1 Prescriptive design approach

Information in this section was drawn from (Purkiss, 2007), unless stated otherwise. A series of critical failure criteria, known as the fire-limit-state (FLS) has been identified from standard fire testing and listed below.

1. Load bearing capacity: The element under consideration should be able to have sufficient load bearing capacity to resist the applied load for the entire duration of the test.
2. Insulation: The temperatures on the unexposed face should maintain a temperature low enough not to ignite combustible material in contact with it.
3. Integrity: The integrity of the unexposed face should be maintained throughout the test by not letting any flame or enough heat to pass through any weakness or cracks developed during the tests due to deformations or inherent weaknesses in the construction itself.

Keeping this design philosophy in mind, prescriptive methods for designing structures were developed by interpreting the data collected from standard fire tests over time. These were typically developed into tabulated data sets in the design codes that could easily be understood and used by the designer without much understanding of structural fire engineering. As stated in Purkiss (2007), these are prescriptive methods in that the designer is told what parameters to use rather than being able to calculate these values. Depending on the nature of the structure, a “Fire Resistance Rating” will be required. Based on standard fire testing until one of the fire limit state failure criteria are met, a grading classification is given to the structure in terms of time (minutes), i.e., 30, 60, 90, 120, 180 or 240 minutes. Using this grading, a specified thickness of fire protection or protective system could be applied to the structural elements to achieve the required fire resistance. One of the most well-known guides used today was developed by the Association for Specialist Fire Protection (ASFP), also known as the “Yellow book” (ASFP, 2014).

## 2.4 Performance-based design

By the early 1920s', it was established that standard fire testing was not representative of a real fire and by the 1980s' a change in testing methodology was demanded. Margaret Law presented a paper at the 1981 ASCE Spring Convention in New York, presenting the work she and her colleagues had completed at Arup Fire using performance-based design to engineer the structural fire safety of prominent structures at the time (Bisby *et al.*, 2013). She had used this opportunity to give much needed criticism to the predominant standard fire testing methodology. Although standard fire testing still remains the predominant method of fire design, there have been several major structural fires in the past three decades that have brought to light the mostly already known shortcomings, and thus reaffirming previous criticism by the likes of Law.

Many countries have now started adopting performance-based codes, giving designers the opportunity to take a rational engineering approach and allowing them to use any fire safety strategy they wish, granted they demonstrate adequate safety (Buchanan and Abu, 2017). The SFPE Engineering Guide to Performance Based Fire Protection defines performance-based design according to the following three criteria: (1) agreed upon fire safety goals and objectives, (2) deterministic and/or probabilistic analysis of fire scenarios, and (3) quantitative assessment of design alternatives against the fire safety goals and objectives using accepted engineering tools, methodologies, and performance criteria. It is further stated that three key attributes can be identified from this definition on performance-based design: (1) a description of the desired level of fire safety in a building (or other structure) in the event of a fire, (2) a definition of the "design basis", which includes the identification of the types of fires, occupant characteristics, and building characteristics for which the fire safety systems in the building are intended to protect, and (3) engineering analysis of proposed design strategies to determine whether they provide the desired level of protection (Hurley *et al.*, 2015). It can be taken from this that prescriptive design is based on data collected and refined over an extended period and only considers a single element or assembly of the structure, while performance-based design evaluates the structure as a whole and have unique solutions to the design.

### 2.4.1 Eurocode parametric fire curves

Around the early 1970's, Swedish engineers Pettersson, Magnuson and Thor developed a method of predicting the gas temperatures of compartment fires by considering the heat balance in a compartment fire based on Kawagoe's equation for heat release rate. Based on these ventilation controlled fire experiments, they developed what is now known as the Swedish curves (Buchanan and Abu, 2017).

This model formed the basis of EN 1991-1-2 (BSI, 2002) parametric fire curve and was used as background theory by Wickström (1981/2,1985a) who proposed this approach (Purkiss, 2007). Wickström suggested that the compartment time-temperature relationship was entirely dependent on the ratio of the opening factor  $\frac{A_v \sqrt{h_{eq}}}{A_t}$  to the thermal inertia  $\sqrt{\rho c \lambda}$  of the compartment (Purkiss, 2007). The equations used in the Eurocode were derived to give a good approximation to the Swedish curves. It gives a more realistic representation of a real

fire as the equation considers input variables such as the ventilation conditions, fire load and thermal properties of the compartment. Below we have the expression for this method and explained as in Wang *et al* (2012), for a more comprehensive and in detail understanding please refer to the EN 1991-1-2 (BSI, 2002) as only key components are discussed here.

$$\theta_g = 20 + 1325(1 - 0.324e^{-0.2t^*} - 0.204e^{-1.7t^*} - 0.427e^{-19t^*}) \quad (2.4)$$

Here  $t^* = t\Gamma$

Where  $t$  is time given in hours, and  $\Gamma$  is a dimensionless quantity computed by the various input data. The input data for  $\Gamma$  depends on whether the fire is predicted to be ventilation or fuel controlled. This prediction depends on the time  $t_{max}$  at which the peak gas temperature occurs, and the cooling phase begins. When the fire is ventilation controlled,  $t_{max}$  is determined by the expression below.

$$t_{max} = 0.2 \times 10^{-3} q_{dt} \frac{A_t}{A_v \sqrt{h_{eq}}} \quad (2.5)$$

Where  $q_{dt}$  is the fire load density related to the total surface area of the compartment  $A_t$  ( $m^2$ ) given in terms of  $[MJ/m^2]$ ,  $A_v$  is the area of the ventilation openings and  $h_{eq}$  is the weighted average height of the openings. However, when we have the case of

$$t_{lim} > 0.2 \times 10^{-3} q_{dt} \frac{A_t}{A_v \sqrt{h_{eq}}} \quad (2.6)$$

The fire is then said to be fuel controlled, and  $t_{max} = t_{lim}$

The values of  $t_{lim}$  depend on whether the fire is considered to grow at a slow, medium, or fast rate.

In the case of ventilation-controlled fire and in a compartment that has boundaries made of uniform, thermally thick materials,  $\Gamma$  is given as below.

$$\Gamma = 8.41 \times 10^8 \left( \frac{A_v}{A_t} \right)^2 \left( \frac{h_{eq}}{\rho c \lambda} \right) \quad (2.7)$$

With  $\lambda$ ,  $c$  and  $\rho$  being the conductivity, specific heat capacity and density of the compartment boundaries respectively.

When we have a fuel-controlled fire,

$$\Gamma = 8.41 \times 10^8 \left( \frac{0.1 \times 10^{-3} q_{td}}{t_{lim}} \right)^2 \frac{1}{\rho c \lambda} \quad (2.8)$$

It should be noted that this expression does not contain the opening factor of the compartment, indicating that the fire is not influenced by the availability of ventilation to the fire.

For the cooling phases of the parametric fire, we have:

$$\theta_g = \theta_{max} - 625(t^* - t_{max}^*x) \quad \text{for } t_{max}^* \leq 0.5 \quad (2.9)$$

$$\theta_g = \theta_{max} - 250(3 - t_{max}^*)(t^* - t_{max}^*x) \quad \text{for } 0.5 < t_{max}^* < 2 \quad (2.10)$$

$$\theta_g = \theta_{max} - 250(t^* - t_{max}^*x) \quad \text{for } t_{max}^* \geq 2 \quad (2.11)$$

Where  $x = 1$  for  $t_{max} > t_{lim}$ , and  $x = t_{lim}^\Gamma / t_{max}^*$  for  $t_{max} = t_{lim}$

## 2.5 Fire behaviour

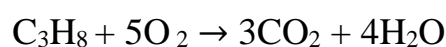
To obtain a deeper understanding of structural fire engineering, there are important topics to be discussed on the behaviour of fire and its effects on structures. This will be presented by introducing what fire actually is, followed by key principles in fire dynamics of heat transfer.

### 2.5.1 What fire really is

The following information presented was mainly drawn from Quintiere (2016) unless specified otherwise. The scientific definition for fire is not as simple as one may think. Fire is a chemical reaction involving fuel and an oxidizer, which would typically be the oxygen in the air. However, this is not a perfect description as rusting and yellowing of newspaper print fits this definition as well. Consequently, the distinction to be fire is that a significant amount of energy must be released (Quintiere, 2016). There might also be the misconception that fire and combustion can be distinguished from one another, when in fact they are synonymous in scientific terms, that is to say, fire is combustion that is not controlled. Fire emits heat energy in the form of light, the colour of the light depends on the chemical composition of the burning fuel. The light emitted by fire does not necessarily have to be visible light as in the case of burning hydrogen ( $H_2$ ) with oxygen to produce only water vapour (Quintiere, 2016).

All solid and liquid fuels have to be converted to a gaseous phase before they can burn. For liquids, this phase change in the presence of heat is *evaporation*. Some polymers go through a process of *thermal decomposition* into new volatile products. Solids are *melted* when heated into liquids which can subsequently be evaporated into a gaseous state to burn. However, some other fuels, including most wood products, thermally decompose to transition directly from a solid to gaseous state. This form of transition is known as *pyrolysis* of wood (Buchanan and Abu, 2017).

In nature, fire typically burns using hydrocarbon-based fuels, fuels composed mostly of hydrogen and carbon atoms in the presence of oxygen to produce water vapour and carbon dioxide (Buchanan and Abu, 2017). Below we have a simple example of the complete stoichiometric chemical reaction of propane given by:



The chemistry is simplified here, when in fact the chemistry is continuously changing throughout the combustion process depending on the temperatures, pressures and availability of fuel.

A concept used to describe the components that are essential for a fire is known as the fire triangle as shown in Figure 2-2 below. The triangle consists of (1) the available fuel combining with (2) the available oxygen in a chemical reaction to release (3) energy and other by-products as demonstrated below. The heat produced by the fire is transferred back to the oxygen and fuel to keep the combustion process ongoing (Quintiere, 2016).

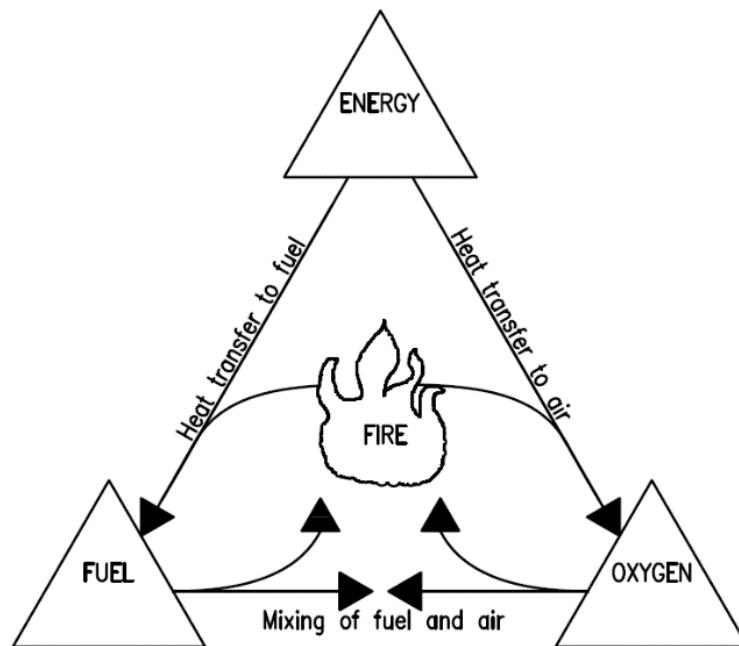


Figure 2-2 Fire triangle. (Drawn using AutoCad by author)

### 2.5.2 Heat transfer mechanisms

Heat is defined as thermal energy in motion from a “hot” region with a high internal energy to a “cold” region with a low internal energy. The mechanisms by which the heat is transferred, exchanged or redistributed are governed by two laws, one describes the energy travel within matter and the other in the absence of matter such as the vacuum of space. The former describes conduction heat transfer, and the latter describes radiation heat transfer, making these two the fundamental modes of heat transfer. Convection, which is a third mechanism of heat transfer, is a subset of conduction and does not need its own law to predict it. Conceptually it is the combined effects of conduction (and/or radiation) within a moving medium (Hurley *et al.*, 2015). These “Laws” are not as perfect as the laws of conservation of mass and energy; though they are very good approximations (Quintiere, 2016).

## Conduction

Joseph Fourier formulated the law of heat conduction back in the early 1800s, it described the rate of heat flow through matter as directly proportional to temperature differences divided by the distance between those temperatures in the substance (Quintiere, 2016). In more simpler terms, conduction is the mechanism of heat transfer in solid materials from a point of higher temperature to a point of lower temperature, as well as from one solid to another that are in contact with each other (Kloos, 2017; Quintiere, 2016). Heat is transferred through the interactions of free electrons within the material. This form of transfer relationship is analogous to that of the flow rate of electrons in a metal, for this reason it is generally accepted that a material with good electrical conduction are good heat conductors as well (Kloos, 2017; Quintiere, 2016). Depending on the scenario at hand, different formulations of the conduction equation can be utilised and have broadly been split into two categories, steady-state heat conduction and transient heat conduction. For steady-state heat conduction, the transfer of heat is directly proportional to the temperature gradient between two points, with the constant of proportionality known as the thermal conductivity ( $\lambda$ ). Hence, for steady-state heat conduction temperature does not change with time and if the thermal conductivity does not change with temperature (i.e.,  $\lambda = \text{constant}$ ), the temperature gradient between the two points become linear. For transient heat conduction the temperature varies with time and the amount of heat required to change the temperature of the material must be considered by introducing the material density ( $\rho$ ) and specific heat capacity ( $c$ ) to the equation (Hurley *et al.*, 2015). The one-dimensional steady-state heat conduction and the transient heat diffusion equations are as shown below.

$$\text{Steady-state} \qquad q_{con} = \lambda \frac{dT}{dx} \qquad (2.12)$$

$$\text{Transient} \qquad \frac{\partial T}{\partial t} = \frac{\lambda}{\rho c} \frac{\partial^2 T}{\partial x^2} \qquad (2.13)$$

Where

$\lambda$  is the thermal conductivity (W/mK)

$\rho$  is the material density (Kg/m<sup>3</sup>)

$c$  is the specific heat capacity (J/KgK)

T is temperature (°C or K)

t in the time (seconds)

x is distance in the direction of heat flow (m)

$q_{con}$  is the rate of heat flow per unit area (W/m<sup>2</sup>)

### **Convection**

As stated above, conceptually convection is the combined effect of conduction (and/or radiation) and the motion of the transmitting medium (Hurley *et al.*, 2015). Calculations usually involve the heat transfer between the surface of a solid and a surrounding fluid which cools or heats the solid material, the fluid can be either gases or a liquid (Buchanan and Abu, 2017). The distinction made between convection and conduction is associated with whether the medium has some ordered flow or velocity. Hence, heat transfer when there is a averaged mass velocity is termed convection, while conduction takes place in a stationary frame of reference (Hurley *et al.*, 2015). Although convection is in its own category of heat transfer, it does not require a separate “law” to predict it as mentioned earlier, as the formulas used here can be derived from the law of conduction. However, the temperature differences and distances traversed near the surface are not measured or derived from pure conduction considerations (Quintiere, 2016).

This form of heat transfer plays a significant role in the upward transport of smoke and flame spread. The rate at which heating, or cooling occurs depend on many factors, especially on the velocity of the fluid surrounding the solid material (Marx, 2018). The fluid passing the solid surface can either be forced convection, natural convection or a combination of both. Natural convection is driven by buoyancy forces induced by the density differences caused by an increase in temperature (hot air rises and cold air rushes to replace it). Forced convection occurs when the flow of the fluid is induced by an external force such as the wind or a fan. The simplest representation of the heat flux generated is given by:

$$q_{conv} = h\Delta T \quad (2.14)$$

Where

$q_{conv}$  is the heat flux generated (W/m<sup>2</sup>)

$h$  is the heat transfer coefficient (W/m<sup>2</sup>K)

$\Delta T$  is the temperature difference between the solid and the surrounding liquid or gas (°C or K)

### **Radiation**

It took nearly 100 years after the formulation of the law of conduction for Max Planck’s quantum theory to lead us to the theoretical basis of radiation heat transfer in the early 1900s. Simply put, radiation is the transfer of energy by electromagnetic waves through a vacuum of space, or through a transparent solid or liquid (Buchanan and Abu, 2017). Radiation allows for spatially distant objects to exchange heat with one another while convection and conduction must be in contact to make the heat transfer (Hurley *et al.*, 2015). Understanding radiation heat requires some knowledge of electromagnetic wave theory. Electromagnetic waves have both a frequency and a speed, all electromagnetic waves have the same speed, which is at about 29,979,245,800 cm/s but not the same frequencies. The different frequency ranges of these waves determine the name or phenomena associated with the radiation (Quintiere, 2016). Electromagnetic radiation is the propagation of a collection of particles normally referred to as photons. These photons that are generated by the sub-molecular processes

created by the objects internal energy carry different energies. The energy of the photon is proportional to the frequency of the wave with the constant of proportionality being Planck's constant ( $6.626 \times 10^{-34}$  J·s) (Hurley *et al.*, 2015).

Radiation heat plays an important role as it is the main mechanism of heat transfer from the hot flames to the fuel surfaces, or the hot smoke to building objects (Buchanan and Abu, 2017). The radiant heat flux from the emitting surface to the receiving surface is given by:

$$q_{rad} = \epsilon_{res} \sigma \varphi (T_e^4 - T_r^4) \quad (2.15)$$

Where

$q_{rad}$  is the resultant heat flow from the emitting surface to the receiving surface ( $W/m^2$ )

$\sigma$  is the Stefan-Boltzmann constant given as  $5.67 \times 10^{-8} W/m^2 k^4$

$T_e$  and  $T_r$  are the absolute temperatures (K) of the emitting and receiving surfaces, respectively.

$\epsilon_{res}$  is the resultant emissivity of the two surfaces given by:

$$\epsilon_{res} = \frac{\epsilon_e \cdot \epsilon_r}{\epsilon_r + \epsilon_e - \epsilon_e \cdot \epsilon_r} \quad (2.16)$$

Where

$\epsilon_{res}$  is the resultant emissivity between the emitting and receiving surfaces.

$\epsilon_r$  is the emissivity of the receiving surface.

$\epsilon_e$  is the emissivity of the emitting surface.

The emissivity indicates the efficiency of the emitting surface as a radiator, with values that range from 0 to 1.

$\varphi$  is the configuration factor (sometimes referred to as the view factor) and is a measure of how much of the emitter is 'seen' by the receiving surface (Buchanan and Abu, 2017). The equation used to calculate the configuration factor between an emitting and receiving surface is as given below.

$$\varphi = \int_{A_{emitter}} \frac{\cos \theta_{emitter} \cos \theta_{receiver}}{\pi r^2} dA_{emitter} \quad (2.17)$$

## 2.6 Steel structures exposed to fire

Information presented in this section was mainly drawn from Buchanan and Abu (2017) and Purkiss (2007). When compared to reinforced concrete or heavy timber structures, steel structures tend to perform poorly. This is in part due to its high thermal conductivity and steel elements usually being much thinner. In other words, steel loses its strength and stiffness rapidly with an increase in its temperature. That being said, well-designed steel structures are capable of resisting severe fires without collapse, even if some of the main load-bearing members remain unprotected (Buchanan and Abu, 2017).

This section will cover the behaviour of steel structures in fire and how to assess the performance of steel structures in fire, starting with an introduction to structural design in fire. Thereafter a discussion on some protective systems for steel structures is presented, followed by the thermal and mechanical properties of steel at elevated temperatures. Finally, a brief discussion on the behaviour of cellular beams in fire is presented.

### 2.6.1 Steel design in fire

As stated by Buchanan and Abu (2017), the design process for fire resistance requires that the provided fire resistance exceeds the design fire severity. This verification can be done in three domains, namely the *time domain*, the *temperature domain*, and the *strength domain*. Verification in the *time domain* requires that the design time value of fire resistance should be equal to or more than the required fire resistance time. In *temperature domain* verification, the critical material temperature should be equal to or higher than the design value of the material temperature. In *strength domain* verification, the design value of the resistance of the member should be equal to or higher than the design value of the relevant effects of actions in the fire situation.

The structural Eurocodes will be adopted in this research as mentioned before. The codes are based on ultimate limit state. There is one set of standards for each of the main construction methods, for which Part 1-2 deals with fire resistance design, with EN 1993-1-2 (BSI, 2005) specifically for structural steelwork in fire.

### 2.6.2 Protective systems for steel structures

Protective systems of structures are split into two categories, active protection systems and passive protection systems. Active protection systems require some form of outside input or must be triggered by some action, whereas passive protection systems are inherently built into the structure and do not need any outside action or involvement (Buchanan and Abu, 2017).

Active protection systems can either be triggered automatically, as in the case of sprinkler systems and smoke detectors, or need some outside input, like a fire extinguisher and firemen. These will not be discussed in detail as they do not fall in the scope of this research.

There are many different passive protection systems used today to reduce the rate of temperature increase in steel elements. They all come with their own unique advantages and shortcomings. According to Purkiss (2007), there are essentially five basic methods of fire protecting steelwork: board systems, spray systems, intumescent paints, brickwork and concrete encasement. We will only consider the first three as they are the most widely used.

**Board systems:** The steel elements are protected by encasing them with protective boards. There is a wide range of proprietary board systems available, with most of them manufactured from calcium silicate or gypsum plaster. Some of the advantages of using boards systems are that they are quick and easy to install with relatively little mess as it is a dry process, and the building decorative material can easily be applied directly for an aesthetically pleasing finish. That being said, they are slower and more expensive than spray-on systems

(Buchanan and Abu, 2017; Purkiss, 2007). These systems do not work as well when the geometries of the steel members become too complicated, thus making installation a complicated process.

**Spray-on systems:** This system works by spraying a wet gunite-type material to the steel members. They are usually cement-based with some form of glass or cellulosic fibrous reinforcing to hold it together. Spray-on systems are usually the cheapest form of fire protection, and the mixture can be easily and quickly sprayed on the structural members. However, this is a wet and messy process that gives a finish that is not aesthetically pleasing; thus, they are generally used to protect beams where there are false ceilings (Buchanan and Abu, 2017; Purkiss, 2007).

**Intumescent paint:** This is a special paint material which when exposed to heat foam up into a thick charred mass. This layer of char provides insulation for the steel member beneath in the form of aerated carbon. The advantages to using intumescent paint systems are that it normally gives an aesthetically pleasing finish and can be applied to complicated geometries like normal paint. This form of fire protection typically costs much more when compared to board or spray-on systems (Buchanan and Abu, 2017; Purkiss, 2007)

### 2.6.3 Thermal and mechanical properties of steel at elevated temperatures

Understanding the material properties of steel at elevated temperatures forms an integral part of structural fire engineering and some of the relevant aspects will be addressed in this section. Having knowledge on how the thermal and mechanical properties behave at elevated temperatures gives the designer the ability to more accurately model the structural response under different circumstances of fire growth and solving the Fourier equation of heat diffusion (Purkiss, 2007; Wang *et al.*, 2012). Fortunately, there is an extensive body of knowledge available on the subject from numerous experiments conducted with published papers and textbooks (Purkiss, 2007). Some of the earliest values reported in literature will be presented where applicable, however, the Eurocode formulations EN 1993-1-2 (BSI, 2005) will be utilized throughout this dissertation. This section will be presented in two parts, with the thermal and mechanical properties considered separately.

#### **Thermal conductivity**

The thermal conductivity ( $\lambda$ ) of a material represents the rate at which heat is conducted through it. In other words, it's the rate of energy conducted per second (in watts) per square meter at a point to the temperature gradient (in °C or K) at this point (Wang *et al.*, 2012). Typical values of the thermal conductivity of steel were first reported in (Malhotra, 1982; Pettersson *et al.*, 1976). Interestingly, it should be noted that the thermal conductivity values of steel are slightly dependant on the steel strength, the reason for this is unknown, but fortunately it does not make a significant difference and may be ignored (Purkiss, 2007). The expression below represents the thermal conductivity values of steel as defined in EN 1993-1-2 (BSI, 2005), and is shown in Figure 2-3 below.

$$\text{for } \theta_a = 20^\circ\text{C to } \theta_a = 800^\circ\text{C} : \quad \lambda_a = 54 - 3.33 \times 10^{-2}\theta_a \quad \text{W/mK} \quad (2.18)$$

$$\text{For } \theta_a = 800^\circ\text{C to } \theta_a = 1200^\circ\text{C} : \quad \lambda_a = 27.3 \quad \text{W/mK} \quad (2.19)$$

Where  $\theta_a$  is the temperature of the steel in °C and  $\lambda_a$  the thermal conductivity of the steel in W/mK.

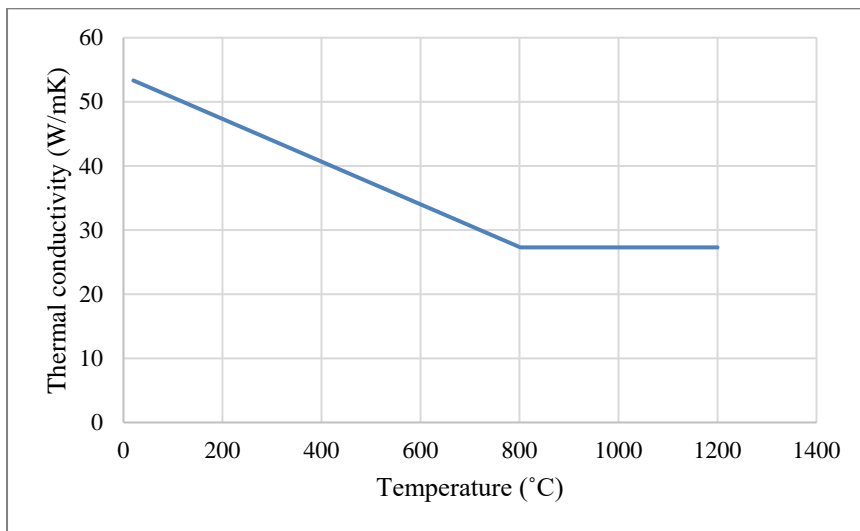


**Figure 2-3 Thermal conductivity of carbon steel as a function of the temperature (BSI, 2005).**

### ***Specific heat capacity***

Specific heat capacity of any material is the amount of energy (joules) that it needs to gain to raise the temperature of a unit mass (1 Kg) of the material by 1 °C. Some of the earliest test data and formulation for the specific heat capacity of steel was also reported by (Malhotra, 1982; Pettersson *et al.*, 1976), however, the test data and formulation did not account for the phase change that occurs around 750 °C and only given up to this temperature (Purkiss, 2007). EN 1993-1-2 defines the specific heat capacity up to a temperature of 1200 °C and accounts for the phase change that occurs within the 700-800°C range. This spike in the graph (Figure 2-4) represents the input needed to allow the endothermic process of the crystal structure phase change from body-centred to face-centred to take place. Below we have the specific heat capacity as defined in EN 1993-1-2 with the sequence of equations that express the characteristics of carbon steels, and is shown in Figure 2-4 below.

For  $\theta_a = 20^\circ\text{C}$  to  $\theta_a = 600^\circ\text{C}$

$$c_a = 425 + 7.73 \times 10^{-1}\theta_a - 1.69 \times 10^{-3}\theta_a^2 + 2.22 \times 10^{-6}\theta_a^3 \text{ J/kgK} \quad (2.20)$$

$$\text{For } \theta_a = 600^\circ\text{C} \text{ to } \theta_a = 735^\circ\text{C} : c_a = 666 + \frac{13002}{(738 - \theta_a)} \text{ J/kgK} \quad (2.21)$$

$$\text{For } \theta_a = 735^\circ\text{C} \text{ to } \theta_a = 900^\circ\text{C} : c_a = 545 + \frac{17820}{(\theta_a - 731)} \text{ J/kgK} \quad (2.22)$$

$$\text{For } \theta_a = 900^\circ\text{C} \text{ to } \theta_a = 1200^\circ\text{C} : c_a = 650 \text{ J/kgK} \quad (2.23)$$

Where  $c_a$  is the specific heat capacity of the steel in J/KgK

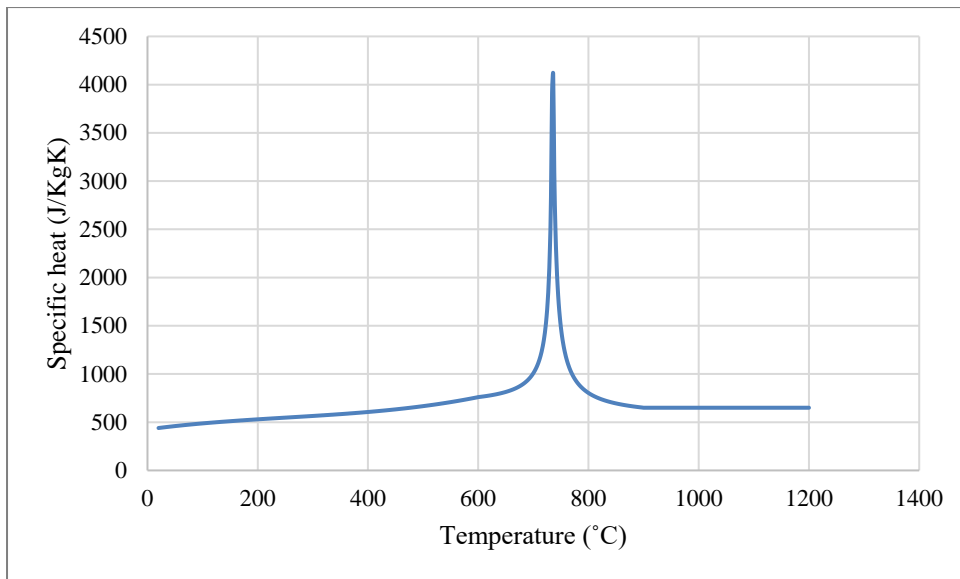


Figure 2-4 Specific heat of carbon steel as a function of temperature (BSI, 2005).

### ***Thermal expansion***

Thermal expansion is normally neglected in simple fire engineering calculations. However, when one has the case of steel members that support a concrete slab, the differential thermal expansion caused by the shielding of the concrete on the top flange and the heat-sink function of the concrete may cause thermal bowing. When using advanced model calculations, it should always be borne in mind that the structural elements in the fire compartment are restrained by the cool surrounding structure, thus, giving considerably different results than that of an unrestrained furnace test (Wang *et al.*, 2012). Below is the thermal expansion of carbon steel as given in the EN 1993-1-2 (BSI, 2005) and defined by the following curve-fitting equations, and is shown in Figure 2-5 below.

For  $\theta_a = 20^\circ\text{C}$  to  $\theta_a = 750^\circ\text{C}$  :

$$\Delta l/l = 1.2 \times 10^{-5} \theta_a + 4.0 \times 10^{-8} \theta_a^2 - 2.416 \times 10^{-4} \quad (2.24)$$

$$\text{For } \theta_a = 750^\circ\text{C} \text{ to } \theta_a = 860^\circ\text{C} : \quad \Delta l/l = 1.1 \times 10^{-2} \quad (2.25)$$

$$\text{For } \theta_a = 860^\circ\text{C} \text{ to } \theta_a = 1200^\circ\text{C} : \quad \Delta l/l = 2 \times 10^{-5} \theta_a - 6.2 \times 10^{-3} \theta_a \quad (2.26)$$

Where

$l$  is the length at  $20^\circ\text{C}$

$\Delta l$  is the temperature induced length

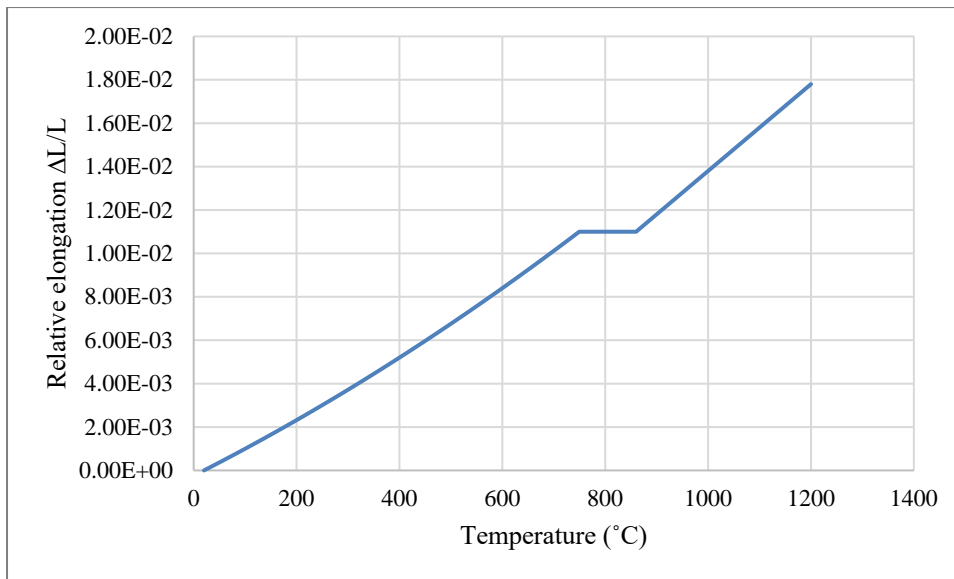


**Figure 2-5 Relative thermal elongation of carbon steel as a function of the temperature (BSI, 2005).**

Alternatively, a constant value of  $1.4 \times 10^{-5}$  may be used as recommended by the European Convention of Constructional Steelwork (Kloos, 2017).

### ***Stress-strain relationship at elevated temperatures***

Below we have the stress-strain curve as defined in EN 1993-1-2. Based on the lower bound of transient test results, EN 1993-1-2 developed stress-strain curves that vary only with temperature. It should be noted that a conservative approach is adopted here to account for the effects of creep. The curve may be summed up in four parts as described below:

1. The linear range that runs from zero stress to the limit of proportionality  $f_{p,\theta}$ . The gradient of this line represents the elastic modulus  $E_{a,\theta}$ , which is decreased as the temperature rises.
2. An ellipse is then constructed to be tangential to both the final point of the linear range ( $f_{p,\theta}, \epsilon_{p,\theta}$ ) and the horizontal at the yield point ( $f_{y,\theta}, \epsilon_{y,\theta}$ ) where strain is at 2%. The yield stress is decreased as the temperature rises.
3. A stress plateau runs from the yield point ( $f_{y,\theta}, \epsilon_{y,\theta}$ ) to the strain  $\epsilon_{t,\theta}$ , which is set at 15%.
4. The final phase represents the final fracture process and is presented by a negative linear range from  $\epsilon_{t,\theta}$  at 15% to  $\epsilon_{u,\theta}$  set at 20%.

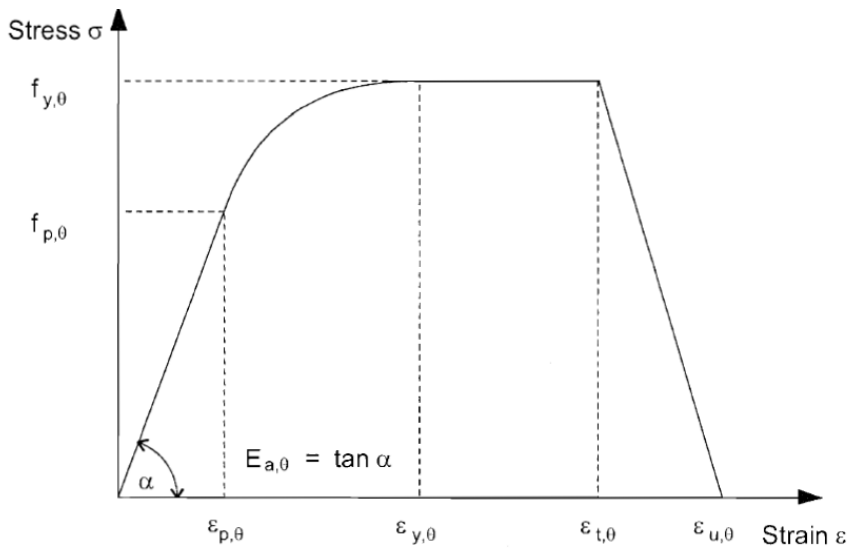


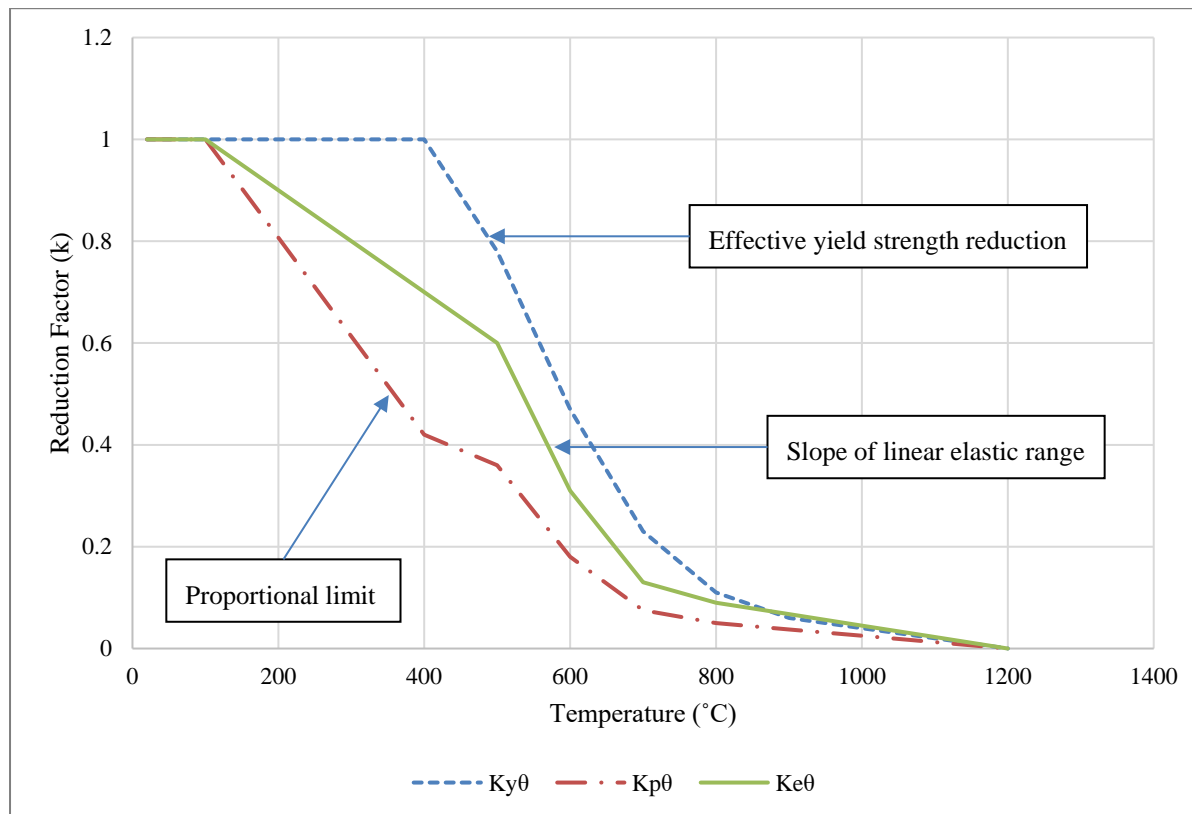
Figure 2-6 Stress-strain relationship for carbon steel at elevated temperatures (BSI, 2005).

Table 2-1 below presents the equations used to produce the general stress-strain curve:

Table 2-1 General equation used to produce the general stress-strain curve as defined in EN 1993-1-2 (BSI, 2005).

Strain Range	Stress $\sigma$	Tangent Modulus
$\varepsilon \leq \varepsilon_{p\theta}$	$\varepsilon E_{a\theta}$	$E_{a\theta}$
$\varepsilon_{p\theta} < \varepsilon < \varepsilon_{y\theta}$	$f_{p\theta} - c + (b/a)[a^2 - (\varepsilon_{y\theta} - \varepsilon)^2]^{0.5}$	$\frac{b(\varepsilon_{y\theta} - \varepsilon)}{a[a^2 - (\varepsilon_{y\theta} - \varepsilon)^2]^{0.5}}$
$\varepsilon_{y\theta} \leq \varepsilon \leq \varepsilon_{t\theta}$	$f_{y\theta}$	0
$\varepsilon_{t\theta} < \varepsilon < \varepsilon_{u\theta}$	$f_{p\theta} \left[ 1 - \frac{(\varepsilon - \varepsilon_{t\theta})}{(\varepsilon_{u\theta} - \varepsilon_{t\theta})} \right]$	-
$\varepsilon = \varepsilon_{u\theta}$	0.00	-
<b>Parameters</b>	$\varepsilon_{p\theta} = f_{p\theta} / E_{a\theta} \quad \varepsilon_{y\theta} = 0.02 \quad \varepsilon_{t\theta} = 0.15 \quad \varepsilon_{u\theta} = 0.2$	
<b>Functions</b>	$a^2 = (\varepsilon_{y\theta} - \varepsilon_{p\theta}) (\varepsilon_{y\theta} - \varepsilon_{p\theta} + c / E_{a\theta})$	
	$b^2 = c(\varepsilon_{y\theta} - \varepsilon_{p\theta}) E_{a\theta} + c^2$	
	$c = \frac{(f_{y\theta} - f_{p\theta})^2}{(\varepsilon_{y\theta} - \varepsilon_{p\theta}) E_{a\theta} - 2(f_{y\theta} - f_{p\theta})}$	

Using the above equations to construct the general stress-strain curve, data giving the elastic modulus, limit of proportionality and yield strength as a function of temperature would be required. For this reason, EN 1993-1-2 has conveniently defined these variables in terms of reduction factors and is represented graphically in a piecewise-linear form as given below.



**Figure 2-7 Reduction factors for the stress-strain relationship of carbon steel at elevated temperatures (BSI, 2005).**

#### 2.6.4 Testing of cellular beams in fire

With the growing popularity of long-span cellular steel beams, steel framed structures have become more competitive compared to reinforced concrete buildings. The structural element is known to be widely used in multi-storey buildings, commercial and industrial buildings, warehouses, and portal frames, in the UK and Europe. The use of cellular beams allows for all services to be integrated within the web openings, thus saving on the floor-to-floor height of the structure, and a composite concrete slab significantly increases the flexural capacity of the beam while also acting as a heat sink (Nadjai *et al.*, 2007, 2016; Vassart, 2009).

Furthermore, the performance assessment of structures in fire has also become increasingly relevant with time. This sparked an interest into the behaviour of cellular beams in fire conditions and how to assess the design effectively (Vassart, 2009). Design recommendations from analytical methods have been proposed over the past decade on the design of cellular beams in fire (Nadjai *et al.*, 2008; Vassart *et al.*, 2008; Vassart, Hawes, *et al.*, 2011). These methods are mainly based on the experimental results from multiple single element (simply supported) composite cellular beams tested in standard fire furnaces while loaded. The majority of the focus for the experimental testing was on the behaviour of cellular beams with composite concrete floors on top. In the

next section, a closer look at some of this experimental and numerical data published is provided and a summary of the literature provided in Table 2-2 below.

An early paper describes the experimental and numerical study of full-scale composite floor cellular beams at ambient and elevated temperatures (Nadjai *et al.*, 2007). The aim of the paper was to provide data on the structural web post failure temperature. Four test samples grouped into pairs of two, with each group having a different steel geometry were tested under monotonic one- and two-point loading, respectively. One beam from each pair was tested until failure at ambient temperature, while the other was tested at elevated temperatures. Positive results were gained in the elevated temperature tests as the beams failed beyond the expected time and temperature. The failure modes for both beams tested at elevated temperatures was web post-buckling. A finite element model was also developed using the software SAFIR with good correlation made between the experimental and numerical results.

With the use of the experimental results gained in Nadjai *et al* (2007), and the ArcelorMittal web post-buckling model developed by CTICM for cellular beams in cold conditions, an analytical model representing the web-post-buckling for cellular beams in fire was developed by Vassart *et al* (2008). A parametric study using the developed SAFIR finite element model was carried out to check the validity of the analytical model developed. When compared to the numerical model and experimental results, the analytical model gives accurate and conservative results. Furthermore, a simple calculation method of composite cellular beams at elevated temperatures was also developed and published, and the same experimental results obtained by Nadjai *et al* (2007) was used for comparison (Nadjai *et al.*, 2008).

Further studies were conducted on composite cellular beams with the experimental and numerical modelling of cellular beams with circular and elongated web openings at elevated temperatures (Naili *et al.*, 2011b). The focus of the paper was to investigate and understand the performance and failure mechanisms under a standard heating regime with temperature distributions through the specimens. Three test samples with different steel geometries and elongated web openings were subjected to one- or two-point loading tests while heated. The main failure modes observed in two of the specimens was Vierendeel bending associated with web post-buckling, and web post-buckling was the main failure mode of the third specimen. A finite element model was also developed for the beams in fire conditions with good correlation to the experimental results.

With the commission of the FICEB+ project, funded by the research fund for coal and steel, multiple experiments were conducted on composite cellular beams, including a full-scale natural fire test on a composite concrete floor with cellular beams (Vassart, Hawes, *et al.*, 2011). The focus was to validate and further develop analytical models to be used as design guides for cellular beams in fire. Large-scale standard fire tests were conducted as part of the project, consisting of four composite beam samples that were simply supported and subjected to two-point loading while heated. With the use of finite element modelling software (SAFIR, ANSYS and CAST3M), mechanical and heat transfer models were developed. Using the FEM models as a basis, a

parametric study was also further developed. The purpose of the parametric study was to validate the analytical model developed by Vassart (2009) for the design of cellular beams in fire (Vassart *et al.*, 2010).

The second test conducted on cellular beams as part of the project was the full-scale fire test on a concrete composite floor slab incorporating long span cellular steel beams. The tested floor area (9.6 m × 15.6 m) was supported on a steel frame spanning 9 m × 15 m between four corner columns (Nadjai *et al.*, 2012). This was one of the most successful and cited full-scale experiments conducted to date on composite cellular beams (Khan, 2019). Five test specimens were considered that made up most part of the horizontal framing system of the structure, two of which were secondary beams that were left unprotected during the test. The failure modes were described in detail for the secondary beams. Due to the combined composite action of the supporting cellular beams and slab, distortional buckling of the cellular beams was the governing mode of structural failure rather than web post-buckling or Vierendeel bending as observed by most small-scale single element fire testing. The main purpose of this test was to prove that the use of cellular beams with composite floors did not jeopardize the membrane mechanism floor slabs form during a fire (Nadjai *et al.*, 2012). Simple design guides were developed at the end of the project, with the first part devoted to simplified calculation methods for the assessment of cellular beams in fire and the second part was devoted to the general behaviour of the whole floor structure in membrane action (Vassart, Brasseur, *et al.*, 2011).

With this, it is noted that the majority of research is focused on the behaviour of cellular beams in fire with composite concrete floors on top due to the construction methods popularity for long-span steel beam structures. The design recommendations used in the analytical models developed are conservative and only apply to structures similar to those tested (i.e. non-sway steel framed structures with composite floors) (Vassart, Hawes, *et al.*, 2011).

As mentioned above in Section 1.4, there is a scarcity of experimental data on cellular beams tested in large to full-scale setups. The CBS system is quite different from the conventional cellular beam building systems (using concrete composite floors on top) used in today's construction. The departure from the norm comes from the fact that the system does not include any wet work (i.e., concrete) and that the flooring system is attached to the bottom of the horizontal structural members to provide inherent fire protection to the structural members and housed services. Hence, the research conducted in this work may provide new solutions to the complex fire design of cellular beam structural systems.

**Table 2-2 Selected literature on the design and testing of cellular beams in fire.**

Title	Research conducted
Performance of cellular composite floor beams at elevated temperatures (Nadjai <i>et al.</i> , 2007)	Experimental testing on cellular beams at ambient and elevated temperatures (Single element, simply supported). Development of numerical models with the use of the finite element method (FEM).
Simple calculation method of composite cellular beams at elevated temperatures (Nadjai <i>et al.</i> , 2008)	Presents a simple model to calculate the shear buckling capacity at the web post and bending resistance of composite cellular beams at elevated temperatures.
Analytical model for the web post-buckling in cellular beams under fire (Vassart <i>et al.</i> , 2008)	Presents the development of an analytical model representing the web post-buckling for cellular beams at elevated temperatures.
Experimental and numerical modelling of cellular beams with circular and elongated web openings at elevated temperatures (Naili <i>et al.</i> , 2011a)	Experimental testing on cellular beams (Single element, simply supported) with circular and elongated web openings under standard fire conditions to investigate and understand the performance and failure mechanisms. Numerical models which include material and geometrical non-linearities were also developed and compared to the experimental results.
FICEB+ Project (Vassart, Brasseur, <i>et al.</i> , 2011)	The aim for the project was to develop a detailed design guide for cellular beams in fire. The project included the curation of all data available on cellular beams tested in fire, conducting single element fire tests on composite cellular beams, and conducting the largest full-scale natural fire test on composite cellular beams.
Analytical model for cellular beams made of hot rolled sections in case of fire (Vassart, 2009)	Development of an analytical model for cellular beams made of hot rolled sections in fire. The research was conducted as part of the FICEB+ project.

## 2.7 Profiled steel sheet dry board composite flooring systems

The use of profiled steel sheet dry board (PSSDB) composite flooring systems was first proposed by (Wright *et al.*, 1989) as a replacement to existing timber joist floors in construction. PSSDB composite panel systems is essentially a lightweight composite structure composed of a profiled steel sheet and dry boards which are assembled together with a series of screws (connectors). The SD system proposed in this work is a variation of a PSSDB composite flooring system. Studies on the performance and implications of PSSDB systems to be used as flooring, walling, and roofing systems in construction have been performed in the past by various researchers (Awang *et al.*, 2009; Awang and Badaruzzaman, 2011; Badaruzzaman *et al.*, 1996; Jahan, 2018; Wan Badaruzzaman *et al.*, 2003). The next section will introduce the components of the SD system studied in this work and the thermal material properties used in the numerical models developed. Previous studies and development of the tested and chosen components introduced in this section of the SD system is detailed in Chapter 3.

### *2.7.1 Components, material properties, and modelling considerations*

Each component of the SD system contributes to the overall design of the system as detailed below. Specific details of the materials sourced for testing in this dissertation are provided. The mechanical and thermal properties of the material components used in this work have been derived from small-scale tests, as described in Chapter 4, and literature, respectively. The yield strength of the profiled steel sheeting was determined from small-scale tensile tests, while the bending and crushing strengths of the dry boards (CSB and FCB) were determined from small-scale three-point bending and crushing tests, respectively. The thermal properties of the profiled steel are assumed to be the same as normal structural steel as presented in Section 2.6.3 above, while the dry boards thermal properties were derived from literature as detailed below. The mechanical and thermal properties of the components were used to develop mechanical and thermal response models of the SD system and benchmarked against experimental data as detailed in Chapter 6 and Chapter 7, respectively. Furthermore, as the CSB is considered the main fire-resistant component of the SD system, a more detailed discussion on the CSB with regards to obtaining the thermal properties used in the numerical models is provided.

#### ***Profiled steel sheet***

Various types of profiled steel sheets have been examined in the past and sorted into different sets based on its shape and depth. The performance of PSSDB systems is significantly influenced by the shape and depth of the steel sheeting used and the stiffness of the sheet increases along with the depth of the profile. The yield strength of profiled steel sheets typically vary between 350MPa – 550MPa, with thicknesses that vary in the millimetres (Awang and Wan Badaruzzaman, 2010; Jahan, 2018). The profiled steel sheeting utilized in this study as part of the SD system is manufactured and supplied by Voidcon, who also specialize in manufacturing composite suspended flooring systems (VOIDCON, 2020). The VP profiled steel sheeting provides the tensile and compressive reinforcement and in combination with the inner FCB constitute the load bearing component of the SD system.

#### ***Calcium silicate board***

The Calcium Silicate board (the ceiling board) serves as the built-in fire-resistant component of the system. The CSB are manufactured by Promat and supplied in South Africa through the Etex Group South Africa under the brand name Promatec-H. The Promatec-H Calcium Silicate (CSB) boards are non-combustible matrix engineered mineral boards and reinforced with selected natural fibres and fillers (PROMAT, 2020).

There has also been a growing interest in the fire performance of cold-formed light-weight steel framed (LSF) walls and floor-ceiling systems lined with insulating board materials (Ariyanayagam and Mahendran, 2017; Steau *et al.*, 2020; Steau and Mahendran, 2021; Wang *et al.*, 2018). The most commonly used fire-resistant material in light-weight steel framed systems is gypsum board, known by the chemical name of calcium sulphate dihydrate ( $\text{CaSO}_4 \cdot 2\text{H}_2\text{O}$ ), which is a naturally occurring non-combustible mineral. As a result, a much deeper understanding of gypsum plasterboards has been gained over time with regard to their thermal properties at

elevated temperatures, phase transitions due to decomposition chemical reactions at elevated temperatures and manufacturing processes (Steau and Mahendran, 2021).

Alternative materials, such as Calcium Silicate ( $\text{Ca}_2\text{SiO}_4$ ) and Magnesium Oxide (MgO) boards, have been increasingly used in light-weight steel framed systems in recent years, with claims of superior fire protection when compared to gypsum boards (Steau and Mahendran, 2021). However, unlike gypsum boards, the thermal properties and behaviour of these materials have not been as thoroughly documented (Oliveira *et al.*, 2018; Steau and Mahendran, 2021). There is limited systematic data in literature on the temperature-dependent thermal properties and behaviour of these alternative materials. There are numerous factors contributing to the scarcity of data in the literature, some of which are as follows: (1) Manufacturers frequently only provide thermal properties at ambient temperatures, (2) no universal standardized testing methods have been implemented around the world, meaning that data cannot be consistently compared between testing methods, and (3) data can be presented for a specific material under the same generic brand name but have different compositions (Steau and Mahendran, 2021). The following sections will detail the thermal properties of the dry boards used in the thermal analysis of the SD system as detailed in Chapter 7.

### Thermal conductivity

Several recent studies have been performed on CSB and magnesium oxide boards used in light-weight steel framed systems and compared to that of gypsum boards with regard to their performance at elevated temperatures (Ariyanayagam and Mahendran, 2017; Steau *et al.*, 2020; Steau and Mahendran, 2021). The general consensus from these studies are as follow: (1) CSB perform similarly to gypsum plaster boards in terms of their thermal behaviour at elevated temperatures, such as, similar endothermic dehydration reaction temperature intervals, similar specific heat capacity at elevated temperatures (Ariyanayagam and Mahendran, 2017), (2) magnesium oxide boards perform considerably worse than the two other counterparts (Steau *et al.*, 2020), and (3) CSB exhibit superior mechanical properties at elevated temperatures with regard to vertical deflection in comparison to gypsum boards (Steau *et al.*, 2020). However, these studies only provide visual observations from the test results and indicate the resemblance CSB have to gypsum boards, with no detailed information pertaining to the actual chemical processes taking place at elevated temperatures in the CSB presented.

Two studies have been identified (Degler, 2016; Oliveira *et al.*, 2018), where the temperature-dependent thermal conductivity and specific heat capacity were determined for Promatec-H calcium silicate boards, which is the same material used in this study for the SD system. Oliveira *et al.*, (2018) conducted a study to determine the temperature-dependent thermal conductivity of two types of calcium silicate boards, one of which was the Promatec-H calcium silicate board. Two experimental methods were investigated, namely the guarded hot plate and transient plane source theory (hot disk method). However, the data obtained from the guarded hot plate only has a temperature range of up to 40°C, as a result, only the data obtained from the hot disk method was implemented in this work. Figure 2-8 below presents the temperature-dependent thermal conductivity values

reported by various researchers of calcium silicate boards. Based on the similarity between the work by Oliveira et al (2018), and the consistent results obtained relative to experimental data, the aforementioned material properties are incorporated in this work.

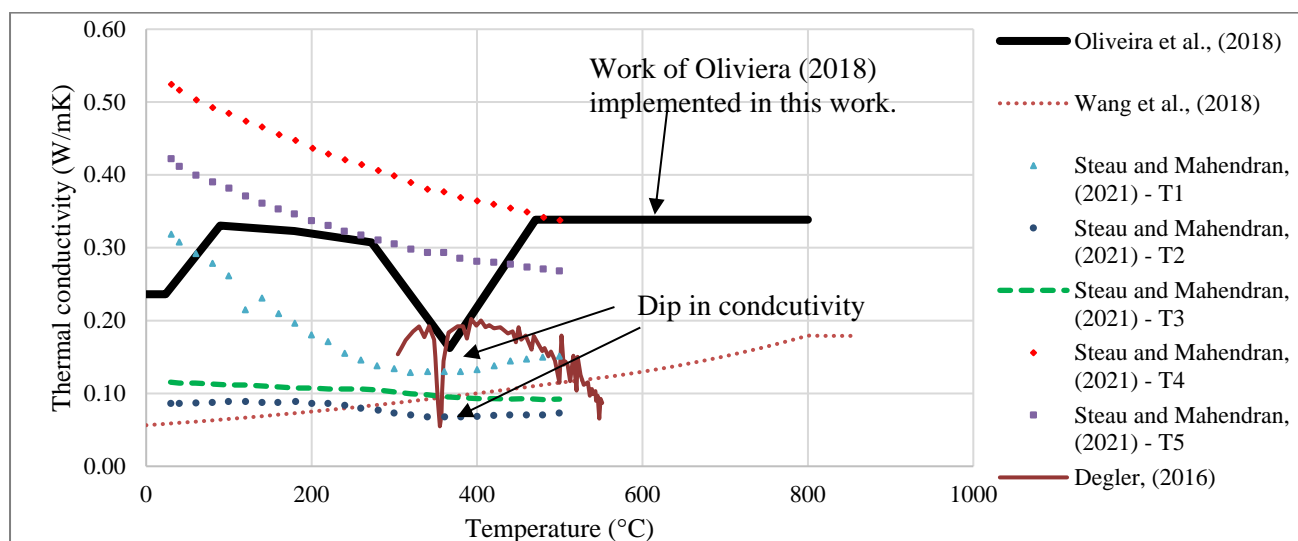


**Figure 2-8 Temperature-dependent thermal conductivity values of Calcium Silicate Boards reported by various authors.**

Degler (2016) conducted cone calorimeter tests to determine the temperature-dependent thermal conductivity of six Promatec-H calcium silicate board samples. Degler used TASEF and Excel models to calculate the thermal conductivity values of the samples using the data obtained from the cone calorimeter. Only one of the results reported in Degler (2016) has been included in Figure 2-8 above. Interestingly, when comparing the data acquired from Oliveira (2018) and Degler (2016), the same sharp drop in conductivity is found in the temperature range of about 350°C-370°C, although the authors provide different reasons for the behaviour. Oliveira (2018) suggests that this behaviour is due to chemical reactions that occur in this temperature range, while Degler (2016) suggests this was due to the experimental setup used in the work. Hence, this phenomenon is not well understood or clearly stated in the studies. Furthermore, data reported from other researchers do not exhibit this behaviour, and thus it is likely an intrinsic material property specific to the Promatec-H calcium silicate boards. The data reported by Degler (2016) also exhibits a continuous decrease in conductivity at higher elevated temperature intervals of 400°C-550°C. The data obtained from Oliveira (2018) is only given up until a temperature range of 470°C, thus, the last recorded conductivity was assumed constant for higher temperatures in this work.

### Specific heat and enthalpy

Following discussions in the previous section, in order to perform the Excel and TASEF models, Degler (2016) calculated the specific volumetric enthalpy ( $J/m^3$ ) of the samples at four temperature intervals according to the formulation proposed by Wickström (2016). In short, the formulation proposed by Wickström allows for the addition of the latent heat required to model the chemical and physical phase changes that may occur within construction materials, such as dehydration reactions. This formulation is similar to the formulation proposed

by Wang (1995) as detailed in the following section below. The dehydration reactions that occur in the calcium silicate boards is assumed to be between the temperature interval of 100°C to 120°C only. The average volumetric enthalpy calculated for each temperature interval of the six tested samples by Degler (2016) is implemented in this work. This was achieved by converting the volumetric enthalpy ( $\text{J/m}^3$ ) to specific enthalpy ( $\text{J/kg}$ ), by dividing throughout with the material density, then deriving the temperature-enthalpy curve to obtain the specific heat capacity as a function of temperature.

However, the resulting temperature-dependent specific heat capacity increases suddenly (i.e., a step-wise function) where the dehydration reaction is assumed to occur. This characteristic, or shape, in specific heat capacity curve may cause convergence issues in the numerical analyses. Wang (1995) proposed a solution to this by assuming a more gradual increase and decrease in specific heat capacity (triangular shaped) with a single peak value. However, the required energy for the various phase changes or moisture evaporation-condensation migration under high pressure should not be altered (i.e., overall additional latent heat energy).

Thus, using the solution method proposed by Wang (1995), the specific volumetric enthalpy calculated by Degler (2016) was converted into specific heat capacity, and the latent heat energy distribution altered (to form a triangular shape). The final shape of the specific heat capacity was obtained through a sensitivity analysis carried out in this work, where different triangular variations and peak specific heat capacity values were tested. Additionally, variations were also tested with two peak values, by assuming two separate dehydration reactions occur. Furthermore, it was identified through this sensitivity analysis that the total specific enthalpy change from 100°C to 120°C (as in Degler (2016) Figure 2-9 below), which was calculated to be 381 MJ/Kg, was not sufficient to fully predict the dehydration process observed in the experimental data. Thus, the total enthalpy change within this temperature interval was multiplied by a factor of 1.32 (32% increase), equating to 503 MJ/Kg. This value increase is based on the data reported by Feng *et al.* (2003) and Rahmanian (2011), who calculated similar extra latent heat energies in their respective models. Hence, this value increase is based on specific heat values for gypsum boards, however, given the similarities reported in literature for gypsum and calcium silicate boards, it was assumed to be similar in this work as well.

The modified specific heat capacity graph is presented below in Figure 2-9 (referred to as modified CSB model), along with the originally derived specific heat capacity from Degler (2016), and the reported values from various other authors for gypsum and calcium silicate boards, including those mentioned above. A temperature interval of 90°C to 110°C was assumed for the dehydration reaction to occur, with a peak value of 24 MJ/Kg at 100°C. Additionally, a more gradual decrease in specific heat capacity between the temperature intervals of 110°C to 400°C was assumed, with a maximum value of 2600J/kg°C at 110°C. Care was taken not to alter the total amount of enthalpy change of 503 MJ/Kg when assuming the shapes of the specific heat capacity.

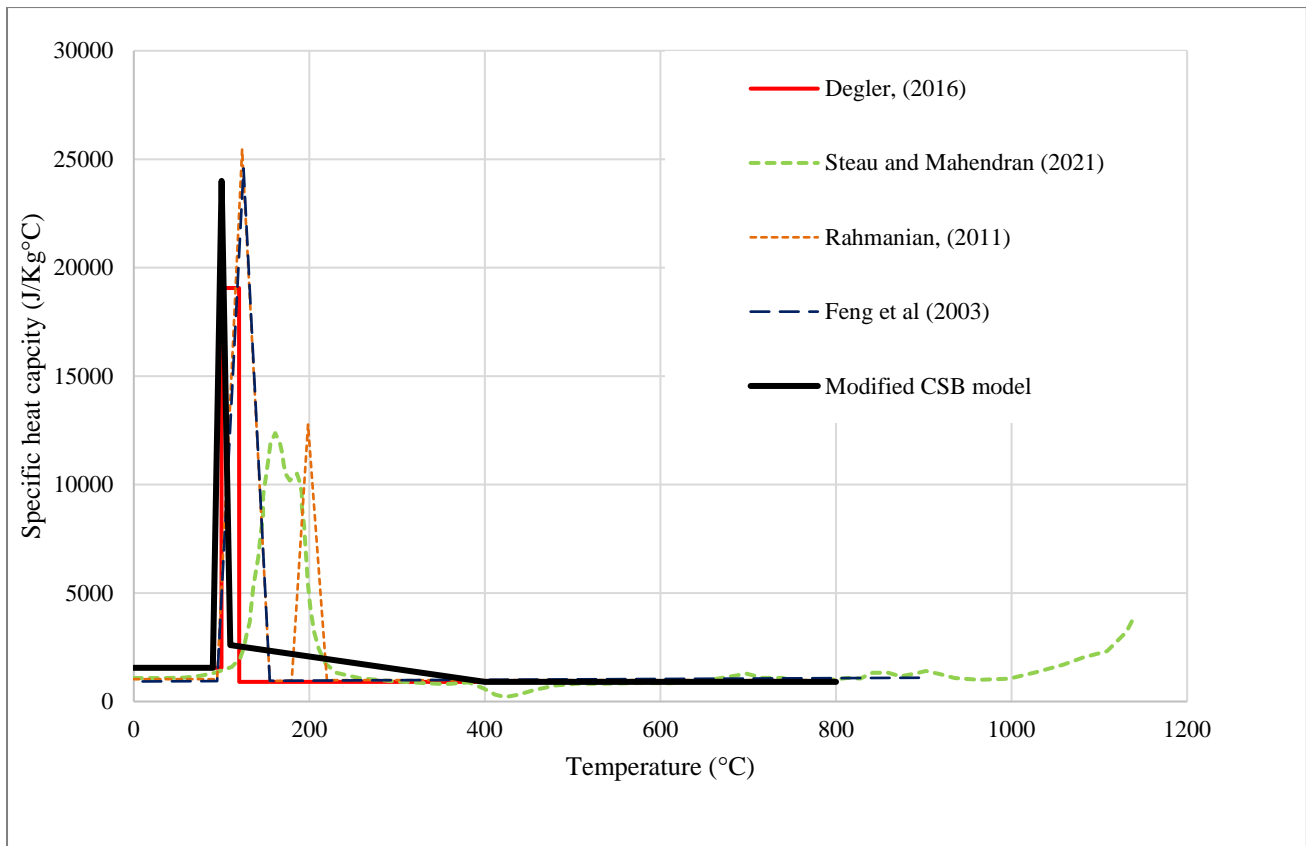


**Figure 2-9 Specific heat capacity of Calcium Silicate Board**

#### Density and emissivity

The average wet and dry densities obtained by Degler (2016) of the six tested samples was also implemented in this research. A simplified linear piece-wise curve was assumed where the density of the material decreases linearly between the temperature interval of 100°C to 120°C, from the average wet density to the average dry density of the material. Finally, a value of 0.3 was chosen for the resultant emissivity of the exposed side of the CSB, which is based on the research conducted by Marx (2018). Several emissivity values were also investigated in this research for the CSB, ranging from 0.3 to 0.6, and have shown that an emissivity of 0.3 yields the best results in the numerical models developed in this work. The final material properties of the calcium silicate board used in this study are as listed below in Table 7-2.

#### ***Fibre cement board***

The FCB enhances the flexural capacity and strength of the system while also providing a flat surface for the access flooring. The FCBs used were manufactured by Kalsi and supplied through the Etex Group South Africa under the brand name KalsiFloor. The boards are manufactured on a Hatschek machine from a precise combination of cement, silica, and natural organic reinforcing fibres (KALSI, 2020). The KalsiFloor FCB boast several benefits, such as being impact resistant, resistant to water, mould, and moisture. The FCBs are environmentally friendly and do not give off any harmful gas emissions. The light-weight nature and mechanical strength provided by the boards make it an excellent alternative to that of concrete slabs flooring. In the

concluding sections of the dissertation, it is discussed that for practical reasons it may be necessary to use a 20mm FCB in real structures to prevent punching from the false flooring and to minimise potential cracking during erection and installation of the system. However, the use of the 9 and 12mm FCB systems provide a conservative configuration from which capacity can be ascertained, and are shown to be suitable. Ultimately economics, constructability and requirements such as acoustics will significantly influence some of the specifications employed for real structures.

Very little data is reported in the literature on the temperature-dependent thermal properties of FCB. Hence, the thermal conductivity and density of the fibre cement board was obtained from the manufacturer's technical data sheets (ETEX Group, 2020). Unfortunately, the manufacturer only supplies a single value for thermal conductivity, namely 0.25W/mK. However, it was found that the numerical solution provides satisfactory results based on this constant value. Similar to the conductivity, only a single density value of 1250kg/m<sup>3</sup> was implemented in the numerical model, as supplied by the manufacturers.

A specific heat capacity of 2500J/kg°C was assumed initially, based on the research conducted by Marx (2018). However, Marx did not include the effects due to moisture in the numerical models. In this research, the specific heat capacity was modified according to the Wang (1995) formulation to account for the moisture content. The additional latent heat energy required for evaporation of the water can be obtained from (Eq – 2.27) below, where the latent heat of vaporisation of water is taken as 2.25 MJ/Kg.

$$DCp = \frac{(2.25 \times 10^6)(u)}{\Delta T} * \Lambda \quad (2.27)$$

Where:

$DCp$  is the additional average specific heat (J/kg°C).

$u$  is the moisture content expressed as a fraction by weight.

$\Delta T$  is the magnitude of the given temperature interval (°C)

$\Lambda$  is a correction factor.

A moisture content of 15% was used in the formulation as supplied by the manufacturers. This extra latent heat energy calculated was added to the assumed constant specific heat capacity of 2500J/kg°C. With a moisture content value of 15% and a correction factor of 1.9, equates to 641 MJ/kg calculated for the additional latent heat required for evaporation of the moisture. The correction factor  $\Lambda$  is used to account for the required moisture evaporation-condensation migration under high pressure as stated by Wang (1995), and other endothermic chemical reactions that may occur within this temperature interval that has not been accounted for. Approximately 45% of this extra energy was distributed over a temperature range of 290°C, from 110°C to 400°C, similar to that of the CSB. The remainder of the energy was distributed between the temperature range of 90°C to 110°C, with a peak specific heat capacity value of 37 MJ/kg°C at 100°C. Finally, it was also identified

during the preliminary modelling stage that using a specific heat capacity of 2777J/kg°C, instead of 2500J/kg°C, in the temperature range of 0°C to 90°C provided better correlation with the experimental data.

The final specific heat capacity values implemented in this research is as depicted and listed in Figure 2-10 and Table 7-2 below, respectively.

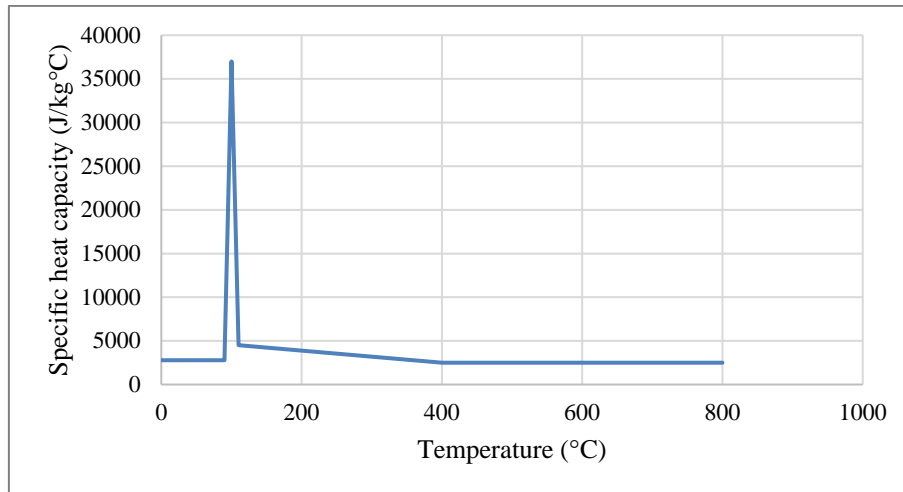


**Figure 2-10 Modified specific heat capacity of Fibre cement board.**

### ***connectors***

A composite beam with partial interaction is intermediate between a composite section with full interaction (i.e. acts as a single monolithic unit) and individual sections with no shear interaction (Newmark *et al.*, 1952). Hence, these latter two cases can be thought of as the upper and lower limits for the load carrying capacity of the composite section. This independence of each of the elements can cause a sudden change in the strain distribution at the plane of the surfaces in contact, and violates Euler-Bernoulli assumptions of plane-sections remaining plane and perpendicular to the neutral axes. This behaviour can be demonstrated using Figure 2-11 below, where the bottom fibres (Red) of Element 1 are lengthened, while the adjacent top fibres (Blue) of Element 2 are shortened. The lengthening and contraction of the adjacent fibres cause slippage to occur at the plane of the contacting surfaces.

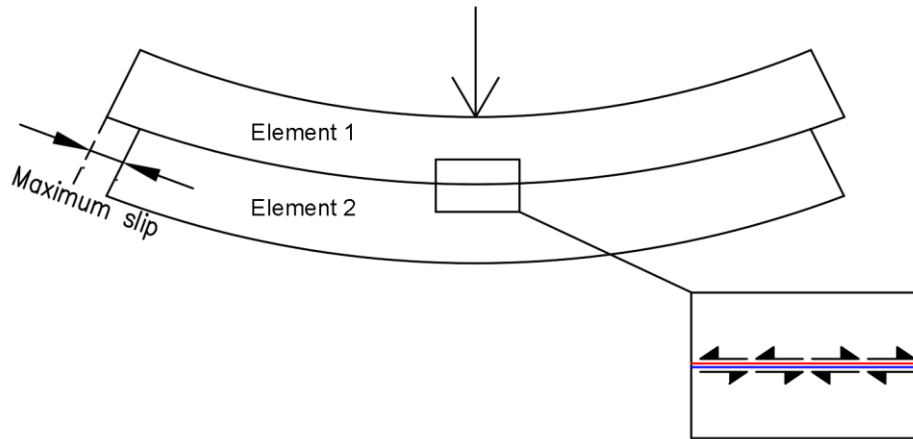


**Figure 2-11 Simplified load-slip behaviour of a composite section.**

Shear connectors in a composite section prevent the slippage from occurring by transferring the horizontal shear forces between the two elements. However, in a composite section with partial interaction, the shear connectors only transfer a portion of this horizontal shear and allow some slippage to occur. Hence, the degree of composite action (stiffness) within a section depends on the performance of the shear connectors (Jahan, 2018; Newmark *et al.*, 1952).

More specifically, the amount of slip depends directly on the stiffness of the shear connection in the composite section which, in turn, depends on the spacing and stiffness of the individual shear connectors (Jahan, 2018; Newmark *et al.*, 1952). The stiffness of a screw connection is calculated as the amount of shear force transferred per unit distance of shear displacement by its shear modulus. The shear modulus, and total shear capacity, of a screw is typically determined from push-out tests (Jahan, 2018). When considering the specific case above, due to the symmetric nature of the composite section, the maximum slip will occur at the ends of the composite section, while no slip occurs at the geometrical centre, as the fibres are contracted inwards and lengthened outwards from the centre of the section where the load is applied.

## 2.8 Advanced calculation methods

This section is aimed to give more insight to advanced calculation methods employed and the complexities which have to be considered that would have otherwise been ignored when doing analysis at ambient temperature. These complexities have been explained following Wang *et al* (2012). When considering a design at ambient temperature, the loading or “actions” applied to the structure are the worst-case scenario forces to be expected during the lifetime of the structure, and these combinations vary from country to country. The two most common forces designed for are wind and earthquake loadings in combination with gravity. Importantly, it should be noted that these forces are considered to be invariant with time and consequently the stresses caused by them can be considered as constant. More simplifications are made when considering that structural materials are very stiff, and the serviceability requirements that have to be met result in structures that have small deflections when under normal loading. This made it plausible for geometric non-linearity to be neglected in

analyses. Furthermore, we take advantage of the fact that it is usually possible to assume the material used to have linear-elastic or rigid-plastic behaviour, this makes analyses, without considering material non-linearity, also plausible.

When considering structures at elevated temperatures the situation is quite different. When considering fire as an “action” on the structure, we refer to the heat fluxes that result from the exposure to hot gasses and radiation. The structure or parts of the structure experience heating when the fire grows, and cooling when the fire starts to decay. As the rate of heating and cooling is different for various parts of the structure, and structural elements expand when heated, stresses are induced due to compatibility requirements. A relevant example of this is the case of having a compartment fire within a larger building, the heated elements within the compartment that are surrounded by the cooler structural members from the rest of the building give rise to internal stresses. This means thermal equilibrium will not occur in a typical fire, and as a result we cannot consider the stresses produced to be constant with time as in the case of ambient design. Material properties also get affected by fire as discussed earlier, and with the heating nor the cooling occurring simultaneously throughout the structure, the material strengths of the structure may be increasing in some areas and decreasing in the other at any point during the fire. Lastly, due to the large deflections and second order effects that result in structures exposed to fire, geometric non-linearity certainly must be considered in the analyses processes (Buchanan and Abu, 2017). Consequently, when conducting analyses of structures in fire, the strength varies with time and temperature, and geometric and material non-linearity must be taken into consideration.

Now that we have discussed some of the complexities associated with the analysis of structures in fire, we will look at some of the tools used for analysis. For every stage of the design process, there is available software to employ, starting with models that predict the gas temperatures of a compartment fire, models to predict the thermal response and models for the structural response. Depending on the problem being solved, level of accuracy required and available input data, different types of analysis may be used (Wang *et al.*, 2012).

Figure 2-12 below gives a simplified visual representation of the different stages of analysis when considering structures is fire.

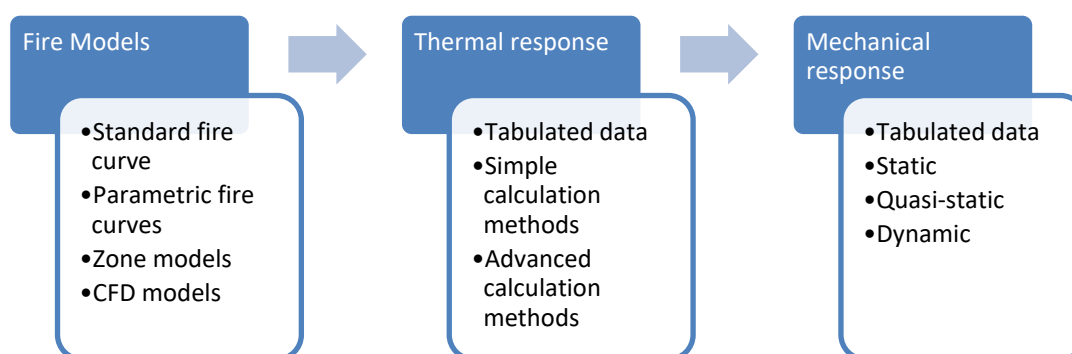


**Figure 2-12 Stages of analysis when considering structures is fire.**

### 2.8.1 Thermal response analysis

After the gas temperatures in the compartment are attained, the thermal response can be predicted using one of the three methods as listed in the Figure 2-12 above. We will only consider the advanced calculation methods used as the other have already been discussed in previous sections

#### ***Finite element solution to heat transfer problems for structural elements***

According to Purkiss (2007), the finite element method (FEM) is a numerical analysis tool for generating approximate solutions to a wide range of engineering problems. It presents a consistent technique for modelling the "whole" as an assemblage of discrete parts and allows a user to solve a complex continuum problem by subdividing it into a series of simpler interrelated problems. The temperature field is the field variable in the heat transfer problem, and it is a function of each generic point in the body or solution region. By splitting the solution region into elements and defining the temperature field in terms of assumed interpolation functions within each element, finite element analysis simplifies the problem to one with a finite number of unknowns. The temperature field values at specific points termed "nodes" are used to define the interpolation functions. The behaviour of the temperature field within the elements is totally defined by the nodal values of the temperature field and the interpolation functions for the elements. For the finite element representation of the heat transfer problem the nodal values of the temperature field become the unknowns. The matrix equations expressing the properties of the individual elements are determined from the governing equation by using the weighted residual approach. The global matrix equations for the entire system are then combined from the individual element matrix equations. The global matrix equations can be numerically solved once the boundary conditions have been imposed. The interpolating function defines the temperature field throughout the assemblage of elements once the nodal values of the temperature field are found. Depending on the sophistication of the software package, the definition of the nodes and elements can be done automatically through a graphical user interface or by generating an input text file. Examples of commonly used software packages that use graphical user interface are Abaqus, Ansys, and Safir (Buchanan and Abu, 2017).

#### ***Coupled vs De-coupled analysis***

De-coupled heat transfer analysis is done by first calculating the temperatures within the structure, then afterwards the results are used as input data for the mechanical analysis that is done separately. This gives the advantages of being able to use different models and software packages for the heat transfer and mechanical analysis. Marx (2018) and Kloos (2017) adopted this approach with the first analysis of the cellular beam system. On the other hand, fully coupled thermomechanical analysis is when the thermal and mechanical response is calculated simultaneously using a single model. This approach is rarely adopted for fire engineering problems and only used in special or particular cases such as when spalling of concrete or other damage that changes the exposure of the structure is being modelled. The advantage of using this approach is that only one analytical process is required, which means that no data transfer from a heat transfer analysis to a structural analysis is needed (Wang *et al.*, 2012).

## Methodology

Abaqus version 6.17-1 (Dassault Systemes, 2016) was chosen to develop all numerical models presented in this work. The de-coupled thermal analysis procedure was utilised in this to develop the thermal response model, where actual temperatures obtained from experiments were used as the input temperature. Figure 2-13 below depicts the boundary conditions and governing equations, as described above, for a generic structural element exposed to a fire on the one side and ambient temperature on the opposite side. Abaqus offers the capability of modelling all three heat transfer mechanisms, conduction (magenta), convection (red), and radiation (blue). To simulate conduction heat transfer, the thermal properties of the material are required, specifically, the thermal conductivity ( $\lambda$ ), density ( $\rho$ ), and specific heat capacity ( $c$ ). Convection and radiation are defined as boundary conditions on the surface of the material to model the combined convective and radiative heat flux emitted onto (fire side) or from (ambient side) the material surface. The convective heat transfer coefficient ( $h$ ) is required to model the convective heat flux, while the Stephan-Boltzmann constant ( $\sigma = 5.67 \times 10^{-8} \text{ W/m}^2\text{K}^4$ ), the configuration factor ( $\phi = 1$  for closed surfaces), and the emissivity ( $\epsilon$ ) are required to model the radiative heat flux. The Eurocode recommends a convective heat transfer value of  $25 \text{ W/m}^2\text{K}$  when modelling elements exposed to standard fire furnace tests (BSI, 2002). Abaqus also offers the capability to model cavity radiation with the formulation based on grey body radiation theory (Dassault Systemes, 2016; Holman, 2009). Cavity radiation is the exchange of radiative heat between surfaces that can “see” each other, where the surfaces that make up the cavity are referred to as facets (Marx, 2018). The configuration factor ( $\phi$ ), as discussed in, is automatically calculated by Abaqus, which also takes radiation blocking into account. Radiation blocking occurs when certain parts of the object are in the way of the radiation path between two radiating surfaces. Abaqus only allow for a single emissivity value to be defined when modelling cavity radiation, hence, in the case when the cavity is comprised of surfaces with different emissivity values, the resultant emissivity will have to be used ( $\epsilon_{res}$ ) as described above. The reader is referred to the literature for further details (Dassault Systemes, 2016; Holman, 2009).

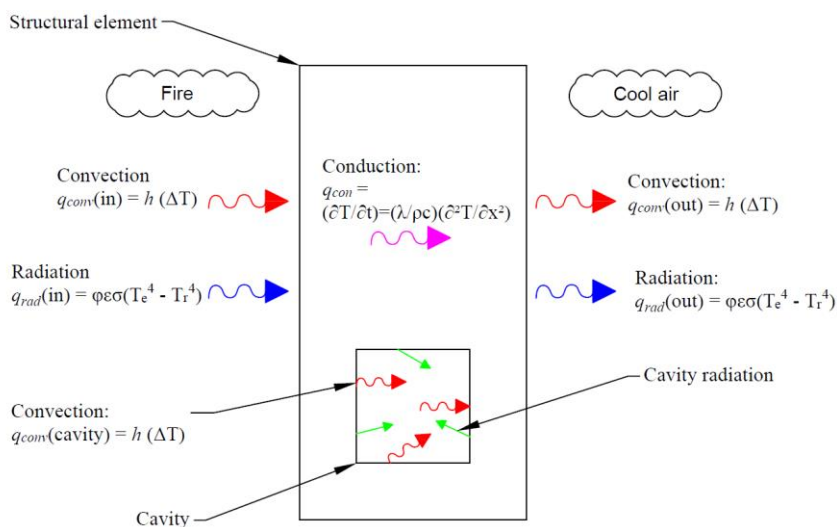


Figure 2-13 boundary conditions and governing equations for a generic structural element exposed to a fire.

### 2.8.2 Mechanical response analysis

The finite element method is the best tool to account for the varying capacities of the whole structure, as individual members lose their strength or are subjected to increased loading. It also allows for the definition of the mechanical actions on the structural members or frame while accounting for the material changes with temperature, can simulate the progressive deformations of complex structures, and can predict the collapse mechanisms or failure (Buchanan and Abu, 2017). Again, depending on the type of problem at hand and the phenomena that need to be represented, there are a number of different kinds of mechanical analyses available. The most significant factor between them is the degree to which time has physical meaning. When doing hand calculations, loads are considered as constant and time has no physical meaning, we are only able to calculate the stresses for one set of loads and temperatures. Using numerical models, we are able to represent time in various ways, as explained in the following sections (Buchanan and Abu, 2017).

#### **Static analysis**

When using static analysis, time has no physical meaning and is much similar to that of non-computer-based calculations. It allows the sequence of loads to be applied to a numerical model and the numerical equilibrium state to be calculated for that specific load set. In other words, the loads or actions can be changed for every step sequence but the time over which they are applied make no difference. This makes static analysis the simplest and most common method used for the analysis and design of both heated and ambient structures. Consequently, time-dependant phenomena, such as inertial forces cannot be modelled (Wang *et al.*, 2012). The “general static” algorithm solution has been utilized to perform all mechanical and thermal-stress model analyses in this work.

#### **Quasi-static analysis**

Using quasi-static analysis, we are able to introduce some time-dependant effects, such as creep. This becomes an important consideration when doing the analysis of heated structures, as creep effects are accelerated at high temperatures. That being said, many authors have been able to represent the phenomena of creep in numerical models without modelling creep itself numerically. This may be a consequence of the fact that creep effects are included in some form in the material input data used for the analysis. As mentioned earlier, the Eurocode stress-strain data for steel give slightly more conservative results to account for the effects of creep. It should be noted that although the effects of creep may be represented, inertial effects are still not included (Wang *et al.*, 2012).

#### **Dynamic analysis**

With dynamic analysis, time has physical meaning, making it possible to calculate inertial forces. Dynamic analysis can be done using one of the following two numerical schemes, namely, *explicit* time integration and *implicit* time integration. Explicit time integration works by using the known (explicit) state of a numerical model at the end of one incremental step to calculate the state at the end of the next time step, while implicit dynamic analyses solve the dynamic equilibrium equations by direct integration in an iterative process (Wang *et al.*, 2012).

## 2.9 summary

This chapter has covered the fundamentals required for developing the work in the remainder of this dissertation. Material models for steel at elevated temperature will be used in the modelling of the CBS. Heat transfer analyses will be conducted to understand the performance of the Sandwich Decking system in fire, and will be compared to experimental data. The overall work utilises a performance-based design approach to modelling the entire system, but with the standard fire being used for the fire exposure. Negligible large-scale experimental work has been carried out on cellular beam structures similar to that considered in this work.

## Chapter 3 Cellular beam structure and sandwich decking system background and specifications

### 3.1 Introduction

The Cellular Beam Structural (CBS) system was first conceived nearly a decade ago by Dr Hennie de Cleerq and proposed by Amanuel Gebremeskel in a concept paper published by the SAISC in 2013 at the Steel Future Conference (Gebremeskel, 2013). Since its inception, the CBS system design has been examined by various parties (including the SAISC, University of the Witwatersrand, and Stellenbosch University) as part of a larger overall research and development project spearheaded by the SAISC. As a result, the initial design has evolved over time, especially in terms of the flooring system components used. Hence, to gain insight to the development history of the CBS system, a brief description of the original CBS system structural design and layout is presented first. Following that, a concise overview of research previously conducted pertaining to the CBS system is provided. Only research that falls within the scope of this study and the changes made leading to the CBS system tested in this work are presented. The chapter continues by introducing the experimental structural frame of the CBS system tested in this work, giving more insight to the rationale of the design, layout, and the terminology used throughout this dissertation. Finally, the Sandwich Decking (SD) system tested in this work is presented, highlighting important aspects of the components used in the system and the terminology thereof.

### 3.2 Originally proposed Cellular Beam Structural System

The initial design of the CBS system is well documented in Marx (2018) and Kloos (2017), hence, only a brief description is presented in this section. The structural design of the CBS system remains largely unchanged, with the exception of a minor design modification implemented through the research conducted by Kloos (2017), as described in Section 3.3.2 below. Figure 3-1 below depicts a single sub-structure of the CBS system, which comprises of three modules. Additional sub-structures are then further assembled to form larger structures as desired.

The main horizontal structural members of a single sub-structure comprise two primary beams (P-beams), spanning 12.5 m, and connected to four columns; four secondary beams (named J-Beams because of their “J” shape), spanning 7.925 m, and connected to the P-Beams; and six tertiary beams (named C-Beams as they are channels) connected to the J-Beams. The total floor size of a typical single sub-structure is thus 12.5 m × 7.925 m, with a floor-to-floor height of 2.56 m. The primary and secondary beams consist of built-up cellular beams, whilst the tertiary beams are tapered channel beams. Connections that provide moment continuity are utilized between the interconnecting modules for the P-Beams to ensure the complete sub-structure behaves as a single monolithic structure. Furthermore, the P-Beams also have a 40 mm top and bottom flange notch, as indicated in Figure 3-1 below, where the columns need to be connected. A J-shaped beam section is utilized for the secondary beams as depicted in Figure 3-1 below. However, an additional angle is attached to the beam during

the assembly process resulting in a beam section that resembles regular I-Beam sections upon completion. This technique is utilized to expedite the assembly process during construction of the interconnecting modules. The fly bracing also consists of tapered channel sections, whereas the lateral bracing consists of angle beam sections. The fly and lateral bracing provide lateral support to the structure in the X- and Y-directions, respectively. In addition to the lateral support, the fly bracing also provides vertical load bearing support to the tertiary beams. The technical drawings of the CBS system can be found in the online repository of data stemming from this dissertation (Claasen *et al.*, 2021). A prototype of the structure has been built which is shown in Figure 3-2.

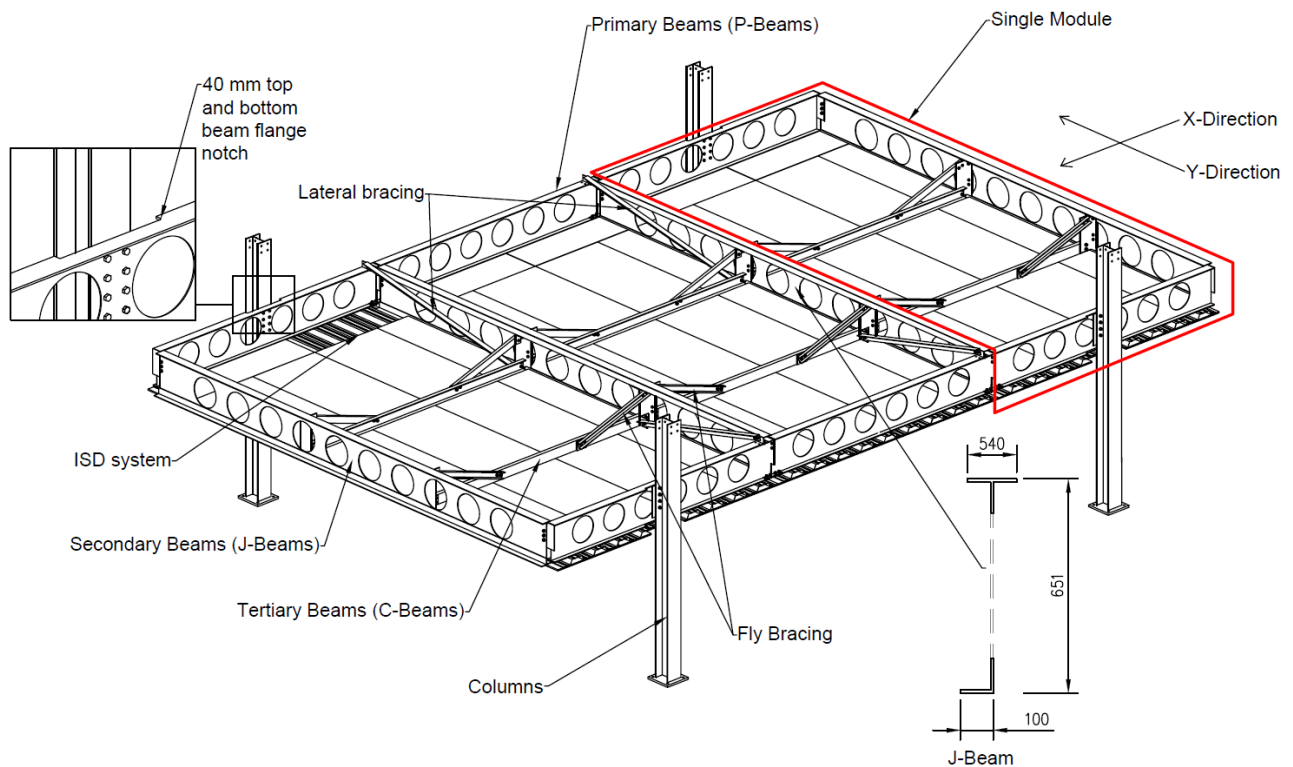


**Figure 3-1 Isometric view to illustrate terminology and the configuration of a single sub-structure of the CBS system.**



**Figure 3-2 Prototype of the CBS showing the system without the ceiling or false floor in place.**

The SD system's original configuration, which was integrated into the CBS system's access flooring, consisted of a 75 mm deep and 0.8 mm thick Bon-Dek profiled steel sheeting with a 9 mm thick inner Fibre Cement Board (FCB) attached on top, and a 15 mm Gypsum Board (GB) ceiling attached to the bottom. The profiled steel sheeting is first attached to the bottom of the P- and C-Beams, followed with the attachments of the top (FCB) and bottom (GB) boards. With the SD system attached to the bottom of the beams, pedestals are then placed on top of the inner FCB, and followed by another 9 mm FCB attached to the top of the pedestals to form the access plenum where all the horizontal structural members and services are enclosed. In the interest of clarity, the initial design of the SD system will be referred to as the ISD system, which is not to be confused with the SD system tested by Marx (2018) and the currently proposed and tested SD system as described in Sections 3.3.1 and 3.5, respectively. Figure 3-3 below depicts the initial access flooring design of the CBS system as proposed by the SAISC.

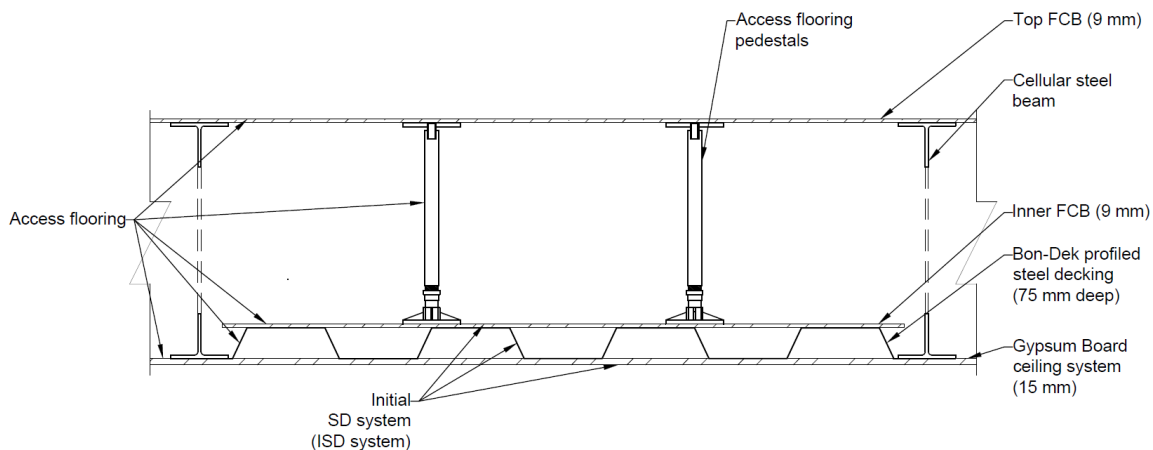


**Figure 3-3 Cross-sectional configuration of the initial access flooring components of the CBS system. (Note: Image not drawn to scale)**

### 3.3 Previous research conducted and findings

As mentioned in Chapter 1, two previous studies have been conducted on the CBS system to evaluate the performance of the structural system at elevated temperatures. Marx (2018) investigated the thermal behaviour of the CBS system at elevated temperatures, whilst Kloos (2017) investigated the structural response of the CBS system at elevated temperatures. The work performed by both authors and the findings thereof are summarised below.

#### 3.3.1 Research conducted by Marx (2018)

Marx (2018) conducted four small-scale standard fire (StF) experiments of the SD system, with each having a different configuration. The aim of the experiments was to investigate the temperature distributions through the cross-sections of the SD system. However, at that time the ISD system was not finalized and assumed that it could vary from project to project. Thus, instead of using the same components proposed in the ISD design as described above in Section 3.1, Marx used readily available materials in South Africa with a suitable fire rating to perform the experiments. The test specimens consisted of VP50 Voidcon profiled steel sheeting with a fibre cement board (FCB) (manufactured by Nutec) attached on top. Two of the samples had Calcium Silicate Boards (CSB) (manufactured by Promat and supplied by the Etex group) attached to the bottom, while the remaining samples did not. The rationale for the tested samples with no CSB attached, was to represent a worst-case scenario where the steel sheeting would be directly exposed to the fire. Due to the size of the testing furnace available, the decking flute and trough areas had to be tested individually. Samples of the flute and trough areas were tested both with and without a CSB attached to the bottom as indicated in Figure 3-4 (Top-Right) below. Rhinoboard Firestop Gypsum boards (manufacture by Saint-Gobain Gyproc) were attached to the sides of each sample to form a closed system. All test samples were exposed to a 60-minute standard fire time-temperature curve (StF) from the bottom, leaving the sides and top unexposed, with the temperature measurements of the sections taken using K-type thermocouples. The configuration for each test sample including the thermocouple layouts (Left), and the furnace setup (Bottom-Right) is depicted in Figure 3-4 below.

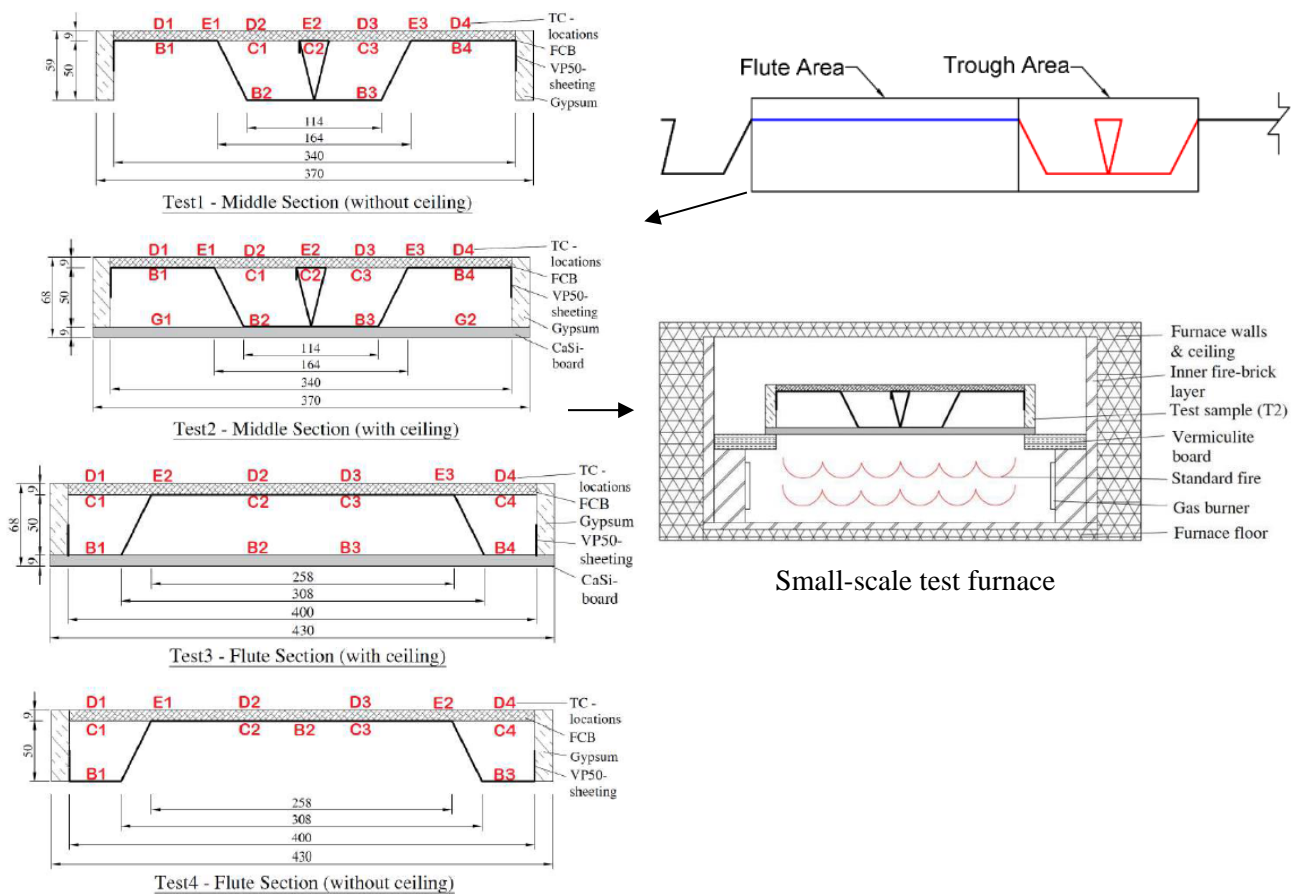


**Figure 3-4** The respective Flute and Trough areas of the VP 50 profiled steel sheeting (Top-Right), the configuration of each of the test samples (Left), and a schematic of the test furnace setup (Bottom-Right). (Marx, 2018)

The data gained from the experimental tests were used to develop and benchmark Finite Element (FE) thermal response models of the SD system. This was achieved by means of conducting heat transfer analyses and comparing the numerical results to that of the experimental data. Using the calibrated parameters of the benchmarked models and experimentally verified parameters from literature, Marx (2018) was then able to develop FE models of the CBS system design as proposed by the SAISC, which included the ISD system, as described above in Section 3.2. The FE models were developed to predict the thermal response of the ISD system and the temperature evolution of the main horizontal structural members.

The numerically predicted thermal response data of the ISD system was utilized to evaluate the structural system in terms of its insulation failure criteria, and the temperature evolution of the structural members was utilized by Kloos (2017) to investigate the structural response of the CBS system. FE models of each of the main horizontal structural members, namely, the primary beam (P-beam), the secondary beam (J-beam), and the tertiary channel beam (C-beam), with the ISD system on the bottom was developed as depicted in Figure 3-5.

Three thermal load cases were produced from each of the FE models: (1) The system exposed to a 60-minute StF with the ceiling included (which refers to the inclusion of the Gypsum board ceiling) (StF-C), (2) the system exposed to a 60-minute StF without the ceiling included (StF-NoC), and (3) the system exposed to a 120-minute parametric fire (ParF) with the ceiling included.

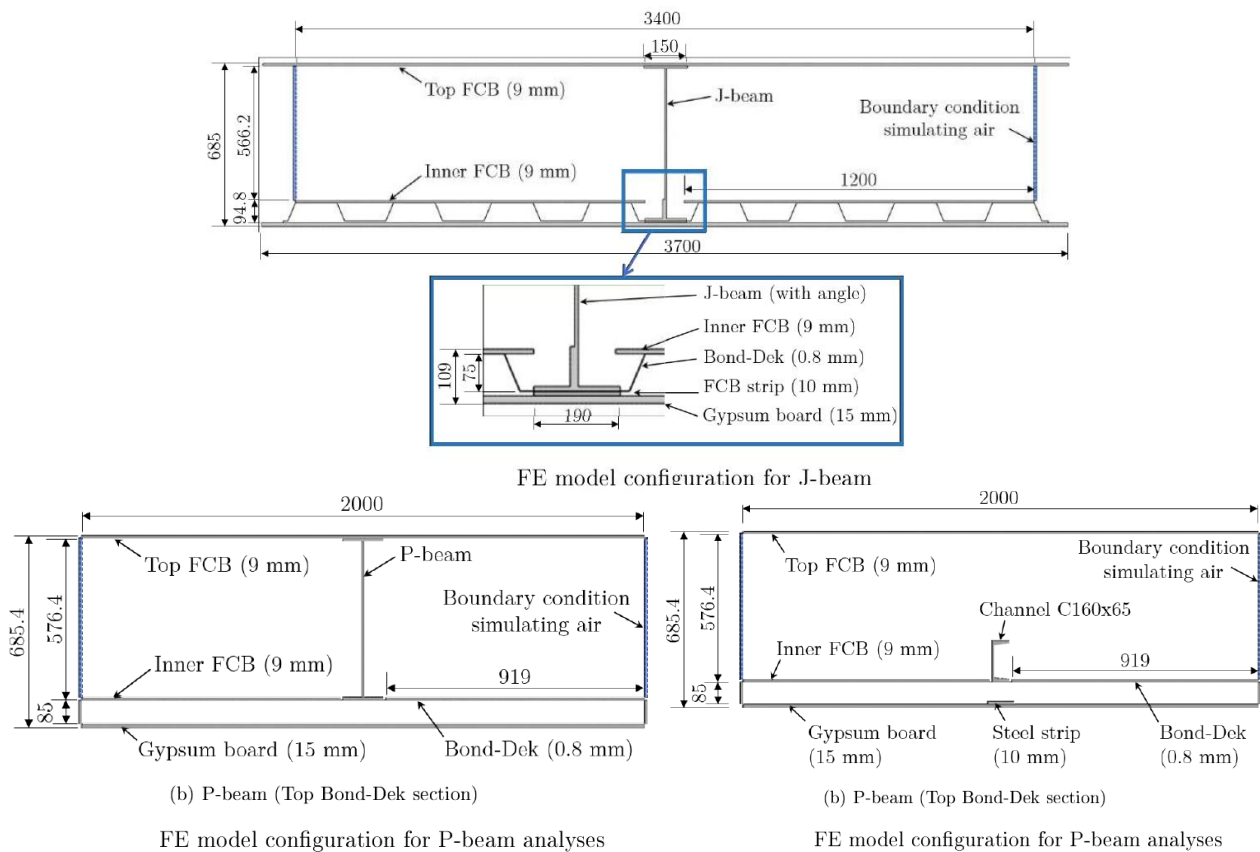


**Figure 3-5** FE model configuration of each of the main horizontal structural members, including the ISD system. (Marx, 2018)

### ***FE model of the CBS system with a ceiling board attached (StF-C)***

The FE model scenario of the CBS system with a gypsum board (GB) ceiling attached to the bottom (called the StF-C setup) revealed that the ISD system did not satisfy the Fire Limit State (FLS) insulation criteria. It was found that the inner FCB exceeded the limiting average and single point temperatures by 60°C and 68°C, respectively. Furthermore, the FE models also indicated that the Bon-Dek profiled steel sheeting experiences a significant temperature increase and reached temperatures that varied between 500°C and 440°C. A temperature increase of this magnitude could potentially result in undesired stresses being developed in the insulating boards caused by the linear thermal expansion of the steel sheeting. Moreover, the numerically predicted temperatures of the horizontal structural members revealed that there is a large temperature gradient between the top and bottom beam flanges, with the bottom flanges being hotter than the top as the structure is heated from the bottom.

### ***FE model of the CBS system without a ceiling board attached (StF-NoC)***

The FE model scenario of the CBS system with no ceiling (StF-NoC) attached to the bottom of the ISD system, yielded significantly higher maximum temperatures for both the flooring and the structural components when compared to the StF-C finite element model maximum temperatures. With temperature differences ranging from 322°C and 357°C for the inner FCB flooring component, and between 300°C and 531°C for the structural members. Temperature differences of this magnitude could lead to excessive thermal bowing and linear thermal expansion of the decking and structural members, and a significant reduction of strength and stiffness in the structural members, which could ultimately cause catastrophic failure of the system. This highlighted the crucial importance of the ceiling to remain intact and that its integrity be maintained during a fire. Localised failure of the ceiling leading to failure of the floor was also observed in this dissertation as shown in Chapter 5.

### ***Parametric study***

Marx (2018) used the FE scenarios of the CBS system to conduct a parametric study, which investigated the effect of topological parameters pertaining to the ISD system on the overall performance of the CBS system at elevated temperatures. The parameters investigated included the type and depth of profiled steel sheeting used, potential alternative materials that could be used for the ceiling and their thicknesses, and thicknesses of the inner insulation board. The parametric study also included investigating the thermal performance of the system under a severe parametric fire curve (as described above and shown in Figure 3-6 below), which included both a heating and cooling phase. The calculated parametric fire resulted in a more rapid initial heating phase, reaching a peak temperature of 1188°C within the first 20 minutes, followed by a rapid cooling phase where the temperature decreased linearly for a duration of 20 minutes to 20°C, where it remained for the rest of the 120 minutes as shown in Figure 3-6 below.

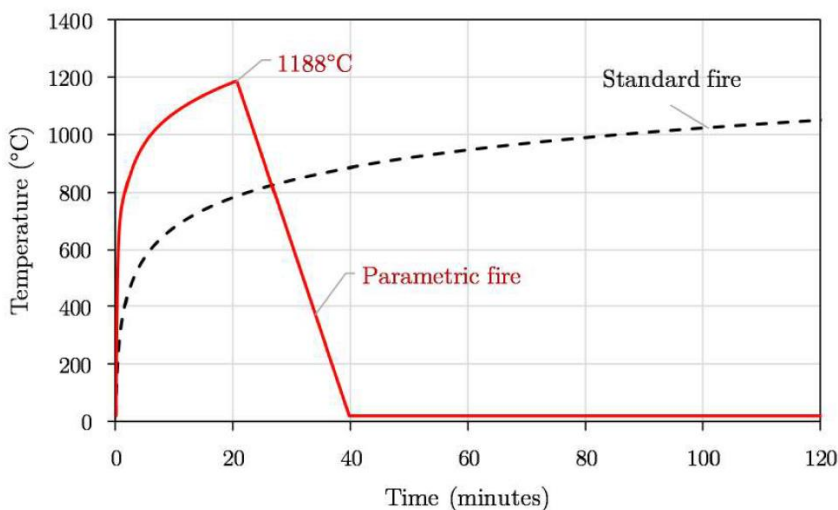


**Figure 3-6 A 2-hour parametric fire curve for the CBS system and standard fire curve (Marx, 2018).**

The most significant findings of the parametric study are the required thicknesses and type of materials that could be used for the ceiling board, and the required thickness of the inner FCB, to satisfy the FLS insulation criteria. Two potential materials for the ceiling board were investigated, namely, gypsum board (GB), which was part of the initial design, and Promatec-H Calcium Silicate board (CSB), which was used in the small-scale tests. The findings of the study revealed that the GB performed better than the CSB in terms of its insulation. A 25 mm CSB would be required to satisfy the insulation criteria, whilst only a 20 mm GB would suffice. However, the moisture content of the GB is higher than that of the CSB, which would lead to more shrinkage at elevated temperatures, resulting in a higher probability of the board cracking, and ultimately threatening the integrity of the ISD system. This is a major concern and is more likely to lead to structural failure or compartmentation loss than the insulation temperature criteria being exceeded. Furthermore, it was also identified that an inner FCB with a minimum thickness of 15 mm would be required to satisfy the insulation criteria. Thus, for the ISD system to satisfy the insulation criteria, the viable options would be to (a) increase the GB ceiling thickness to 20 mm, (b) replace the GB ceiling with a 25 mm CSB, or (c) keep the ceiling board unchanged and increase the thickness of the inner FCB to 15 mm.

Furthermore, Marx also investigated the influence of the type and depth of profiled steel sheeting that could be implemented in the SD design, namely, 75 mm Bond-Dek steel sheeting, which was implemented in the original SD system, Voidcon VP50, which was implemented in the small-scale experimental tests, and VP115 steel sheeting. The results indicated that the specified profiled steel sheeting had a negligible effect on the fire resistance of the SD system. However, the structural and serviceability stiffness of the SD is significantly influenced by the depth of the sheeting.

The investigation of the thermal performance of the system under a severe parametric fire was also aimed at estimating the temperature evolution of the horizontal steel members. Due to the higher initial heating phase of the Parametric Fire, the FE models of all the beam sections experienced significantly higher temperatures during the first 20 minutes, when compared to the standard fire models. This is followed by a decrease in steel temperatures during the cooling phase, with the bottom flanges of all beam sections cooling more rapidly in relation to the webs and top flanges of each section, respectively. This resulted in lower bottom flange temperatures in the ParF scenarios at the 60-minute mark compared to the StF scenarios.

### *3.3.2 Research conducted by Kloos (2017)*

The results from Marx's standard and parametric fire (StF-C, StF-NoC, and ParF) thermal models, were used by Kloos (2017) as the input data to develop thermal-stress models of the horizontal structural members on both a single element and on a global structural scale. Single element thermal-stress models of the primary P-beams and secondary J-beams were developed, investigating the thermal-stress response of the sections under both the StF-C, StF-NoC and the ParF load cases, whilst varying the end boundary conditions. The ParF load case analyses were conducted to investigate the behaviour of the sections under higher peak temperatures and to estimate if any tensile forces develop in the beams during the cooling phase. Four boundary condition variations

were investigated in the J-beam models, namely: Fixed-Fixed (FF), Fixed-Roller (FR), Pinned-Pinned (PP), and Pinned-Roller (PR). Since the P-beams are connected to the columns, the longitudinal expansion of the P-beams is resisted by the columns. As a result, Kloos calculated the stiffness of the columns about their weak-axes and applied it as a spring boundary condition in the longitudinal direction of the P-beams, whilst having the vertical and lateral translations fully fixed. A second approach was also investigated for the P-beams boundary conditions, where the longitudinal spring BC was removed and the translation fixed, i.e., the columns were assumed to provide full lateral restraint. Lastly, Kloos developed a global structural model of a single sub-structure, where different fire case scenarios were investigated under all three thermal loads. The findings of each model case will be briefly summarized below.

### ***J-beam thermal-stress models***

The most significant findings produced by both the StF-C and StF-NoC scenarios were: (1) Support conditions that induce axial force, by preventing longitudinal expansion, resulted in higher mid-span vertical deflections, as would be expected. This can lead to lateral torsional buckling of the top flange at higher elevated temperatures, as experienced in the StF-NoC case. The asymmetry of beams makes them susceptible to lateral-torsional buckling. (2) Supports that provided moment fixities resulted in lower mid-span vertical deflections. However, providing moment fixities in an actual connection is challenging and the models indicated that these supports induce larger lateral deflections. (3) Due to the asymmetry of the J-beam, the bottom flange experienced an outward lateral deflection at elevated temperatures as shown in Figure 3-7 below. Thus, Kloos (2017) recommended designing the beam end connections as pinned with slotted bolt holes to provide space for the thermal expansion of the beams.

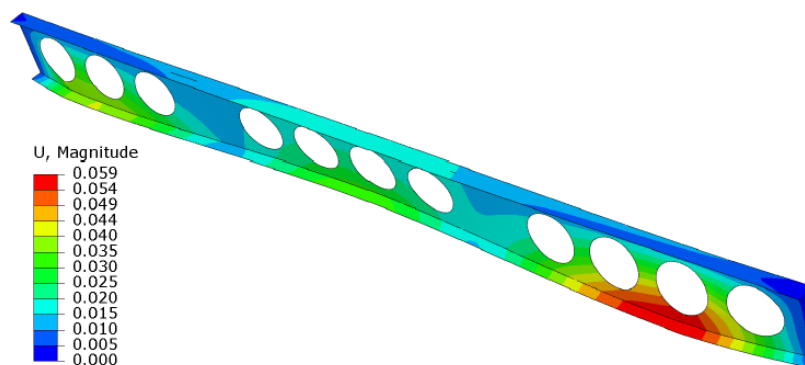


**Figure 3-7 Fixed-fixed (FF) J-beam experiencing lateral deflection of the bottom flange caused by restrained thermal expansion. The total deflection is shown in (m). (Kloos, 2017)**

The ParF scenario yielded comparable results to the StF scenarios with regards to the lateral outward bending of the beam's bottom flange. Apart from the pinned-roller support case, all models sustained permanent plastic deformations with regards to the lateral deflection. However, most strain was recovered during the cooling phase. Furthermore, in both the fixed-roller and pinned-roller boundary condition cases, due to the lack of induced axial forces, negligible plastic strain was experienced, and the beams were able to recover most of the vertical deflection during the cooling phase. Tension forces were developed during the cooling phase for the

fixed-fixed and pinned-pinned support cases, with the pinned-pinned case experiencing the largest tensile force of 268kN. This should be kept in mind when designing the connections of the J-beams, in that connections may no longer only have to transfer shear forces if axial restraint is present.

### ***P-beam thermal-stress models***

The P-beam StF-C and StF-NoC scenarios yielded the following results, similar to those above: (1) preventing longitudinal expansion of the beams at the columns, i.e., when the columns are assumed to provide full lateral restraint, resulted in significantly higher induced axial forces when compared to the spring support models, for both the fire load cases. (2) The 40 mm top and bottom beam flange notch where the beam connects to the columns renders the beam asymmetrical; as a result, the load carried by the beam induces a torsional force due to a shift in the shear centre. Under ambient conditions while loaded, this causes the top flange of the beam to deflect laterally by 3.3 mm as depicted in Figure 3-8 (a) below, which precipitates a significant lateral deflection at elevated temperatures. (3) Furthermore, as the bottom flange deflects laterally under elevated temperatures, it is held back by the rest of the beam, which further exacerbates the already prevalent torsional force in the beam, causing the bottom flange of the beam to deflect upwards, mimicking a twisting action as depicted in Figure 3-8 (Right) below. Consequently, the lateral deflections dominated when compared to the vertical deflections of the beam. (4) Plastic failure occurred during the StF-NoC scenario, resulting in a runaway deflection, with the plasticity concentrated around the connections area to the columns. This indicates that highly elevated temperatures can cause serious structural failure in the P-beams. Hence, if the ceiling system fails the steel structural system is likely to fail due to the high temperatures attained.

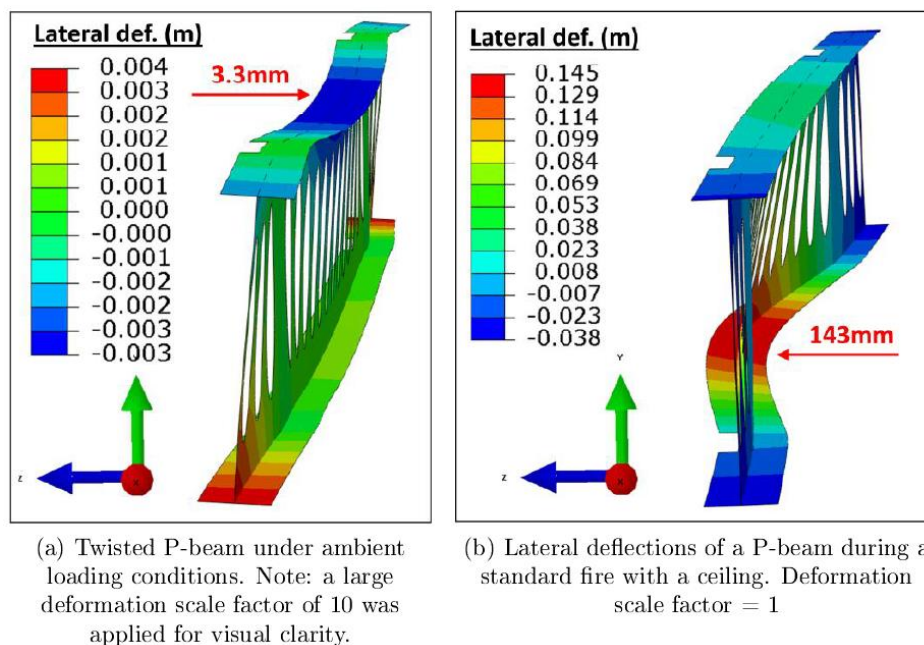


**Figure 3-8 P-Beam single element model under ambient temperatures (Left) and standard fire (Right) conditions. (Kloos, 2017)**

The parametric fire model yielded comparable results to the standard fire models, with significantly higher induced axial forces for the fixed column boundary conditions. Similarly, the lateral deflections dominated, causing the bottom flange to deflect upwards. However, no major failure mechanisms occurred, and despite the significant deflections, the beam was able to recover almost entirely during the cooling phase. Finally, the maximum tensile force developed in the beam during the cooling phase was only 62 kN for the axially fixed case, suggesting that the beam to column connection will most likely not experience any high-tensile forces.

### ***Global structural models***

The global model comprised the structural elements of a single sub-structure, however, the columns and lateral bracing were excluded as depicted in Figure 3-9 (Left) below. Three different fire scenarios were investigated, namely: (FS1) Fire Scenario 1 - a localized fire heats up only a single J-beam (J2), whilst the rest of the structure remains at ambient temperature. (FS2) Fire Scenario 2, a compartment fire heats up a single bay (in this case, the middle bay B, Figure 3-9 (Right)), whilst the rest of the structure remains at ambient temperature. (FS3) Fire Scenario 3, compartmentation within the structure is lost, and the entire structure experiences elevated temperatures. The StF-C, Stf-NoC, and the ParF steel thermal temperatures were applied to each fire scenario, totalling nine global structural models. Main findings of some of the fire scenarios under each thermal loading case are briefly summarized below. The terminology (Left) of the beam sections used for the global model and a diagram of the different fire scenarios (Right) are depicted in Figure 3-9, with the latter being discussed below.

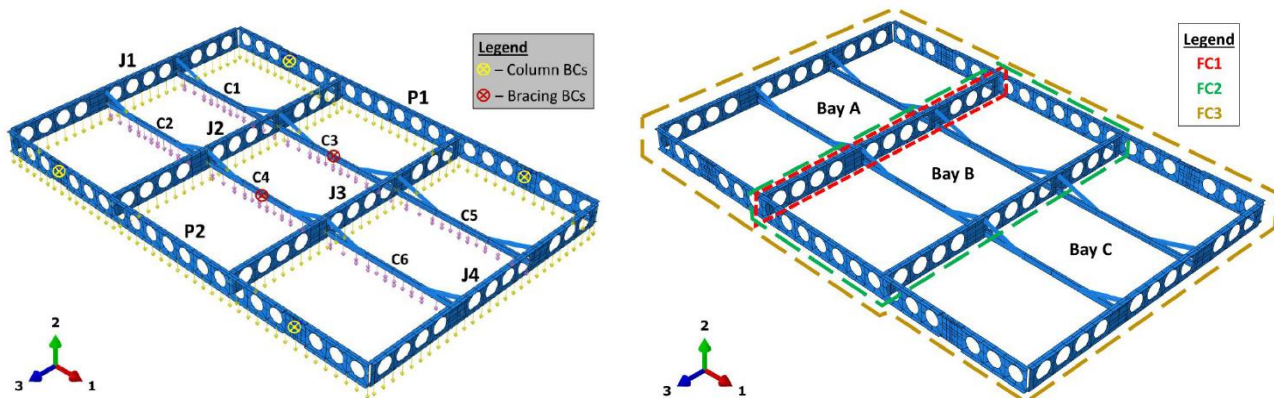


**Figure 3-9 Terminology used for global structural components (Left) and diagram of the three fire cases and the corresponding structural element that experience elevated temperatures (Right). (Kloos, 2017)**

During the preliminary stages of the global structural modelling, Kloos identified that the use of fin plate end connections from the J-beams to the P-beams results in a 76 mm distance between the J-beam web end and the P-beams web face as depicted in Figure 3-10 below. The resultant eccentricity caused by this distance induces a torsional force within the P-beams. This further exacerbates the twist action already prevalent in the P-beams as described above for the P-Beam single element models. Thus, through correspondence with the SAISC, a double angle cleat connection design was henceforth implemented to connect the J-beams to the P-beams. This design change results in only a 3 mm eccentricity between the J-beam end and the P-beam web face, which Kloos then implemented in the global structural models.

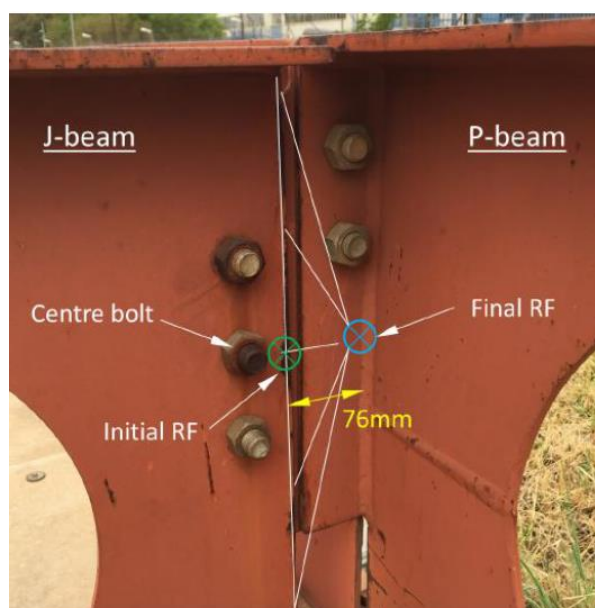


**Figure 3-10 Initial connection detail of the J-Beams to the P-Beams (Kloos, 2017), which was modified to reduce torsional effects.**

### ***Fire scenarios for global structural behaviour***

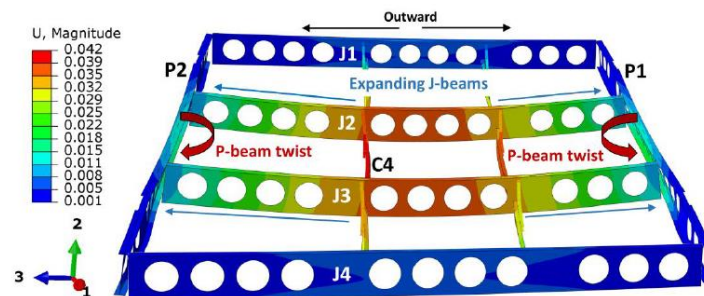
Following the models of single beams presented above, Kloos carried out finite element analyses of a full sub-structure with different fire scenarios to understand the structural response at elevated temperature. Each scenario represents different portions of the structure being heated.

#### **Fire Scenario 1 (FS1) – Single J-beam affected by fire**

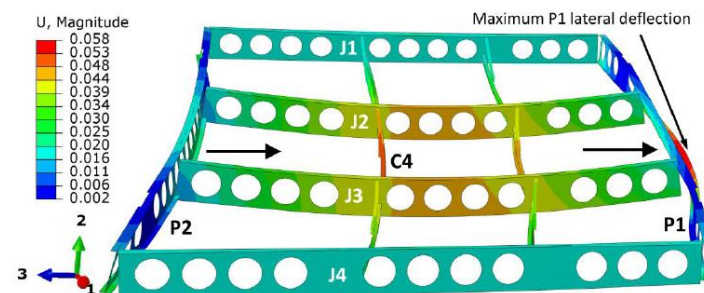
The behaviour of the heated J-beam (J2) in the global model was compared to that of the single element J-Beam (StF-C) pinned-roller and pinned-pinned models and showed a good correlation with the pinned-roller single element model. This indicates that negligible axial forces develop in the J-beams, as the P-beams offer little axial restraint and bend about their weak axis as the J-Beams expand. Furthermore, the vertical deflections of the J- and C-Beams were all well within the specified limit as recommended in Part 20 of BS 476 (BSI, 2009) of span/20, even for the Stf-NoC and ParF cases. No major failure mechanisms occurred in any of the cases. Furthermore, the J-beams and channels were able to recover all thermal strain during the ParF cooling phase, i.e., no plasticity occurred.

### Fire Scenario 2 (FS2) – Single bay affected by fire

The following are the results for the three thermal load cases (StF-C, StF-NoC, and ParF): (1) The P-beams tried to expand longitudinally due to the elevated temperatures, but were restrained by the columns and the cooler external bays, resulting in axial forces in the beams. These induced axial forces exacerbate the initial twist caused by the 40 mm notch in the beam flanges. (2) The thermal loads were applied to both J-beams, increasing the lateral deflections experienced by the P-Beams as the J-Beams expanded longitudinally. The P-Beams undergo a series of buckling events. Initially, the P-Beams buckle laterally away from the structure in the outwards direction, i.e. in opposite directions away from the structure. (3) The J-beams, on the other hand, keep the P-Beams from deflecting outwards. This continues until P1's outward force overcomes P2's outward force, allowing P1 to buckle further outwards in the same direction while pulling P2 along with it. This behaviour is depicted in Figure 3-11 below. (4) P1 had a significantly greater lateral deflection than J2, indicating that caution should be exercised when connecting the ceiling to the P-beams to ensure that they remain intact during a fire. As a result, the main findings of these models were that lateral deflections of beams, caused by factors such as beam asymmetry, could compromise the ceiling system's integrity. As introduced above, failure of the SD is likely to lead to failure of the structure, and lateral deflections in the deflections are likely to lead to diaphragm stresses in the ceilings.



(a) 51 minutes - both P-beams are still rotating and deflecting outwards, in opposite directions relative to one another. P2 buckles shortly after 51 minutes, causing both P-beams to deflect as shown in (b).



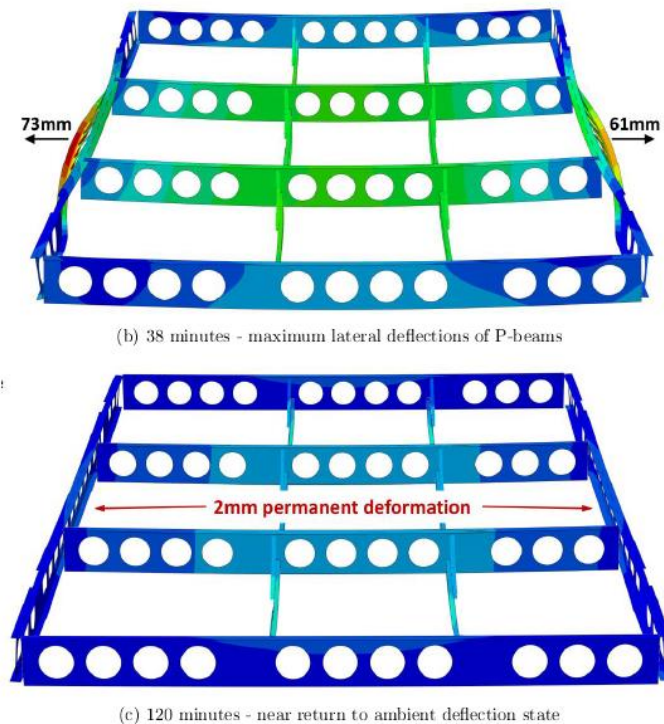
(b) 60 minutes - P2 has buckled, causing both P-beams deflect laterally to the right.

Fire case 2 (FC2) - global model at 51 and 60 minutes in the standard fire with the ceiling remaining intact analysis (StF-C). The total deflection is shown (in m), with a deformation scale factor of 10.

**Figure 3-11 Initial buckling behaviour of the P-Beams in opposite directions away from the structure (Top) and the eventual buckling of both P-Beams in a single direction (Bottom). (Kloos, 2017)**

### Fire Scenario 3 (FS3) – Entire structure effected by fire

For the StF-C case, FS3 exhibits the same general behaviour as FS2. However, because the P-Beams' entire lengths are exposed to high temperatures, larger axial forces are induced, and the structure buckles in the same direction sooner. Severe yielding occurred around the connection area of the P-beams to the columns in the StF-NoC case. In single element models, the P-Beam also experienced this plastic failure mechanism. Initially the P-Beams experience the same twisting action as in the single element models, however, as the steel starts to yield, the downward deflection of the entire structure dominates, resulting in a runaway deflection failure. This is significant, as this failure corresponds with the ultimate fire resistance of the CBS system. The ParF thermal case in FS3 exhibited different behaviour when compared to FS2, where the outward deflection of the P-Beams in opposite directions away from the structure persists throughout the entire heating phase of the parametric fire as depicted in Figure 3-12 (Top) below. Significantly, the structure was able to achieve a near-ambient deflection state during the cooling phase of the parametric fire as indicated in Figure 3-12 (Bottom) below.



Fire case 3 (FC3) - global model at 0, 38 and 120 minutes in a parametric fire analysis. The total deflection is shown. Deformation scale factor = 5.

**Figure 3-12 Fire case 3 (FS3) – global model at 38 (Top) and 120 (Bottom) minutes in a parametric fire analysis. (Kloos, 2017)**

### 3.4 Design of experimental CBS frame

Based on the investigations conducted above a structural system representative of buildings designed using the CBS was developed in this work, but incorporating lessons learnt from research to date. As introduced previously, the system consists of two distinct systems – the structural steel frame and the sandwich flooring system, where the latter will be addressed in the following section. Figure 3-13 below gives a visual representation of the thought process behind the design of the experimental frame tested in this work. The design of the experimental frame was based on the design of a single sub-structure module. However, due to the size of the standard fire furnace available, some modifications had to be implemented as the full 12.5 x 7.925 m system could not be tested. Figure 3-13 below shows the experimental frame shortly after being assembled (Bottom-Right), and a top view of the main horizontal structural components (Bottom-Left). The attachment of the trafficable VP50 SD system to the bottom of the horizontal structural components is presented in Chapter 5, which was also part of the experimental setup.

The experimental frame horizontal structural components comprises of two primary beams (PB 1 and PB 2), spanning 3.64 m, and connected to the columns; two secondary cellular beams (CB 1 and CB 2), spanning 5.66 m, connected to the primary beams; and two tertiary beams consisting of channels that support the SD (PC 1 and PC 2) connected to the secondary beams. The primary beams consisted of 203×133×25 UB sections, whilst the secondary beams consisted of 285×133/133×25 cellular beams, with 220 mm diameter cells spaced at 280 mm. The tertiary beams consisted of PC180×70 parallel flange channels. PB1 and PB2 represent the sectional P-Beams of a single module configuration, whilst CB1 and CB2 represent the J-Beams, and PC1 and PC2 represent the C-Beams. For preliminary sizing the secondary beams were designed using CELLBEAM software developed by Kloeckner metals.

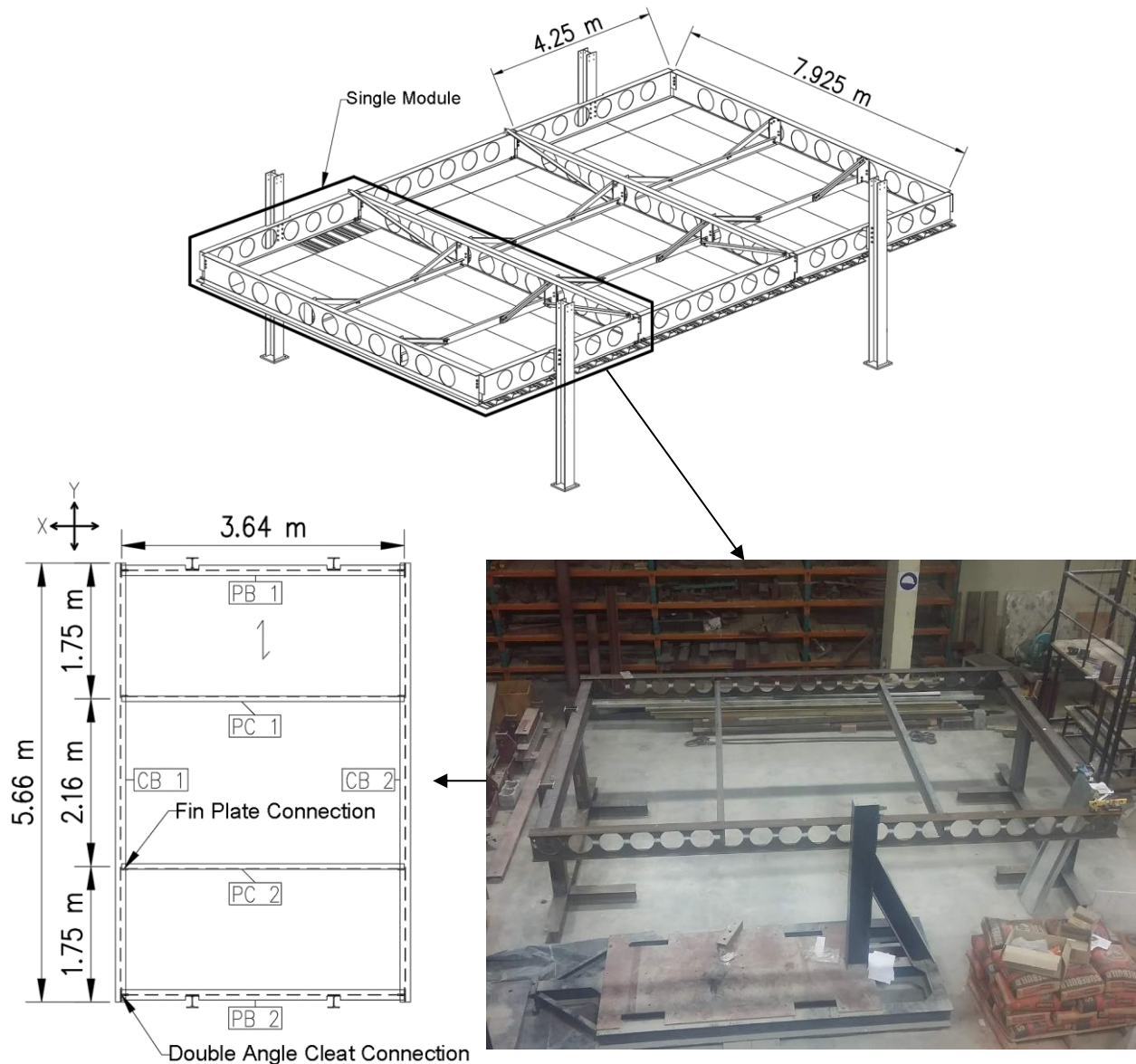


**Figure 3-13 Diagram of the experimental frame layout and structural components terminology.**

While the general configuration of the experimental frame remained the same as in the CBS module, some differences should be noted. Firstly, due to the size of the experimental frame, I-Beam sections were utilized for the primary beams. This stems from the fact that cellular beams are normally utilized as long-span beams and including this in the experimental frame would have led to an over-design. Secondly, as the experimental frame only represents a single module of the CBS system, the fly-bracing was excluded from the design. The fly-bracing only works as intended when they are connected on both sides of the beams (in this case, CB1 and CB2), which is only achieved when the entire sub-structure is assembled. Thus, parallel channel beams were employed instead. Lastly, for the experimental frame to be a self-supporting structure, two columns were connected to the primary beams instead of only one as in a single CBS module. A spreader beam footing system was attached to the bottom of the columns to further enhance the stability of the experimental frame and to ensure that no damage would be inflicted to the furnace floor.

An important factor to note is that the J-shaped beams used in the initial design and previous work discussed above has been replaced by an I-shaped cellular beam. There are two reasons for this: (1) an angle is connected to the back of the J-beam meaning that if sufficient connectivity is provided the beam will behave as an I-shaped section, or (2) based on modifications to how the floor is supported the use of the J-beam + angle is less critical, and a single I-beam can be utilised in practice.

Double angle cleat connections were used to connect the secondary beams to the primary beams, and fin plate connections to connect the tertiary beams to the secondary beams. End-plate connections were also used to connect the primary beams to the columns, similar to the CBS system module design. The technical drawings and layouts of the experimental frame can be found in the online repository (Claasen *et al.*, 2021)

### 3.5 Development of SD specifications to be investigated in this work

As mentioned above, the initial design of the SD system has changed as a result of the research conducted by Marx and as identified in this research. The tested design of the SD system considered in this thesis is presented in this section, highlighting the material component changes, configuration and nomenclature.

There are multiple configurations for the SD system depending on the selected FCB thicknesses and VP50/115 profiled decking used. These configurations have been categorised according to the profiled steel decking used into two versions of the SD system, namely, the VP50 SD system and the VP115 SD system. These two systems are then further subdivided according to the FCB thickness used in each configuration as described in Chapter 4.

Figure 3-14 below depicts the general configuration and components of the VP50 SD version (Top) and VP115 SD version (Bottom) tested in this work. It should be noted, when the SD system is utilized as a stand-alone flooring system, the inner FCB that normally supports the false floor becomes the top FCB as indicated in Figure 3-14 below.

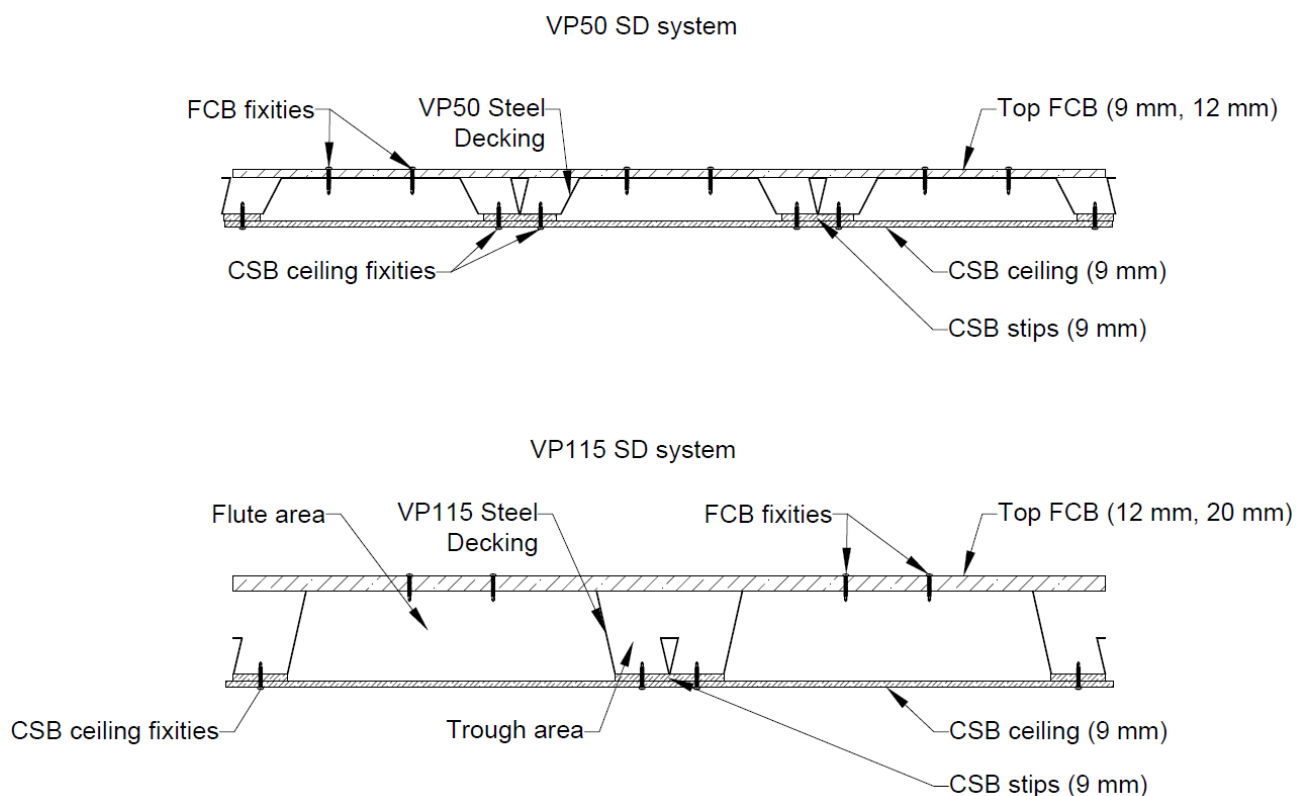


**Figure 3-14 Proposed and tested variations of the SD system and their components.**

The following component changes to the SD system have been made as identified through the research conducted by Marx (2018), and identified during this work. Firstly, it was established through the parametric study conducted by Marx that using different profiled steel decking results in a negligible change with regards to the fire resistance of the system. Thus, the Bond-Dek profiled steel sheeting was henceforth replaced by the Voidcon profiled steel sheeting due to availability and the different deck sizes that could be considered (50 and 115mm deep options). Secondly, although it was identified that the performance of a gypsum board ceiling performed better compared to the Promatec-H Calcium Silicate board (CSB) with regards to insulation, the high moisture content of the boards could potentially pose a threat to the integrity of the system in case of a fire as they become brittle. Thus, the gypsum board initially specified by the SAISC, was henceforth replaced by the CSB ceiling, which also matches the materials used by Marx for testing. Furthermore, it has been identified through this work that implementing CSB strips as part of the CSB ceiling improves the fire resistance of the SD system, is more practical for fixing on site, and acts as a joint between adjacent CSB. This is also indicated in Figure 3-14 above, where the CSB strips are situated beneath the trough of the profiled steel sheeting. The strips significantly reduce the amount of energy conducted into the steel decking. Hence, even though Marx's work it was calculated that a 20mm thick gypsum board ceiling was required, it will be shown in this work that a 9mm CSB with 9mm strip gives a suitable performance. The CSB strips also have practical importance in that they are required where boards are connected to each other.

Finally, the FCB component has not been changed in the design of the SD system. However, the FCB used in the small-scale tests differs slightly in composition from the FCB implemented in this research with regards to the supplier due to availability of materials. The components implemented in this research for the SD system is discussed in more detail in the section to follow

### 3.6 Conclusion

This chapter introduces the original proposed CBS and SD system designs, highlighting structural components, layout, and terminology. The chapter then moves on to present previous research conducted on the CBS and SD systems regarding the performance of the systems in fire, as well as some of the design changes made as a result of that research. The experimental frame, which was built to the design aspects of the CBS system and tested in this study, is then presented. Finally, the changes made to the SD system as a result of previous research conducted are presented, and the SD system's final configuration as tested in this work is described.

## Chapter 4 Small-scale and medium-scale experimental setups and results

### 4.1 Introduction

As part of an extensive experimental program carried out in this work, a series of tests were conducted to investigate various aspects of the CBS system, ranging from small-scale material tests to large-scale standard fire tests. The following chapters (Chapter 4 and Chapter 5), aim to provide insights into the different experimental setups, testing methodologies, materials used throughout the testing regimes, and their respective results. The information pertaining to the experiments is provided in an ascending order with regards to the geometrical size of each test conducted, where the test setups and results are presented from the geometrically smallest test to the geometrically largest test in the sections and chapters to follow. This ascending structure also then correlates to the complexity of each test, where the complexity increases as the scale of the test increases. The number of experimental tests that have been conducted and the order of presentation are as follows:

- Small-scale material tests – Chapter 4
- Sandwich decking configurations under load – Chapter 4
- Large scale test on the SD only – Chapter 5
- Large scale test on the SD and CBS – Chapter 5

Hence, this chapter is dedicated to presenting the small-scale materials and medium-scale four-point bending tests carried out in this work, and their respective results. The chapter will be presented in four sections. This section (Section 4.1) serves as a brief introduction to the sections that follow. Section 4.2 details the findings of small-scale tensile tests performed on the structural steel used in the experimental frame and the Voidcon VP profiled steel. The section continues by detailing the small-scale material tests conducted on the Fibre Cement and Calcium Silicate boards (FCB and CSB) utilized in the SD system. Section 4.3 then describes the four-point bending setup used to test the isolated medium-scale flooring systems (SD system), along with the respective results of each flooring configuration. The chapter is concluded with a summary of the findings in Section 4.4.

### 4.2 Small-scale material tests conducted and results

All small- and medium-scale tests discussed in this section were conducted at the Stellenbosch University (SU) structures laboratory, i.e., the structural and VP profiled steel tensile tests, the FCB and CSB materials tests, and the four-point bending tests. This section presents the findings of the small-scale tensile and materials tests conducted. The tests were conducted with the use of a Zwick static testing machine with an axial load capacity of 100 kN. The data acquired from the small-scale tests was subsequently employed in the Finite Element Models (FEM) of the SD systems and large-scale tests, as detailed in Chapter 6, Chapter 7, and Chapter 8.

#### 4.2.1 Structural and Voidcon VP profiled decking steel tensile tests and results

The tensile tests that were conducted gave the load deformations curves, from which the yield strength can be calculated. Samples of the structural steel (285×133/133×25 CB, Grade S355 (CB 1)) used in the tested experimental frame and the VP profiled decking steel sheeting (Voidcon VP50/115 decking profile) used in the SD system were tested. The general procedure for the tensile tests is well documented and was done according to SANS 6892-1 (SABS, 2010). The test samples were machined according to the guidelines in tables B1 and D2 of the appendix of SANS 6892-1 for the VP profiled decking and structural steel, respectively.

A total of four samples of the profiled decking steel and two samples of the structural steel was machined to the depicted dimensions below in Figure 4-1 with thicknesses of 0.8 mm for the VP50/155 profiled decking steel and 7.8 mm for the structural steel. The resulting stress-strain graphs and the calculated average yield strengths of the tested materials (i.e., the average yield strength calculated from the four VP decking samples and the two structural steel samples) are as shown and listed below in Table 4-2 and Table 4-1, respectively. The modulus of elasticity of the steel was taken as 200 GPa (de Clercq, 2016), as per South African norm.

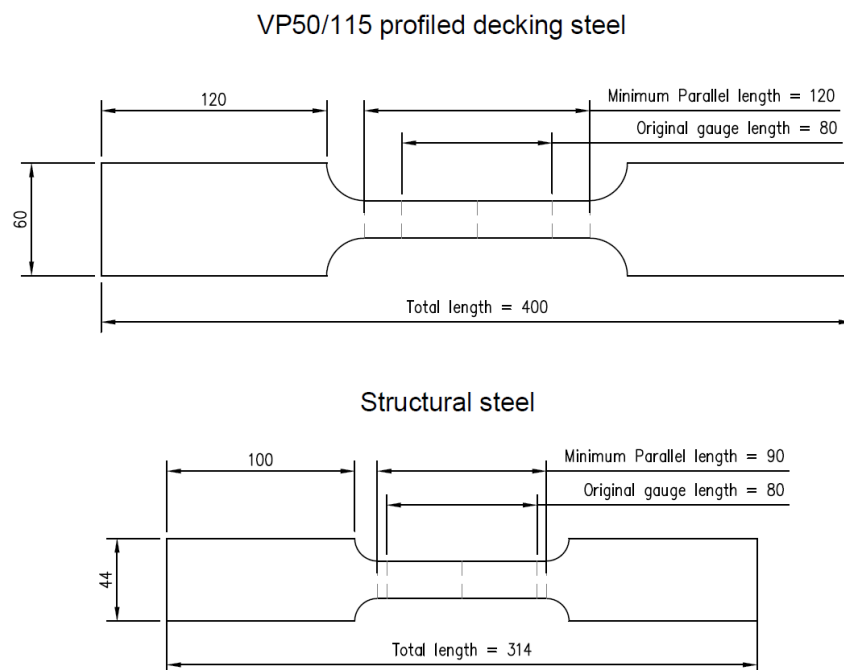


**Figure 4-1 Dimensions of tensile test samples (mm).**

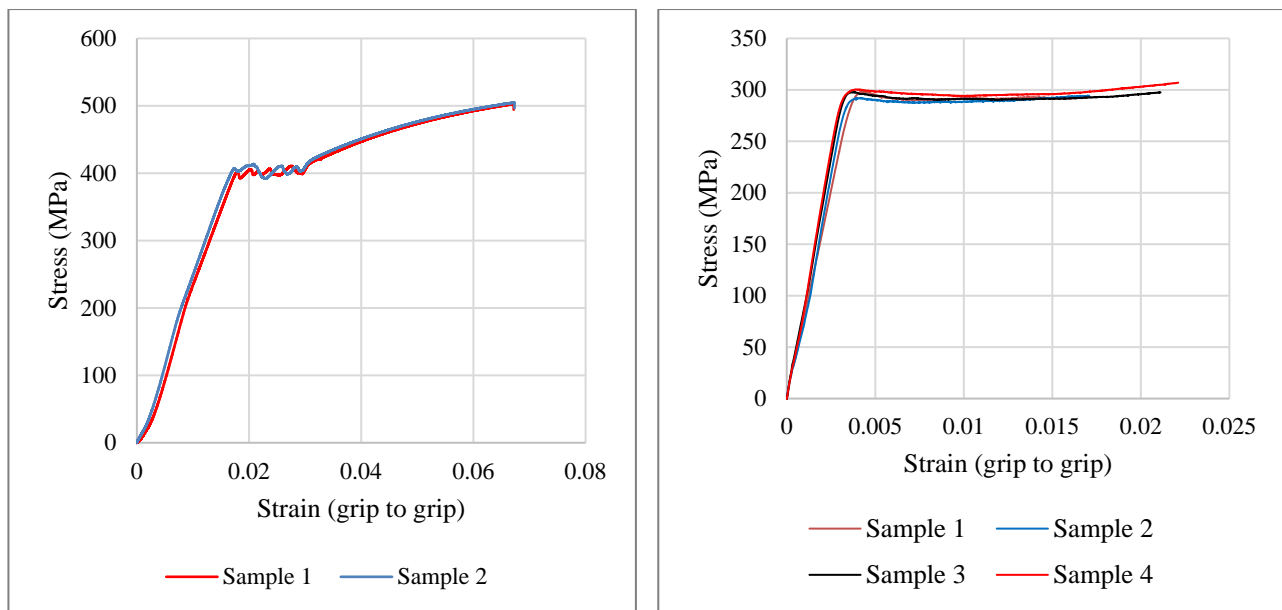


**Figure 4-2 Stress-strain graphs of the structural steel (Left) and profiled steel sheeting (Right).**

**Table 4-1 Mechanical properties of structural and VP profiled decking steel.**

Mechanical property	Structural steel	VP decking steel
Yield strength (MPa)	408	297

#### 4.2.2 Fibre cement and calcium silicate boards materials tests and results

A series of small-scale three-point bending, and compression tests were conducted on the FCB and CSB utilized in the SD system. The aim of the tests was to investigate the mechanical properties of the boards. The three-point bending tests were employed to determine the modulus of rupture (MOR) and modulus of elasticity (MOE) of the boards, whilst the compression tests were used to determine the crushing strength. The same testing methodologies were followed for both the FCB and CSB for each type of test conducted. All tests were conducted with 9 mm CSB and 12 mm FCB.

The three-point bending tests were conducted according to BS-EN 310:1993d (BSI, 1996). A total of twelve samples were tested for the FCB, where three samples were tested for each orientation (longitudinal and transverse) and face (top and bottom). Similarly, a total of 14 samples were tested for the CSB, where four samples were tested on the top face for each orientation, and three samples on the bottom face for each orientation. The load-deflection curves obtained from the tests were then used to calculate the MOR and MOE values for each sample tested.

The compression tests were conducted by crushing the boards on the sides, in both the longitudinal and transverse directions. Four 50 mm × 50 mm cube samples were tested for each orientation, making a total of eight tests conducted for each of the boards. The crushing strengths of the cubes were calculated using the load-deformation curves obtained from the tests.

Figure 4-3 below depicts the final test setup of a given sample for the three-point bending (Left) and compression (Right) tests.



**Figure 4-3 Materials in three-point bending (Left) and compression (Right) tests setups.**

Figure 4-4 - Figure 4-7 below depict the results of the three-point bending and crushing tests performed on the fibre cement and calcium silicate boards. The notation of the three-point bending test samples were designated according to the orientation (i.e., Longitudinal (Long), Transverse (Trans)), the face (Top (T), Bottom (B)) and sample number (SX). Similarly, the notation used for the crushing test samples were designated according to the orientation and sample number.

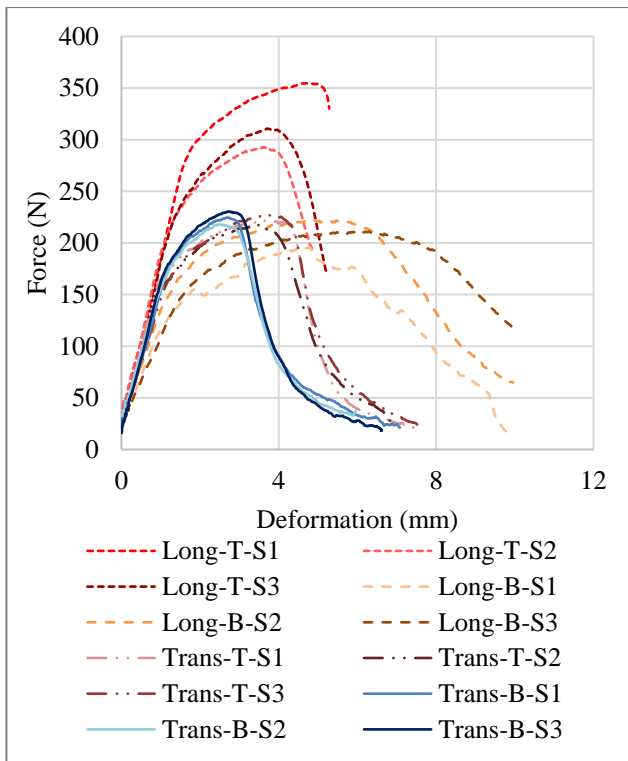


Figure 4-4 Fibre cement board bending tests results.

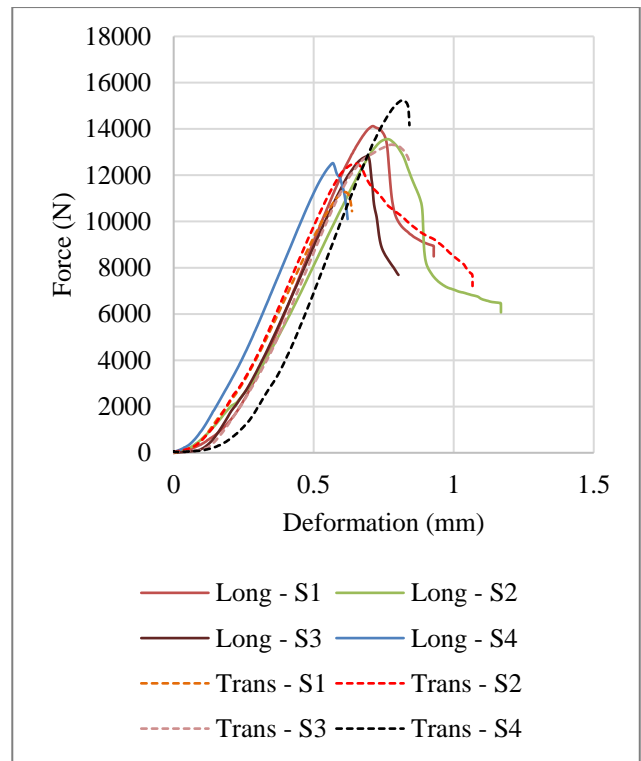


Figure 4-5 Fibre cement board crushing tests results.

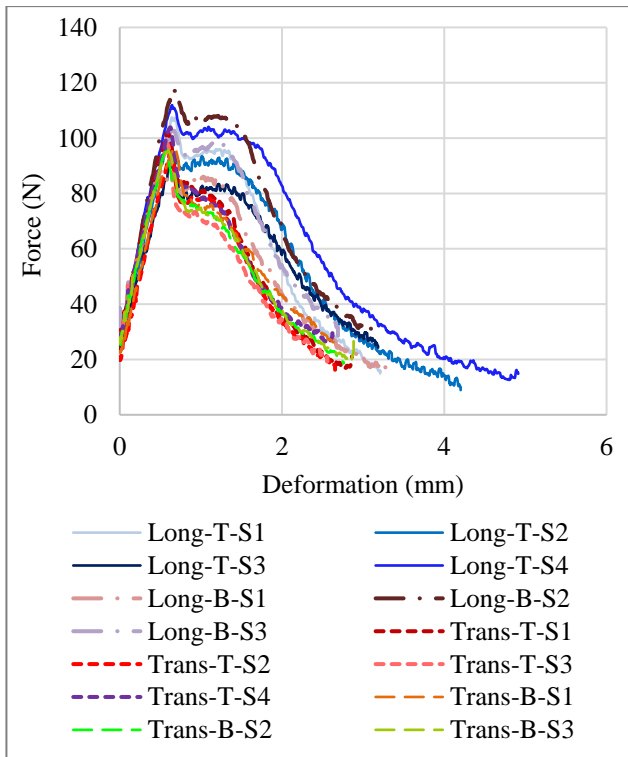


Figure 4-6 Calcium silicate board bending tests results.

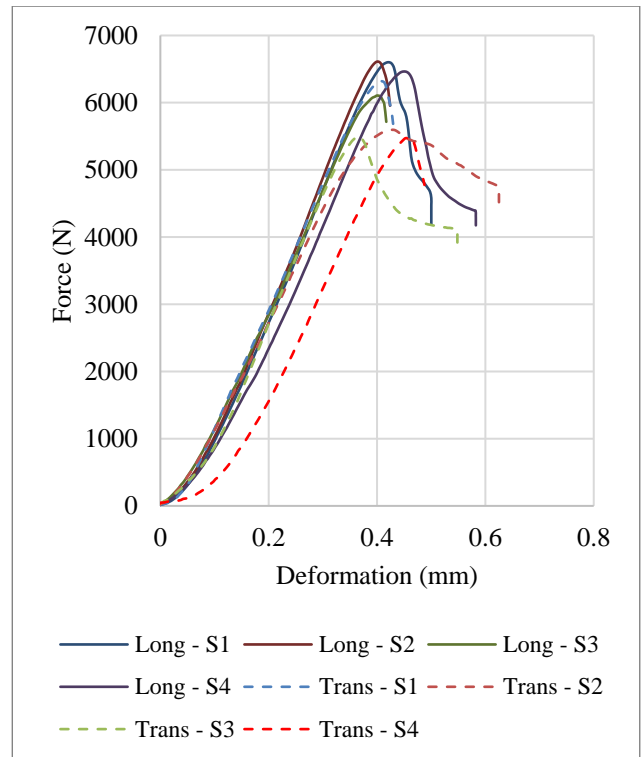


Figure 4-7 Calcium silicate board crushing tests results.

The bending and compression test results are listed in Table 4-2 and

Table 4-3 below, respectively. Only the average values corresponding to each orientation and face tested in the bending tests, and the orientation of the sides tested in the compression tests are listed.

**Table 4-2 MOR and MOE properties of the FCB and CSB.**

Material	Orientation	Face	Average MOR (MPa)	Average MOE (MPa)
Fibre Cement Board	Longitudinal	Top	16.2	6169
		Bottom	11.8	4784
	Transverse	Top	11.5	5485
		Bottom	11.7	5609
Calcium Silicate	Longitudinal	Top	7	5413
		Bottom	7.4	5434
	Transverse	Top	6.8	5308
		Bottom	6.5	5261

**Table 4-3 FCB and CSB average crushing strength properties.**

Material	Orientation	Average crushing strength (MPa)
FCB	Longitudinal	21.9
	Transverse	20.4
CSB	Longitudinal	13.6
	Transverse	12.8

### 4.3 SD system four-point bending tests and results

A series of medium-scale flooring configurations were built to the design aspects of the SD system layouts described in Chapter 3. The tests were intended to examine the decking system's performance under four-point loads and determine the maximum span lengths achievable and their associated failure modes. Two sizes of Voidcom decking profiles, namely VP50 and VP115, were examined in conjunction with different FCB thicknesses and fixity arrangements. The 9 mm CSB and CSB strips at the bottom of each composite sample remained unchanged (i.e., only the FCB thicknesses were varied). Additionally, four-point bending tests using isolated VP50/115 profiled steel sheets with no boards attached to the top or bottom were also performed.

This was to ultimately establish if the flexural capacity of the SD system would be adequate to span the lengths required for the CBS system and safely carry the loads to the respective structural beams. Additionally, the investigation was also aimed at determining the maximum span lengths achievable when using the system as a stand-alone flooring system in other structural designs. Hence, the SD system's flexural capacity was investigated according to SANS10162-1 (SABS, 2011b) for the ultimate and serviceability limit states (ULS and SLS).

### 4.3.1 Test specimens setup

The four-point bending tests performed, as well as the nomenclature used for each sample and their respective material components, are listed below in Table 4-4. Two thicknesses of FCB were tested in combination with each of the VP50 and VP115 profiled steel decking. Hence, each SD system version has been further classified based on the FCB thickness used; for instance, when using the VP50 SD system in combination with a 9 mm FCB, the system is designated as the VP50-9 SD system. If more than one test is conducted on a specific layout then the reference TX refers to the number of the test. Furthermore, a sample of the VP50 and VP115 profiled steel decking was also tested in isolation, such that the capacity of the profiled steel decking can be determined without any boards attached to the top or bottom. The isolated VP profiled decking samples are denoted as VP50-ISO and VP115-ISO for the VP50 and VP115 profiled steel decking, respectively. It is important to note that the VP50 configurations are currently the specified system for the CBS. However, the VP115 tests were included to provide a wider data set, to investigate alternative configurations which may be more efficient, and to allow further studies on serviceability limit state behaviour. The VP115-12 and VP115-ISO sample tests were performed last and not during the same time period as the rest of the samples. As a result, the test setup of these samples differed slightly from the rest of the samples tested before them. These differences will be discussed below in Section 4.3.1 and pertain only to the support conditions and sample lengths.

**Table 4-4 Complete list of samples tested under four-point bending.**

Tests	FCB thickness (mm)	CSB and strip thickness (mm)	Fixities spacing (longitudinal direction, mm)	Test nomenclature
<b>VP50 SD system tests</b>				
<b>1</b>	N/A	N/A	N/A	VP50-ISO
<b>2</b>	9	9	200	VP50-9-T1
<b>3</b>	9	9	200	VP50-9-T2
<b>4</b>	12	9	200	VP50-12-T1
<b>5</b>	12	9	200	VP50-12-T2
<b>VP115 SD system tests</b>				
<b>6</b>	N/A	N/A	N/A	VP115-ISO
<b>7</b>	12	9	200	VP115-12-T1
<b>8</b>	12	9	200	VP115-12-T2
<b>9</b>	20	9	200	VP115-20-T1
<b>10</b>	20	9	200	VP115-20-T2
<b>11</b>	20	9	300	VP115-20-T3
<b>12</b>	20	9	400	VP115-20-T4

Figure 4-8 and Figure 4-9 below depict a detailed cross-section view of the SD system variations tested in this work

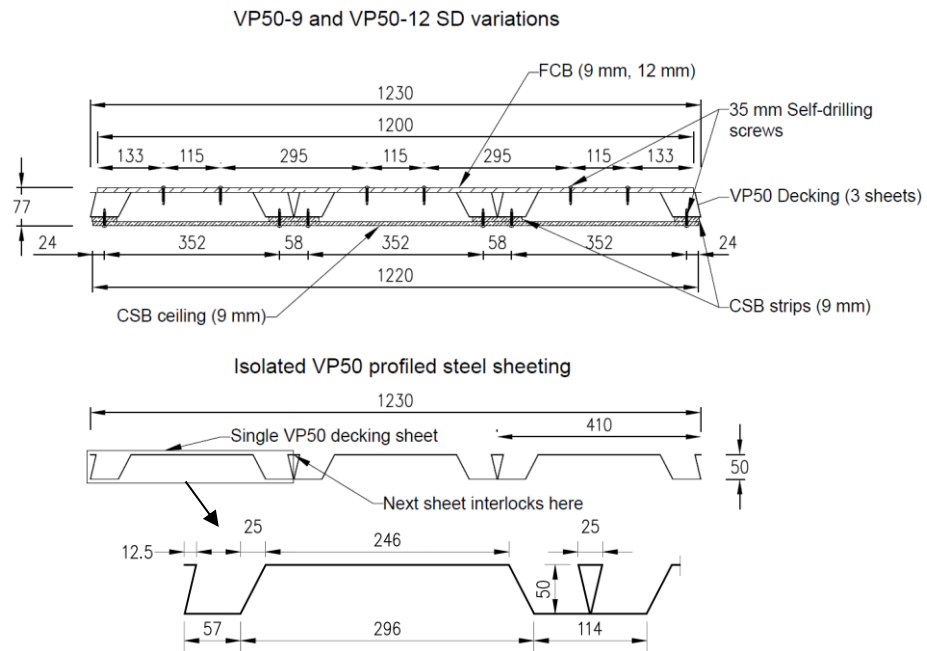


**Figure 4-8 VP50-9 and VP50-12 cross-sectional view.**

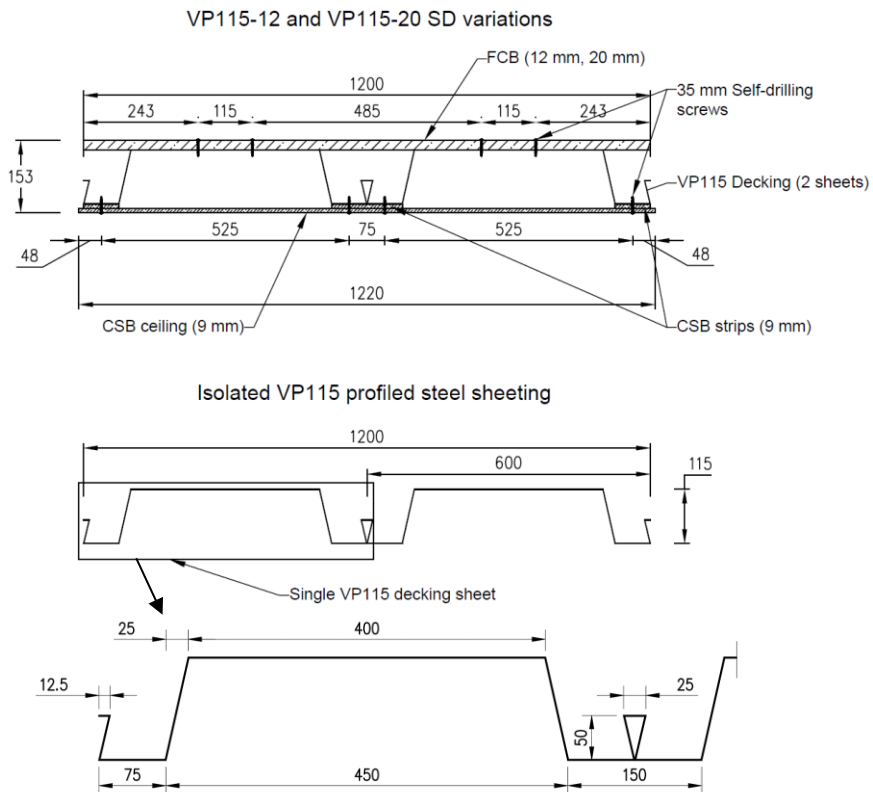


**Figure 4-9 VP115-12 and VP115-20 cross-sectional view**

In each of the VP50-9 and VP50-12 SD test specimens, three VP50 profiled steel sheets spanning 2.6 m and 1.23 m wide were used, with the sheets interlocked side-to-side at the trough sections as depicted in Figure 4-8 above. A single full-sized FCB, spanning 2.4 m and 1.2 m wide, was attached to the top of each sample, with a 9 mm and 12 mm FCB attached to the VP50-9 and VP-12 samples, respectively. Following that, the CSB ceiling was attached, with 100 mm wide CSB strips positioned immediately beneath the profiled steel sheeting's inner trough sections and 50 mm wide CSB strips positioned beneath the outer trough sections (which refers to the trough section on the sides of the specimens) with all the strips spanning 2.44 m. The specimens had a single full-sized CSB attached to the bottom, spanning 2.44 m and 1.22 m wide, with the CSB strips sandwiched between the profiled steel decking trough sections and the CSB. 35 mm self-drilling screws were used to secure the boards to the top and bottom of the profiled steel decking. The FCB were attached to the profiled steel decking along the centre lines of the top flute sections with pairs of two screws spaced 115 mm apart in the transverse direction and 200 mm apart in the longitudinal direction. The CSB and CSB strips were attached using pairs of screws spaced at 58 mm in the transverse direction and 200 mm in the longitudinal direction along the centre lines of the bottom trough sections. Single screws were used along the specimens' outer trough sections and spaced 200 mm apart in the longitudinal direction. The screws would go through the CSB first, followed by the CSB strips, and finally the profiled steel sheeting. The isolated VP50 profiled steel decking test consisted of three steel sheets interlocked side-to-side, spanning 2.6 m and 1.23 m wide.

Each of the VP115 SD specimens were made up of two VP115 profiled steel sheets, spanning 2.6 m and 1.2 m wide for the VP50-20 SD samples and spanning 3 m and 2.6 m wide for the VP115-12 samples. Following that, a single full-sized 20 mm FCB was attached to the top of each VP115-20 sample, and a 12 mm FCB was attached to the top of the VP115-12 samples. The FCB were attached in an analogous fashion to the VP50 SD samples, with a pair of two screws spaced at 115 mm transversely and 200 mm longitudinally and drilled along the centre lines of the profiled steel sheeting's top flute area. Furthermore, 150 mm wide CSB strips were placed along the inner bottom trough section of the profiled steel decking, while 75 mm wide strips were placed along the outer bottom trough sections, with all strips spanning 2.44 m. Following the CSB strips, a single full-sized CSB was attached with a pair of two screws spaced at 75 mm in the transverse direction and 200 mm in the longitudinal direction along the inner bottom trough section's centre lines. Single screws were used along the outer trough sections. Two VP115 profiled steel sheets, spanning 3 m and 1.2 m wide, were used in the isolated VP115 profiled steel decking test. The fixities arrangement of the VP115 SD system (Bottom-Middle and Bottom-Right) and the VP50 SD system (Bottom-Left) configurations are depicted in Figure 4-11 below. Figure 4-10 (a and b) also depict the fixities arrangements for a given VP115-12 sample. Finally, stiffeners were attached to the ends and mid-point of one of the VP115-20 samples, which is identified in Table 4-4 above as VP115-20-T2 and is also depicted in Figure 4-10 (c) below. When using VP115 profiled steel decking in concrete composite construction, these stiffeners are typically used to hold the concrete in place during the curing stage. This was to explore if the stiffeners had any positive effect on the SD system's moment capacity.

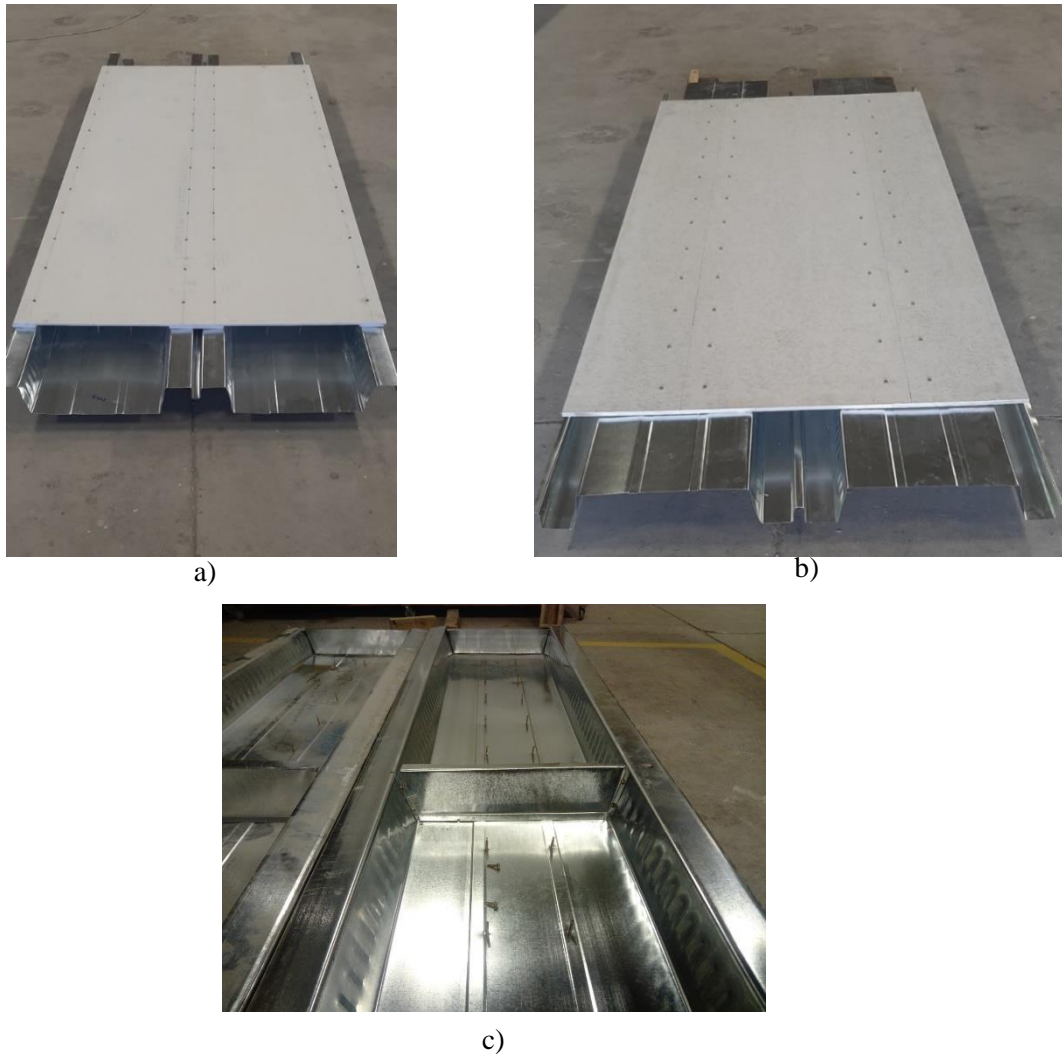


**Figure 4-10 CSB (a) and FCB (b) fixities arrangement for a given VP115-12 sample, and Sample VP115-20-T2 Stiffeners (c).**

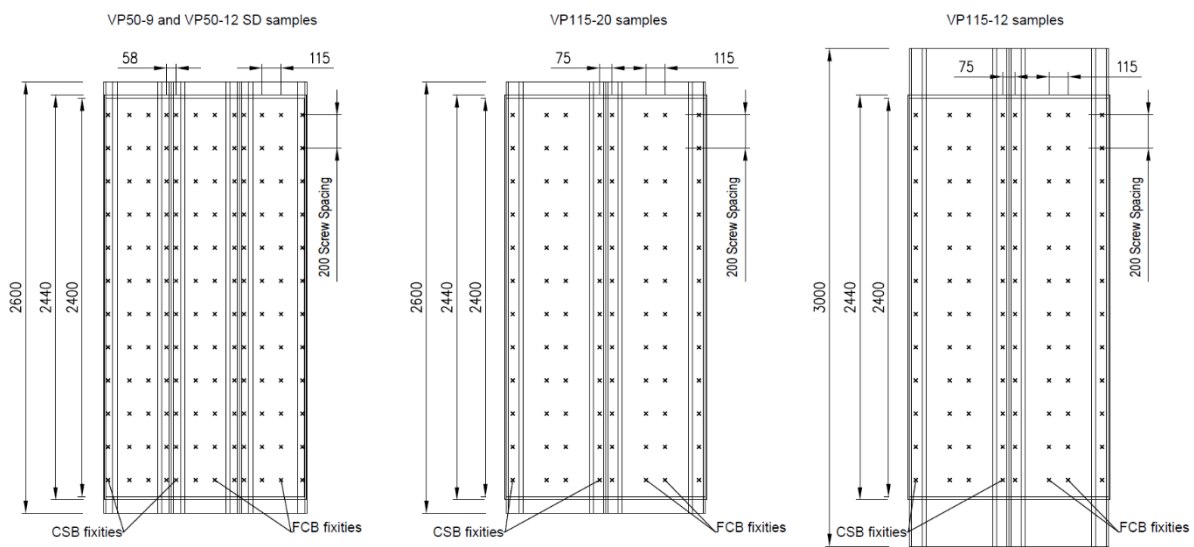


**Figure 4-11 Top view of the fixities arrangement for each composite test conducted.**

#### 4.3.2 Universal testing machine setup (Instron)

All tests were conducted with the use of an Instron universal testing machine at the SU structures laboratory. A single I-beam section (Spreader beam), which ran parallel to the test samples, was attached to the Instron. Two I-beam sections (Loading beams) were connected to the spreader beam in a perpendicular direction to the test samples. As shown in Figure 4-12 below, the loading beams spanned the width of the test samples (i.e., 1.2 m) and were spaced at 745 mm from centre-to-centre.

Roller supports were used to support the VP50 and VP115-20 SD specimens at 20 mm from the edge of the CSB (i.e., the supports were 2.4 m apart, with a total overhang of 100 mm), as shown in Figure 4-12 (Right) below, with the samples placed on the CSB. A loadcell was attached between the Instron and spreader beam to measure the applied load. A linear variable displacement transducer was placed on both sides of each sample at the midpoint to measure vertical deflections as the load was applied. The VP50, VP115-20, VP50-ISO, and the VP115-ISO samples were loaded until ultimate failure.

After the initial tests discussed above a modification was made to the setup for the VP115-12 and VP115-ISO specimens. Since the support applied an unrealistically narrow bearing area (i.e., the top of the circular roller) it was decided to change the supports to have a timber beam instead, which more accurately represents the CBS support plates that will be flexible and rotate with the SD. This reduces the occurrence of a local bearing failure above the support, to be comparable to how it would be in reality. Wooden block supports at 270 mm from the edge of the decking (i.e., the supports were 2.46 m apart, with a total overhang of 270 mm), as shown in Figure 4-13 (Right) below. As the distance between the supports were slightly increased, the length of the VP115 profiled decking was also subsequently increased to a length of 3 m, as shown in Figure 4-13 (Bottom-Right) above. However, the size of the boards and strips attached remained the same. The samples were placed on the decking, with a 10 mm space between the block supports and the CSB edge to allow free movement. The load-deflection data was obtained directly from the Instron machine.

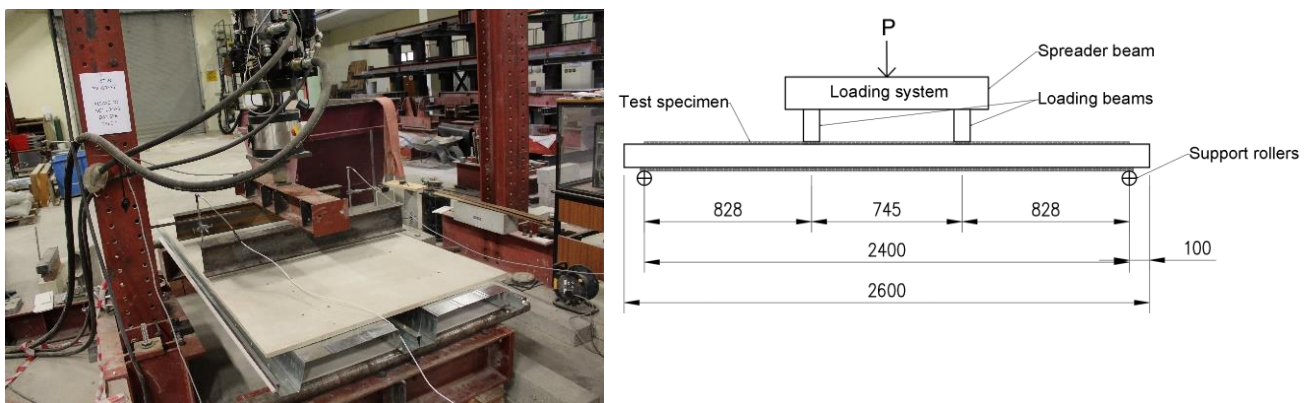


**Figure 4-12 Experimental setup (Left) and schematic (Right) of VP50 and VP115-20 samples tested.**

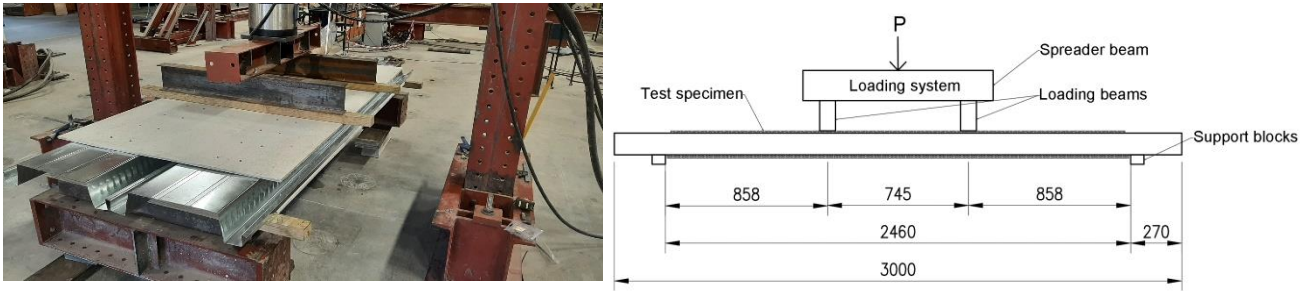


**Figure 4-13 Experimental setup (Left) and schematic (Right) of VP115-ISO and VP115-12 samples tested.**

*4.3.3 Decking only tests – VP50-ISO and VP115-ISO sample results*

Figure 4-14 and Figure 4-15 below present the load-deflection curves of the isolated VP50 and VP115 profiled steel decking tests, respectively. This data is useful to understand how the decking behaves when no boards are attached to it, or at positions where boards are not continuous.

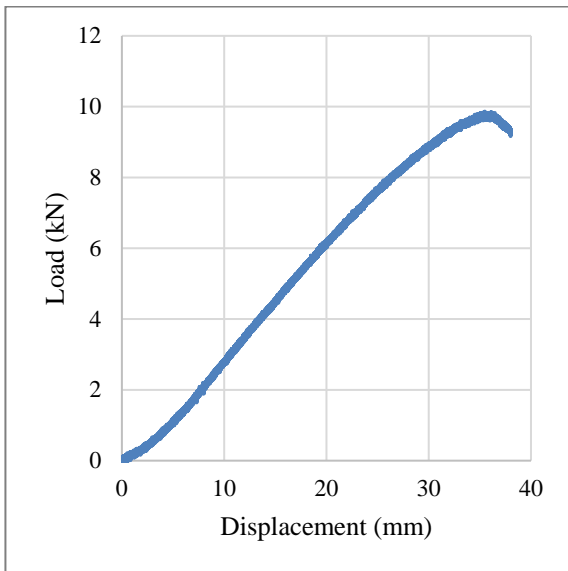


**Figure 4-14 VP50-ISO load-deflection curve.**

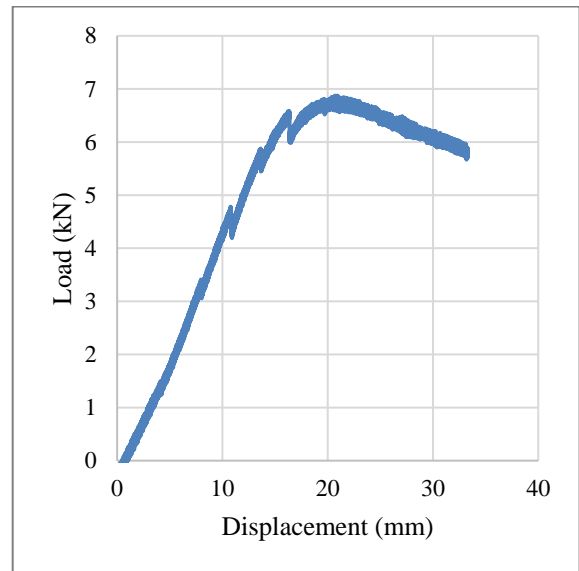


**Figure 4-15 VP115-ISO load-deflection curve.**

The VP50 decking test recorded an applied ultimate load of 9.86 kN at a deflection of about 35 mm, while the VP115 decking test recorded an applied ultimate load of 6.87 kN at a deflection of about 21 mm. Using the above load-deflection curves and the standard moment equation for four-point bending, the actual ultimate moment of the isolated VP50 and VP115 profiled steel decking can be calculated, giving 3.88 kNm for the VP50 decking and 2.95 kNm for the VP115 decking. The actual ultimate moment calculations were based on the number of decking sheets used in the experimental setup (i.e., three sheets for the VP50-ISO sample and two sheets for the VP115-ISO sample) and not for a single decking sheet. Although the VP115 decking is deeper and stiffer, it failed prematurely due to local buckling as discussed below.

The theoretical ultimate moment can be calculated using SANS 10162-2 (SABS, 2011c) for cold formed steel structures using the effective width method as detailed in the code. The theoretical ultimate moment of resistance was calculated for a single profiled sheet section using the effective width method, and the result was multiplied by three for the VP50 isolated decking and multiplied by two for the VP115 isolated decking to give their final theoretical ultimate moment of resistances as is in the experimental setup.

Using the theoretically calculated moment of resistances and the standard moment equation for four-point bending, the theoretical ultimate load capacities can be back calculated. Furthermore, the theoretical web crippling capacity was also calculated using the procedures outlined in SANS 10162-2 (SABS, 2011c). The actual load capacities, theoretical load capacities, and the theoretical web crippling capacities of the VP50-ISO and VP115-ISO samples are as listed in Table 4-5 below. Because these experiments are not the focus of this dissertation, only the final results are included in Table 4-5 below. The online repository contains the complete set of calculations (Claasen *et al.*, 2021). The error difference between the actual load capacity and the theoretical load capacity, along with the actual load capacity and the theoretical web crippling capacity has also been included in Table 4-5 below. Figure 4-16 below serves as a visual representation of the results listed in Table 4-5. The error difference is presented in terms of the absolute difference divided by the experimental value.

**Table 4-5 VP50-ISO and VP115-ISO ULS and theoretical load capacities.**

<b>Tests</b>	<b>Experimental load capacity (kN).</b>	<b>Theoretical flexural load capacity (kN).</b>	<b>Theoretical web crippling capacity (kN)</b>	<b>Error difference (Theoretical load)</b>	<b>Error difference (Web crippling)</b>
<b>VP50-ISO</b>	9.86	8.6	33.84	12.8	243%
<b>VP115-ISO</b>	6.87	9.7	8.5	36.4	23.7%

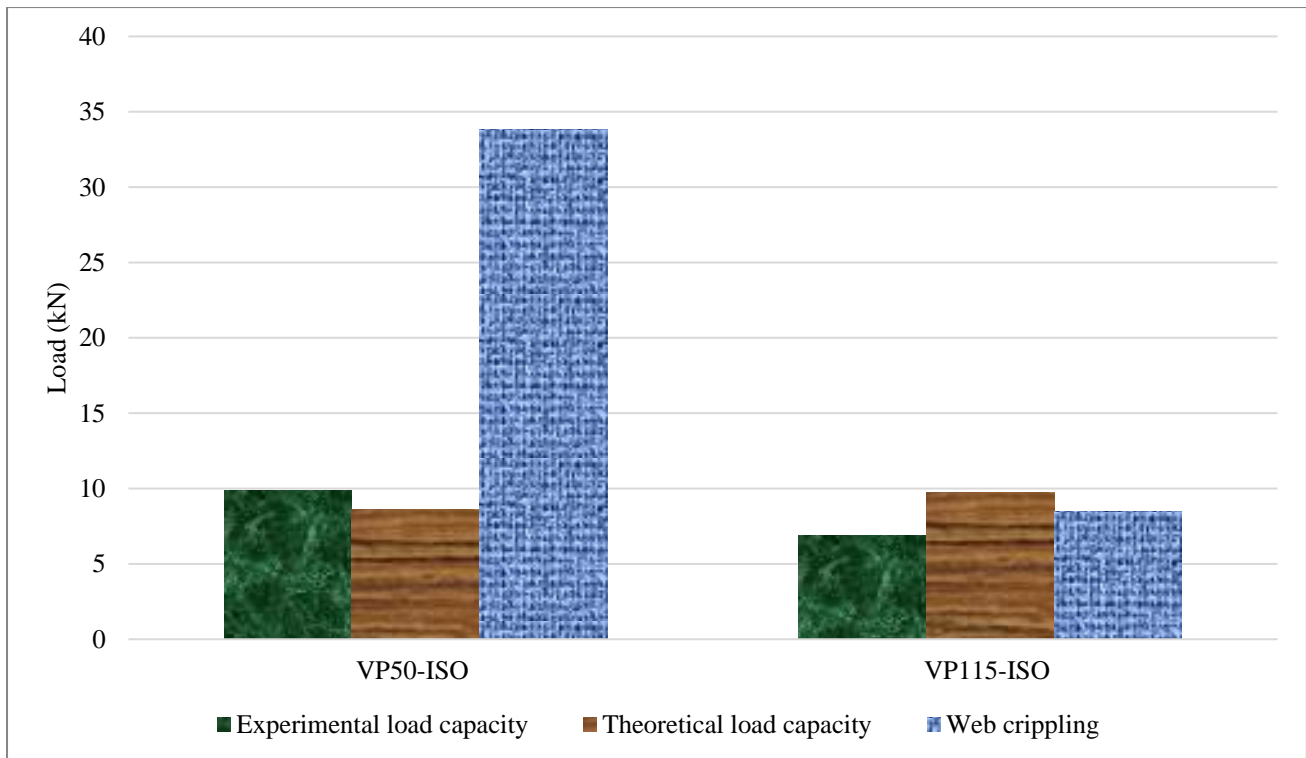


**Figure 4-16 VP50-ISO and VP115-ISO Experimental and theoretical results.**

As seen from Figure 4-16 above, the theoretical and actual load capacities compare well for the VP50-ISO sample, with a maximum error of 12.8%. However, the effective width method was not able to adequately predict the flexural capacity of the VP115-ISO sample, with a maximum error of 36.4%. Nonetheless, the method proved to be successful in the prediction of the VP50-ISO sample's load capacity to within an acceptable range. The VP50-ISO sample experienced failure via local buckling of the top flute and trough steel at the points of load application, whilst the VP115-ISO sample failed via local buckling at the points of load application and global buckling of the top flute section between the points of load application.

#### 4.3.4 VP50 and VP115 sample results

The following three sub-sections present the results of the VP50-9, VP50-12, VP115-12, and VP115-20 SD system configurations. The first sub-section describes the failure modes captured on film. Following that, the ultimate and serviceability results of the tested specimens are then presented. The theoretical and experimental ultimate moment capacities of the tested samples are then detailed and compared in the final sub-section.

##### **Failure modes**

The failure modes experienced by each specimen tested and filmed is presented in Table 4-6 below. Due to an experimental error the footage of VP50-12-T1 could not be used so the failure mechanism could not be identified. Figure 4-17 below depicts the failure modes of the VP50-9-T1 and VP115-20-T4 samples.

**Table 4-6 Failure modes of all composite samples tested.**

<b>Test Specimens</b>	<b>Failure that occurred first</b>	<b>Failure that occurred second</b>	<b>Comments</b>
<b>VP50-9-T1</b>	Local buckling of steel decking flute and top trough sections along the lines of load application (Figure 4-17 (Left)).	N/A	The FCB and CSB stayed intact for the entire duration of the test
<b>VP50-9-T2</b>	Local buckling of steel decking flute and top trough sections along the lines of load application.	N/A	This test specimen experienced a similar failure mode to that of VP50-9-T1.
<b>VP50-12-T2</b>	Cracking of CSB along the line of fixities between the two points of load application where pure bending occurs.	N/A	Negligible deformation or buckling of the steel decking was observed.
<b>VP115-12-T1</b>	Local buckling at steel decking top flute area between the points of load application where pure bending occurs	Shear failure of the CSB in the longitudinal direction along the line of fixities.	N/A
<b>VP115-12-T2</b>	Local buckling at steel decking top flute area between the points of load application where pure bending occurs	Cracking of CSB between the point of load application where pure bending occurred.	N/A
<b>VP115-20-T1</b>	Local buckling of steel decking trough sections at the supports and followed shortly with shear failure/crushing of CSB at the supports near the trough areas of the decking.	Local buckling at steel decking top flute area between the points of load application where pure bending occurs.	The local buckling of the steel between the points of load application occurred shortly after the first failure at the supports.
<b>VP115-20-T2</b>	Local buckling of steel decking trough sections at the supports and followed shortly with local buckling at top flute area occurring between the points of load application.	Shear failure/crushing of CSB at the support near the trough sections of the decking.	This specimen had similar failure modes when compared to VP115-20-T1, only the order in which the different failures occur are different.
<b>VP115-20-T3</b>	Local buckling of the steel decking flute between the points of load application.	Fixities (Screws) pull-out failure	Negligible deformations of the steel decking occurred at the supports.
<b>VP115-20-T4</b>	Buckling/warping of steel decking flute between fixities, between the points of load application where pure bending occurs. (Figure 4-17 (Right)).	Local buckling of steel decking flute between the point of load application where pure bending occurs	Fixities (Screws) pull-out failure also started occurring during the test due to the steel buckling/warping between the points of fixities.

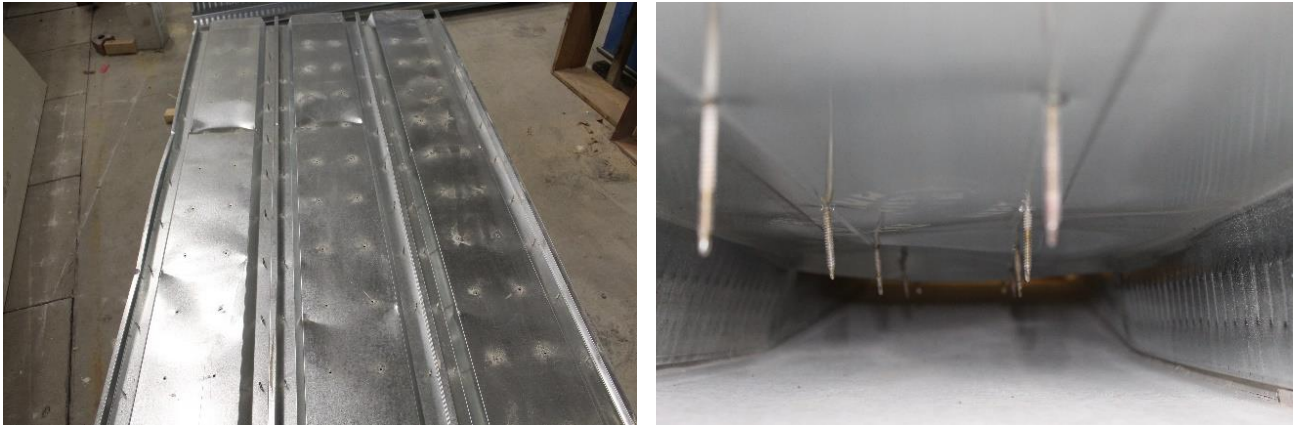


**Figure 4-17** Local buckling of steel of VP50-9-T1 (Left) and warping/buckling of steel between the points of fixities of VP115-20-T4 (Right).

***Experimental ultimate and serviceability state results***

Figure 4-18 and Figure 4-19 below present the load-deflection curves for the VP50-9, VP50-12, VP115-12, and VP115-20 samples tested.

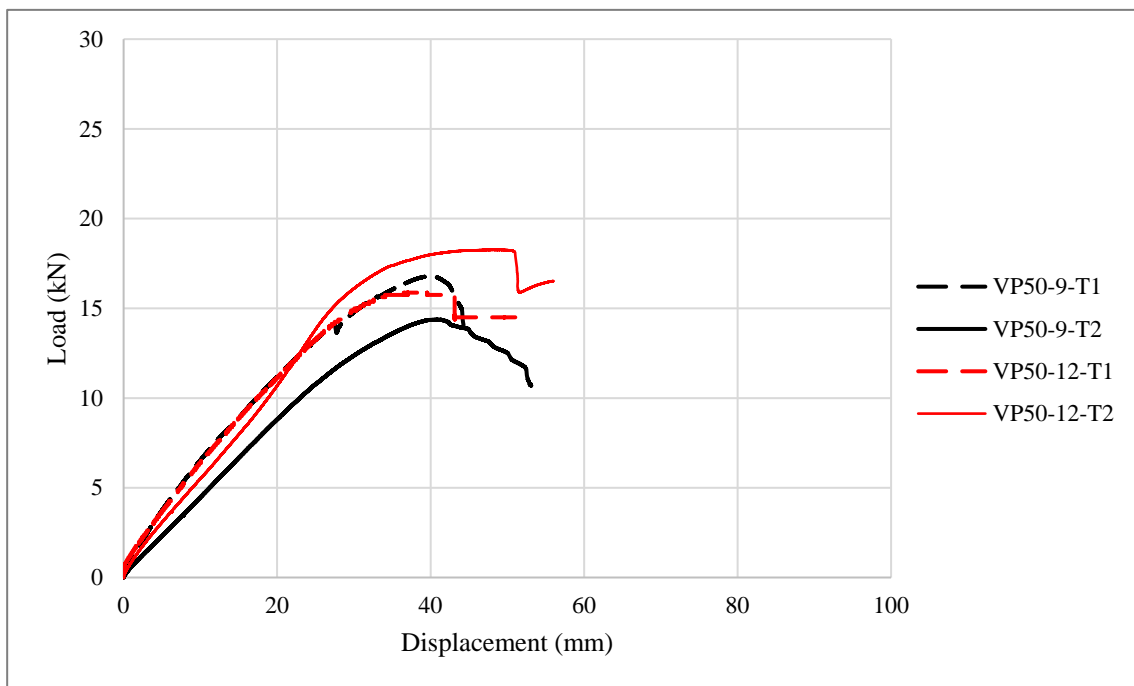


**Figure 4-18** VP50-9 and VP50-12 samples load-deflection curves.

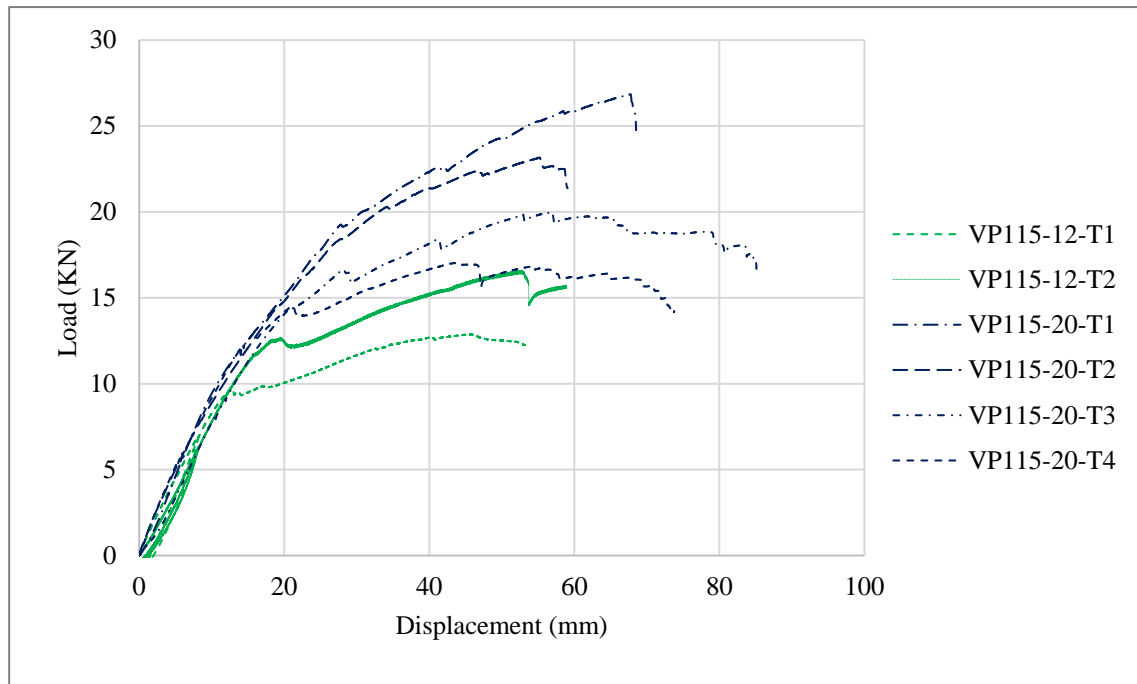


**Figure 4-19 VP115-12 and VP115-20 samples load-deflection curves.**

As stated in Table D.1 in the annex of SANS10160-1 (SABS, 2011d), the maximum midspan deflection for floors with partitions that follow the movement of the floors is span/500 to span/300. Hence, the maximum allowable medial deflection of the floor samples for the SLS is 8 mm (2400/300) for the 2.4 m long samples and 8.2 mm (2460/300) for the 2.46 m long samples. With this, the actual SLS load capacity and the actual effective flexural rigidities ( $EI_{\text{eff}}$ ) can be calculated at this limit. The actual ultimate moment of resistance can be calculated using the standard moment equation for 4-point loading and the ultimate applied load as given by the experimental results above. Furthermore, as stated in Table 4 of SANS 10160-1 (SABS, 2011d), the required live load carrying capacity of the proposed SD systems are  $2.5 \text{ kN/m}^2$  when intended for office building usage. A load of  $0.8 \text{ kN/m}^2$  will be added to this live load to account for the potential addition of partitions, giving a total unfactored required live load capacity of  $3.3 \text{ kN/m}^2$ .

Table 4-7 below presents the ULS load (i.e., total load applied by Instron) and moment capacities of the tested samples, along with the maximum deflection at failure. The maximum load and  $EI_{\text{eff}}$  at the SLS is also given along with the calculated maximum spans achievable for office building use. The maximum capable spans were calculated based on the effective flexural rigidities  $EI_{\text{eff}}$  at SLS, the required unfactored load for office buildings, and the standard deflection equation for a uniformly distributed line load.

**Table 4-7 ULS and SLS experimental results for all tested samples.**

Test	Ultimate Limit State			Serviceability Limit State		
	Ultimate load (kN)	Moment of resistance (kNm)	Vertical deflection (mm)	Load at serviceability limit (kN)	Flexural rigidities (kNm <sup>2</sup> )	Max capable lengths (m)
<b>VP50 samples</b>						
<b>VP50-9-T1</b>	16.80	6.955	40	5.46	171.1	2.43
<b>VP50-9-T2</b>	14.37	5.95	41	3.59	112.4	2.19
<b>VP50-12-T1</b>	15.88	6.57	40	5.38	168.5	2.42
<b>VP50-12-T2</b>	18.27	7.56	48	4.55	142.5	2.32
<b>VP115 samples</b>						
<b>VP115-12-T1</b>	12.97	5.56	46	7.1	235.4	2.63
<b>VP115-12-T2</b>	16.6	7.12	52	6.29	208.6	2.55
<b>VP115-20-T1</b>	26.84	11.11	67	7.68	240.7	2.65
<b>VP115-20-T2</b>	23.16	9.59	55	7.49	234.6	2.63
<b>VP115-20-T3</b>	19.97	8.27	58	6.07	195.9	2.49
<b>VP115-20-T4</b>	17.02	7.05	44	7.58	188.6	2.64

***Elastic analysis***

A full interaction elastic analysis has been conducted for the VP50-9, VP50-12, VP115-12 and VP115-20 SD samples, similar to that conducted in Al-Shaikhli *et al* (2017). The full interaction analysis assumes that the boards and profiled steel decking do not allow for any interfacial slip and act as a single unit. The theoretical ultimate moment of resistance can be calculated by transforming the top FCB into an equivalent steel section, as shown below in Figure 4-20. The calculations have been carried out using a repetitive section of the decking system and the transformed section method. The CSB and CSB strips have been excluded from these analysis as they do not form part of the load bearing components of the systems. The material properties used to calculate the theoretical moment of resistance are listed in Table 4-1 to Table 4-3 above.

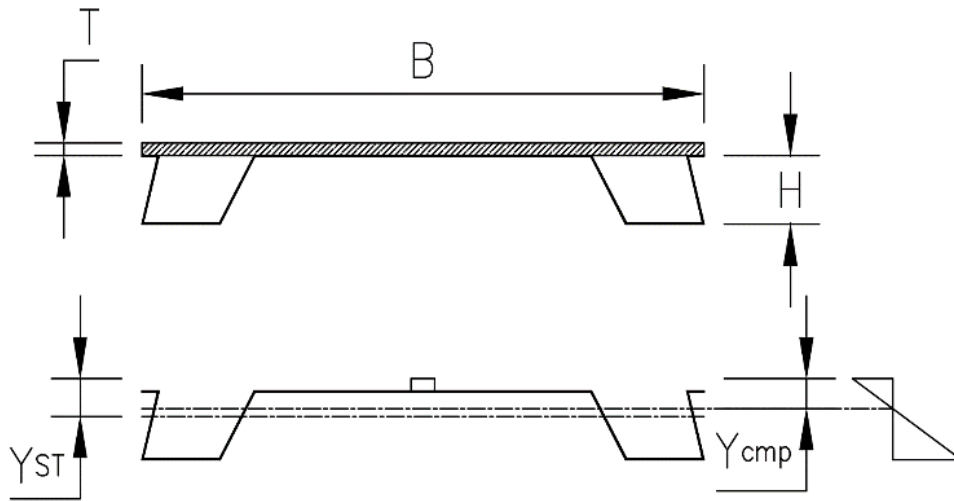


**Figure 4-20 Original section (Top) and the transformed section (Bottom) with representative elastic stress gradient**

To calculate the neutral axis of the transformed section.

$$Y_{cmp} = \frac{(A_{ST} \cdot Y_{ST}) + \left(n \cdot B \cdot T \cdot \frac{T}{2}\right)}{(A_{ST} + B \cdot T)} \quad (4.1)$$

Where:

$$n = \frac{E_{FCB}}{E_{ST}} \quad (4.2)$$

To calculate the second moment of area.

$$I_{cmp} = I_{ST} + (n \cdot I_{FCB}) \quad (4.3)$$

Depending on whether the FCB or VP decking failing first, either Eq (4.4) or (4.5) will be used.

$$M = \frac{(\sigma_{st} \cdot I_{cmp})}{(T + H - Y_{cmp})} \quad (4.4)$$

$$M = \frac{(\sigma_{FCB} \cdot I_{cmp})}{(Y_{cmp})} \quad (4.5)$$

Where:

$A_{st}$  is the area of the profiled steel sheeting.

$Y_{st}$  is the neutral axis (x-x) of the profiled steel sheeting.

$E_{st}$  is the modulus of elasticity of the profiled steel sheeting.

$E_{FCB}$  is the modulus of elasticity of the FCB.

$I_{st}$  is the second moment of area of the profiled steel sheeting.

$I_{FCB}$  is the second moment of area of the FCB.

$\sigma_{(st)}$  is the maximum allowable stress at the extreme bottom fibre of the profiled steel decking.

$\sigma_{(FCB)}$  is the maximum allowable stress at the extreme top fibre of the FCB.

The maximum theoretical load capacities for each of the samples calculated as detailed above are shown in Figure 4-21 below, along with the actual ultimate load capacities. The experimental and theoretical results of the isolated VP50 and VP115 samples, as detailed in Section 4.3.3 for the steelwork, have also been added to Figure 4-21 for clarity.

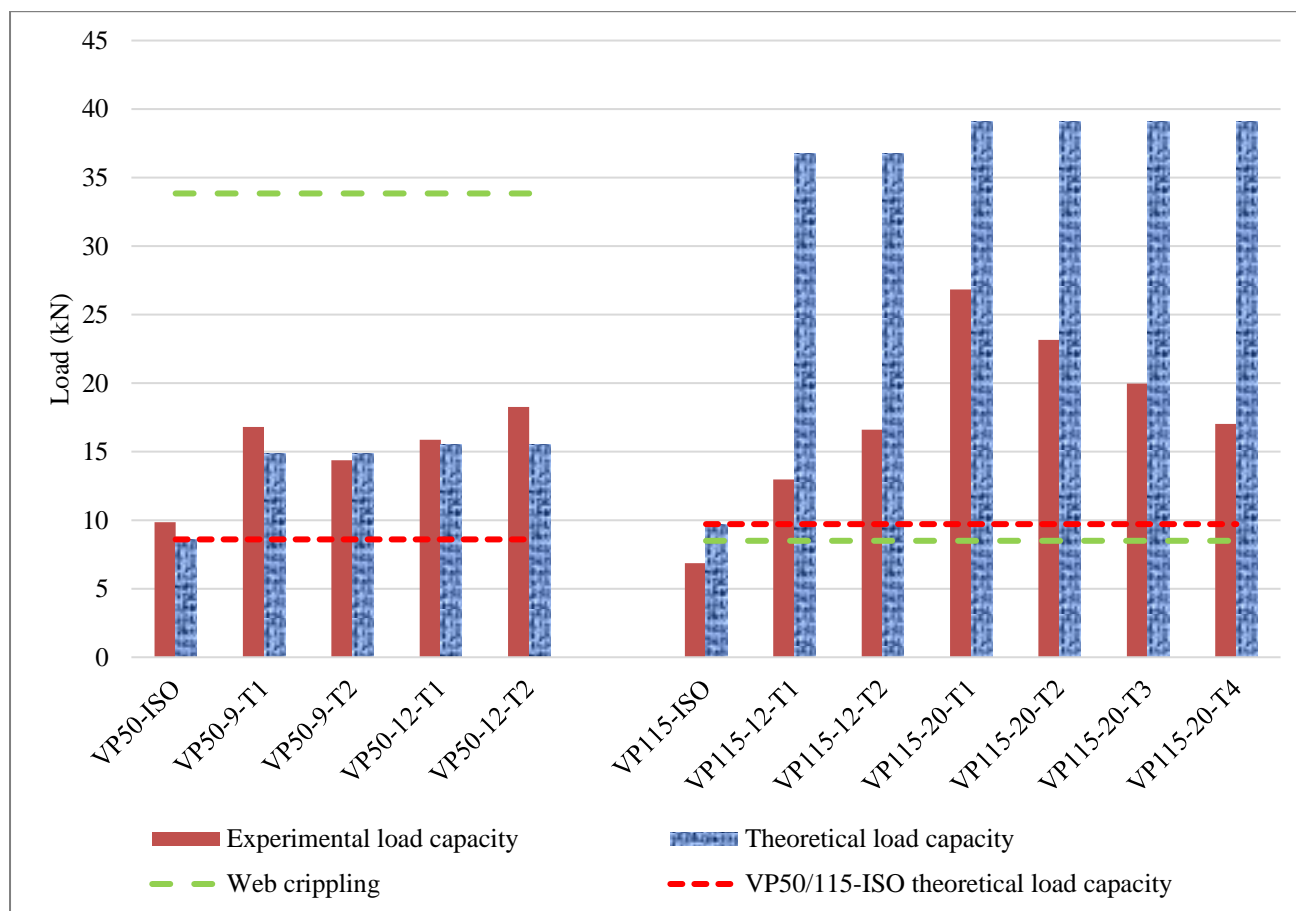


**Figure 4-21 Theoretical and experimental ultimate load capacities for all floor tests conducted.**

The following section delves into the comparison of the theoretical and experimental results. Based on the experimental results presented above, it is evident that the design capacity of the SD systems is primarily governed by the SLS requirements, as the ULS load capacity is much higher than that of the SLS load capacity for all samples tested. The theoretical load capacities of the VP50-9 and VP50-12 SD systems were 14.8 kN and 15.5 kN, respectively, while the VP115-12 and VP115-20 SD systems theoretical load capacities were 36.7 kN and 39 kN, respectively. The VP50 SD samples' capacities compare well with the theoretical calculated capacities, with a maximum error difference of 11.6% for the VP50-9-T1 and 15% for the VP50-12-T2 samples, respectively. Furthermore, the elastic analysis was able to predict the governing failure components of the VP50-9 samples as well, with the decking steel failing first for the VP50-9-T1/T2 samples in both the experimental tests and theoretical calculations. The same conclusion could not be drawn for the VP50-12 samples as the CSB and CSB strips were not included in the elastic analysis, however, preliminary calculations which included the CSB and CSB strips showed that the governing component was the CSB for the VP50-12 samples. This proves

to be consistent with the experiments as the VP50-12 samples failed via cracking of the CSB between the points of load application where pure bending occurred. When comparing the flexural load capacity of the VP50 SD samples to the isolated VP50 sample, the presence of the FCB on top increased the load capacity by 70.4 % and 85.3 %, respectively, when compared to the VP50-9-T1 and VP50-12-T2 samples.

The elastic analysis was not able to accurately predict the theoretical ultimate load capacities of the VP115 SD samples, with the theoretical calculations over-predicting the actual load capacities. Maximum differences of 173% and 129.5% was found for the VP115-12-T1 and VP115-20-T4 samples, respectively. This large difference suggests that the VP115 samples had little composite interaction between their components, whereas the VP50 samples exhibited near complete interaction between their components. This stands to reason as the VP50 samples used more fixities to attach the FCB, CSB, and CSB strips than the VP115 samples, with 36 more fixities used in the VP50 samples when compared to the VP115 samples with 200 mm screw spacing. Hence, a more robust method of evaluating the theoretical capacities has been exploited in this research with the use of FEM, which is able to take into account the partial interaction between the components of the VP115 SD samples. The theoretical results of the VP115 samples are further discussed in Chapter 6.

Furthermore, test sample VP115-20-T2, which included the stiffeners, had a 15.9% lower ultimate moment capacity than the VP115-20-T1 sample. This suggests that the stiffeners had no positive impact on the VP115 SD system's flexural performance and would not be pursued any further. Moreover, increasing the spacing between the connectors resulted in lower ultimate moment capacities, with differences of 34.4 % and 57.7 % for the VP115-20-T3 and VP115-20-T4 samples, when compared to VP115-20-T1, respectively. These results further validate the influence the number of fixities have on the composite action between the components of the samples. Furthermore, the failure mechanisms of the samples were also influenced by the number of fixities as indicated by the failure of sample VP115-20-T4, where buckling/warping of the steel between the fixities caused premature fixity pull-out failure in the test. Finally, the use of the FCB in the VP115 SD systems increased the flexural capacity of the isolated VP profiled decking by 290% when compared to VP115-20-T1. When considering the experimental data of the VP115-12-T1 and VP115-12-T2 samples, similar failure modes occurred with regards to the local buckling of the steel between the points of load application, however, sample VP115-12-T1 had a subsequent shear cracking failure of the CSB, whilst the VP115-12-T2 sample had a subsequent cracking failure of the CSB in the transverse direction between the points of load application. Similar failure modes also occurred in the VP115-20-T1 and VP115-20-T2 samples with regards to the local buckling failure of the steel between the points of load application. However, given the difference in the thickness of FCB used, it is difficult to make any direct comparison to whether the support conditions had any influence on the capacity of the system. As a result, more testing is required to assertively establish the influence of the support conditions. However, it appears the support conditions did not have a significant impact on the results, highlighting that the width of supports was not critical for these specific tests.

The VP50-9-T1 and VP115-20-T1 test samples yielded the highest maximum possible lengths for each of the VP50 and VP115 SD system configurations, with theoretical capable span lengths of 2.43 m and 2.65 m, respectively. The maximum span length required from the decking system by the CBS system is 2.95 m, with this, it can be observed in Table 4-7 that none of the tested samples yielded suitable span lengths adequate for the CSB system. Using the standard equation for deflection of a uniformly distributed beam, the deflection limit at SLS (8 mm), and the unfactored load required for an office occupancy type building, a relationship between the flexural rigidity and the length can be made as shown below in Figure 4-22. With this, it can be concluded that for the SD system to span the required length of 2.95 m, the SD system would need a flexural rigidity of at least 370 kNm<sup>2</sup> as indicated on Figure 4-22 below. This represents a 53.7% increase required in the flexural rigidity when compared to the VP115-20-T1 sample, which yielded the highest flexural rigidity of all the tested samples at the SLS limit.

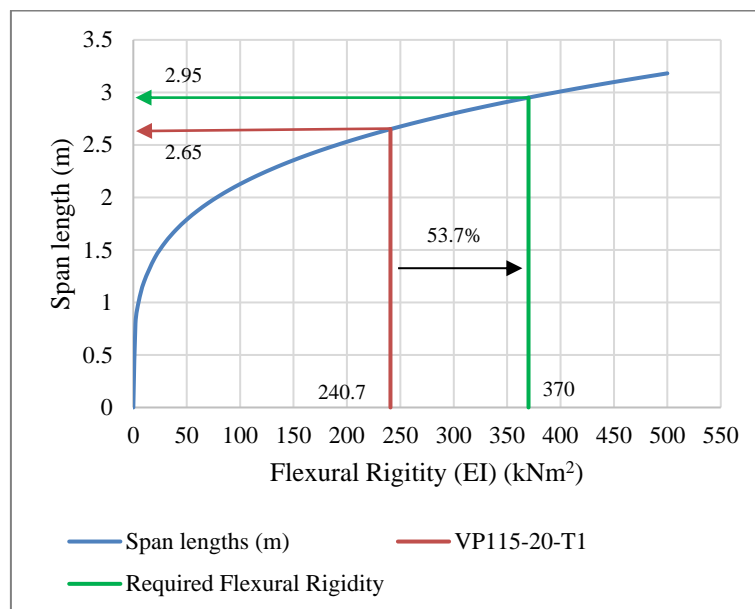


**Figure 4-22 Relationship between the flexural rigidity and length using the deflection formula for a uniformly distributed beam.**

Based on the data presented above, it is more likely that the VP115-20 SD system will be adopted in the CBS system in the future. Furthermore, through ongoing consultation with practitioners in the construction industry, it has become more evident that the use of FCB with a thickness of less than 20 mm for structures the size of the CBS system is not recommended. It has been indicated that the use of 9 mm or 12 mm FCB boards may affect operations due to practical requirements, such as acoustics, cracking and punching shear when point loads are placed onto the boards.

Furthermore, the tests conducted above only included single spans of the SD system variations and based primarily on the size of the boards attached to the top and bottom. Hence, the behaviour of the SD systems spanning across multiple spans is still unknown. Moreover, when using the SD system for larger floor areas (i.e., floor areas where multiple FCB's are required), no joints are specified in the design tested in this work, such as for the CSB ceiling system, where the strips also serve as a joint connection between adjacent boards. Consequently, the continuity of the current configuration of the system is limited to the length and width of the FCB's. With this, it is evident that the performance of the SD system may be influenced by many factors, such as construction details, how the boards are fixed to the decking steel (i.e., number and arrangement of fixities used), whether joints for the FCB's are implemented in the construction of the floors or not. Due to these uncertainties, further testing of the SD system will still be required in the future, especially with regards to performance of the system over multiple spans, as detailed in Chapter 9. As a result, with the current design of the SD system, it would be more practical to base the capacity of the system on the strength of the VP50/115 profiled steel decking alone, as this would serve as a more conservative and practical approach. Nonetheless, the flexural rigidity increase required for the VP115-20 SD system to be used in the CBS system may still be attainable through simple design implementations, as further discussed in Chapter 9.

#### 4.4 Conclusion

This chapter described both the small-scale materials and the medium-scale four-point bending tests carried out in this work. The small-scale materials tests were conducted on the structural steel used in the experimental frame introduced in Chapter 3, and the materials components used in the SD system, which includes the VP profiled decking steel, the Fibre Cement and Calcium Silicate boards. All small-scale tests were conducted with use of a Zwick universal testing machine with a 100 kN load capacity. The structural and VP profiled decking steel was tested by means of coupon tensile tests to obtain the yield strength of each material. Two types of tests were conducted on the Fibre Cement and Calcium Silicate boards: (1) three-point bending tests to obtain the modulus of elasticity and the modulus of rupture values for each of the materials, and (2) compression tests to obtain the crushing strength of each of the materials. The results for each of the small-scale tests can be found in Table 4-1 to Table 4-3.

A total of 12 medium-scale four-point bending tests were conducted on variations of the SD system, including an isolated test for each of the VP50 and VP115 profiled decking steel, without any boards attached on top or the bottom. All composite samples were tested with 9 mm Calcium Silicate board and strips attached to the bottom. The list of samples tested can be found in Table 4-4 above, which includes the board thicknesses and fixity spacing used in each of the samples. Additionally, a single VP115-20 SD sample included stiffeners as depicted in Figure 4-10 (c) above. The aim of the tests was to determine the flexural performance of the SD system variations according to the SANS10162-1 (SABS, 2011b) national building code for both the Ultimate and Serviceability limit states. Additionally, the influence of different connector spacings and the inclusion of stiffeners was also investigated.

Furthermore, the theoretical moment capacities were calculated for the isolated VP50 and VP115 profiled decking steel using the effective width method as detailed in SANS 10162-2 (SABS, 2011c). Moreover, an elastic analysis was conducted using the transformed area method to calculate the theoretical load capacities of the composite samples tested, which was then compared to the experimental data captured. The failure modes for each of the composite samples tested can be found in Table 4-6 above and summarized as follows: (1) the VP115-12-T1 sample experienced shear failure of the CSB in the longitudinal direction along the line of fixities. (2) The VP115-12-T1 and the VP115-12-T2 samples failed via local buckling of the steel flute between the points of load application. The local buckling failure was followed by shear failure of the CSB for the VP115-12-T1 sample, and cracking failure of the CBS between the points of load application for the VP115-12-T2 sample. (3) The VP115-20-T1 sample experienced two different failure modes, firstly, local buckling of the steel at the bottom trough and crushing of the CSB at the supports, which was followed closely by local buckling failure at the steel top flute area between the points of load application. (4) The VP115-20-T2 sample failed via local buckling of steel decking trough sections at the supports and followed shortly by local buckling at the steel top flute area between the points of load application. (5) Sample VP115-20-T3 experienced failure via local buckling of the steel decking flute between the points of load application and fixities through pull-out failure as the test continued. (6) Sample VP115-20-T4 experienced failure via warping/local buckling of the steel top flute area between the points of fixities located between the points of load application.

The implications of the successful implementation of the SD system can be significant, especially since such construction methods are not widely used in the South African construction industry. As stated in Chapter 1, the SD system has the potential to be incorporated into other structural designs such as domestic and educational buildings, which do not require high flexural resistances ( $1.5 - 2 \text{ kN/m}^2$ ) to meet the code requirements. This type of system can be easily assembled off-site, transported by truck, and installed on-site by unskilled labour. Furthermore, the lightweight nature of the system and the fact that no wet trade is involved result in no formwork needed and potentially less dependency on heavy equipment (lift crane) on site. These factors could result in a more efficient construction process, which, in turn, would result in earlier completion and occupation. Furthermore, past research has shown that this type of system can be used not only as flooring units, but also as walling and roofing systems in construction as described in Section 2.7 above. In addition, this specific system (SD system) will be fire-rated, which is an added advantage when compared to most proposed system of this kind.

However, the development of such systems can take a considerable amount of time, as numerous aspects of the system need to be investigated, such as the damping the system can provide, the acoustics, and the performance of the system in multi-span experimental setups. Hence, this work has only investigated one aspect of the SD system (flexural performance in single-span experimental setups) and should lay the foundation of future research to be conducted as discussed in Chapter 9.

The results of each of the samples tested can be found in Table 4-5 and Table 4-7 above. The main findings of the tests conducted are as listed below:

- VP50 SD samples
  - The theoretically calculated moment capacity of the isolated VP50 profiled steel decking compared well with the experimental moment capacity with a maximum error difference of 12.8%.
  - The presence of the FCB increased the load capacity of the VP50 profiled decking steel by 70.4% and 85.3% when used with the 9 mm and 12 mm FCB, respectively.
  - The theoretically calculated load capacities compared well with the experimental load capacities obtained by the VP50 SD samples tested, with a maximum error difference of 11.6% for the VP50-9-T1 and 15% for the VP50-12-T2 samples, respectively.
- VP115 SD samples
  - The theoretically calculated moment capacity of the isolated VP115 profiled steel decking did not compare well with the experimental moment capacity with a maximum error difference of 36.4%.
  - The presence of the Fibre Cement board in the VP115 SD systems increased the flexural capacity of the isolated VP profiled decking by up to 290% when compared to VP115-20-T1.
  - The elastic analysis was not able to accurately predict the theoretical ultimate load capacities of the VP115 SD samples. Maximum differences of 173% and 129.5% was found for the VP115-12-T1 and VP115-20-T4 samples, respectively.
  - The results of the elastic analysis indicate that the VP115 SD system has limited composite behaviour at ULS. As a result, a more robust method of evaluating the theoretical capacities that takes partial interaction behaviour into account needs to be investigated, as further discussed in Chapter 5.
  - Test sample VP115-20-T2, which included the stiffeners, had a 15.9% lower ultimate moment capacity than the VP115-20-T1 sample. This suggests that the stiffeners had no positive impact on the VP115 SD system's flexural performance and will not be pursued any further.
  - Increasing the spacing between the connectors resulted in lower ultimate moment capacities, with differences of 34.4 % and 57.7 % for the VP115-20-T3 and VP115-20-T4 samples, when compared to VP115-20-T1, respectively.

## Chapter 5 Large-scale experimental setups and results

### 5.1 Introduction

Two large-scale standard fire furnace tests (LST-1 and LST-2) were carried out as part of this work. Both tests took place at the Ignis Fire Testing facility (Ignis Testing, 2021) located in Cape Town, South Africa. According to the SANS 10400 Part T (SABS, 2011a) of the national building codes, an office occupancy type building with 3 to 10 storeys, require a fire rating of 60 minutes. Hence, both tests were conducted for a duration of 66 minutes as per SANS 10177-2 (SABS, 2005), while temperature and deflection measurement data was recorded as discussed in detail below. This chapter is broken down into four key sections to discuss the experimental setup and results. This section (Section 5.1) serves as an overview of the chapter and the subsequent sections to follow. LST-1 and LST-2 are presented in Sections 5.2 and 5.3, respectively, with details on the experimental setups, instrumentation, and experimental results highlighted in each section. Section 5.4 concludes the chapter with a summary of the main findings.

### 5.2 Large-scale test 1 (LST-1) setup and results

The team at the testing facility built a horizontal standard fire testing furnace with inner dimensions of 4 m × 6 m, and the same setup was used for both experiments (except for burner positioning as discussed below). The furnace was built using normal 230 mm cement bricks, and had a height of 1.185 m. The inside walls of the furnace were lined with a fire-resistant vermiculite plaster and then covered with a final layer of fibre ceramic blanket. The furnace was heated using two 300 kW diesel burners and multiple hand-held gas burners when needed. Finally, both tests were carried out while loaded, with a load that corresponded to the imposed load of an office type occupancy building, plus an assumed load for possible partitions, and factored using the fire limit state factor as described in the following sections.

LST-1 was the first test to be conducted with the newly built furnace and served as an opportunity to investigate if the furnace was capable of producing the desired time-temperature curve, namely the ISO 834 standard fire (STF) curve, required for standard fire testing. Hence, this test conducted primarily served as a dry-run test of the furnace and is not the emphasis of this chapter. However, given the labour and time invested to get the furnace up and running, this was also used as an opportunity to gain some insights into the behaviour of the sandwich decking (SD) system used to cover the furnace top, which in this case was the VP50-9 SD system (with details as specified in Section 5.2.1, namely a VP50 decking coupled with 9 mm Fibre Cement (FCB) and 9 mm Calcium Silicate boards (CSB)). Hence, the secondary purpose of the test was to gain preliminary data on the heat transfer through the various layers of the VP50-9 SD system, and its structural resistance. Thus, only the isolated VP50-9 SD system was utilized in this dry-run test to cover the top of the furnace, and no supporting steelwork. Important results of this test are: (a) temperatures throughout the SD system at multiple positions that can be used for validating thermal models, (b) time to failure and failure mechanisms of the SD decking

under load as sandbags were used to apply a load to the system, and (c) identification of setup issues that were rectified before the main test, LST-2.

### *5.2.1 Ceiling only experimental setup*

The SD system was designed to be supported in a similar fashion as in the actual CBS system. Fibre ceramic protected heavy timber beams were selected for this purpose as depicted in Figure 5-3 (Bottom) below. The SD system was supported by the timber beams with no attachments made and fitted within the furnace dimensions. The configuration of the SD system is analogous to that tested in the medium-scale floor samples with the fixities of the FCB being the very same in terms of spacing as depicted in Figure 5-1 (Right) below. However, the CSB and CSB strips were attached to the VP50 decking using a different configuration, with the strips running in the transverse direction instead of the longitudinal direction as depicted in Figure 5-1 (Left). This was done to investigate how different configurations of the CSB strips would influence the fire resistance of the SD system. The single strip running in the longitudinal direction was fixed using a pair of two screws spaced at 58 mm apart and spaced at 200 mm in the longitudinal direction as depicted in Figure 5-1 (Bottom-Left), where the strips have been shown in blue and the fixities in green in the interest of clarity. The transverse strips that joined two CSB together were fixed using groups of 4 screws spaced at 50 mm in the Y-direction and 58 mm in the X-direction from each other, and spaced at 410 mm in the transverse direction as depicted in Figure 5-1 (Bottom-Left). A pair of two screws spaced at 50 mm in the Y-direction and spaced at 410 mm in the X-direction were utilized to fix the transverse strips not joining any boards together.

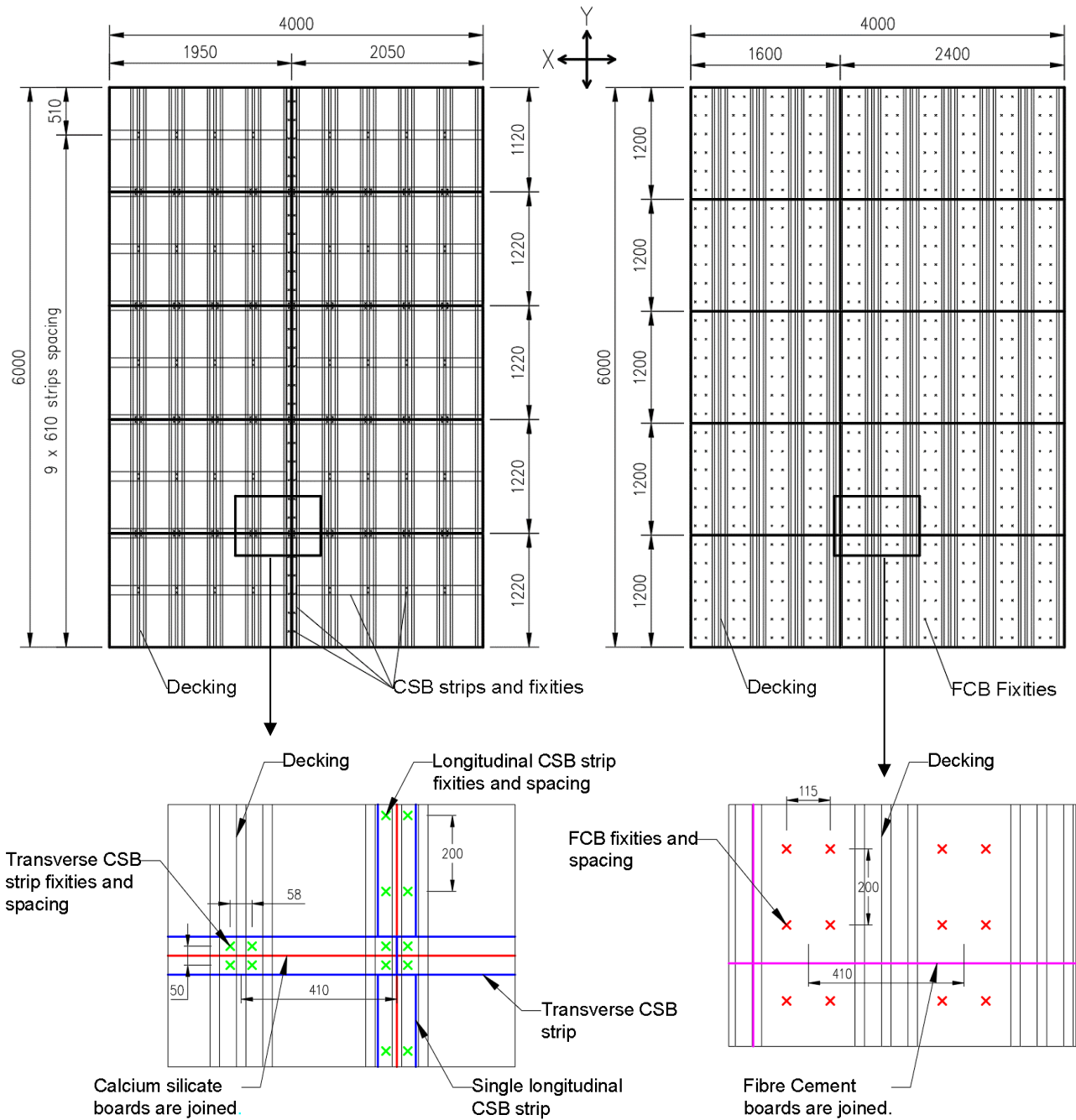


**Figure 5-1 LST-1 CSB ceiling system (Left) and FCB (Right) configurations and fixities arrangements. (All units in mm). Colours used: CSB strips – blue; CSB strip fixing screws – green; CSB joints/edge – red; top FCB joints – magenta; top FCB screws – red.**

A characteristic imposed load of  $2.5 \text{ kN/m}^2$  was used which corresponds to that of an office type occupancy building plus a partition load of  $0.8 \text{ kN/m}^2$ . Using the fire limit state (FLS) load factor of 0.5, a final factored load of  $1.65 \text{ kN/m}^2$  is calculated. The loading was applied using 40 kg sandbags positioned as a uniformly distributed load on the SD system as depicted in Figure 5-6 below. A single layer of fibre ceramic blanket was placed on top of the FCB and beneath the loading sandbags to protect the sandbags from melting. This also created a more extreme testing scenario in terms of heat transfer, compared to reality, since the ceramic fibre prevents the top of the SD system from losing heat to the environment, i.e., negligible radiative and convective losses.

The final test setup prior to instrumenting is as depicted in Figure 5-2 and Figure 5-3 below, with the boards and strips attached to the VP50 decking while supported on top of the protected beams within the furnace. The first location of the burners situated at the south wall was chosen on the basis that the fuel tanks were nearest to this location, hence, less pressure was needed to pump the fuel to the burners.

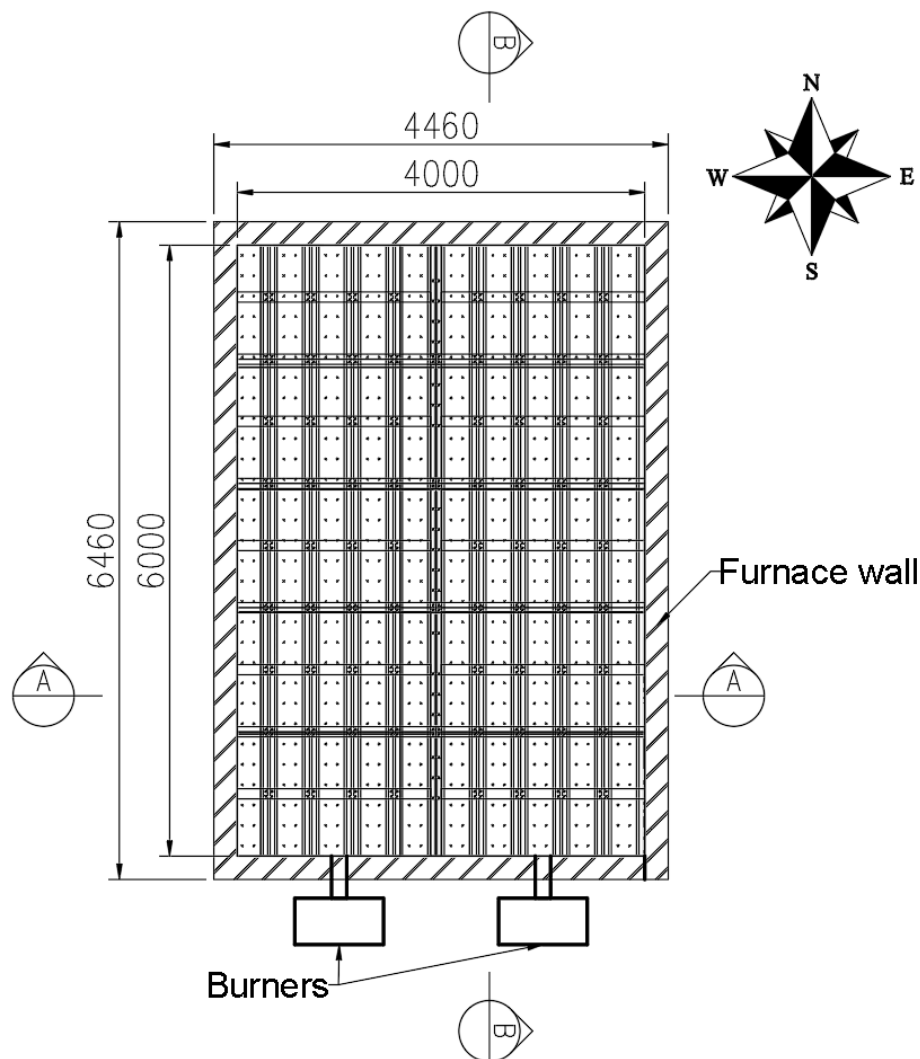
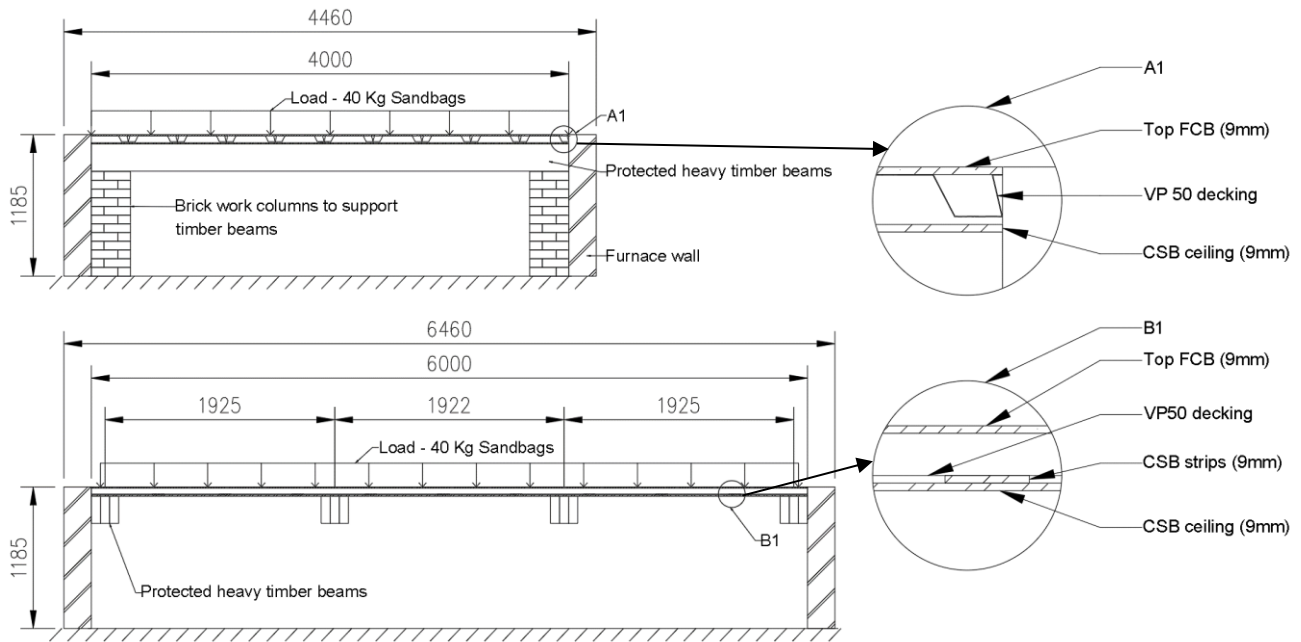


Figure 5-2 LST-1 experimental setup top view.



**Figure 5-3 Section A-A view of LST-1 setup (Top) and Section B-B view of LST-1 setup.**

### 5.2.2 Instrumentation

Multiple temperature measurements were taken during the test with K-Type thermocouples, which had a tip diameter of 1.5 mm. The thermocouples were placed in groups (denoted as G1-G6 as depicted in Figure 5-4) at various points of interest along the SD system, with each group having the same thermocouple arrangement throughout the boards and decking layers of the SD system. A total of eight thermocouples were used at each group location. Table 5-1 below describes the nomenclature of the thermocouple locations, and the specific locations are depicted in Figure 5-5 for each group.

**Table 5-1 LST-1 Thermocouple legend.**

Thermocouple list Legend	Denotation
Top of calcium silicate Board ceiling	<b>BT</b>
Top of steel Decking with CSB Strip under, trough area	<b>TD-S</b>
Top of steel Decking with No CSB strip under, trough area	<b>TD-N</b>
Top of steel Decking with CSB Strip under, Flute area	<b>FD-S</b>
Top of steel Decking with No CSB strip under, Flute area	<b>FD-N</b>
Furnace gas temperature	<b>F</b>
Top of FCB, Flute area (Unexposed surface)	<b>F-FC</b>
Top of FCB, Trough area (Unexposed surface)	<b>T-FC</b>

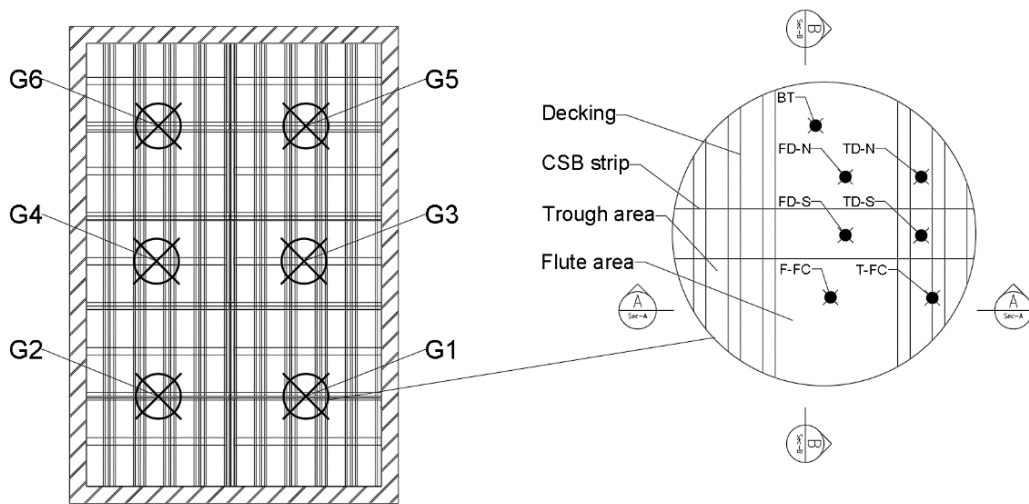


**Figure 5-4 LST-1 Thermocouple groups layout (Right) and top view of each group thermocouple layout (Left).**

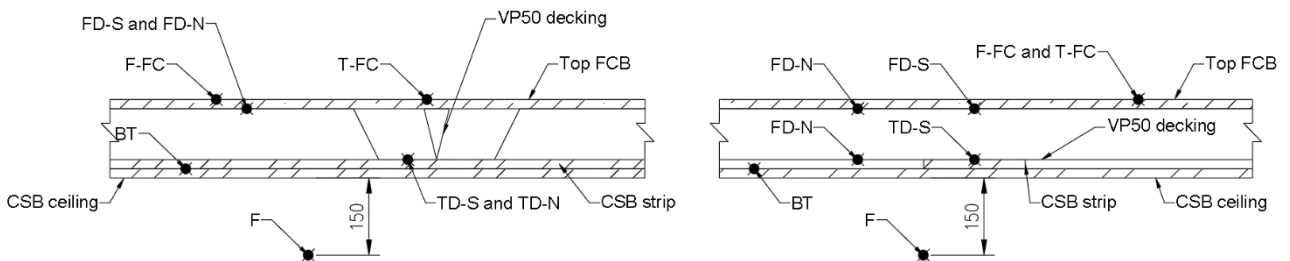


**Figure 5-5 Section A-A (Left) and Section B-B (Right) of thermocouple groups.**



**Figure 5-6 Final test setup prior to testing.**

### 5.2.3 Experimental results and discussion

The average furnace temperature is presented first in comparison to the ISO 834 standard fire curve in Figure 5-7 below. Next, due to the large amount of data captured, only results from two of the measured Groups (Group 2 and Group 6) have been presented. The two groups were selected based on their location (i.e., a group from each far side of the experimental setup). Furthermore, Group 2 yielded the highest measured temperatures and is located nearest to the failure that occurred during the experiment as discussed in detail below, while group 6 yielded some of the lowest recorded temperatures, such that a full range of the captured data can be visualized. Hence, Figure 5-8 and Figure 5-9 below presents the time-temperature curves for Group 2 and Group 6, respectively. Additionally, the same position average temperatures have also been presented below in Figure 5-10. Finally, the average unexposed surface temperatures are compared to the average FLS temperature in Figure 5-12. The complete set of time-temperature curves for all the groups can be found in the online repository of this dissertation (Claasen *et al.*, 2021). Where data is incomplete or missing, the thermocouple malfunctioned during the test.

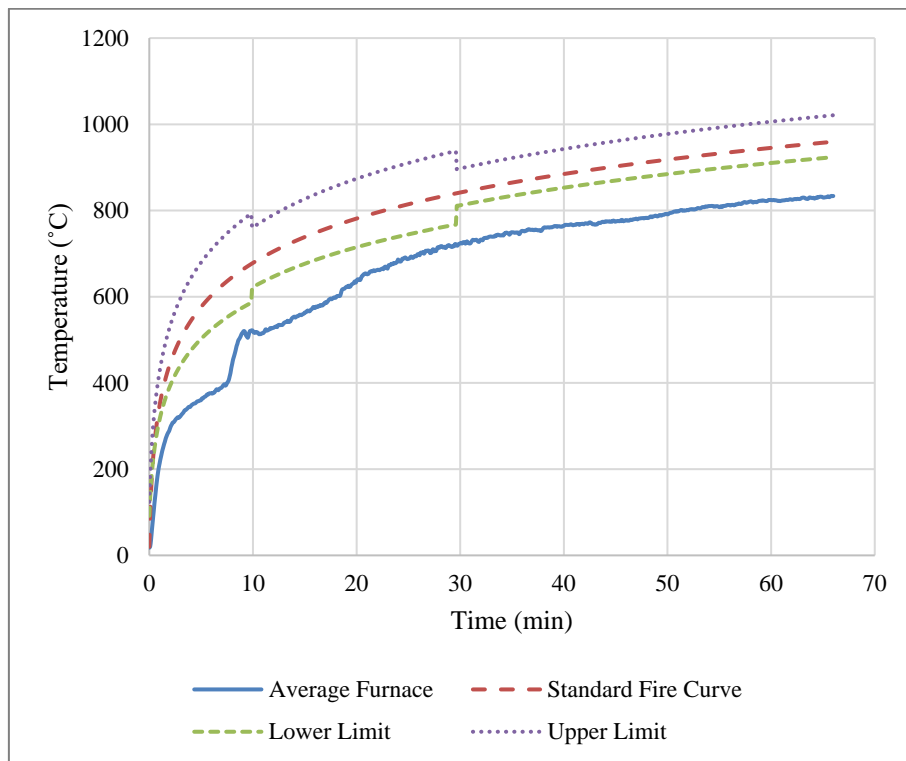


**Figure 5-7 LST-1 Average furnace temperature VS the Standard Fire curve.**

As seen above in Figure 5-7, for the first period of operation of the furnace, the desired average temperature output was not realized and missed the lower tolerance time-temperature curve for standard fire testing. Furthermore, a temperature gradient was observed from the south wall towards the north wall caused by the placement of the burners at the south wall as depicted in Figure 5-2 above. The length of the long side of the furnace (6 m) proved to be too much for the burners to achieve a uniform temperature within the furnace volume.

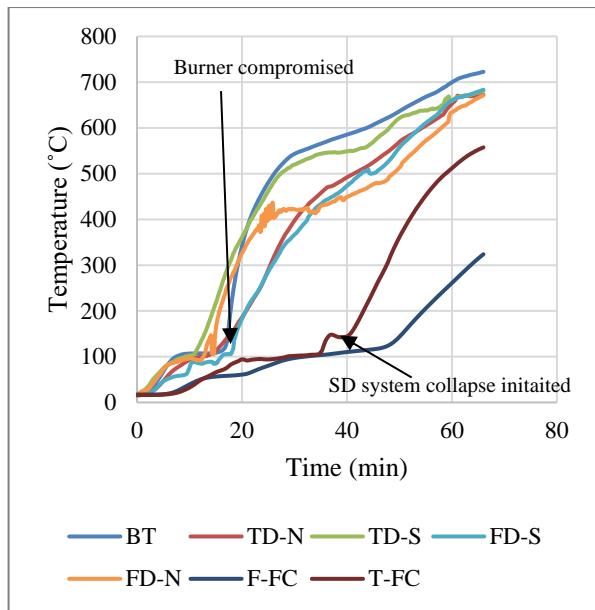


Figure 5-8 LST-2 Group 2 Time-Temperature curves.

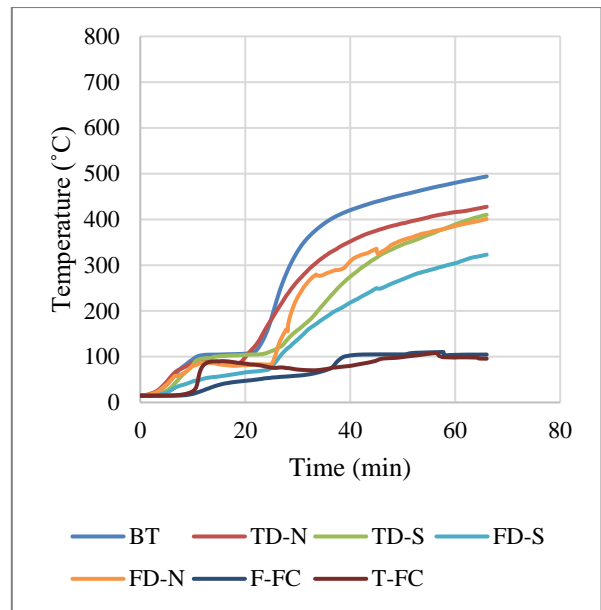


Figure 5-9 LST-1 Group 6 Time-Temperature curves.

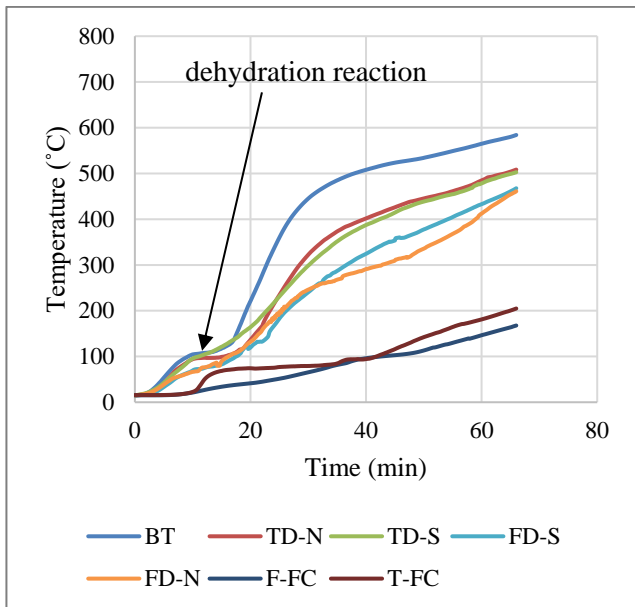
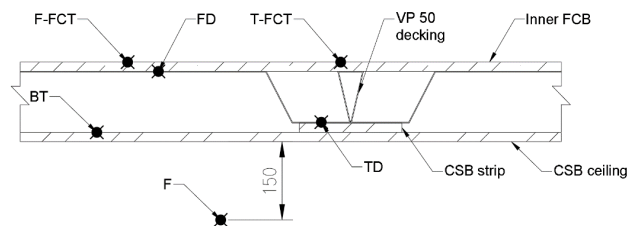


Figure 5-10 LST-1 Average Time-temperature curves for all groups (G1-G6).



Failure of the VP50-9 SD system was experienced at the south-west corner of the furnace. It appears that the steel was heated to a point at which its capacity was reduced, and load-carrying capacity was compromised, resulting in localised failure. Observations captured on film indicate that this failure was primarily caused by the burner near the south-west corner being compromised. It appears a piece of fibre ceramic blanket detached from the protected heavy timber beam located at the south wall and consequently covered the hole of the diesel burner. This caused a significant rise in temperature at this location and the subsequent failure of the SD system within this area as depicted in Figure 5-11 below. Hence, it appears hot burner gases may have been directed

straight onto the bottom of the SD and resulted in more rapid failure. Furthermore, failure to obtain the desired temperature output within the furnace can also be in large part attributed to the compromised burner.

The sequence of events are as follows: (1) when observing Figure 5-8 above, a steep temperature rise is observed at the 18<sup>th</sup> minute mark for the VP profiled steel (TD and FD locations), this marks the point at which the burner was compromised. (2) A subsequent steep rise in temperature is then observed at the 40<sup>th</sup> minute mark for the unexposed T-FC location, which marks the start of the decking collapse. (3) As the experiment was continued from the 40<sup>th</sup> minute mark, a progressive collapse of the SD system took place towards the end of the experiment, until complete failure occurs at the end of the test. The failure of the SD system can also be observed in the data collected as the readings are not consistent from one group to the other. The data collected from these groups suggest that heat was able to enter the flute and trough areas within the decking, right above the location of the compromised burner, and affected the desired heat transfer from the bottom to the top through the system. Nonetheless, some conclusions and analysis can still be drawn from the captured data.



**Figure 5-11 Failure of SD system at the South-West corner.**

As seen from the groups G2 and G6, and the average temperature data collected above, the top of the CSB temperatures steadily rise to a temperature of about 100°C, after which the curve flattens for some time, varying from 4.5 minutes to 11 minutes and an average time of 8 minutes for all positions on top of the Calcium Silicate board (BT locations), before starting to rise again. This is due to the water content within the CSB reaching its boiling point and evaporating, with the extra latent heat energy needed to evaporate the water from the boards halting the rise in temperature. After all the water has been evaporated, a rapid rise in temperature takes place. This moisture phenomenon also limits the rise of temperature of all the subsequent layers above the CSB during this period. The same phenomena occurs for the FCB at the top (F-FC or T-FC positions) as this material contains moisture. The influence of the water content within the CSB and FCB are important characteristics of the system that have a considerable influence on the overall performance and fire resistance. This is further detailed in Chapter 7 when looking at the finite element heat transfer model of the decking system.

Furthermore, utilizing Figure 5-10 above, comparisons can be made between the average temperatures for the FD-S and FD-N locations (i.e. at the Flutes on the Decking with Strips or No strips), and the TD-S and TD-N locations (i.e. at the Trough of the steel Decking with Strips or No strips). For the first 30 minutes of the test, the average temperatures of the FD-S and FD-N locations are similar with no notable difference. Progressing further, the average temperature at the FD-S locations become higher with a maximum difference of 14%, until converging to a similar final temperature at the end of the experiment. In general, the temperatures of the trough areas with and without strips running underneath them are similar, with the only notable difference occurring from the 10th to the 24th minute of the test, where the average temperature of the TD-N locations is lower than the TD-S locations, with a maximum difference of 24%. After which the average temperatures become similar again with the average temperatures of the TD-N locations being slightly higher for the rest of the test with a maximum difference of only 7.7%, and also converge to a similar final average temperature. From this data, it is difficult to conclude whether the strips running in the transverse direction have a notable effect on the heat transfer through the system. However, results from LST-2 clarify this issue.

Figure 5-12 below presents the unexposed average surface temperatures for both the trough and flute areas separately, as well as the total average temperatures from all the measured locations of the unexposed surface and compared to the FLS average temperature limit. As discussed in Section 1.2, it is important that the temperature on top of the SD be limited to prevent ignition of services in the plenum, and to obtain a standard fire rating.

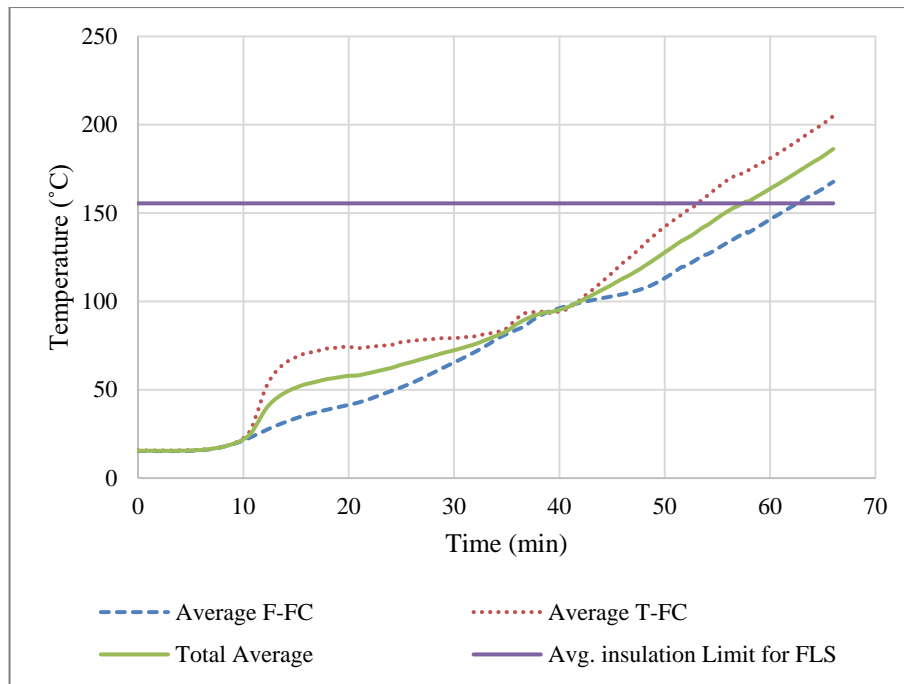


**Figure 5-12 LST-1 Unexposed surface average time-temperature curves on top of the FCB above the flutes (F-FC) and troughs (FC-T) of the decking**

Although no conclusions could be drawn whether the presence of CSB strips running beneath the steel decking at the flute and trough areas in the transverse direction make a difference, it is clear from the data that the heat transfer at the flute areas is lower than that of the trough areas on average with a maximum difference of 69% on the unexposed surface as observed in Figure 5-12. This indicates that the heat transfer through the system via conduction through the steel trough section has a higher influence than the heat transfer through the flute area via cavity radiation. This is in contradiction to the evidence found from the small-scale tests conducted by Marx (2018) where the average flute temperatures were much higher indicating that the governing mechanism of heat transfer is cavity radiation within the decking flute area. Due to this fact, the initial assumption that cavity radiation is not the governing heat transfer mechanism will be further investigated in the second experiment (Section 5.3) and FEM modelling in Chapter 7.

Furthermore, the average temperature of the unexposed surface is higher than the insulation fire limit state criteria of SANS 10177-2 average temperature of 155.5°C (ambient 15.5 °C + 140 °C), surpassing the limit temperature 57 minutes into the experiment. Hence, the SD system marginally failed in this regard. Additionally, the insulation fire limit state criteria for a single point temperature increase of 180°C above ambient, according to SANS 10177-2, was also exceeded. The single point measurements from G2 surpassed this limit for both the flute and trough areas at the 43<sup>rd</sup> and 54<sup>th</sup> minutes mark respectively, as well as G3 at the 59<sup>th</sup> minute and G4 at the 64<sup>th</sup> minute for the single point measurements at the flute and trough areas respectively. Due to the failure of the SD system during the test, the integrity and load-bearing function fire limit state criteria were also violated. However, as noted above, this was linked to a more extreme exposure to burner gases and the thermal environment is likely not representative of standard fire conditions.

### 5.3 Large-scale test 2 (LST-2) setup and results

The second large-scale test conducted in this work constitutes the main experimental component of this dissertation. With the insight gained from the first experiment, some changes were implemented to improve the experimental setup of the second test as detailed in the sections to follow. The second experiment consisted of a more comprehensive experimental setup that included the experimental frame detailed in Chapter 3, along with the attachment of the VP50-9 SD system.

#### 5.3.1 *Experimental setup*

The experimental steel frame structural elements were transported to the Ignis Testing facility and erected inside the furnace first. With the frame reassembled inside the furnace, the VP50-9 SD system was attached to the bottom of the beams. The frame was designed to be independent from the furnace walls with an approximate 100 mm gap between the furnace walls and the frame all round to allow for free movement. For the final stage of setup before testing, the structure and the SD system was instrumented with thermocouples for temperature measurements, and linear variable displacement transformers (LVDT) to measure vertical deflections of the horizontal steel beams. Hence, important data from this test setup are (a) temperatures of both the steelwork and the SD system at various locations, (b) no failure of the SD under load during the full test, and (c) deflections of the system under load. The test was run for 66 minutes.

The VP50 decking was first attached to the bottom of the beams. This was done by having a 100mm wide and 10mm thick steel plate run parallel underneath the primary and channel beams, in which the VP50 decking can be sandwiched in between and connected by means of hanger bolts as depicted below in Figure 5-13 (a, b, and c). The 10mm thick steel plates are approximately the same thickness as the CSB strips used when attaching the ceiling boards and are located in the same cavity. This makes the attachment of the CSB possible without any stresses being created in the boards by the steel plates. Consequently, counter sunk bolts were used for the hangers to have a flush finish on the steel plates at the bottom for the CSB boards to be attached as shown in Figure 5-13 (b).



**Figure 5-13 Steel plates used to support the decking of the SD system showing (a) a view from the bottom with the decking on top of the plate, (b) counter-sunk connectors which are used to hang plates from beams above, and (c) a top view of a channel with hangers connected through it.**

With the VP50 decking in place, the CSB were attached to the decking in the exact same fashion as in the medium-scale floor tests, with the CSB strips and fixities being the same in terms of its configuration and screw spacing of 200mm along the lengths of the trough sections. Single screw lines were used along the trough sections not joining two CSB together. Furthermore, the CSB ceiling was extended over the top of the furnace wall all round and sealed using the same vermiculite mixture used to line the inside of the furnace wall and covered with fibre ceramic blanket as depicted in Figure 5-17 below. This was to ensure the furnace is sealed off from the outside and was a closed system.

The FCB were attached to the decking in the exact same fashion as in the first test, with a screw spacing of 200mm along the flute section as depicted in Figure 5-15 (Right) below. With this, each component of the VP50-9 SD system was installed, with the FCB top and CSB ceiling attached to the VP50 decking, and the VP50 decking attached to the steel frame.

Loading of the structure was done in the exact same manner as in the first test with a uniformly distributed load of  $1.65\text{KN/m}^2$ . The sand bags were placed inside what would be the access flooring space, directly on top of the inner FCB, but without a layer of fibre ceramic blanket between the boards and the sand bags as shown in Figure 5-14 below. However, due to space limitations the bags had to be laid flat and provided almost continual coverage on top of the FCB. With the loading in place, the horizontal structural members were boxed in with the use of CSB on the sides and FCB on top to form a closed system and mitigate as much heat loss as possible as depicted in Figure 5-17 below.



**Figure 5-14 Uniformly distributed load on structure applied using sandbags in the plenum. FCB boards were placed over the bags upon completion to simulate the false floor.**

The location of the burners was changed to the east wall on the long side of the furnace, as depicted in Figure 5-16. This was to mitigate the temperature gradient formed within the furnace as seen in the first experiment. In addition, multiple hand-held gas burners were also placed at various locations around the furnace to be used as needed. Drawings of the final structural setup of the experiment prior to instrumentation is depicted in Figure 5-17 below.

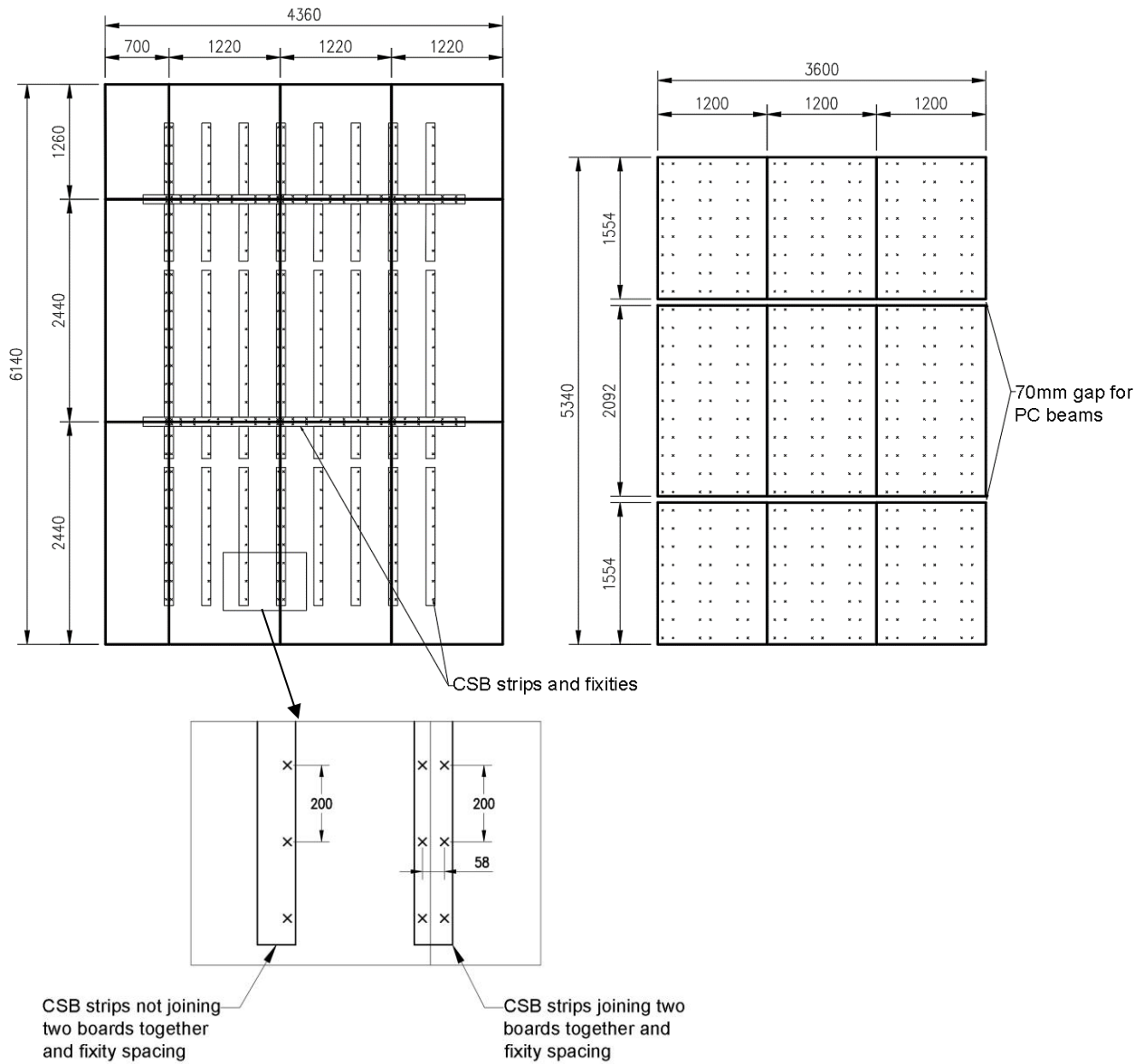


**Figure 5-15 CSB ceiling system (Left) and FCB (Right) configuration and fixities arrangements. The CSB system covered the side walls of the furnace, whereas the FCB fitted within the steel beams, hence the difference in size,**

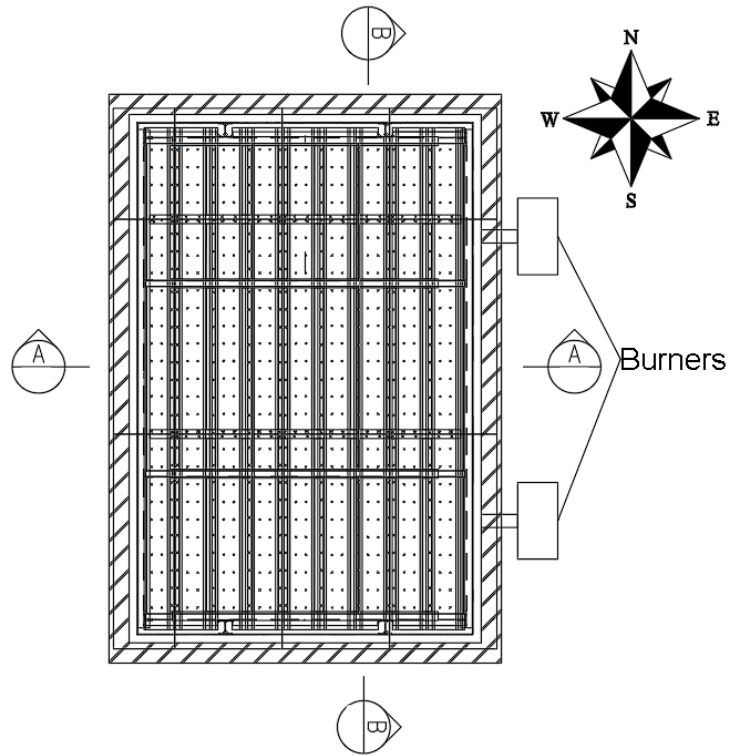


**Figure 5-16 Experimental setup top view.**

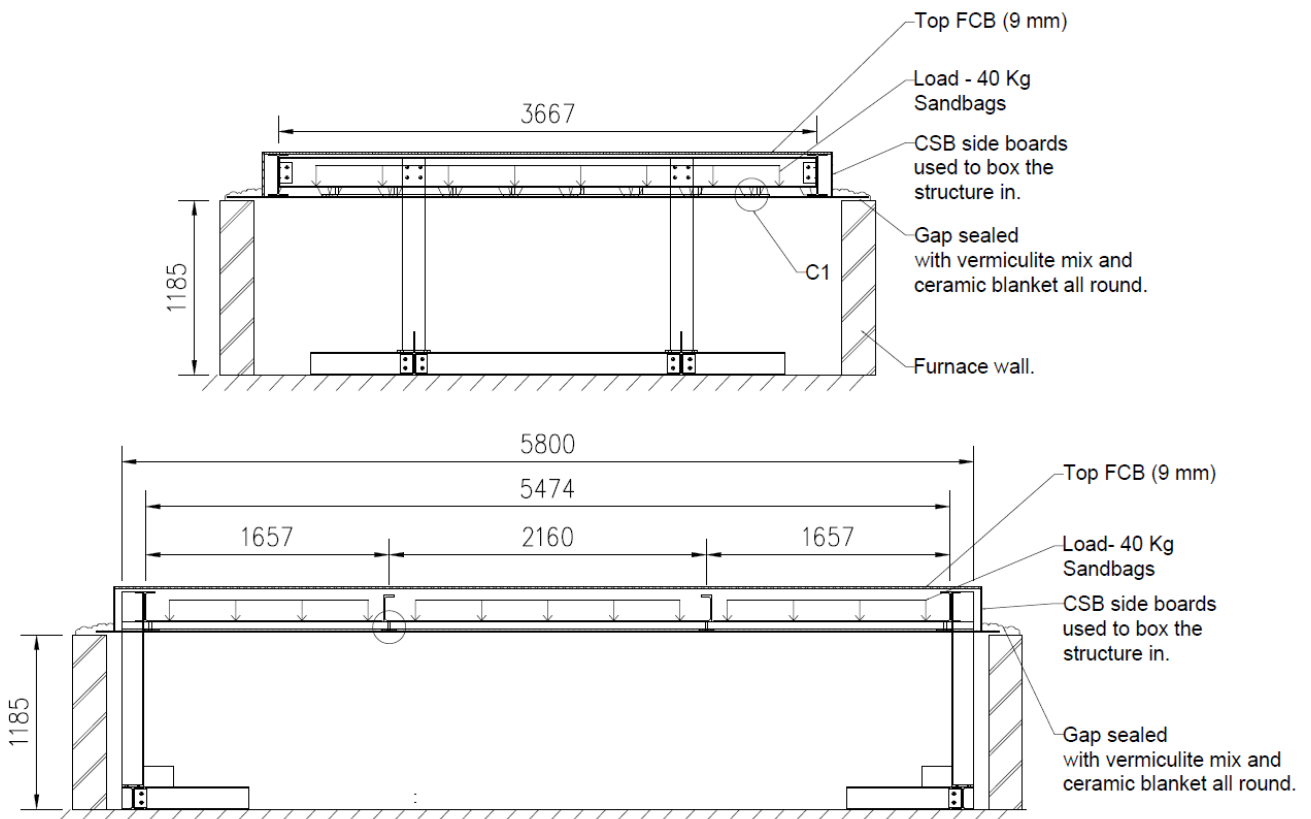


**Figure 5-17 Section A-A (top) and Section B-B (bottom) of LST-1 top view.**

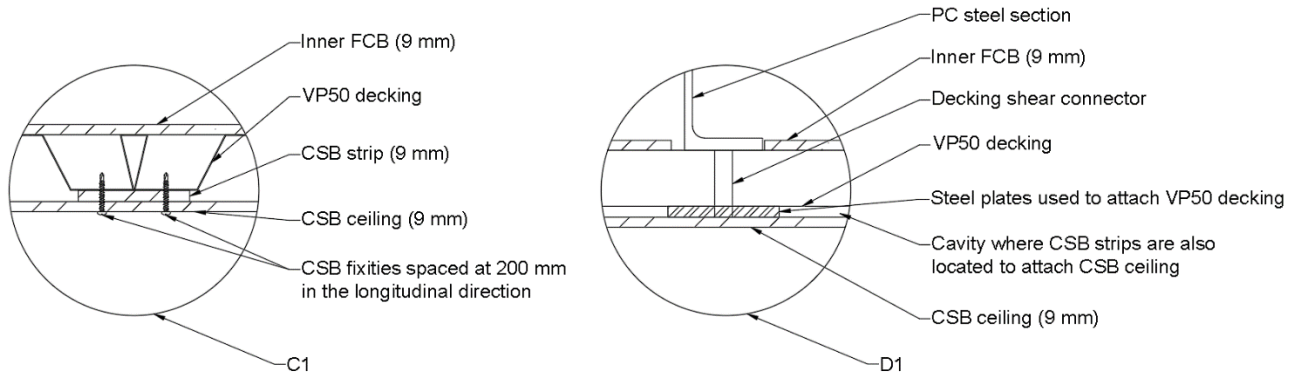


**Figure 5-18 Enlarged view of decking system C1 and D1**

### 5.3.2 Instrumentation

Thermocouples were placed along the decking system in groups of six, denoted as G1-G6, in the exact same fashion as in the first experiment and as depicted in Figure 5-19 below. Only six thermocouples per group were needed for this test due to the absence of the CSB strips running in the transverse direction. The specific locations of the thermocouples for each group are depicted in Figure 5-20 below. In addition to the decking system thermocouples, multiple thermocouples were also placed along the lengths of the horizontal framing steel sections in groups, each group of thermocouples measured along the height of the section. Each beam had three groups of thermocouples placed at intermediate points as depicted in Figure 5-21 below (a, b, c). When referring to Figure 5-21 (a, b) below, the denotations for each of the individual thermocouple locations are done accordingly. For instance, when referring to a thermocouple from group A2 at the bottom flange of PB 1, the denotation will be A2-B. Table 5-2 below describes the legend for the thermocouple location abbreviations used for the SD system.

**Table 5-2 LST-2 Thermocouple legend.**

<b>VP50-9 SD System Thermocouple Legend</b>	<b>Denotations</b>
<b>T</b> op of calcium silicate <b>B</b> oard ceiling	<b>BT</b>
<b>T</b> op of steel <b>D</b> ecking, trough area	<b>TD</b>
<b>T</b> op of steel <b>D</b> ecking, flute area	<b>FD</b>
<b>F</b> urnace gas	<b>F</b>
<b>T</b> op of <b>F</b> CB, <b>F</b> lute area (Unexposed surface)	<b>F-FCT</b>
<b>T</b> op of <b>F</b> CB, <b>T</b> rough area (Unexposed surface)	<b>T-FCT</b>

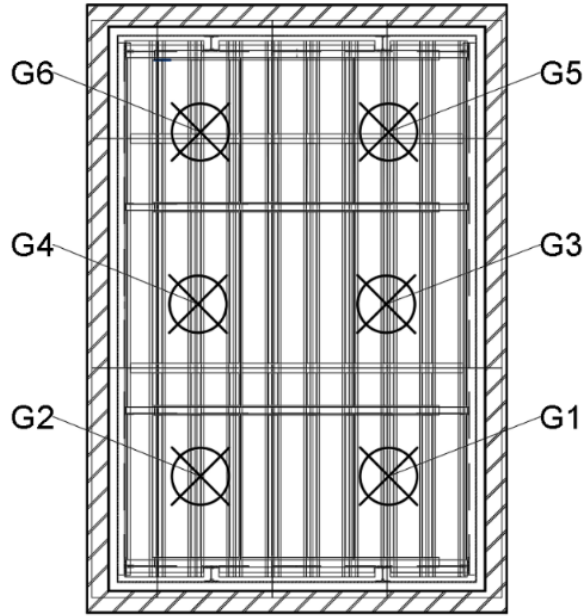


Figure 5-19 LST-2 Decking thermocouple groups layout.

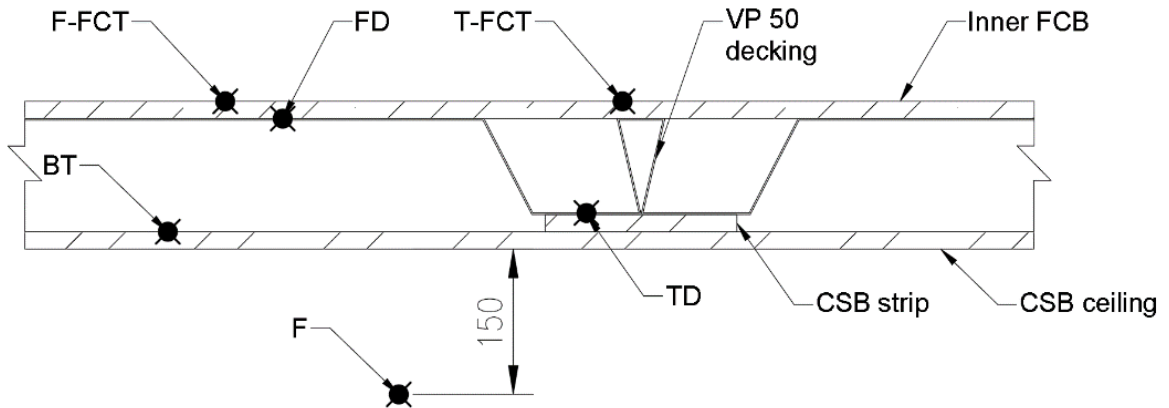
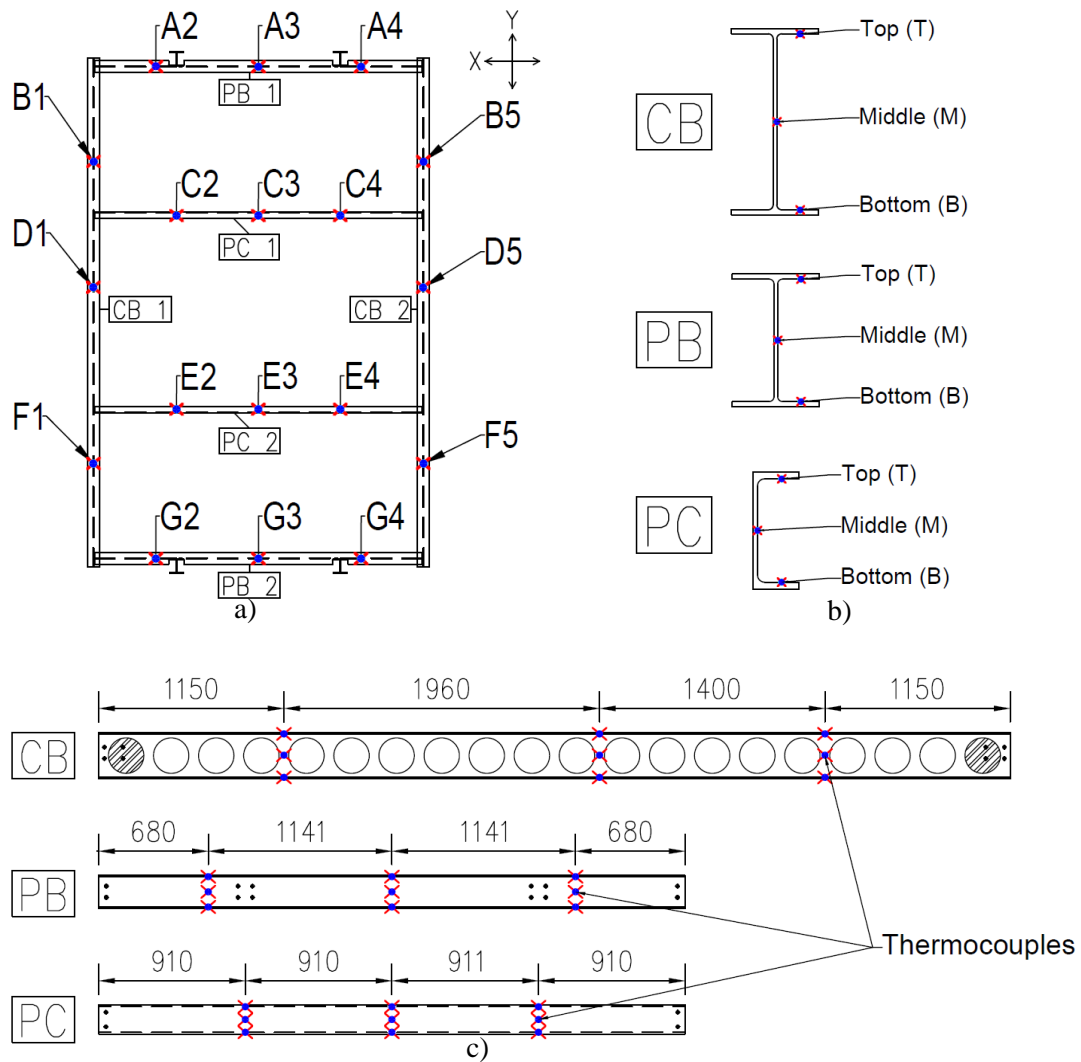
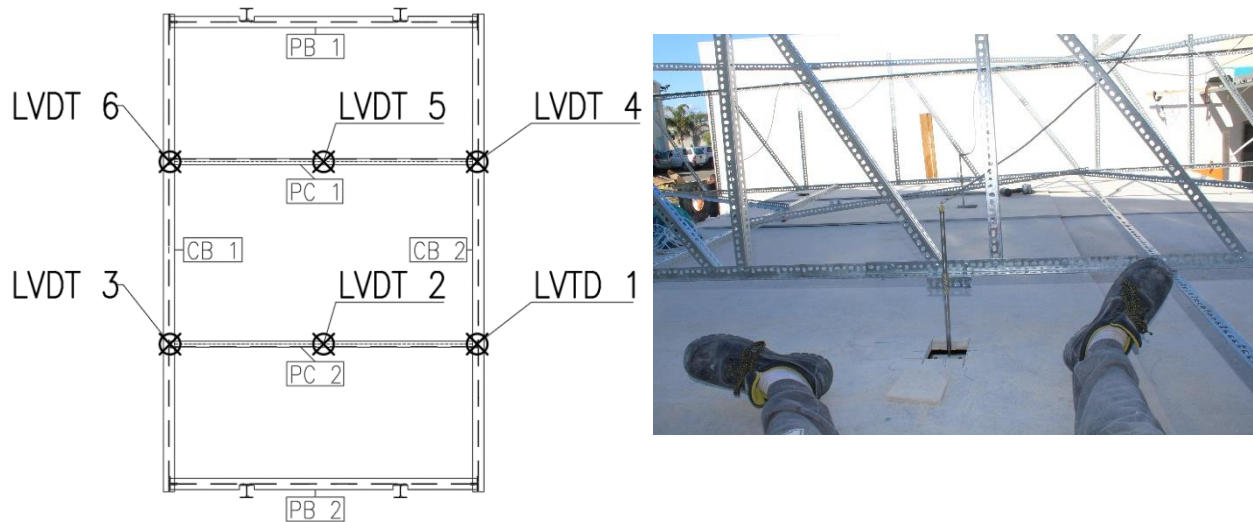


Figure 5-20 LST-2 Decking thermocouple layout for each group.



**Figure 5-21 Horizontal steel frame thermocouple group locations (Top-left), thermocouple locations per group along the height of beam sections (Top-right) and thermocouple group locations along beams section (Bottom).**

Apart from the thermocouple instrumentations, multiple 50 mm and 100 mm linear variable displacement transducers were also placed along the lengths of the secondary cellular beams and tertiary parallel channel beams. With the use of a large truss system, an independent frame from the experimental setup was built to attach the LVDT's. Four 50 mm LVDT's (LVDT 1, 3, 4, 6) were placed at the connection points of the cellular and channel beams, and two 100 mm LVDT's (LVDT 2, 5) were placed at the mid-points of the channel beams to make a total of six locations to be measured, as depicted in Figure 5-22 (Left) below.



**Figure 5-22 LST-2 LVDT locations (Left) and image of attached LVDT to truss system (Right).**

The layer of fibre ceramic blanket was replaced on the inside of the furnace. The supporting columns and spreader beams were also covered with multiple layers of fibre ceramic blanket so as to reduce thermal expansion of columns which would affect deflection measurements. Figure 5-23 below shows the experimental setup on the inside (Bottom) and outside (Top) of the furnace just prior to testing.



**Figure 5-23 Outside (top) and inside (bottom) images of the final test setup prior to testing.**

### 5.3.3 Experimental results and discussion

For this section, the decking thermal results are presented first, followed by the thermal and deflection data of the steel beams. Due to the large amount of data collected, only the most important data is presented, with the complete data set available in the online repository (Claasen *et al.*, 2021). Where data is incomplete or missing, assume the thermocouple or LVDT malfunctioned during the test. The data will be presented in a similar order as in Section 5.2.3.

#### **Decking system time-temperature data**

Figure 5-24 below presents the average furnace temperature in comparison to the standard fire curve and the upper and lower tolerances for standard fire testing according to SANS 10177-2 (SABS, 2005).

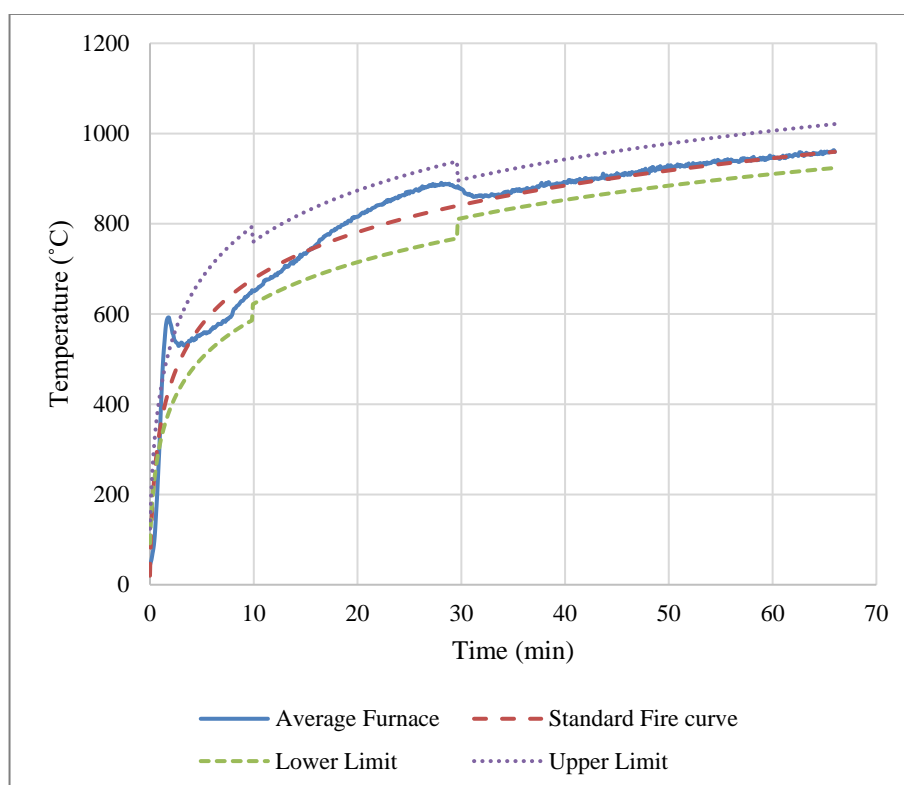


**Figure 5-24 LST-2 Average furnace temperature versus the Standard Fire curve.**

As seen above in Figure 5-24, the average furnace temperature agrees well with the standard fire curve and is well within the standard fire testing tolerance temperatures. Furthermore, the relocation of the burners towards the east wall of the experimental setup proved to be successful, with no notable temperature gradients formed within the furnace volume. At 3 minutes into the test the furnace was found to be over-shooting the standard fire curve upper limit and was manually adjusted, causing the localised change and correction.

The time-temperature curves for G2, G6 and the same location average temperatures for all groups (G1 to G6) are presented below in Figure 5-25 to Figure 5-27. These results should be kept in mind, as the average temperatures (Figure 5-27) will be presented with error bars in Figure 7-6 when comparing the data with FEM predictions.

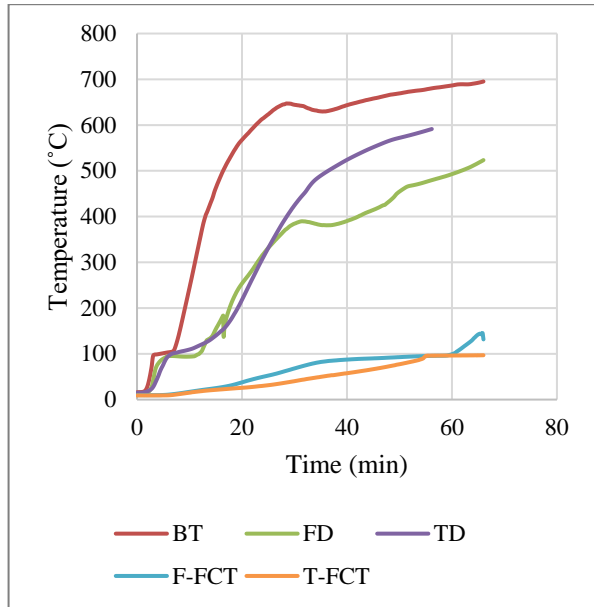


Figure 5-25 LST-2 Group 2 time-temperature curves.

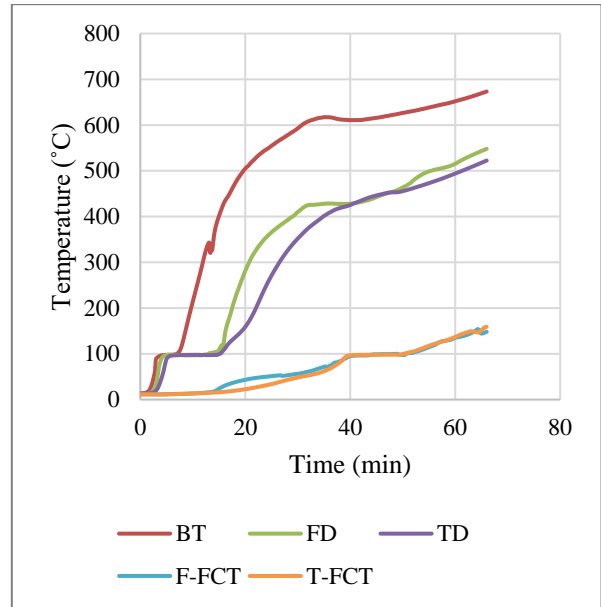


Figure 5-26 LST-2 Group 6 time-temperature curves.

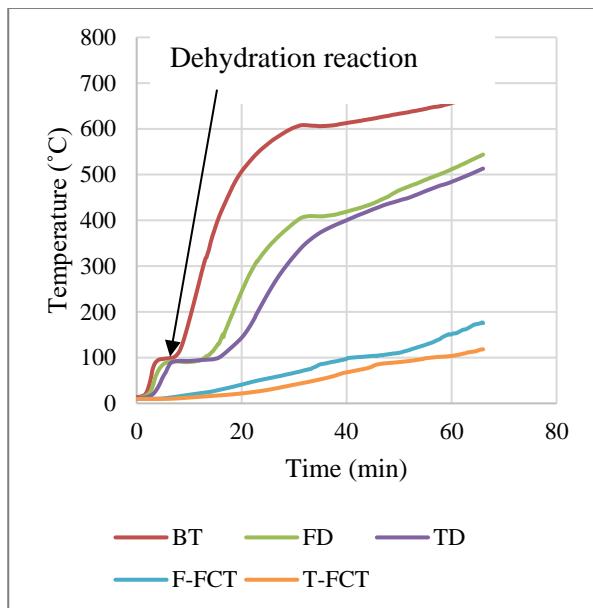
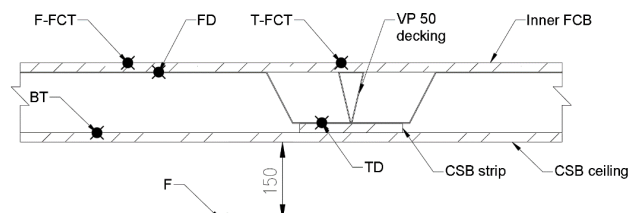


Figure 5-27 LST-2 groups average time-temperature curves.



No structural failure of the decking or steel beams occurred during this test and burner operation was not affected as per LST-1. Hence, more reliable thermal data was captured as the system was tested as intended. Observations of the heat transfer through the layers of the decking system can be made, with the highest temperatures captured at the BT locations, followed by the temperatures at the FD and TD locations and the lowest at the F-FCT and T-FCT locations, as would be expected.

Starting with the top of the ceiling board (BT) locations, similar observations can be made compared to LST-1, with a rapid rise of temperature from the start of the test up to a temperature of 100°C, followed by a halt in the temperature rise for a brief period, then a rise in temperature again consistent to the rise of temperature in the furnace. This rise in temperature to 100°C takes about 8.7 minutes from the start of the test and is halted for about 8 minutes in LST-1, while it only took LST-2 to reach this temperature in 3.6 minutes and is halted for about 4.4 minutes on average for all BT thermocouple locations. This discrepancy is caused by the difference in energy output from the burners at the start of each test, with LST-2 having higher initial temperatures. Visual observations of white smoke/steam were made starting at about 4 minutes into the experiment, which is consistent with the temperature data captured. This white smoke/steam was primarily caused by the water evaporation from the CSB and FCB and endured for most of the duration of the experiment. The highest temperature was recorded at G2 for this location with a temperature of 695°C at the end of the experiment.

Moving to the steel decking temperatures of the flute (FD) and trough (TD) locations, it can be observed that the temperatures for all FD locations are higher than that of the TD locations, apart from G2. This is in part due to the CSB strips running beneath the trough sections of the decking as in the medium-scale floor tests. The strips increase the distance and amount of material that the heat would need to conduct through to the subsequent top layer (i.e., the VP decking), along the trough areas. This outcome is also more consistent with the evidence gathered by the small-scale tests conducted by Marx (2018) in his thesis and in contradiction with the outcomes found in LST-1. This further highlights that the results captured in LST-1 are less reliable and altered by the failure of the decking system during testing which appears to have been influenced by heated gases being allowed into the SD. This also further illustrates that the main mechanism of heat transfer through the system is by cavity radiation via the flute area, when compared to the conduction of heat through the boards and steel at the trough area. As stated by Marx (2018), the shielding effect of the geometry of the steel at the trough area has an influence on the heat transfer through this section via cavity radiation and thus having lower temperatures at the TD locations. This observation holds for all the groups except G2, where the temperatures within the trough were higher than that of the flute area, this was most likely caused by a small crack in the ceiling during testing, with this crack arising from the loading of the structure or human error during construction of the ceiling. The maximum average temperature difference between the flute and trough area is 72.5%. Again, the highest temperatures were recorded at G2 for the TD location with a temperature of 591 °C at the 56<sup>th</sup> minute, and G5 for the FD location with a temperature of 568°C at the end of the test.

Figure 5-28 below presents the average unexposed surface temperatures for the F-FCT and T-FCT locations, and the combined average temperatures of the F-FCT and T-FCT locations in comparison to the average Fire Limit State unexposed surface temperature of 149.8°C (Ambient 9.8 °C.+140 °C). The unexposed surface single point temperatures for the F-FCT and T-FCT locations are also presented in comparison to the single point Fire Limit State temperature of 189.8 °C below in Figure 5-29.

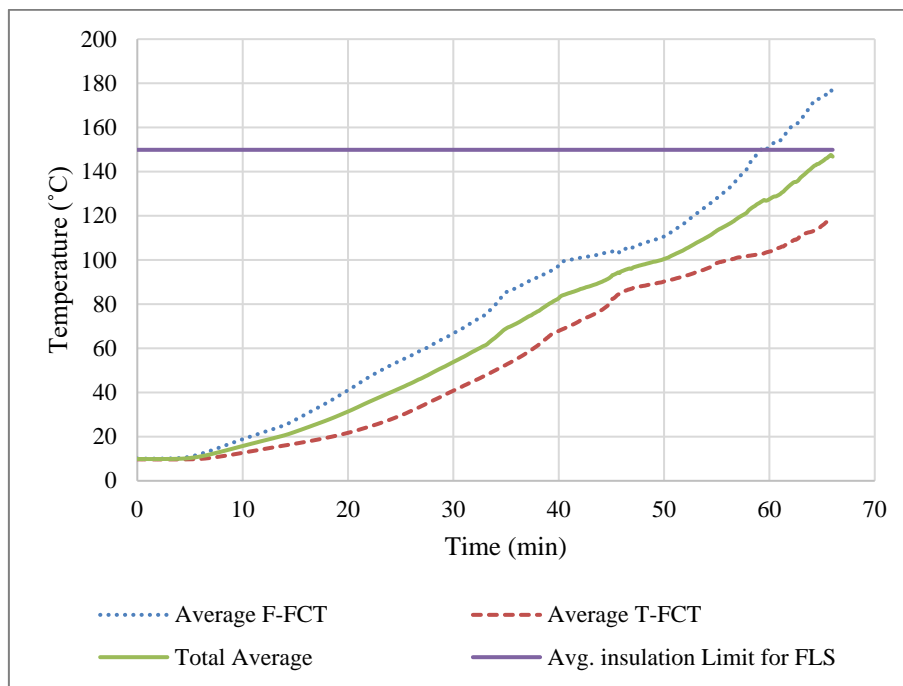


**Figure 5-28 Unexposed surface average Time-Temperature curves.**

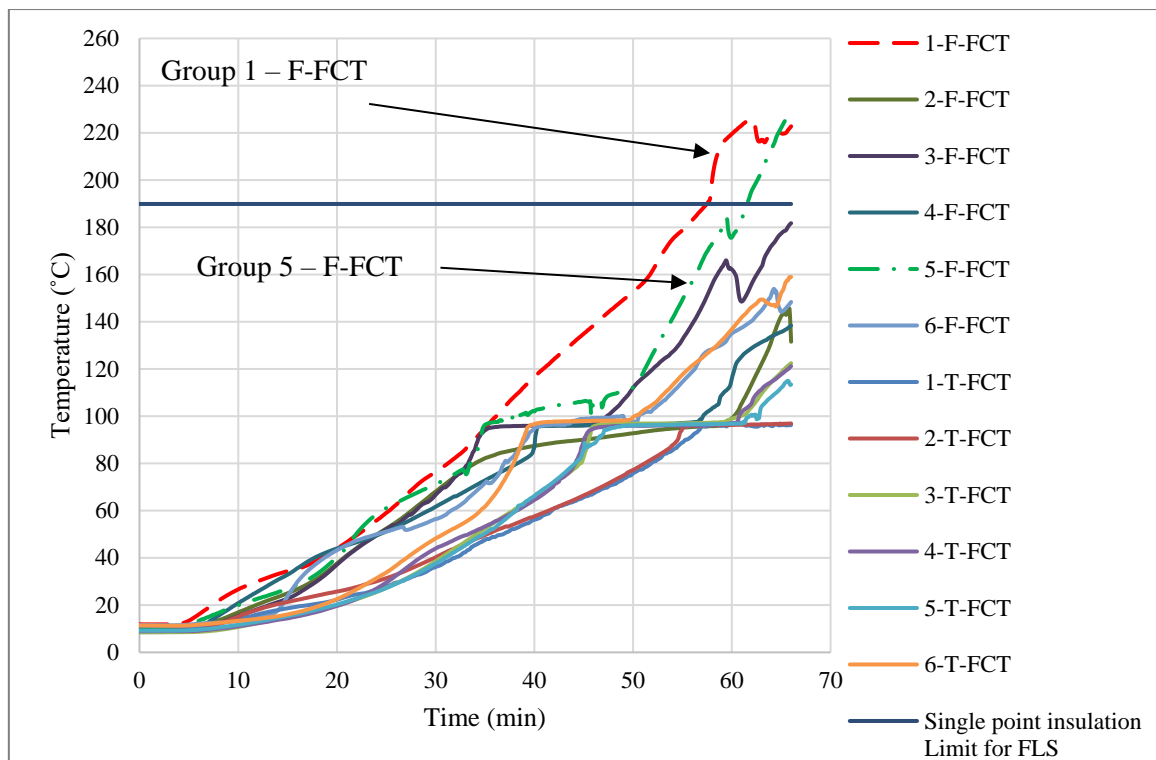


**Figure 5-29 All unexposed surface temperatures vs Single point insulation limit for FLS.**

As seen above in Figure 5-28 and Figure 5-29, the trough area location temperatures are all within the insulation FLS for the single point and average temperature limits. Conversely, the average temperature of the flute area locations surpassed the FLS average temperature at the 59<sup>th</sup> minute and two single point locations surpassed the FLS single point temperature at the 57<sup>th</sup> and 61<sup>st</sup> minute as indicated on Figure 5-29 above. Furthermore, the total average temperature of the trough and flute areas measured are within the insulation FLS average temperature. Thus, it can be concluded that the VP50-9 SD system does not meet the FLS insulation criteria for a 60-minute fire rating, with a fire-rating of 57 minutes. As for the load bearing function and integrity FLS criteria, no structural failure of the decking system was observed during the experiment, hence, it is safe to conclude the load bearing function criteria is met by the decking system.

No direct observations of the decking system could be made during the test as the system was enclosed, making the assessment of the decking system under the integrity criteria challenging. Upon inspection of the decking system after the load was removed, cracks were observed in the ceiling system and the FCB on top, despite this, the SD system was still intact as seen in Figure 5-30 (a, b, c, and d) below. Hence, concluding that the assembly was able to keep its integrity for the entire duration of the tests and not letting sufficiently hot smoke or gasses pass through acceptable. Furthermore, the failure of the decking system according to the insulation FLS criteria occurred towards the end of the test, hence, minor design changes can be implemented to mitigate this and will be discussed in Chapter 9.



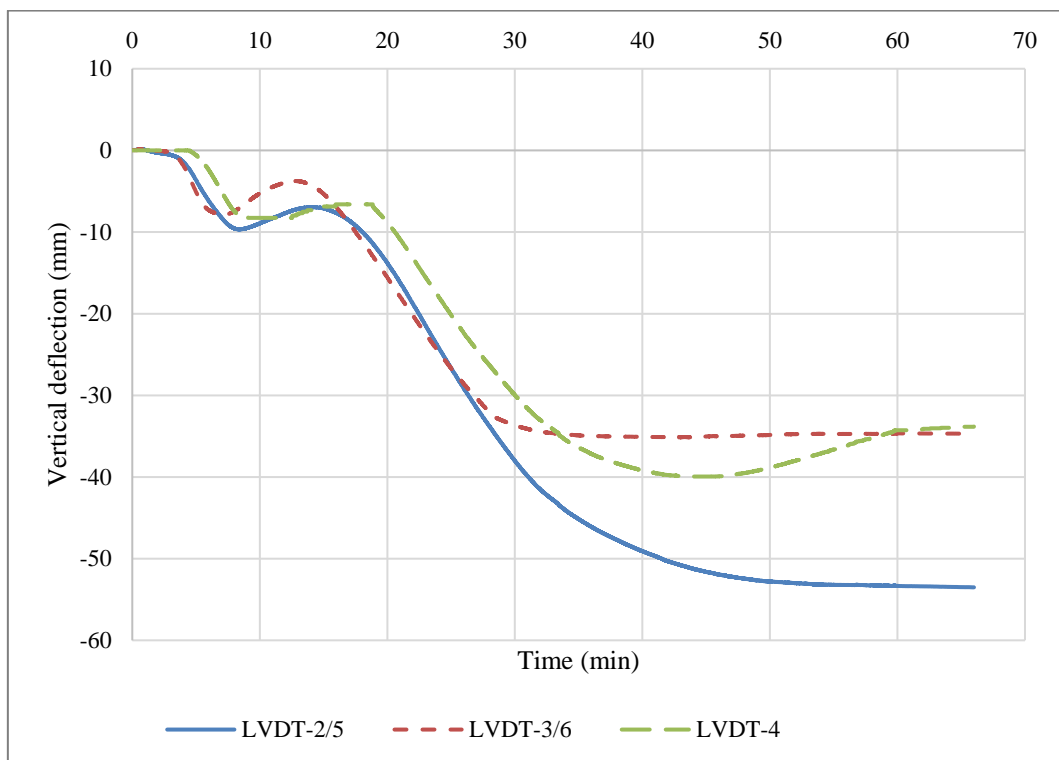
**Figure 5-30 Ceiling system (Left) and FCB (Right) after completion of the experiment.**

Figure 5-30 (Left) above depicts the CSB ceiling system after completion of the test. The CSB ceiling was predominantly intact. The ceiling system developed cracks along the screw fixities and in the transverse direction on some of the CSB during the experiment. Upon inspection of the ceiling system after the furnace cooled, the already present cracks were exacerbated as the structure contracted while cooling and also possibly forming new cracks. Furthermore, due to the downward deflection of the structure during testing, the boards shifted apart from each other, and this is visible in the joint opening between the attached boards along the centreline in both the longitudinal and transverse direction of the ceiling as shown in. This separation caused the boards to crack and break at the intersecting corner of the four boards as shown in Figure 5-30 (a) above.

The colour of the fibre ceramic blanket and ceiling system remained unchanged after the test, and this is a good indication that the burners were having full combustion during the test and no unburnt diesel was observed.

### ***Steel frame experimental data***

Figure 5-31 presents the measured vertical deflections of the horizontal steel beams. Note, the two measured locations for each of the cellular beams (CB 1 and CB 2) and the two measured locations of the channel beams (PC 1 and PC 2) have been averaged into a single reading each. LVDT-1 malfunctioned at the start of the test due to flame damage to a cable. Hence, LVDT-6 and LVDT-3 for CB 1 have been averaged into a single reading and denoted as LVDT-3/6. Similarly, LVDT 5 and LVDT 2 are averaged into a single reading for the channel supports (PC 1 and PC 2) and denoted as LVDT-2/5. Due to LVDT 1 malfunctioning, only LVDT-4 is presented for CB 2. The time-temperature curves of CB 1, PC 1, and PB 1 are also presented below in Figure 5-32, Figure 5-33, and Figure 5-34, respectively. In the interest of clarity, the same line style has been used to group the thermocouple groups together (i.e., Group B1 have the same line style), and the same colour has been used to group the different segments (top flange, web, and bottom flange) along the height of the beams. Figure 5-35 presents the average beam temperatures for the CB 1 measured location of B1 (i.e., average temperature of B1-Bottom, B1-Middle, and B1-Top as depicted in Figure 5-21 above) in comparison to the average vertical deflection of LVDT 3 and 6.



**Figure 5-31 Vertical deflection data for steel beams for LST-2**

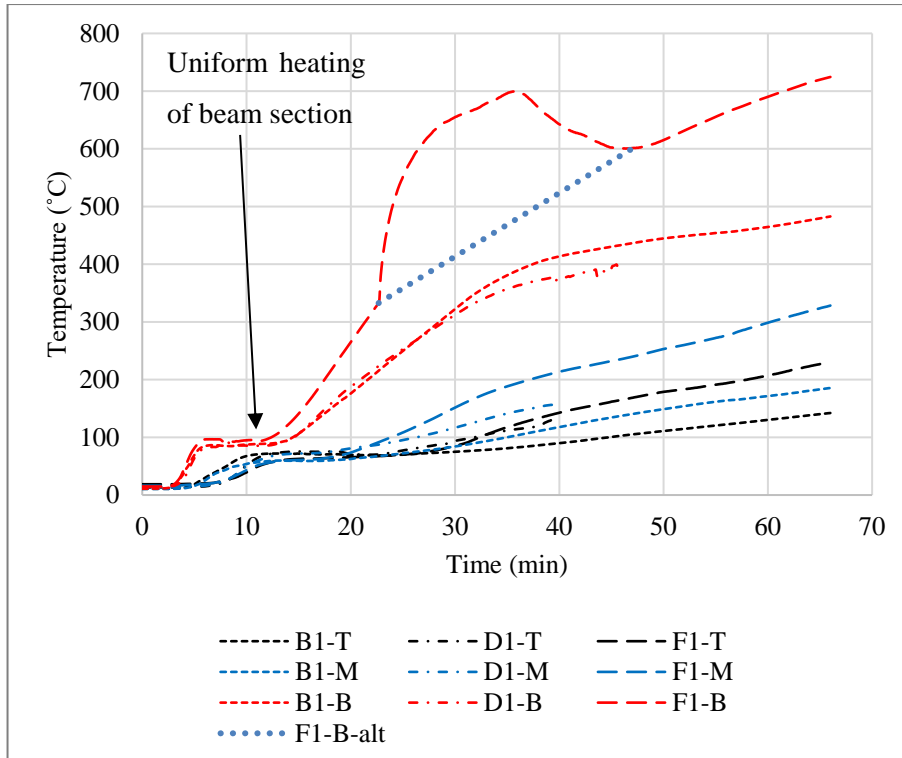


Figure 5-32 CB 1 time-temperature curves showing (T)op, (M)iddle and (B)ottom steel temperatures at positions B1, D1 and F1 along the beam length.

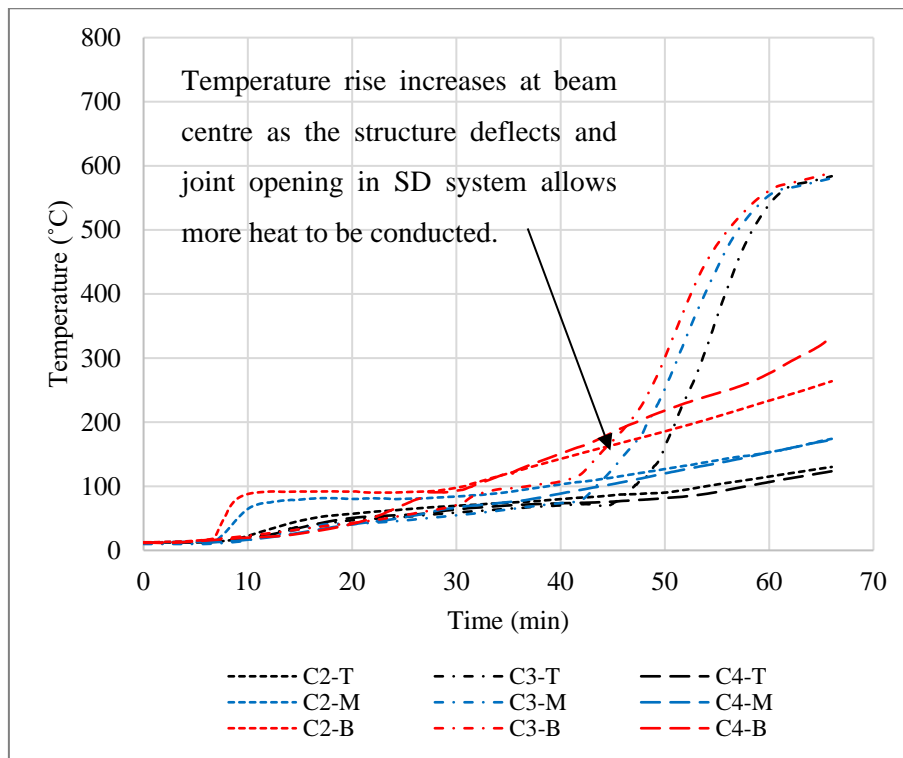
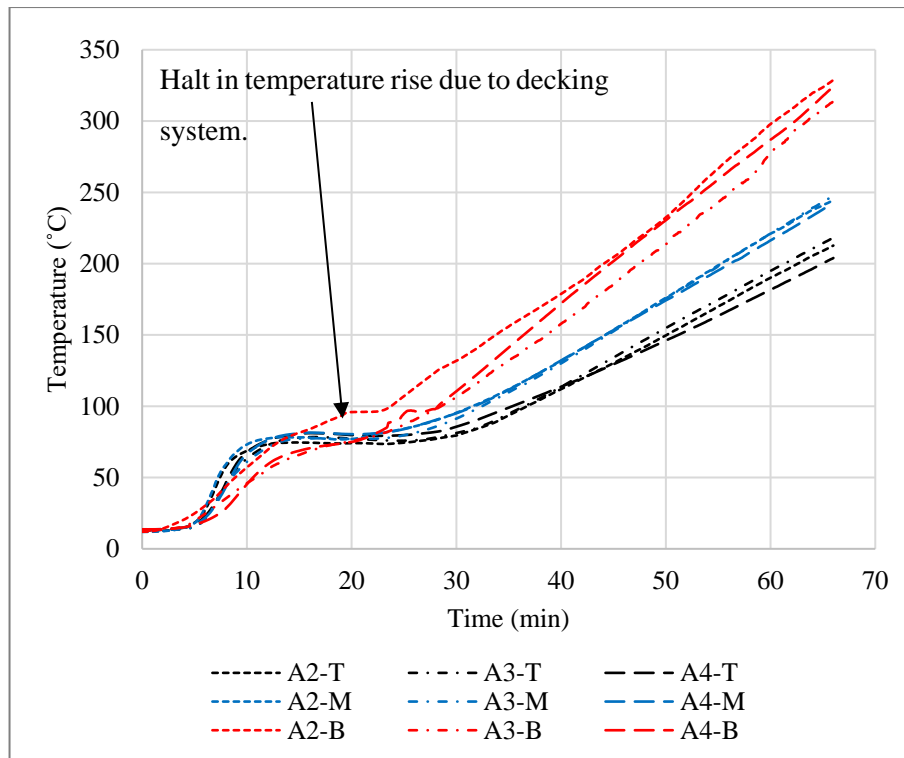
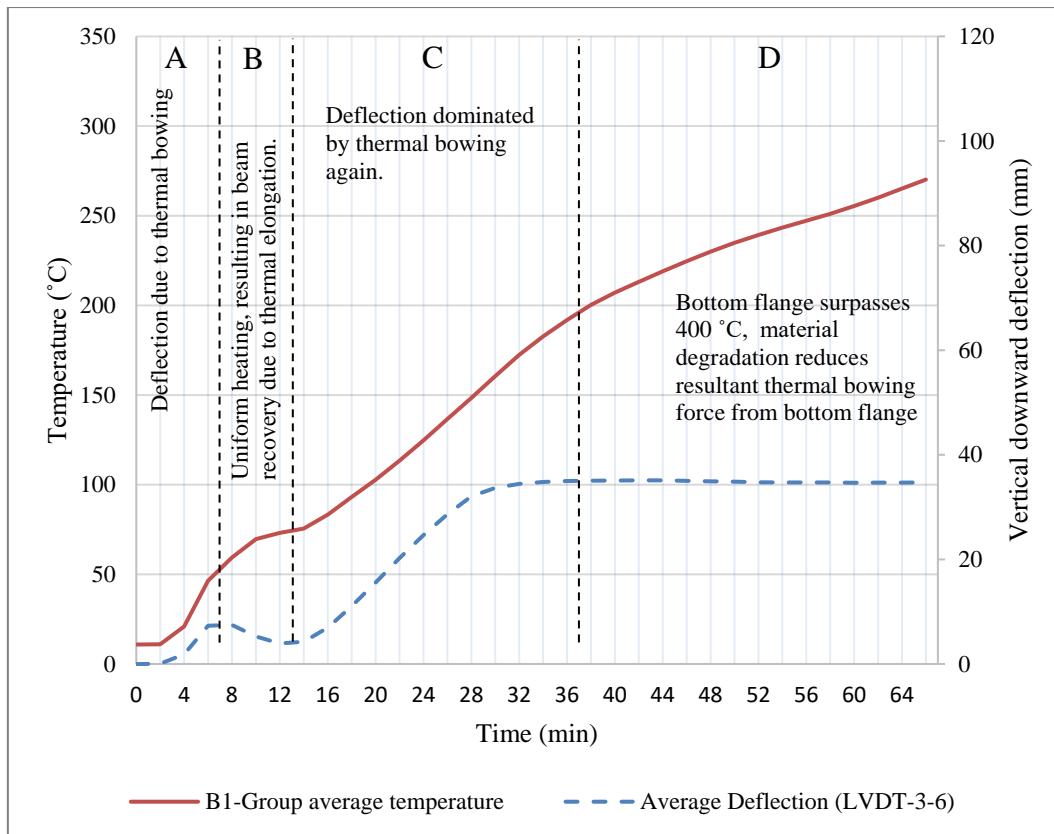


Figure 5-33 PC 1 time-temperature curves showing (T)op, (M)iddle and (B)ottom steel temperatures at positions C2, C3 and C4 along the beam length.



**Figure 5-34 PB 1 time-temperature curves showing (T)op, (M)iddle and (B)ottom steel temperatures at positions A2, A3 and A4 along the beam length.**

The deflection of the structure is comprised of three mechanisms, namely (a) thermal elongation, (b) thermal bowing, and (c) mechanical deflection, and it appears these mechanisms govern behaviour at different times. Thermal elongation refers to the lengthening of the steel beam due to a rise of its temperature as discussed in Section 2.6.3. Thermal bowing is the mechanism by which beams deflect due to a temperature gradient across the cross-sectional height of the beam (i.e., different rates of thermal elongation occur along the cross-sectional height of the beam). Finally, mechanical deflection of a loaded beam is caused by the loss of strength and stiffness as its temperature rises. The deflection behaviour of the structure can be described in four parts as indicated in Figure 5-35 below, where all three deflection mechanisms can be observed. As stated by Nadjai *et al* (2011), for an axially unrestrained beam at low temperatures (less than 400°C), deflections will be dominated by thermal bowing as the beam still retains 100% and 70% of its strength and stiffness, respectively. Whereas for higher temperatures, mechanical deflection will start to dominate, and the rate of deflection increases. All mechanisms will influence deformations at any time and will overlap, but the discussions below seek to simplify the observed structural deformation data.



**Figure 5-35 Group B1 average temperatures vs average deflection of LVDT 3 and 6 (CB 1)**

As the tertiary channel beams deflect in relation to the secondary cellular beams, the cellular beams mainly attributed to the overall deflection behaviour of the structure. Furthermore, both the cellular beams exhibited similar deflection behaviour, hence, the deflection behaviour of the structure will be mainly detailed with regards to a main cellular beam, CB 1. Starting with part A in Figure 5-35 above, and as seen from the data presented above in Figure 5-31, the structure starts to deflect at the 3<sup>rd</sup> minute into the experiment (i.e. a deflection in addition to the ambient mechanical deflection which could not be measured). The cellular beams continue to gradually deflect downwards, until reaching a deflection of about 8 mm at 7 minutes into the test, where the beams stop deflecting downwards and start to recover (i.e., starts to deflect in the upwards direction). Up until this point, the deflections of the structure occurred due to thermal bowing as the bottom flanges of the cellular beams heated up much faster in relation to their webs and top flanges.

Part B of Figure 5-35 depicts the gradual recovery of CB 1 until a vertical deflection of about 4 mm at the 13<sup>th</sup> minute into the experiment, resulting in a total deflection recovery of 4 mm. This recovery is due to the presence of the decking system and the halt in temperature that it provides at the 100°C mark. During this time, the beams become more uniformly heated as indicated in Figure 5-32. As the cellular beams of the structure were not axially restrained and the beams started to heat up more uniformly, thermal elongation of the beams pushed the structure laterally outwards in the longitudinal direction of the cellular beams, and in turn, allowed this recovery to take place. The uniform heating of CB 1 can be observed in Figure 5-32, where there is a rapid rise in temperature of the bottom flange until a maximum temperature difference in flanges of about 85°C. This halt in

temperature starts at about the 5<sup>th</sup> minute and lasts for about 7 minutes, during which it can be observed that the web and top flange of the beam heats up to near the same temperatures as the bottom flange at about the 12<sup>th</sup> minute into the experiment.

In Part C of Figure 5-35, the beam starts to gradually deflect downwards again as the temperature of the decking system starts to rise, and subsequently the measured temperatures of the bottom flange of CB 1. Due to this rise in temperature in the bottom flange of CB 1 and CB 2, a temperature gradient was realized once more along the height of the beam cross-sections and thermal bowing became the predominant mechanism of deflection again.

Part D of Figure 5-35 marks the point where the bottom flange of CB 1 surpassed the 400°C mark, where the strength and stiffness of this portion of the beam starts to decay at a more rapid rate as previously shown in Figure 2-7. The thrust exerted by the bottom flange, and resultant thermal curvature moment, thus does not increase with temperature as increasing strains are offset by decreasing material stiffness. Hence, a complex interaction of effects results in deflections staying almost constant. As shown in Figure 5-17 (Top) above, the web of the cellular beams penetrates through the SD system. Hence, the web could come into contact with cables and other construction items, meaning that insulation resistance requirements for it should also be maintained. In Figure 5-32 the web (Middle) temperatures range from around 180-300 °C at 60 minutes, meaning that insulation requirements are exceeded. This leads to the proposals in Section 9.4.1 where it is proposed that the SD should be installed underneath all beams to protect them from heating to this level. Alternatively, the bottom of the cellular beams will need passive protection.

The highest temperatures are recorded on the bottom flange of CB 1 as seen in Figure 5-32, with a temperature of 724°C at the 66<sup>th</sup> minute. The thermocouple at the location F1-B malfunctioned during the 23<sup>rd</sup> and 47<sup>th</sup> minute, and has been corrected with the linear interpolated straight line. This elevated temperature correlates with the hot temperatures from G2, where the highest temperatures were recorded for the BT and TD locations of the decking system. No failure of the cellular beams was observed during the test and only deflected until the structure started to stabilize from the 30<sup>th</sup> minute onwards. The webs and top flanges of the cellular beams remained relatively cool for the remainder of the test and were able to still retain most of their strength and stiffness, enabling the beams to resist the load. Finally, the highest deflections recorded for the PC and CB beams are around 20 mm (actual deflection of the cellular beam) and 34 mm for PC 1 and CB 1, respectively. This translates into deflections of about span/283 and span/166 for the PC and CB beams, respectively, which is within the recommended FLS of span/20 (BSI, 2009).

The average deflection of the PC beams in relation to the cellular beams is around 54 mm (highest deflection experienced by the structure), as a result, the channel beams were more exposed to the furnace heat at this location when taking the burner locations into consideration. Hence, the temperature within the middle sections of the PC beams started to heat up more rapidly in relation to the outer sections of the beams as seen above in Figure 5-33. Furthermore, the joint opening depicted above in Figure 5-33 runs near the centre of the structure and possibly allowed more heat to be conducted into the SD system and consequently the PC beams.

## 5.4 Conclusion

This chapter presented the two large-scale standard fire tests that were carried out at the Ignis Fire Testing facility on the VP50-9 SD system and an experimental structure of the original CBS prototype with the VP50-9 SD system attached to the bottom of the beams. Both tests were conducted with a newly built standard fire furnace with 6 m × 4 m inner dimensions for a duration of 66 minutes.

The first large-scale test to be conducted, LST-1, was on the VP50-9 SD system alone, and this was to investigate the thermal performance of the decking system and if the newly built furnace was able to produce the desired time-temperature output for standard fire testing. A different configuration of the VP50-9 SD system was investigated, whereby the Calcium Silicate board strips were arranged in the transverse direction. Failure of the decking system was experienced during the course of the first large-scale test at the south-west corner of the furnace due to a piece of ceramic blanket covering the output nozzle of one of the 300kW burners, consequently raising the temperature of this location, and causing the decking to fail. This highlighted how failure of the CSB ceiling is likely to severely affect the performance of the system. Collapse occurred due to severe heating of the steel decking which resulted in a loss of strength.

The second and more comprehensive test, LST-2, was conducted on the experimental structural frame and was carried out successfully for the entire duration of the test with no structural failure to any of the steel beams or SD system attached. SD and steelwork temperatures and deflections were recorded. An unusual deflection profile was obtained, but it was found this was due to a complex interaction of thermal effects and changes in temperature gradients during the course of the experiment.

The tests were scrutinized according to the FLS criteria for standard fire testing, the first large-scale tests failed all three FLS criteria as the SD system failed during the course of the test. The second large-scale experiment failed the insulation FLS criteria at the earliest 57 minutes into the experiment, with the integrity and load bearing function criteria not being violated for the entirety of the experiment, the structure yielded a fire resistance rating of 57 minutes. This is less than the 60 minutes fire-rating required for the CBS system and simple design changes will be implemented as discussed Chapter 9. Furthermore, the temperatures of the cellular beams (CB 1 and CB 2), which are also located within the access flooring plenum, exceeded the FLS limiting temperatures. Hence, design implementations will also be recommended in Chapter 9, such that the thermal exposure of the beams may be reduced.

The second experimental test forms the basis for the numerical modelling of the structural steel system response, as presented in Chapter 8. In this chapter (Chapter 8), the development of the experimental models developed to simulate the thermal-stress response of the experimental frame tested in this work will be presented. Multiple single element models and a single global model will be detailed, where the behaviour of the experimental frame under standard fire conditions will be investigated further.

## **Chapter 6 Sandwich decking (SD) system mechanical performance finite element modelling**

### **6.1 Introduction to modelling chapters**

This chapter is the first in a series of three chapters describing various models developed in this work. A significant amount of experimental data was captured in the experimental programme carried out in this research. The aim of the experimental programme was to obtain data on the structural and thermal behaviour characteristics of the two main components that make up the entire Cellular Beam Structural (CBS) system, which comprises of the SD flooring system and the CBS structural elements. With the use of Finite Element Modelling (FEM), a more in depth understanding of the results obtained in the experimental tests can be achieved, specifically regarding the aspects of the experimental test results that are not yet fully understood. Thus, the data captured from each of the experimental tests have been used as a baseline to develop models that are benchmarked against the experimental results as described in the following three chapters. All models presented in this dissertation were developed and analysed using Abaqus 2017 – version 6.17-1 (Dassault Systemes, 2016). Furthermore, where high computational power was required, the high-performance computer (HPC-2) available at the Stellenbosch University was utilized. The specific aspects of the CBS system that have been further investigated using FEM are as listed below. More details pertaining to each of the models will be presented in each of their respective chapters.

- 1 Prediction of behaviour of the VP115-20 SD system under four-point loading – Chapter 6.
- 2 Thermal response of VP50-9 SD system tested in LST-2 – Chapter 7.
- 3 Thermal-stress response of experimental steel frame tested in LST-2 – Chapter 8.

Due to scope limitations elevated temperature structural models of the SD systems have not been developed and should be pursued as part of future work, as discussed in Chapter 1.

This chapter will be delivered in five sections, with multiple subsections. This section (Section 6.1) serves as a brief introduction to the SD numerical models carried out in this work and in this chapter, with modelling considerations provided in the following section (Section 6.2). Section 6.3 details the parts of the model, along with the chosen mesh densities and element type assignments. It also describes the material properties implemented in the numerical model and the connector stiffnesses used. Section 6.3.5 details the general modelling procedure by giving details on the defined steps in the numerical model and presents a brief summary of the contact modelling formulation utilized in the model. Section 6.3.6 presents a short description on the assumed boundary conditions and details the applied loading. The results and final discussion are presented in Section 6.4, with conclusions being presented in Section 6.5.

## 6.2 Introduction to the modelling of the SD system at ambient temperature

### 6.2.1 Considerations regarding model development and focus

A variety of SD system configurations were tested in Chapter 4. Also, analytical elastic analyses were conducted on the SD, as provided in Section 4.3.4, which provided good agreement with the VP50 experimental results where steel yielding or the calcium silicate board (CSB) ceiling cracking governed failure. Hence, the VP50 systems have analytical models that can predict suitable capacities. However, there was poor agreement between simple elastic models and the predicted capacities of the VP115 systems.

As mentioned above in Section 4.3.4, the VP115 SD samples exhibited reduced composite behaviour. Hence, a more robust method of predicting the capacity and deflection behaviour needs to be explored, which takes partial interaction into consideration. Numerous analytical methods have been proposed and used in the past to calculate the deflection of composite floor sections while taking partial interaction into consideration (Ahmed *et al.*, 1996; Govindan and Madhavan, 2019; Newmark *et al.*, 1952; Oven *et al.*, 1997; Ranzi *et al.*, 2004). However, a unified approach is yet to be proposed as there is no single standardized analysis method to predict the deflection of a composite floor with partial interaction, although various software and numerical systems exist. Hence, Abaqus has been employed in this work to model and predict the ambient temperature deflection behaviour of the VP115 SD system. Test sample VP115-20-T1 and VP-115-20-T3 (excluding the sample with the stiffeners) yielded the highest ultimate load capacities in the experimental programme for the VP115 SD system tests, and are most likely to be used in the future. Hence these samples have been considered in this chapter. The VP115-20-T1 and VP115-20-T3 samples have the same configuration and materials used, with the only difference arising in the connector spacing used to connect the fibre cement board (FCB). Hence only a single model is developed to analyse both the VP115-20-T1 and VP115-20-T3 samples, where only the spacing of the FCB connectors are varied between the two model analyses (i.e., the VP115-20-T1 sample is analysed with a FCB connector spacing of 200 mm and the VP115-20-T3 sample is analysed with a FCB connector spacing of 300 mm in the longitudinal direction).

There are additional reasons to develop models for the VP115 configuration, and especially with the 20mm FCB, and this is based on multiple insights gained throughout the course of this work as stated above in Section 4.3.4. These include (1) ongoing engagement with practitioners has indicated that a 9 or 12mm FCB trafficable surface may not be suitable for ongoing operations due to practical requirements such as acoustics, cracking and punching when point loads are placed onto it. Hence, a 20mm FCB is more likely to be adopted in the future in practice. (2) The VP115 decking provides higher capacity and stiffness, as compared to the VP50 decking, but is only marginally more expensive due to the similar weights of the two. Hence, it is likely that the VP115-20 SD will be adopted in the future, rather than the VP50-9 SD configuration.

### 6.2.2 Considerations of joints and limitations on analysis

As discussed in Section 4.3.4, the structural performance of the SD system will be significantly dependent on construction details and both (a) how the boards are connected to the steel decking and (b) if/how boards are connected to each other where they butt up against each other, i.e. whether joints are continuous or not. In instances with longer spans, and for bigger floor areas, it is probable that top FCBs will not have full continuity where they butt up against each other. CSB ceiling may be continuous, due to the CSB strips as shown in Figure 5-15. However, the CSB is not relied on in terms of strength. The top FCB is needed for strength, and is more challenging to provide continuity to. Hence, in many instances ULS resistance may primarily be governed by the capacity of the steel decking in isolation – i.e. the capacity of the FCB is neglected due to joints.

Basing SD capacity on the decking alone would be a conservative, and more easily predicted, lower-bound solution for the capacity of the SD. However, it is nevertheless important to obtain an understanding of the influence of composite action provided by the trafficable FCB when attached to the decking, especially for the VP115 systems for which elastic analyses were not suitable. In many instances composite action that occurs in spans between FCB joints (i.e. 2.4m spans) may be sufficient to provide the required ULS or SLS resistance needed for systems, especially for shorter spans between channel supports for the CBS. Also, results may indicate the extent to which FCBs should be linked to each other such that additional composite action can be mobilised for longer spans. By providing FCB strips on top of the floor it may be possible to ensure continuity. False floors supported on top of the FCB level would typically be able to accommodate the small change in floor level due to linking strips, and such strips would not affect operations.

## 6.3 Model development and specifications

### 6.3.1 Parts and components

All components of the VP115-20 SD system were included in the numerical model, namely the FCB, the CSB and strips, the VP115 profiled steel sheet, and the fasteners. The dimensions and geometry of the model is as in the experimental setup of VP115-20-T1 and VP115-20-T3, with the only difference being in the connector spacing. As the thicknesses of the boards and sheets are significantly smaller in relation to all the other dimensions, three-dimensional (3-D) shell elements were chosen to model the parts. The strips of CSB were added to the model by sectioning the CSB part at the locations where the strips are to be placed. A thickness of 9 mm was assigned to the part outside the strip sections (Blue section), and an 18 mm thickness was assigned to the strips section (Green section) of the part as indicated on Figure 6-1 (Bottom) below. A thickness of 20 mm was assigned to the FCB part and a thickness of 0.8 assigned to the VP115 profiled steel sheet part. Two loading plates were also implemented in the model to simulate the loading beams used in the experimental setup to apply the load in the model as shown in Figure 4-12 above. The loading plates were modelled as 3-D discrete rigid shell elements. The four-node 3-D bilinear rigid quadrilateral (R3D4) element type was assigned to each of the loading plates.

Numerical integration of stiffness matrices in finite element analysis can represent a significant portion of the overall computational effort. To improve computational efficiency, it has become standard practice of some analyst to “underintegrate” (i.e., reduced integration) the various element stiffnesses (i.e., to employ a numerical quadrature rule of an order less than the required to yield exact values for polynomial integrands defined on regular meshes). While such underintegration can significantly reduce computational effort, the resulting matrices may be rank deficient and solutions to the equations of the resulting discrete system may contain “spurious modes” i.e., zero energy components which are manifested in the computed solution as oscillatory patterns called hourglass modes. However, procedures exists for eliminating or damping hourglass instabilities (Jacquotte *et al.*, 1986). In Abaqus, a small amount of artificial “Hourglass stiffness” is introduced in first-order reduced integration elements to limit the propagation of hourglass modes. The stiffness is more effective at limiting the hourglass modes when more elements are used in the model, which means that linear reduced integration elements can give acceptable results as long as a reasonably fine mesh is used (Rafiei, 2011). Hence, four-node linear shell elements with reduced integration and hourglass control (S4R) were assigned to the boards and profiled steel sheeting parts (Dassault Systemes, 2016). The S4R shell element, which is part of the Abaqus general-purpose shell family, is a robust element type that is valid for both thick and thin shell problems, making it suitable for a wide range of applications. As opposed to the S4 element type, S4R elements only have a single point of integration. Previous studies have also utilized the same element type to investigate the deflection behaviour of similar flooring systems using numerical modelling (Al-Shaikhli *et al.*, 2017; Al-Shaikhli *et al.*, 2017; Seraji *et al.*, 2014).

### 6.3.2 Mesh specifications

All parts of the model were meshed using a global seed size of 25 mm, resulting in a total of 17 650 elements used to analyse the model. A sensitivity analysis was conducted where the mesh densities resulting from a global seed size of 20 mm and 25 mm for all parts was compared, and showed that the difference in the results can be assumed as negligible. The results of the sensitivity analysis can be found at (Claasen *et al.*, 2021). The mesh densities for each of the components are as depicted in Figure 6-1 (Top) below.

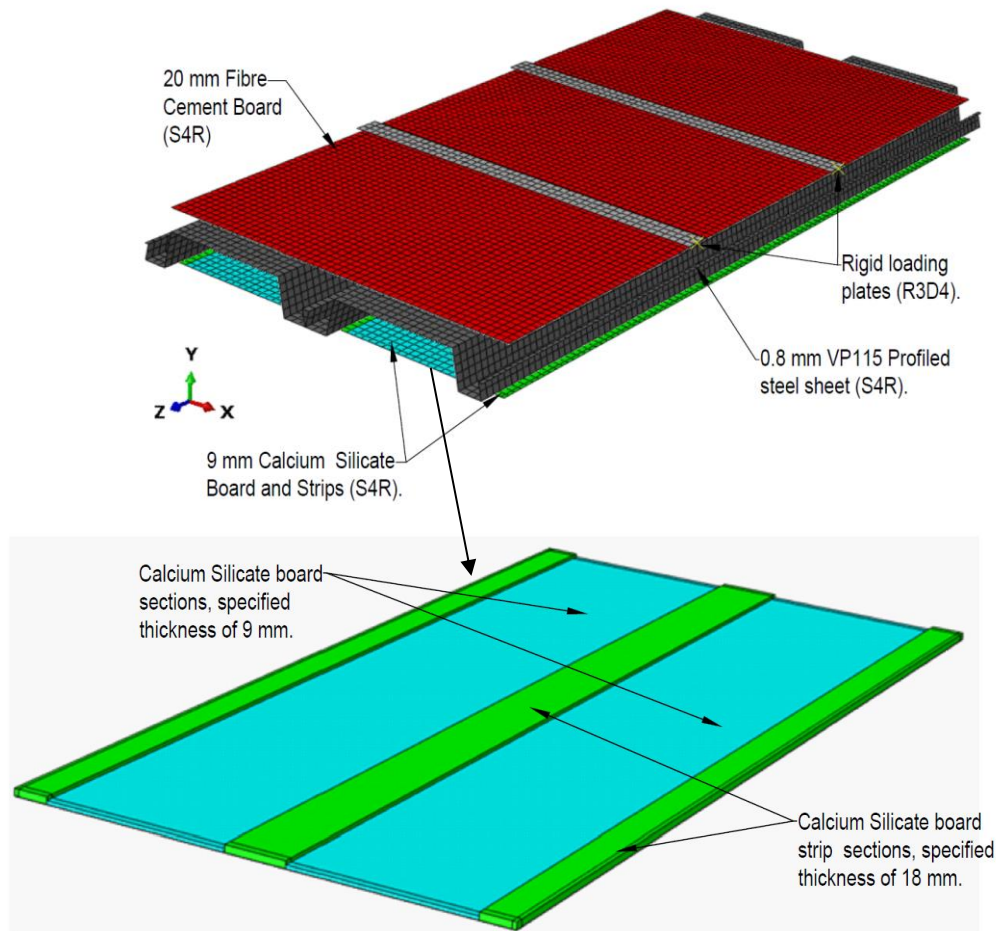


**Figure 6-1** Geometry of VP115-20 SD system model (Top) and implementation of CBS strips in the numerical model (Bottom).

### 6.3.3 Material properties of components

The material properties determined for each of the material components used in the SD system as part of the experimental programme carried out in this research, as listed in Tables 4-1 to Table 4-3 above, have been implemented in the numerical models. The material properties for each component implemented in the numerical models are as listed in Table 6-1 below. All material components were assumed to have simplistic isotropic linear elastic-plastic material properties as depicted in Figure 6-2 below.

**Table 6-1** Material properties of model components

Materials	Modulus of Elasticity (GPa)	Failure stress (N/mm <sup>2</sup> )	Poisson's ratio	Thickness (mm)
<b>VP115 Profiled steel</b>	200	297 - Yield	0.3	0.8
<b>Fibre Cement Board (FCB)</b>	6.169	20.88 - Compressive	0.25	20
<b>Calcium Silicate Board (CSB)</b>	5.424	7.19 - Tensile	0.25	9

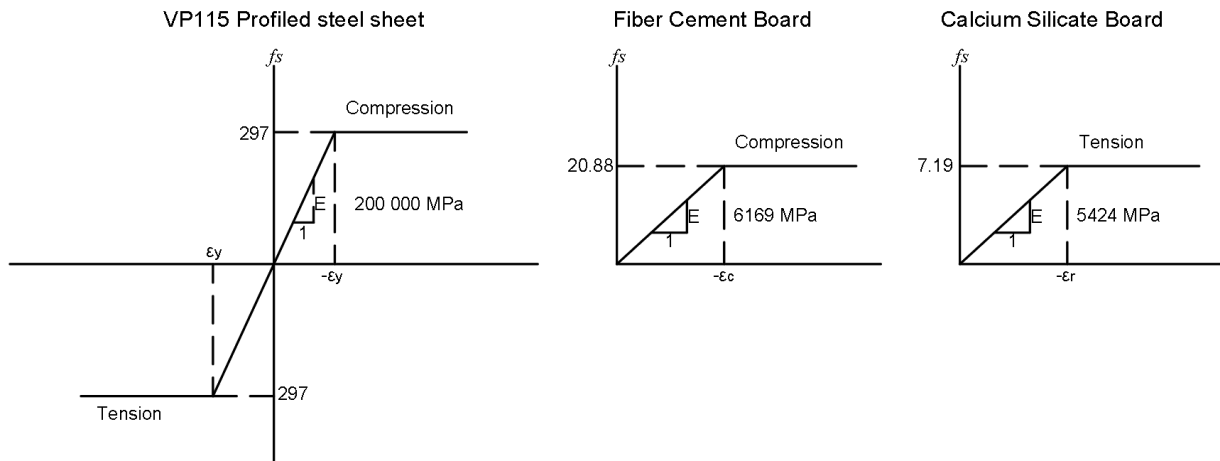


**Figure 6-2 Stress-strain curves of materials.**

The FEM developed in this work allows for consideration of partial shear connection where Euler-Bernoulli assumptions are violated. Figure 6-3 below presents the idealized stress profile of the VP115-20 SD system, where full-interaction is assumed, which will not be used to illustrate the discussions (Section 6.3.4) below.

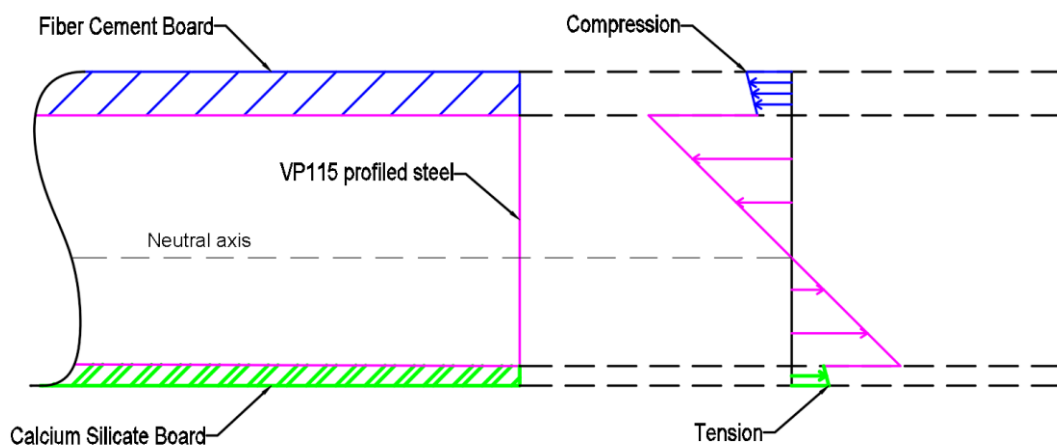


**Figure 6-3 Idealized stress profile of the VP115-20 SD system under bending load.**

When observing the idealized stress profile of the VP115 SD system under bending in Figure 6-3 above, it can be noted that the elastic stress gradient of the Fibre Cement and Calcium Silicate boards are negligible when compared to the stress profile of the VP115 steel. Hence, it was assumed that the FCB and CSB are acting entirely in compression and tension, respectively, with regards to the failure stresses. Thus, the material properties of the boards have been specified accordingly as determined in the experimental programme. Furthermore, as the material properties were assumed to be isotropic, the longitudinal average crushing strength of the board was specified. The Modulus of Elasticity (MOE) which was determined in the longitudinal direction, and on the top face of the board was selected. The tensile strength of the CSB was not determined in the experimental programme, hence, the average MOR value of the board calculated in the longitudinal direction, and on the top face of the board was specified as the ultimate tensile strength. The average MOE of the CSB that was calculated in the longitudinal direction, and on the top face of the board was selected. Lastly,

the Poisson's ratio values of the boards were not specified in their respective technical datasheets, hence, the values implemented in the numerical model have been drawn from literature, where a value of 0.25 is typically used as the Poisson's ratio of the boards. (Al-Shaikhli, Wan Badaruzzaman, Baharom, *et al.*, 2017; Seraji *et al.*, 2014).

#### 6.3.4 Connectors

The stiffness of the connector elements in this work have been derived from literature where they were obtained from studies which have used comparable materials, setups, and numerical models. Rahmadi *et al.* (2013) determined the deflection behaviour of a composite profiled steel sheet medium density fibre board (PSSMDFB) flooring system, and determined a connector stiffness of about 3695 N/mm for the 18 mm fibre board used via pull-out tests. Nordin *et al.* (2009) conducted pull-out tests on a variety of boarding materials, including a commercially available FCB, which yielded a connector stiffness of about 770 N/mm. Jaffar *et al.* (2018) determined the behaviour of the profiled steel sheet dry boards (PSSDB) flooring system, and used a connector stiffness of 710 N/mm in the numerical models, which was also derived from literature. The two highest stiffness values, 3695 N/mm and 770 N/mm per screw, were chosen based on the reported values to analyse the VP115-20-T1 sample and compare the numerical and experimental results. In each of the analyses, the connector stiffness of the FCB and CSB was assumed to be the same. To provide an upper bound estimate, a third analysis was also carried out, in which full interaction was assumed (i.e., fixities were modelled as rigid beam connector elements). A single analysis was conducted for the VP115-20-T3 sample, where a connector stiffness of 3695 N/mm was assumed for both the FCB and CSB. The results for each of the model analyses are further discussed in Section 6.4 below.

Various methods have been reported in literature with regards to implementation of the shear connectors in numerical models. Some researchers modelled the screw connectors as dummy plates (Ahmed *et al.*, 2000), while others suggested modelling the screws as spring elements (Al-Shaikhli, Wan Badaruzzaman, Baharom, *et al.*, 2017) or connector elements (Seraji *et al.*, 2014). For this study, connector elements have been used to model the connections of the SD system. The isotropic connectors were modelled using CARTESIAN connector elements in Abaqus, which presents independent behaviour between the two nodes in the three local cartesian directions. A connector stiffness of 3695 N/mm was applied in both the horizontal x and z shear directions, while a large stiffness of  $2.9 \times 10^6$  N/mm was applied in the vertical y direction (Jaffar *et al.*, 2018).

The spacing of the shear connectors are as in the experimental setup, with a spacing of 200 mm and 300 mm in the longitudinal direction for the VP115-20-T1 and VP115-20-T3 model analyses, respectively. Figure 6-4 below depicts the shear connectors for the VP115-20-T1 model as an example.

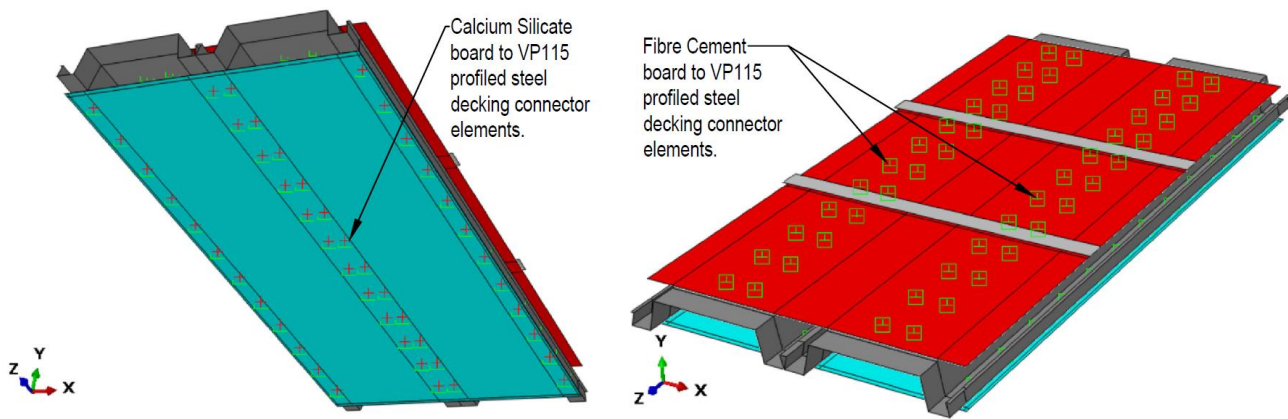


**Figure 6-4 Connector elements implemented in numerical model.**

### 6.3.5 Step and contact/interactions

The model was analysed using Abaqus/Standard, as discussed above. It has the ability to perform static and low-speed dynamic analysis for problems where stress accuracy is critical (Jahan, 2018). A three-step analysis procedure was adopted in this research: Step 1 (initial), where all the support boundary conditions are applied to the structure. Step 2 (contact), a small displacement is applied to the structure as detailed in Section 6.3.6 below, such that contact between the loading plates and the structure is initialized. Step 3 (Loading step), a prescribed deflection is applied to the structure as in the experimental setup. Both the second and third steps were solved using the “general static” algorithm solution.

Contact between all the parts were modelled using the surface-to-surface contact formulation. Abaqus offers a “Find contact pairs” option in the Interaction module, which searches and finds potential surfaces that could come into contact based on a set of search criteria rules specified by the user. Once all the potential contact pairs have been located by Abaqus, the contact pairs may be reviewed by the user, and the selected pairs defined. When using shell elements in contact modelling problems, care should be taken to make sure the surface normal directions of the selected surface pairs specified in the contact module face each other. The finite sliding formulation and two configuration (path) contact tracking was defined for all the contact pairs. Furthermore, to assist with convergence at the start of the analysis, the “Adjust only to remove overclosure” option was utilized in all the contact pairs. The parts' tangential and normal behaviour was defined in the interaction property, with the tangential behaviour assumed to be frictionless (i.e., shear force provided solely by the connector elements), and the default options for Pressure-Overclosure (Hard contact) and "Constraint enforcement method" selected for the normal contact behaviour. However, in the vicinity of where the load is applied it is likely that friction occurs, although the magnitude remains to be determined.

### 6.3.6 Load application and boundary conditions

Two methods are commonly proposed in literature for modelling the load application: load-control and displacement-control. A load-control method involves applying an incremental load as a force to the model from which the results are derived (i.e., stress, strain, displacement etc.). The displacement control method, on the other hand, applies incremental displacement to the model from which the reaction forces are calculated. However, some literature has shown that the load-control method is less suitable for conducting non-linear analyses (Al-Shaikhli *et al.*, 2017; Jahan, 2018). Firstly, there is an imposed linear relationship between the load and displacement in a non-linear analysis, secondly, as the model reaches the maximum load capacity, the increasing incremental load causes an increase in the corresponding displacement which in turn may cause numerical convergence problems (Al-Shaikhli *et al.*, 2017).

Hence, the displacement-control method has been implemented in this work. However, the displacement-control method is normally applied when using concentrated loads, whereas a distributed load is required for this model. To overcome this issue, two weightless rigid loading beams were implemented in the model to apply the load as in the experimental setup, as mentioned above in Section 6.3. This simulates the steel beams which applied the loads. A prescribed vertical (y-direction) displacement of 1 mm was applied in the second step (contact) and a displacement of 68 mm applied in the third step (load), which corresponds to the maximum deflection recorded for the VP115-20-T1 test sample. The prescribed displacements are defined at the boundary conditions of the rigid parts, which have been placed at the reference points of the loading beams as depicted below in Figure 6-5.

To simulate the support provided by the roller-supports in the experimental setup, boundary conditions were applied directly to the VP115 steel decking bottom trough section as depicted below in Figure 6-5. Only translation in the Y-direction ( $U_2 = 0$ ) was fixed, while all the other degrees of freedom (DOF) were free to rotate and translate. In order to prevent rigid body motion of the structure, support in the X and Z-directions was also provided. This was achieved by applying boundary conditions to the corners of the FCB as shown in Figure 6-5 below, where translation in the X-direction ( $U_1 = 0$ ) was fixed. This prevents any rigid body motion in the X-direction and rigid body rotation in the horizontal plane. To prevent any rigid body motion in the Z-direction, a single boundary condition was applied to the geometrical centre of the CSB, where translation in the Z-direction ( $U_3 = 0$ ) was fixed as also shown in Figure 6-5.

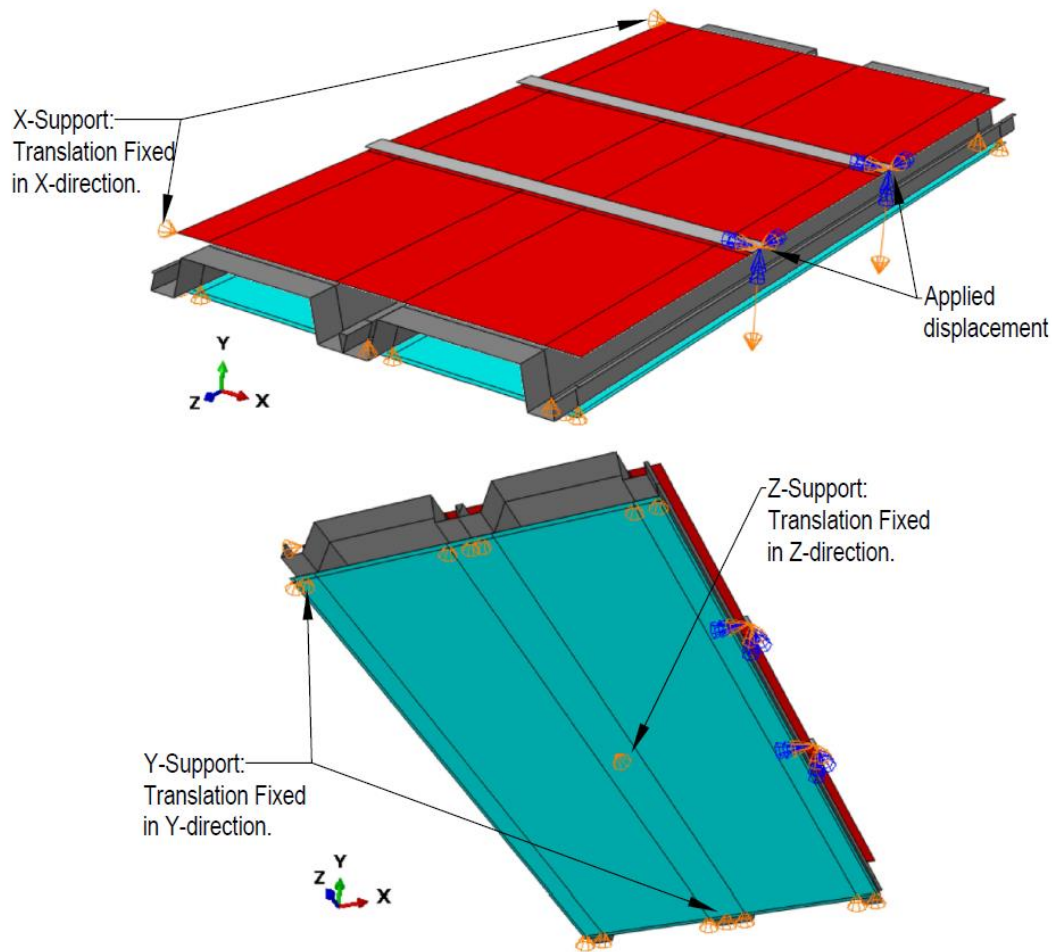


**Figure 6-5 Model boundary conditions and applied loading.**

## 6.4 Results

Figure 6-6 below depicts the FEM results in comparison to the VP115-20-T1 (designated as Experimental-200 Spacing) and VP115-20-T3 (Experimental-300 Spacing) experimental results. The deflection results were obtained from the geometrical centre of the FCB, which is in the same line of action with the measured vertical deflections in the experimental setups. The FEM results are denoted according to the spacing and connector stiffness values used in the analysis, where the spacing is denoted first, followed by the connector stiffness (i.e., FEM-spacing-connector stiffness). Additionally, the experimental result of the isolated VP115 profiled steel decking has also been included in Figure 6-6 below, such that the increase in the capacity due to composite action can be visualised. Considering a 2.4m span, the allowable SLS deflection for the system will be 8mm. It can be seen that maximum experimental deflections are around 9 times this value at maximum capacity (i.e. almost an order of magnitude more), meaning that SLS requirements will typically govern the design, as discussed in Section 6.5.

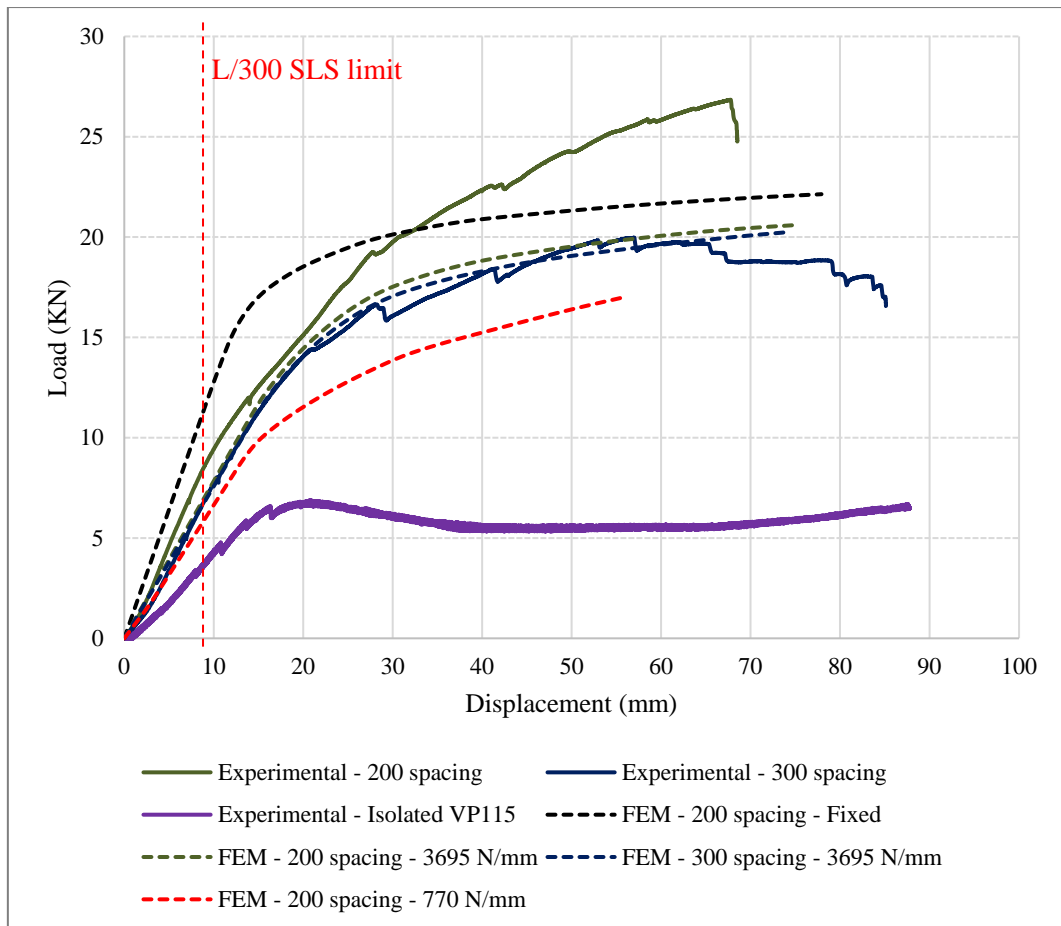


**Figure 6-6 Comparison of numerical and experimental results**

The maximum difference between the Experimental-200 spacing and FEM-200 spacing-3695 N/mm numerical result is 24%, which occurs at the experimental and numerical data's ultimate load capacities. As shown in Figure 6-6, there is a good correlation between the numerical results (FEM-200 spacing-3695 N/mm) and the Experimental - 200 Spacing data up to about 15kN, after which the numerical model begins to under-predict the experimental data deflection behaviour. As a result, the numerical model can accurately predict the composite behaviour of the VP115-20-T1 (200 spacing) SD system during its linear elastic phase. However, when material yielding and failure starts to occur, the numerical model under-predicts the experimental capacity.

Furthermore, when considering the FEM-200 spacing-770 N/mm numerical results, the model consistently under-predicts the deflection behaviour throughout the analysis, for both the Experimental-200 Spacing and Experimental-300 spacing. This indicates that the FCB and CSB connector stiffnesses are higher than the assumed 770 N/mm. However, due to the superior mechanical properties and larger thickness (20 mm) of the FCB, the connector stiffnesses are most likely much higher than those of the CSB.

Furthermore, the numerical model shows that the full interaction (FEM-Full-Interaction) model stiffness is higher than that of the experimental data for the majority of the linear elastic phase when compared to the Experimental-200 Spacing data. This shows that the SD system does, in fact, exhibit partial interaction

behaviour from the start, as expected. When a deflection of about 30 mm is reached, however, the full interaction numerical results begin to under-predict the experimental results. The discrepancy could be caused by a variety of factors. Firstly, the numerical model's simplified material properties, which assumed perfect elastic-plastic material behaviour for both the FCB and CSB's, could be a source of the numerical model inaccuracy. Secondly, the numerical model accuracy is also most certainly influenced by the assumption of the same stiffnesses of the board connectors. Finally, the supports were not included in the model and the boundary constraints applied directly to the steel decking, which could also be a source of the numerical model inaccuracies. At failure the experimental deflection is 68mm which is a large deformation over a span of 2.4 m. Hence, this shows that large displacements are occurring, which will be associated with highly non-linear response. It is also possible that the connectors have caused significant distortion of the FCB and CSB in the areas where the screws bear onto the boards, potentially leading to a strain hardening of the material in the vicinity. Furthermore, friction between the FCB and the steel decking may have influenced behaviour to some extent.

Furthermore, when considering the Experimental-300 spacing and FEM-300 Spacing-3695 N/mm data, it can be seen in Figure 6-6 that the numerical model results are highly correlated with the experimental results, with a maximum error difference of less than 10%. This indicates that the assumed stiffness of 3695 N/mm for all the connectors has a similar stiffness of the combined stiffness of the actual individual stiffness provided by the FCB to steel decking and CBS to the steel decking connectors. The difference between the FEM-200 spacing - 3695 N/mm and the FEM-300 spacing-3695 N/mm numerical results is less than 2% at the end of the analyses. This indicated that the connector stiffness of the FCB has very little influence on the capacity of the numerical models, which as observed by the experimental data does not capture the full behaviour. However, as stated above, the connector stiffnesses of the FCB and CSB are assumed to be the same.

The final stress distribution of the FEM-200 spacing-3695 N/mm numerical analysis, as well as the stress distributions of each of the individual part components and the Mises stress (MPa) output variable legend, are shown in Figure 6-7 below. The stress distribution of the VP115 profiled steel sheeting correlates well with the failure mode experienced by the VP115-20-T1 tested sample, which was local buckling failure between the points of load application in the experiment. This is consistent with the stress distribution of the VP115 profiled steel sheet part depicted below. Furthermore, the model predicts the order of failure within the materials as expected, with: (a) the steel failure due to buckling occurring first, followed by (b) failure of the CSB due to tensile cracking, and finally (c) failure of the FCB due to crushing as load is redistributed. Furthermore, failure of the CSB would normally occur in the form of a transverse crack between the points of load application, which is also consistent with the stress distribution of the CSB component in the model.

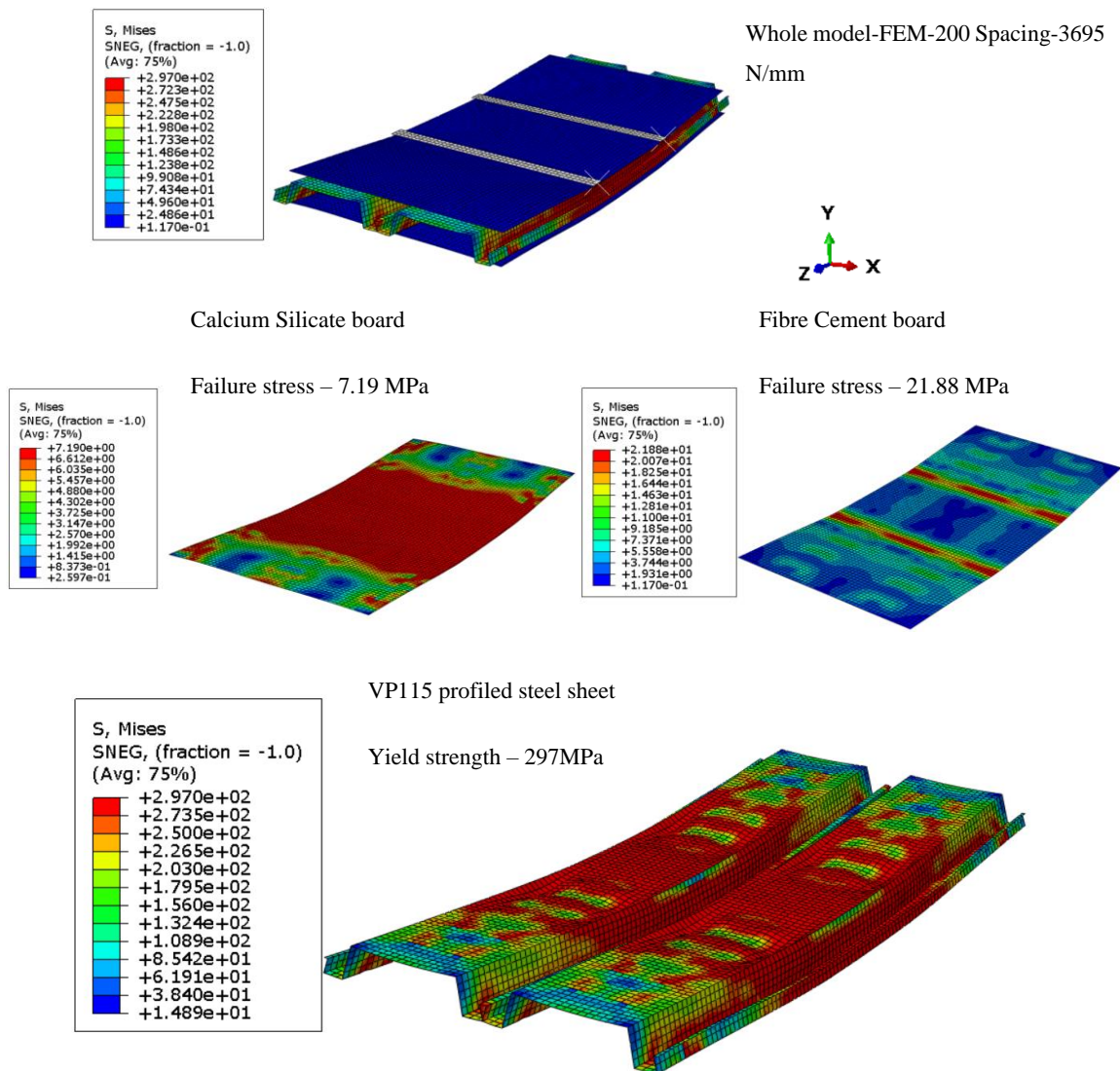


**Figure 6-7 Final Stress distribution of FEM-200 spacing-3695 N/mm numerical model, and the stress distribution of each the individual parts. (Stress values are in MPa)**

Furthermore, previous research has shown that in a composite sample with equally spaced shear connectors, the shear force per unit length transmitted will be lower for connectors near the point of load application (Newmark *et al.*, 1952). This is in line with the simplified partial interaction theory discussed in Section 2.7.1, in which the composite section's maximum slip occurs at the ends. As a result, the further the shear connector is from the point of load application, the more force per unit length must be transmitted, as the rate of slip increases with distance from the point of load application. For the FEM-200 Spacing-3695 N/mm numerical model, the total horizontal shear force of each connector element in the longitudinal direction (Z-direction) is as shown in Figure 6-8 below, where the force per connector element does indeed increase as the distance from the points of load application increases. Similar results are also found in the FEM-300 spacing-3695 N/mm numerical results.

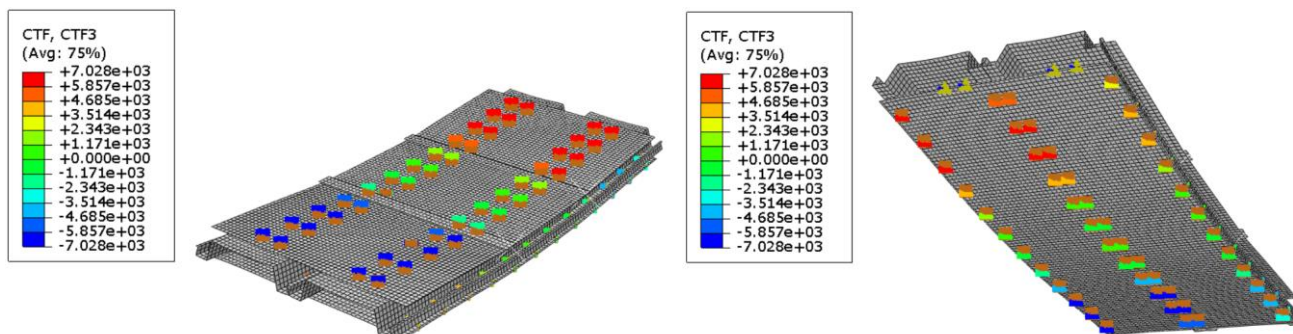


**Figure 6-8 Horizontal longitudinal shear forces for each of the connector element of the Fibre Cement board (Right) and the Calcium Silicate board (Left). (Force in N)**

## 6.5 Conclusion

This chapter presented the numerical model developed to investigate the behaviour of the VP115-20-T1 and VP115-20-T3 SD system samples tested (200 and 300mm shear connector spacings respectively). The layout, geometry, and mesh densities of the model is depicted in Figure 6-1 above, with a mesh density of 25 mm for all the model components. Specifications on the material properties used for the SD system material components are discussed in Section 6.3.3 above, where details of the selected MOE, failure stresses, and Poisson's ratios used for each material are presented. Following this, a brief presentation of the connectors stiffnesses implemented in the numerical model is presented in Section 6.3.4, where details of the selected connector stiffnesses in each of the numerical model analyses are discussed. Sections 6.3.5 detailed the analysis steps defined and contact formulations used in each of the analysis, whilst section 6.3.6 detailed the method of loading applied to the numerical model and the boundary conditions defined in each model analysis.

A total of three analyses were conducted for the VP115-20-T1 sample, where three different connector stiffnesses were investigated, namely 3695 N/mm, 770 N/mm, and fixed (i.e., full-interaction is assumed). A single analysis of the VP115-20-T3 sample was conducted, with an assumed connector stiffness of 3695 N/mm. The results for each of the conducted numerical analyses are presented in Figure 6-6 above in comparison to the experimental results of the VP115-20-T1 and the VP115-20-T3 samples. Additionally, the experimental result for the isolated VP115 profiled steel decking (VP115-ISO) is also presented in Figure 6-6 above, such that the increase in capacity due to composite action can be visualized.

Significant additional stiffness is obtained by adding the CSB and FCB to the steel decking. The initial elastic stiffness at the SLS limits increased by 126.8 and 79% relative to the steel decking for the 200 and 300mm spacing configurations, respectively. The maximum load capacity increased by 290 and 190.5% respectively. Hence, there is significant structural benefit achieved by linking the different materials together. For longer spans it would also indicate the benefit of trying to achieve FCB joint continuity, as discussed in Section 6.2.2. Also, it appears that SLS requirements will often govern designs as deflections at maximum load were almost an order of magnitude greater than SLS requirements.

When considering the numerical analyses results for the VP115-20-T1 sample, implementing a connector stiffness of 3695 N/mm yielded the best results when compared to the experimental data. The model is able to predict the deflection behaviour of the VP115-20-T1 sample well up to a load of about 15 kN, where the model starts to under-predict the experimental deflection data.

When compared to the Experimental-200 Spacing data, the Full-interaction model stiffness is higher than the experimental data for the majority of the linear elastic phase, which is a good indicator that the VP115-20 SD samples do indeed exhibit partial interaction behaviour. However, the model also starts to under-predict the experimental data when a deflection of about 30 mm is reached.

Furthermore, the numerical analysis conducted with a connector stiffness of 770 N/mm, yielded results that consistently under-predict the deflection behaviour of both the VP115-20-T1 and VP115-20-T3 tested samples. Which indicates that the combined stiffness provided by the FCB and CBS connectors are higher than the assumed stiffness of 770 N/mm.

The FEM-300 spacing -3695 N/mm numerical results compare well with the VP115-20-T3 experimental results, with a difference of less than 10% for the entire duration of the analysis. The difference between the FEM-200 spacing-3695 N/mm and FEM-300 spacing-3695 N/mm is less than 2%. Hence, it appears that the overall behaviour has been captured well by the model. Factors such as strain-hardening around connectors, difference in response between the FCB and CSB, large deformations (68mm over a span of 2.4m = span/35) and localised distortion of the materials has led to the ultimate capacity for the experimental system with a 200mm connector spacing being under-predicted. However, it appears the cumulative stiffness and capacity between the 300mm spacing experimental setup and numerical models agree well in terms of predicted deflections, maximum loads and failure modes. Hence, further testing should be done to obtain more accurate load-slip behaviour for the FCB and CSB using the exact screws and sheeting to be applied in practice.

Lastly, the final stress distributions and induced connector shear forces in the horizontal longitudinal direction (z-direction) of the FEM-200 spacing-3695 N/mm analysis is depicted in Figure 6-7 and Figure 6-8 above, respectively. The stress distribution and order of failure in the model components correlated well with failure experienced by the VP115-20-T1 sample. Furthermore, the horizontal shear forces induced in the connectors are as expected, with an increase in the induced force as the distance from the applied loading is increased.

## **Chapter 7 Sandwich decking (SD) system thermal performance finite element modelling (VP50-9)**

### **7.1 Introduction**

This chapter carries out a thermal analysis of the Sandwich Decking (SD) system, using the thermal results from the Large Scale Test 2 (LST-2) in Chapter 5. The thermal model developed in this work is a representative section of the VP50-9 SD system, i.e., it has the 50mm deep steel decking profile (VP decking), with a 9 mm calcium silicate ceiling and a 9 mm fibre cement board (VP50-9). All components of the SD system have been included in the model, namely the fibre cement board (FCB), the VP50 profiled decking, the calcium silicate board (CSB) strips, and the CSB ceiling. With the heat transfer analyses performed, a better understanding of the governing parameters and governing modes of heat transfer is achieved, and thus, a more holistic understanding of the thermal response of the system. The model is compared to the average temperatures from the same thermocouple locations obtained from each group (G1 – G6) in LST-2, as detailed in Chapter 5. The model is developed in Abaqus version 6.17-1, as stated above in Section 6.1. The thermal properties of the boards implemented in this work is as detailed in Section 2.7.1 and the required thermal properties of the VP decking are assumed to be that of normal structural steel as detailed in Section 2.6.3, whilst the temperature-dependent emissivity of the VP decking was obtained from Marx (2018).

This chapter will be delivered in seven key sections as follows. Section 7.1 serves as a brief introduction to the chapter and sections that follow. Section 7.2 gives an overview of the key modelling parameters used in the numerical analysis, such that the reader may get an overview of the model parameters and setup. The section continues with a presentation of the general modelling considerations, which include details of the geometry and size of the model, mesh specifications, element type used, and the analysis procedure followed to analyse the SD system. Details of the interactions defined in the model to simulate the radiative, convective, and conductive heat transfer mechanisms are also presented. Section 7.3 presents the thermal properties implemented in the model as derived from literature. Section 7.4 presents the results of the numerical model in comparison to the experimental data. Section 7.5 concludes the chapter with a summary of the chapter layout and the main findings.

To validate the modelling procedure developed in this work a series of 5 validation studies from the literature were undertaken, three of which was also utilised by Marx (2018). The preliminary validation studies performed are as listed below, the reader is referred to each respective reference for more detail: (a) 2-D Heat transfer in a composite section with cavity radiation (Jeffers *et al.*, 2012; Wickström and Palsson, 1999); (b) Cold-formed thin-walled steel panel systems in fire (Feng *et al.*, 2003); (c) Cavity radiation modelling in a slim-floor beam system (Schaumann and Hothan, 2002); (d) 1-D Heat transfer with moisture evaporation (Jeffers *et al.*, 2012); and (e) Latent heat due to water content – a concrete block with moisture (Wickström and Palsson, 1999). Comparable results to published data was obtained. Hence, results are not presented here as they provide limited novel contribution to the dissertation. The results of the validation studies performed can be found in the online repository of this thesis (Claasen *et al.*, 2021).

## 7.2 Heat transfer model configuration

### 7.2.1 Overview

Figure 7-1 below depicts a simplified schematic of the various heat transfer mechanisms considered, as described in Chapter 2, in the model of the SD floor, with further details to be discussed in the sections that follow. The blue arrows represent the combined convective and radiative heat flux emitted onto (bottom) and from (top) the model. The convective heat transfer coefficients and emissivity values have also been indicated. A value of 0.3 has been used for the resultant emissivity of the furnace onto the ceiling to account for (a) emissivity of the furnace gases and walls, (b) emissivity of the CSB, and (c) to account for the depth of the furnace. Marx (2018) used the same value to develop the experimental numerical models detailed in Section 3.3.1, and showed the best agreement with his experimental results. Marx (2018) based this value on the research conducted by Feng *et al.* (2003), whom used the same resultant emissivity value to develop numerical models of similar sized cold-formed steel panel systems, according to Shahbazian and Wang (2013). This value is, however, lower than would typically be used but also provided the best agreement with experimental values. Due to the furnace configuration and relatively shallow depth, it is possible that the flux emitted is lower than may be experienced in deeper furnaces. The Stephan-Boltzmann constant ( $\sigma$ ) is universally defined, and the configuration factor ( $\phi$ ) is taken as 1. The red arrows represent the convective heat transfer within the cavities. The specific convective heat transfer coefficient ( $h$ ) assumed for each of the respective cavities are also indicated. The green arrows represent the cavity radiation within the model, with the defined resultant emissivity values in Table 7-1. Finally, the magenta arrows depict the conduction within the model material, where the heat diffusion equation is shown as described in Chapter 2. The thermal properties of the boards were derived from literature as described in Chapter 2 and are as listed in Table 7-2 below.

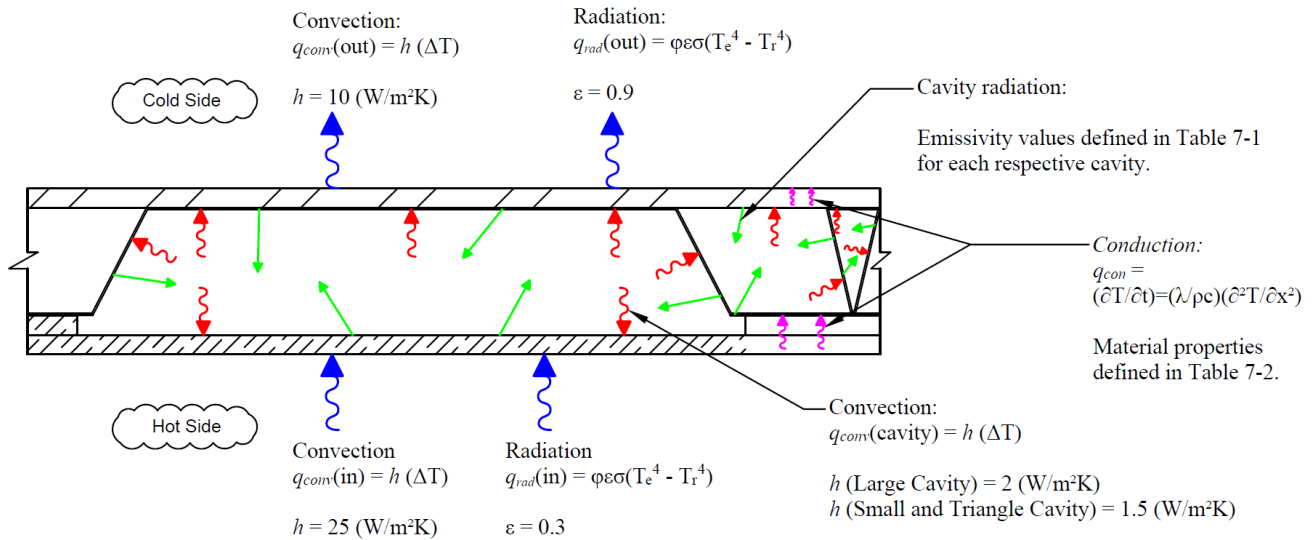
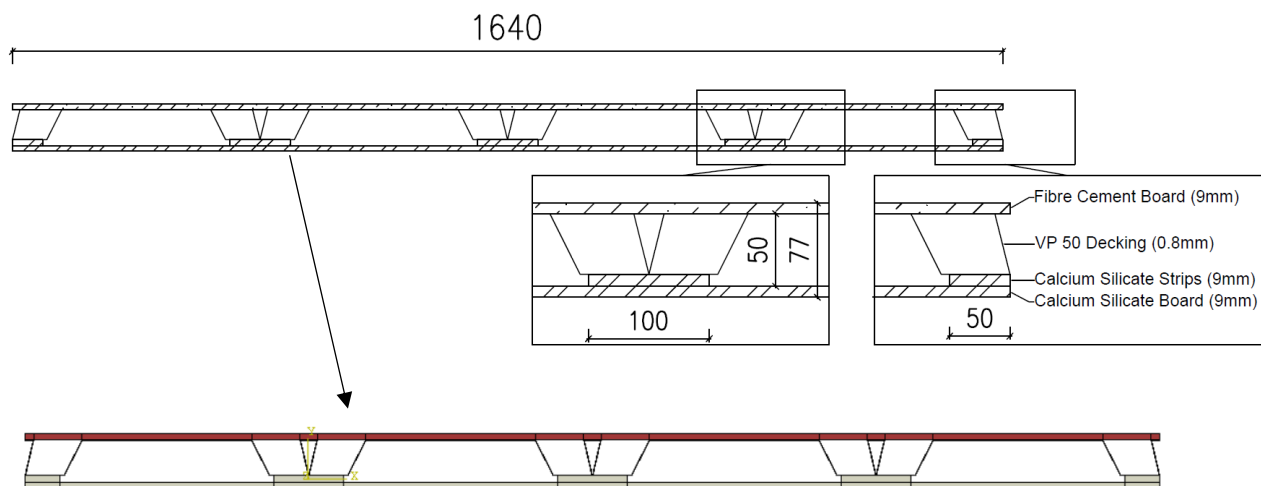


Figure 7-1: Schematic of various heat transfer mechanisms considered in FE model.

As discussed in Section 5.3.1 previously, the sandbags used to apply the loading to the structure in LST-2 were placed directly on the unexposed surface of the experimental setup boxed inside what would be considered the false flooring plenum, and covered most of the inner FCB flooring. As a result, the recorded temperatures on the unexposed surface may have been influenced by the presence of the sandbags, such that the combined radiative and convective heat from the unexposed surface was not lost to the outside/open air but conducted directly into the sandbags, potentially reducing losses. Furthermore, during the removal process of the sandbags after completion of the experiment, some of the sandbags showed evidence of being melted (i.e., bag used to hold sand melted). Hence, the sandbags may have acted as a heatsink to the unexposed surface. The sand was slightly moist, and the moisture would have absorbed energy. Hence, it is difficult to accurately define the total energy flux loss from the top surface. However, models considering convective and radiative losses in the manner described above (i.e., done as if the sandbags are not present) show good agreement with experimental data, although over-predicts the temperatures at the upper surface of the FCB floor. Hence, using the current approach the data will be more applicable to real structures in the future, and be conservative for design approaches. Thus, the modelling procedure proposed does not explicitly consider the sandbags, although the balance between radiative and convective losses appears to implicitly provide good agreement with conservative results being predicted.

### 7.2.2 Model parameters and setup

Two physical constants were assigned for the Abaqus model attributes, namely the absolute temperature ( $-273.15^\circ\text{C}$ ) and the Stefan-Boltzmann constant ( $5.67 \times 10^{-8} \text{ W/m}^2\text{K}^4$ ). Two-dimensional (2-D) shell elements were used, as discussed below, to model each of the VP-50-9 SD system components and assembled in the assembly module as depicted below in Figure 7-2. The dimensions and geometry of the model is based on a 1640 mm wide section of the VP50-9 SD system. Solid homogeneous sections were assigned to each component, where their respective material properties were assigned.



**Figure 7-2 Geometry and dimensions (mm) of the VP50-9 SD system model**

A single transient heat transfer step was used in each of the analyses, with a time period of 3960 seconds, correlating to 66 minutes (i.e. the actual run time of the furnace test). An automatic increment procedure was used, with an initial and maximum increment size of 0.01 and 5 seconds, respectively. The maximum allowable temperature and emissivity change per increment was set to 10°C and 0.1, respectively. A pre-defined temperature field was assigned to the entire model in the initial step, with a temperature of 10°C, which corresponds to the ambient temperature recorded on the day of testing (LST-2).

### 7.2.3 Mesh and mesh interactions

A medium sized mesh was used to analyse the model, with a global seed size of 5 mm for the boards and strips, and split into three elements along the height of each board and strip component, resulting in an approximate mesh size of 3 mm × 5 mm. The VP decking was analysed with a global mesh size of 1 mm × 1 mm. Figure 7-3 (Bottom) below depicts the mesh density used in this work and equates to 4594 elements. The 4-node linear heat transfer quadrilateral element type (DC2D4) was assigned to the model parts. The mesh size is based on the research conducted by Marx (2018), who used a similar mesh density (global mesh of 5 mm for the boards and 1 mm for the decking) for this configuration, and found that using a smaller mesh size had a negligible change on the results. However, the mesh size used in this study is slightly finer as the boards were split into three layers and not two as in the work conducted by Marx (2018), such that the heat transfer through the board layers can be better visualized.

Three interaction types were assigned in the thermal model, namely surface film conditions, surface radiation, and cavity radiation. The convective and radiative heat flux on the exposed side was defined with a surface film condition and surface radiation interaction, with a convective heat transfer coefficient ( $h$ ) of 25 W/m<sup>2</sup>K (BSI, 2002; Marx, 2018). The average experimental furnace time-temperature curves measured in LST-2 was used as an amplitude and assigned to each of the exposed surface interactions. Similarly, the thermal boundary condition of the unexposed side was defined by a combined radiant and convective flux, with a convective heat transfer

coefficient of  $10 \text{ W/m}^2\text{K}$  (Feng *et al.*, 2003; Marx, 2018), and an emissivity value of 0.9 (Marx, 2018), respectively.

Conduction between the interconnected layers was modelled using tie constraints. Ties equate the degrees of freedom of the surface nodes defined in the constraint, including the temperature degrees of freedom, thus allowing heat to be conducted from the one material to the next. A total of three tie constraints were defined, linking the CSB to the CSB strips, the CSB strips to the VP decking bottom trough sections, and the VP decking flute top to the FCB.

As stated above, Abaqus provides the capability to model cavity radiation between the enclosed cavity surfaces. Three types of cavities have been defined in the model, namely the “Large cavity”, the “Small cavity”, and the “Triangle cavity”, as depicted in Figure 7-3 below. Only a single value for the emissivity is specified for each defined cavity. The same emissivity values implemented in previous work (Marx, 2018) have been used in this research. Marx (2018) calculated the resultant emissivity of the CSB and the VP decking for the big cavity, and of the VP decking and the FCB for the small cavity. The resultant emissivity is calculated as described in Buchanan and Abu (2017) and Chapter 2. The emissivity of the triangle cavity is assumed to be that of the VP decking only as listed below in Table 7-1.

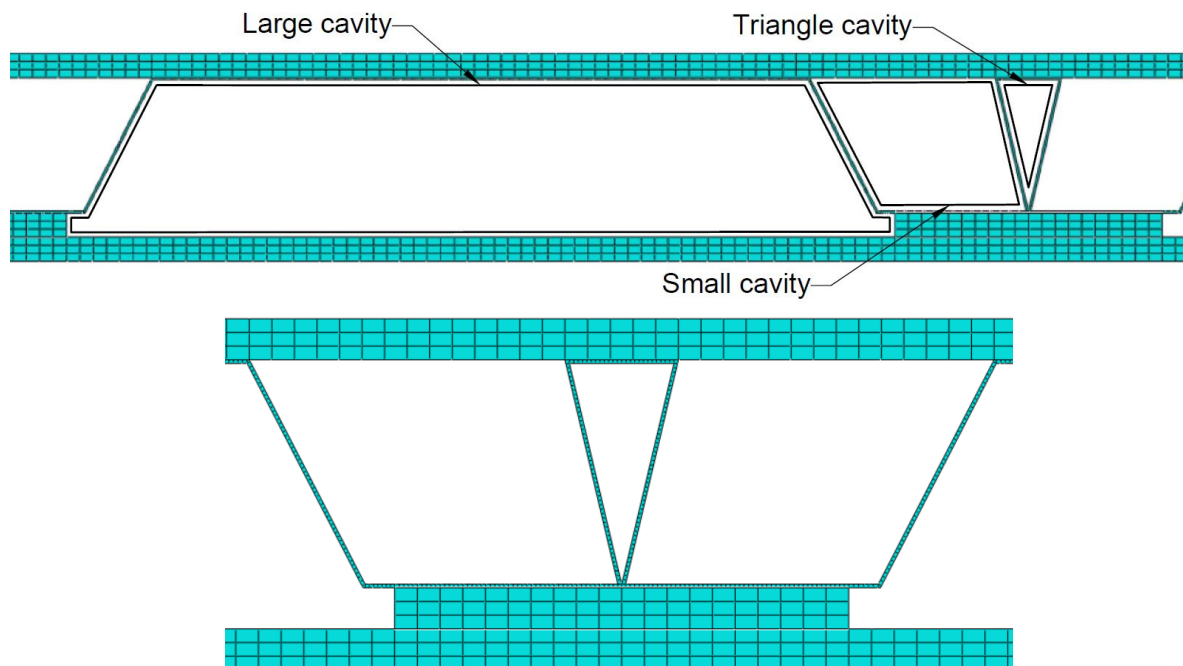


**Figure 7-3 Defined cavities (Top) and mesh densities (Bottom) in FE model**

The assumed individual and resultant emissivity values implemented in this work are listed in Table 7-1 below.

**Table 7-1 Resultant emissivity's for defined cavities.**

<b>Material</b>	<b>Emissivity</b>
<b>CSB</b>	0.8
<b>FCB</b>	0.9
<b>VP 50 Decking (Triangle Cavity)</b>	0.42 at 20 °C 0.8 at 420 °C 0.8 at 800 °C
<b>Material combinations</b>	<b>Resultant emissivity</b>
<b>CSB(e) – VP Decking(r) (Large Cavity)</b>	0.38 at 20 °C 0.67 at 420 °C 0.67 at 800 °C
<b>VP Decking (e) – FCB(r) (Small Cavity)</b>	0.40 at 20 °C 0.73 at 420 °C 0.73 at 800 °C

The same two-part heat transfer analysis procedure was followed in this work as a number of previous researchers considering similar configurations (Feng *et al.*, 2003; Jeffers *et al.*, 2012; Marx, 2018). The average cavity temperatures were obtained from the nodes depicted in Figure 7-4 below. The time-temperature curves from the first analysis were used as amplitudes to apply the convective heat transfer within the cavities as surface film conditions in the second analysis. Factors such as ventilation conditions, gas and flow properties make it difficult to measure the velocity within the furnace and the cavities of the SD system. As these parameters were unknown during testing, the exact values for the convective heat transfer coefficients could not be determined (Marx, 2018). A range (1 W/m<sup>2</sup>k to 3 W/m<sup>2</sup>K) of values were investigated in this work for the convective heat transfer coefficients used inside the cavities and are based on the relatively low values used in the previous validation studies and the work performed by Marx (2018) (Jeffers *et al.*, 2012; Marx, 2018; Wickström and Palsson, 1999). The preliminary results showed that the coefficients inside the cavities have a notable influence on the performance of the SD system. In essence, the higher the coefficient used, the more heat is transferred through the layers of the SD system as more heat is transferred within the cavities via convection. The convective heat transfer coefficient for the big cavity was set to 2 W/m<sup>2</sup>K, and 1.5 W/m<sup>2</sup>K for the small and triangle cavity as these values yielded the best results.

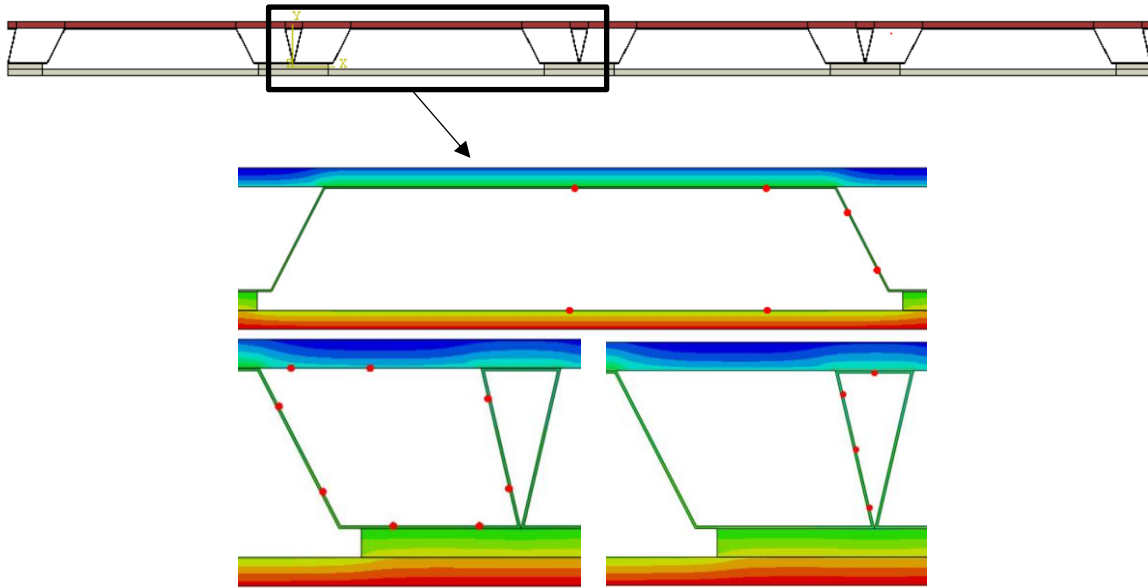


**Figure 7-4 Nodes used to save the average time-temperature histories of the respective cavities**

### 7.3 Material thermal properties

As stated by Wang (1995), it is important to have knowledge of the thermal properties of materials and their changes with temperature, as the values of these properties play a crucial role when conducting heat transfer analyses. Thus, the determination of the thermal properties implemented in this work was considered an important aspect of the study. The thermal properties of the two types of boards (FCB and CSB) used in the SD system were considered separately in the Section 2.7.1 above, where the thermal conductivity ( $\lambda$ ), specific heat capacity ( $c$ ), density ( $\rho$ ) are detailed. Finally, an emissivity value of 0.9 was assumed for the FCB on the unexposed side based on the research conducted by Marx (2018). The final thermal properties of the boards implemented in this work are listed in Table 7-2 below.

**Table 7-2 Material properties of insulation materials in FE model.**

Material Name	Density (kg/m <sup>3</sup> )	Conductivity (W/mK)	Specific Heat (J/kg °C)	Emissivity
<b>Calcium silicate board</b>	943 at 0 °C 943 at 100 °C 818 at 120 °C 818 at 800 °C	0.236 at 0 °C 0.236 at 20 °C 0.330 at 89 °C 0.323 at 179 °C 0.307 at 272 °C 0.162 at 367 °C 0.339 at 470 °C 0.339 at 800 °C	1727 at 10 °C 1727 at 90 °C 24000 at 100 °C 2600 at 110 °C 906 at 400 °C 906 at 800 °C	0.3
<b>Fibre cement board</b>	1250	0.25	2777 at 0 °C 2777 at 90 °C 37000 at 100 °C 4500 at 110 °C 2500 at 400 °C 2500 at 800 °C	0.9

### 7.4 Results and analysis

This section discusses the predicted and experimental temperatures obtained for the SD system. The temperature point selected from the FEM model corresponds to the temperature locations measured in the experiment. The T-FCT (unexposed surface temperature at the trough area) experimental data was compared to that of the average temperatures obtained from the node locations depicted in Figure 7-5 (Top) below. The various final temperature distributions can also be seen in Figure 7-5 (Bottom) below.

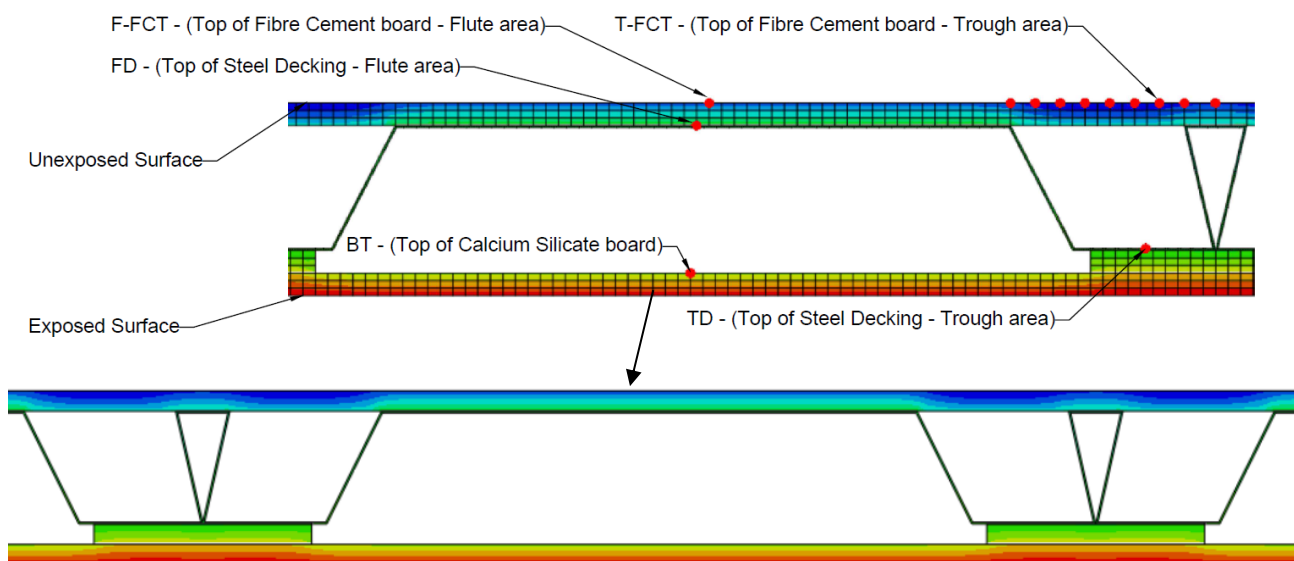


**Figure 7-5 Node locations used to obtain final predicted temperatures and final predicted temperature profile.**

Figure 7-6 below depicts the average temperatures from the same locations of each group (G1-G6) collected from the VP50-9 SD system tested in LST-2, which includes error bars such that the range of experimental data can be visualized, and compared to the FEM analysis results. Overall trends are captured well and there is good agreement between the results, especially in the lower sections of the system. Upper temperatures are slightly over-predicted, especially after 40 minutes. As discussed above, this is likely influenced by the presence of the sandbags whose moisture content might have influenced results.

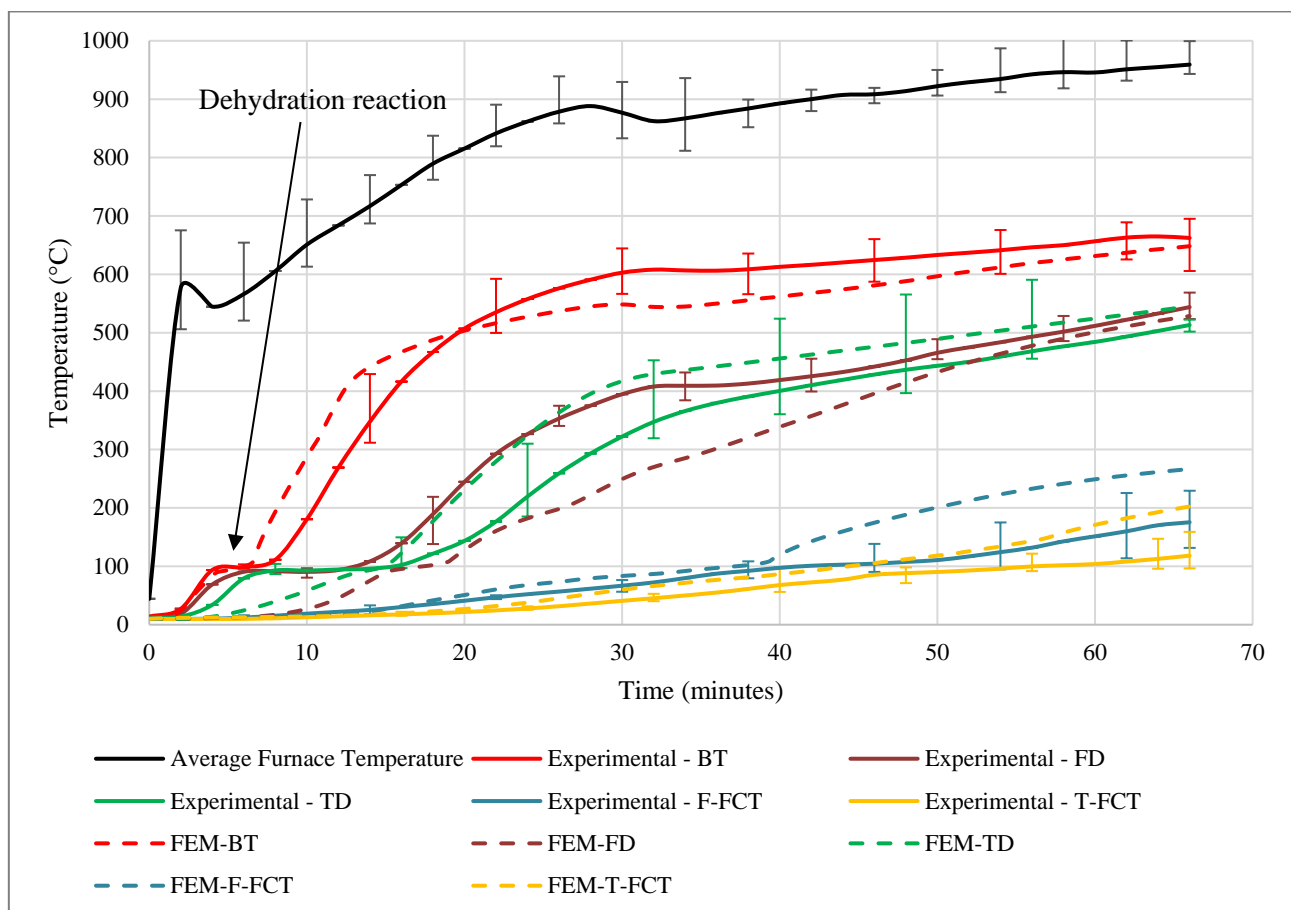


**Figure 7-6 Finite Element Model results compared to the experimental average group temperatures from the same thermocouple locations**

The model was able to predict the temperature evolution of the top of the ceiling board (BT) location to a reasonable degree, as shown by the results presented above, with an error difference of less than 10.5% from the 20<sup>th</sup> minute to the end of the test, and an error difference of only 2.1% in the final temperature. However, the model slightly under-predicts the dehydration reaction period that occurred in the calcium silicate boards in the experiment. When comparing the assumed temperature intervals of 90°C to 110°C at this location, the experimental data experienced a longer dehydration period of about 4.3 minutes, from 3.6 to 8 minutes into the test. The dehydration period predicted by the model only lasts about 2.2 minutes, from 4.3 to 6.6 minutes into the model analysis. After the dehydration period is completed, the model tends to over-predict the temperature evolution of the calcium silicate board. However, the rise in temperature is consistent to the rise in temperature of the experimental data, which is a result of the assumed gradual decrease in the specific heat capacity from a

temperature of 110 °C to 400 °C of the calcium silicate board as detailed above. This continues until a temperature of about 500 °C is reached where the model starts to under predict the experimental data at about the 19-minute mark.

When considering the top of the steel decking at the trough (TD) and flute (FD) temperature locations, there is a noticeable difference in the behaviour of the model and the experimental data. The predicted temperature evolution has a slower increase in temperature during the start of the analysis for the TD location, and consistently under-predicts the temperature evolution at the FD location. The error difference is especially evident for the FD location. This behaviour also occurred in the heat transfer models developed by Marx (2018) and is not well understood. However as stated by Marx (2018), it is possible that the increase in temperature of the bottom part of the VP decking could have caused the steel profile to experience thermal bowing, resulting in small openings being formed between the interconnected sheets, thereby allowing more heat to be transferred to the upper layers through convection and radiation for the FD location in the actual experiment. Furthermore, when considering the temperature evolution after the 15<sup>th</sup> minute mark, the model over-predicts the recorded temperatures for the TD location, while under-predicting the recorded temperatures at the FD location. However, when compared to the experimental data, the model temperatures at these two locations converge to similar final temperatures, with an error difference of 6.2 % and 2.8 % for the FD and TD locations, respectively.

When considering the unexposed surface temperatures at the top of the FCB at the trough (F-FCT) location, the model was able to predict the recorded temperatures well up until the 40<sup>th</sup> minute mark, where the predicted temperatures start to increase at a more rapid rate and diverge from the experimental data. This discrepancy is also not well understood and may be attributed to many factors, including the lack of material data on the FCB and the presence of sandbags on top of the FCB in the experimental setup, which could have acted as a heat sink, thus lowering the temperatures measured in the experiment as discussed above. The error difference in the final temperatures predicted at this location is 52%. Similarly to the F-FCT location, the model was able to predict the temperature evolution of the top of the FCB at the trough (T-FCT) location well up until about the 50<sup>th</sup> minute into the analysis, where the model temperatures also start to increase at a more rapid rate. The error difference in the final temperatures predicted is 71% with a temperature difference of 84°C. Furthermore, the numerical model also indicates that the main mechanism of heat transfer within the SD system is via cavity radiation in the flute area, as the unexposed temperatures of the flute section are higher than that of the trough section, similar to the results recorded in LST-2. Lastly, when comparing the unexposed surface numerical results to the FLS average and single point limit temperatures of 145 °C and 189.9 °C, respectively, the FEM-T-FCT and FEM-F-FCT temperatures surpass both the average and single point temperatures at the 56<sup>th</sup> and 63<sup>rd</sup> minute mark, and at the 42<sup>nd</sup> and 48<sup>th</sup> minute mark, respectively. Thus, the estimated fire resistance rating for the VP50-9 SD system calculated by the model is 42 minutes.

## 7.5 Conclusions

This chapter has presented a thermal model of the VP50-9 SD system. The average time-temperature data captured in LST-2 for the trafficable SD system attached to the experimental frame was used to validate and calibrate the model. Predicted results typically compare well with experimental values, although above the upper FCB predicted temperatures are higher than those recorded. This may have been influenced by a number of factors, including the presence of the sandbags, whose behaviour is difficult to capture. However, for engineering design consideration the over-prediction will typically result in safer calculations, and also be more consistent with the way the structure is used in real-life, where the floor plenum is open and there are not insulation layers on top of the FCB. The predicted temperature for the inner cavity location of the SD system (TD and FD) were under-predicted for the majority of the analysis, but converge to similar final temperature as recorded in the experiment, with error differences of 6.2 % and 2.8 % for the FD and TD locations, respectively. Furthermore, it can be concluded from the numerical data that the main mechanism of heat transfer within the SD system is via cavity radiation in the flute area, as in the experimental setup. Finally, the FEM-T-FCT and FEM-F-FCT surpassed the limiting FLS average and single point temperatures at the 56<sup>th</sup> and 63<sup>rd</sup> minute mark, and at the 42<sup>nd</sup> and 48<sup>th</sup> minute mark, respectively.

The data presented in this chapter was obtained from a unique large-scale experimental setup with a novel structural system with results that are unusual both in their physical size, and in being applied to a non-composite cellular beam system. Hence, the data obtained from LST-2 and the numerical model will add to the empirical evidence in literature that lack systematic research. There are few studies which consider the heat transfer through systems such as the SD system (PSSDB systems) proposed in this work, however, there have been studies performed on light-gauge steel systems lined with insulating materials as stated in Section 2.7.1 above.

The most notable conclusions that can be drawn from this chapter is: (1) the numerical model was able to predict the overall thermal behaviour of the SD system fairly well. (2) The sandbags used to load the structure in LST-2 seems to have had a notable effect on the final temperatures captured on the unexposed surfaces. (3) There is a notable difference in the results between the numerical model and the experimental data when considering the TD and FD locations measured. However, possible reasons for the difference have been provided above. (4) It can be concluded that the main mechanism of heat transfer through the system is via cavity radiation, which is in line with the findings provided by Marx (2018). (5) When considering the numerical model, the estimated fire rating of the VP50-9 SD system is 42 minutes.

## Chapter 8 Structural models of the experimental steel frame (LST-2)

### 8.1 Introduction

This chapter details the development of numerical models to predict the elevated temperature structural response of the steel members tested in large-scale test 2 (LST-2). Both single element models and a full global structural model are developed. The single element models were developed to predict the thermo-mechanical response of the main cellular beams (CB 1 and CB 2) and secondary parallel channel beams (PC 1 and PC 2) in isolation. Single element models are not developed for the edge primary beams (PB 1 and PB 2) that support the cellular beams, and the four support columns, as they experience very low deformations, as will be shown by the global model. By comparing single element models to the global model, the extent to which interactions between beams influences structural behaviour can be studied. Since a number of the members are not symmetric (e.g. channels) and unusual connection details (e.g. with flange cut-outs) are present, as shown in Chapter 3, the torsional response of the structure and expansion of beams is important. The models were developed in Abaqus version 6.17-1, as stated above in Section 6.1.

A total of four single element thermo-mechanical response analyses were conducted, two for each of the single element models (i.e. PC 1, PC 2, CB 1 and CB 2). The global structural model includes all the horizontal structural members and the four columns. The models were loaded as in the experimental setup and exposed to the actual time-temperature curves recorded for each respective structural member in LST-2, as detailed in Section 5.3.3 above.

This chapter is divided into five sections. This section (Section 8.1), serves as a brief introduction to the sections that follow. The second section (Section 8.2) details the common parameters and modelling considerations of both the single element and global structural numerical scenarios. The following two sections (Section 8.3 and Section 8.4), detail the development of the single element models and the global structural model, respectively. The final section (Section 8.5), presents the results of the single element numerical scenarios and the global structural scenario in comparison to each other, and to that of the experimental results.

## 8.2 Common modelling parameters

The following section details the shared parameters and modelling considerations for the numerical models developed. The general modelling procedure used to analyse the single element and global structural models are detailed first. Next, the shared material properties of the models are presented. Following that, the assumed structural loads applied to the respective models are discussed. Finally, the final temperatures (at 66 minutes mark) recorded for the horizontal beams in LST-2 are presented in Table 8-2 below. This will help serve as a reminder of the temperature ranges applied to the elements and serve as a guide as to how the temperatures were applied in each of the respective models. Further details on the application of the thermal loads are discussed in Sections 8.3.3 and 8.4.4 below for the single element models and the global model, respectively.

### 8.2.1 General solution procedure

The same three-step analysis procedure adopted in Kloos (2017) has been implemented in this work for all the model analyses. The solution procedure is as follows: Step-1 (initial step) in which all the boundary conditions of the model are applied and propagated; Step-2 (mechanical-step) in which all the mechanical loads are applied to the model; and Step-3 (thermal-step) in which the time-temperature curves measured of the structural elements in LST-2 are applied as predefined fields to the respective beams over a normalized time period. Both the second and third steps were solved using the “general static” algorithm solution. The automatic time increment procedure was used in both the mechanical and thermal steps of the models, with a set maximum increment of 0.1 and 0.005, respectively, and a step time of 1. Furthermore, as the beam sections are expected to undergo large deflections in the simulations, non-linear geometric effects were also considered (Dassault Systemes, 2016).

Four-node shell elements with reduced integration and hourglass control (S4R) were assigned to both the single element and global structural models. Previous studies have utilized the same element type to investigate the deflection behaviour of beam sections at elevated temperatures using numerical modelling (Najafi and Wang, 2017; Wang *et al.*, 2014).

### 8.2.2 Material properties

The reduced material properties of the steel at elevated temperatures were calculated according to the EN formulations as detailed in Section 2.6.3 for both the yield strength and Young’s modulus. The yield strength of the steel was calculated with an initial ambient yield strength value of 408 MPa. Figure 8-1 below depicts the yield stress-strain curves implemented in this work for a temperature range of up to 1200 °C. A constant value of  $1.4 \times 10^{-5}$  was used for the coefficient of thermal expansion, which is based on the research conducted by Kloos (2017). The Young’s modulus used for all steelwork is 200 GPa. The density of steel was taken as 7850 kg/m<sup>3</sup> for all models.

The sandwich decking (SD) flooring system is important for providing lateral stability to the members to which it is connected through diaphragm action. Steel links were implemented in the global structural model to simulate this lateral rigidity provided as detailed in Section 8.4 below. The ambient VP50/115 profiled steel decking yield stress (297 MPa) and young's modulus, as described in Section 4.2.1, was used as the input material properties of the steel links. If the structure had experienced much larger deformations, it could have caused slippage between the SD floor and plates upon which it was supported, which would lead to the assumed connectivity needing to be adjusted to suit such behaviour, as lateral support would have been influenced.

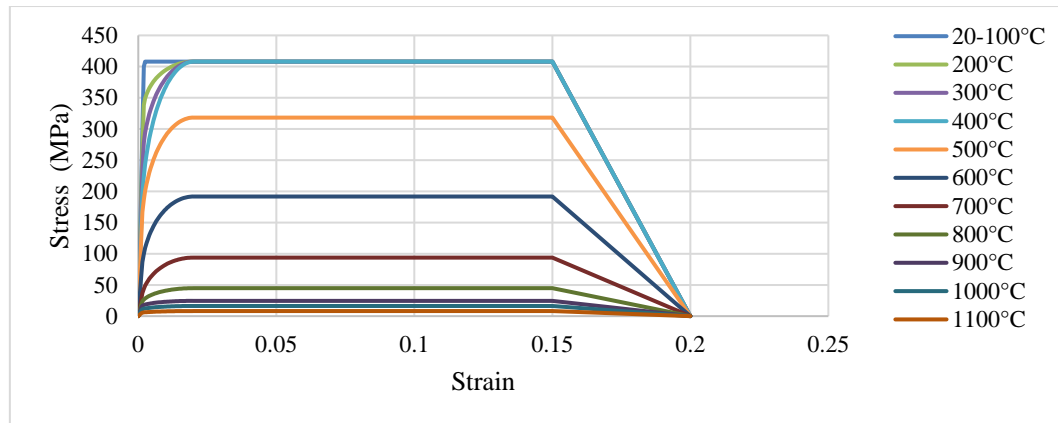


**Figure 8-1 Yield stress of steel at elevated temperatures**

### 8.2.3 Structural loading

The structural load-path behaviour of the experimental frame tested in LST-2 is as depicted below in Figure 8-2. Due to the corrugated nature of the VP decking, the majority of the uniformly distributed load on the three bays is transmitted in a single direction, i.e., along the y-axis. Thus, the loads for each of the beams were calculated based on the assumption of one-way loading, as indicated by the green arrows. The portion of the uniformly distributed load area transmitted to PC 1 is as indicated in orange on Figure 8-2, which corresponds to half of the uniformly distributed load from Bay-A and Bay-B. Due to the symmetrical shape of the structure, the same load can be expected on PC 2. The loads are then carried from the parallel channel beams to the cellular beams and delivered as point loads at the connection points, as indicated by the blue arrows. Finally, the loads are then carried by the cellular beams to the primary (PB 1 and PB 2) beams, which in turn transfers the load to the columns attached to the primary beams, as indicated by the red arrows.

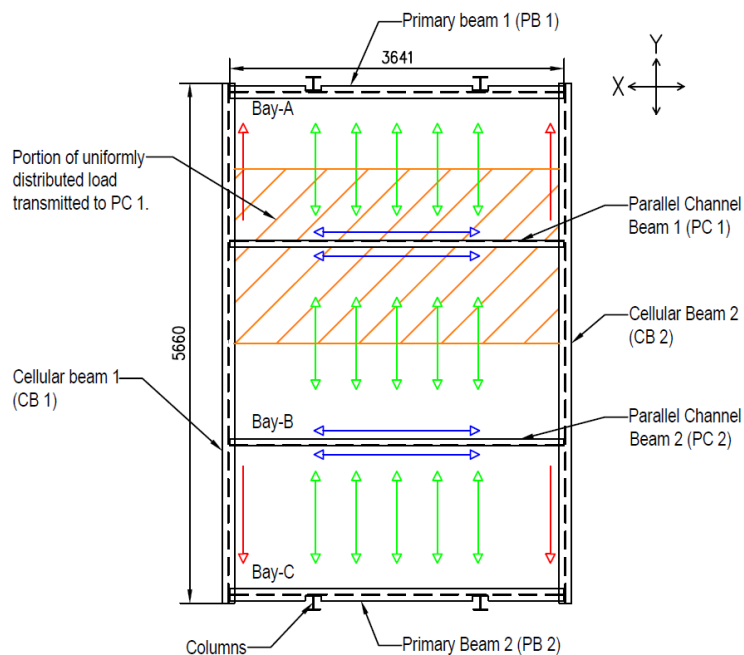


**Figure 8-2 LST-2 experimental frame structural load path.**

The uniformly distributed load was calculated based on the applied loading of the sandbags plus the weight of the VP50-9 SD system. The self-weight of the steel sections were also considered in each respective numerical scenario. The loads used to calculate the applied loads for each respective model are as listed below in Table 8-1. The full set of calculations and assumptions can be found in the online repository (Claasen *et al.*, 2021).

**Table 8-1 Loads used to calculate the applied loads in the models.**

<b>Dead load</b>		
<b>FCB</b>	0.125	kPa
<b>CSB</b>	0.086	kPa
<b>VP50 Decking (per sheet)</b>	0.089	kPa
<b>Primary Beam self-weight (PB 1 and PB 2)</b>	0.245	kN/m
<b>Cellular beam self-weight (CB 1 and CB 2)</b>	0.245	kN/m
<b>Parallel channel beam self-weight (PC 1 and PC 2)</b>	0.207	kN/m
<b>Live load (i.e., sandbags load)</b>		
<b>Calculated uniformly distributed live load</b>	1.56	kPa

### 8.2.4 Final temperatures measured in LST-2

Table 8-2 below presents the final recorded temperatures for each of the horizontal beam sections in LST-2. Additionally, the final average temperatures for the primary beams are also presented. Locations where experimental data was recorded are shown below (i.e., sections A-F)

**Table 8-2 Experimental temperature at 66 minutes. (N/A refers to thermocouples that malfunctioned during the experiment)**

	Experimental temperature (°C)									
	Section	PC 1	PC 2	Section	CB 1	CB 2	PB 1	PB 2	PB 1 Averages	PB 2 Averages
Top flange	A	130	251	D	142	169	212	272	211	241
	A/B	356	216							
	B	583	181	E	186	167	218	221		
	B/C	353	155							
	C	123	129	F	230	165	203	230		
Web	A	173	204	D	185	285	244	325	244	281
	A/B	377	175							
	B	580	146	E	256	258	247	253		
	B/C	376	164							
	C	172	181	F	328	231	242	266		
Bottom flange	A	263	282	D	482	585	328	N/A	321	328
	A/B	426	324							
	B	589	366	E	501	540	313	328		
	B/C	461	428							
	C	333	491	F	724	495	324	N/A		

### 8.3 Single element models

The following section details the development of the single element models for the parallel channels (PC 1 and PC 2) and the cellular beams (CB 1 and CB 2). As noted above, the primary beams (PB 1 and PB 2) and support columns experienced negligible vertical deformations and will be considered in the global model below only. This section covers the geometry and mesh densities used in each numerical scenario. Following that, the structural loading and boundary conditions for each of the scenarios are discussed. Finally, the applied thermal loading to the models are detailed.

### 8.3.1 Geometry and mesh

The single element models developed for the cellular (285×133/133×25 CB) and parallel channel (PC 180×70) beams include the beam connections as in the experimental setup. Hence, the model of the cellular beams includes the fin plate and double angle cleat connection parts, whilst the parallel channel models include the fin plate connection parts. The parts were modelled using three-dimensional (3-D) deformable shell elements as discussed above. Figure 8-3 and Figure 8-4 below depict the geometries of the parallel channel and cellular beam models, respectively. In the interest of clarity, the different parts of the models are represented with different colours, with the beam flanges in blue, the beam webs in red, the fin plate connections in green and the double angle cleat connections in dark grey. The dimensions and thickness of the beam sections, and connections, can be found in the online repository (Claasen *et al.*, 2021). The fin plate connection to the PC beams was implemented by assigning the combined thickness of the beam web and the fin plate to that respective section (green section).

A global seed size of 15 mm was assigned to the parallel channel beam model, resulting in the mesh density depicted in Figure 8-3 below. There are 4860 elements in the channel model. A global seed size of 15 mm was also assigned to the cellular beam model. However, 10 mm edge seeds were assigned to the connection parts of the model due to the high concentrated stresses induced from the concentrated applied loading (i.e., concentrated point loads). This global and edge seed formulation resulted in 12 829 elements used to analyse the cellular beam model, with an element distribution as depicted in Figure 8-4 below. The asymmetry in element distribution along the top flange of the cellular beam is caused by the attachment of the fin plate connections to the top flange (i.e., the top part of the fin plate is connected to the bottom side of the top flange) and their dissimilar mesh densities, resulting in more elements (7) on the side where the fin plate connections are attached. The bottom flange had a symmetrical element distribution, with the same number of elements on both sides of the beam web, totalling to eight elements across the width of the flange (i.e., four elements on each side of the beam web). The mesh densities were based on the convergence study conducted by Kloos (2017), whom used a global seed size of 25 mm in all the models, and found that using a finer mesh size resulted in a negligible change in the final results.

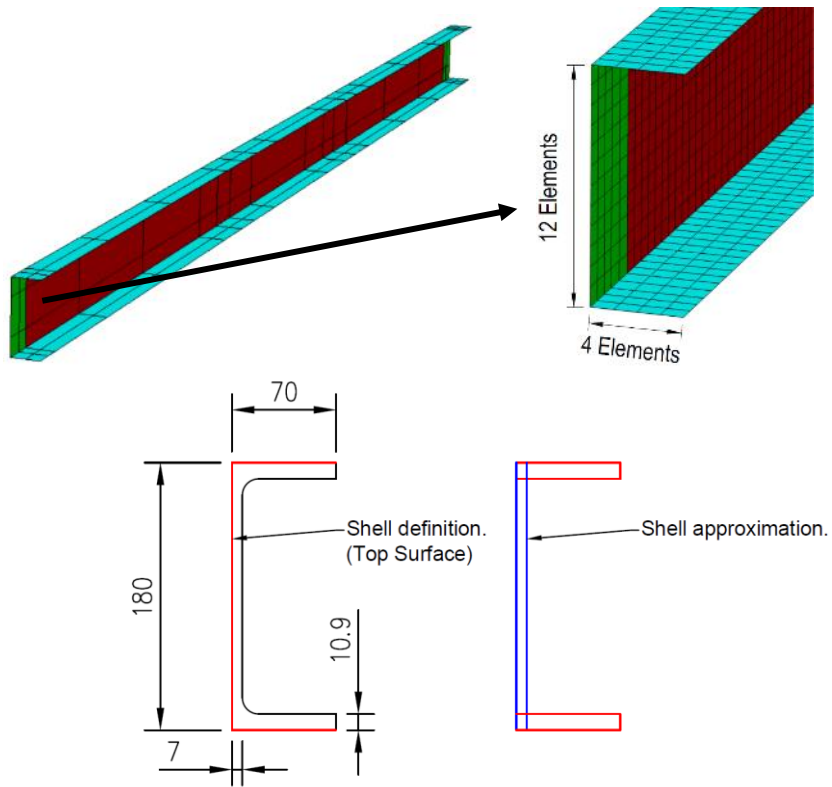


Figure 8-3 Geometry and mesh density of Parallel Channel beam model.

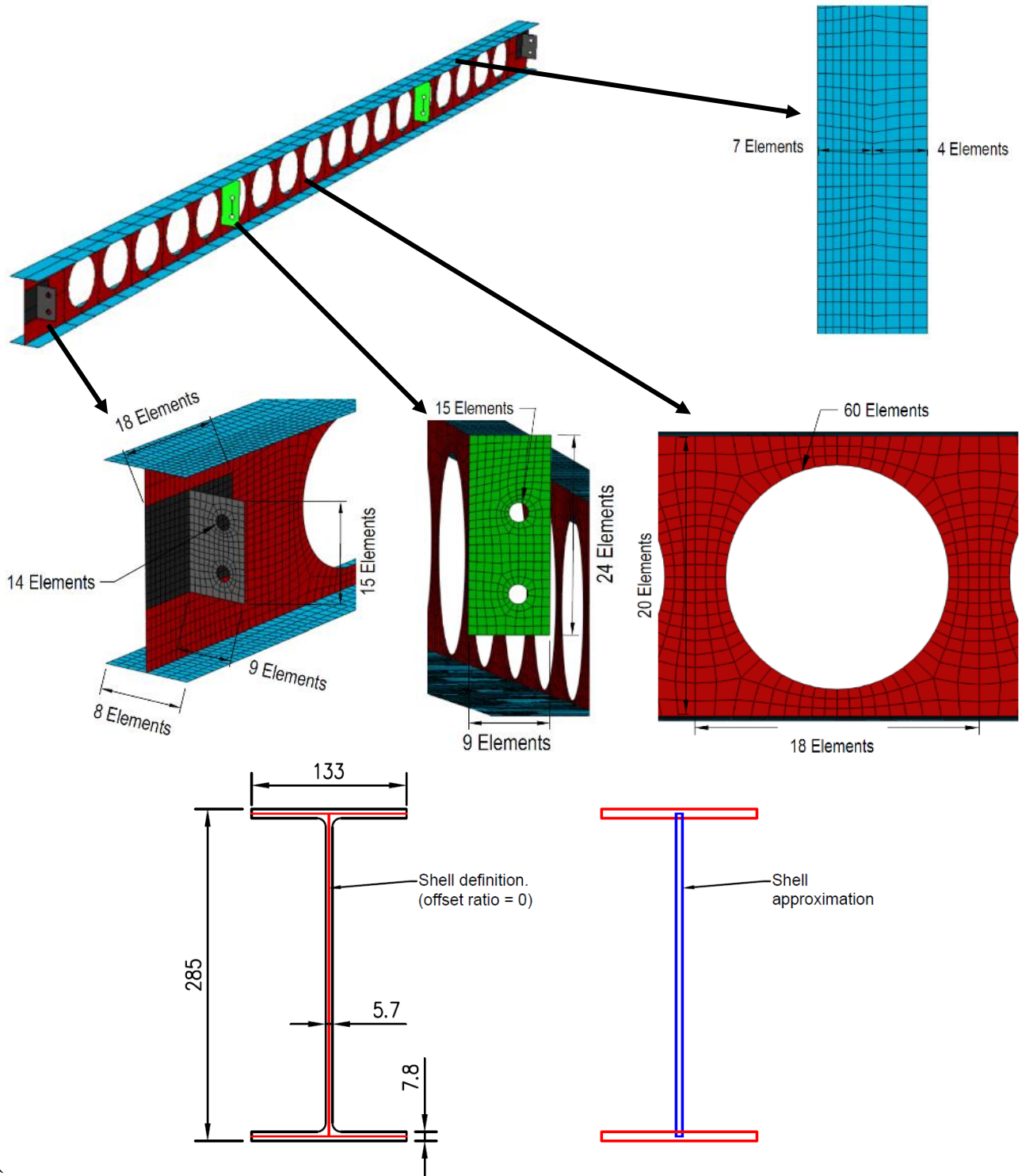


Figure 8-4 Geometry and mesh density of the Cellular beam model.

### 8.3.2 Structural loading and boundary conditions

Each of the single element models are considered separately in the subsections that follow, starting with the parallel channel beam model and followed by the cellular beam model. The loads were applied in the second step (mechanical step) of the analysis and propagated until the end of the analysis.

#### **Parallel channel model loads and boundary conditions**

Figure 8-5 below depicts the structural loading and boundary conditions specified for the parallel channel beam models. A uniformly distributed line load of 3.67kN/m was applied to each of the parallel channel beam model analyses, which includes the self-weight of the beam. This was accomplished by applying concentrated point loads to the nodes along the entire length of the bottom flange of the beams. The boundary conditions due to end supports were specified at the centre of the beam web height and spaced at 45 mm from the beam edge. This location corresponds to the mid-point between the two bolts used to connect the parallel channels to the cellular beams. A coupling constraint was applied to the line of action connecting the bolt hole centres, as depicted in Figure 8-5, with the boundary conditions applied to the control points. Coupling constraints link the nodes of a slave surface to the motion of a control reference point (Dassault Systemes, 2016).

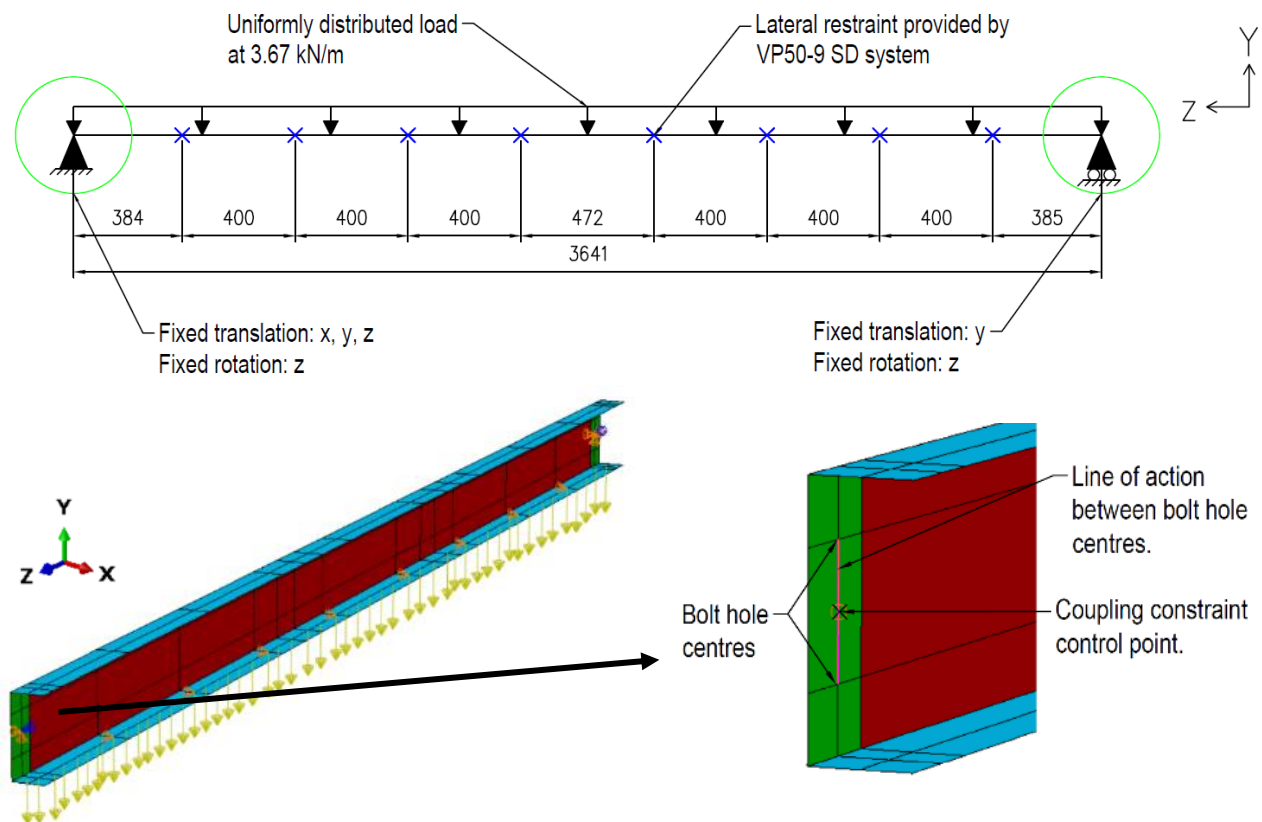


**Figure 8-5 Parallel channel beam model loads and boundary conditions**

Thus, a single boundary condition was defined to emulate the fin plate connection of the PC beams to the cellular beams at each connection point. The boundary conditions of the overall beam were assumed to be pinned-roller, but with the torsional rotation about the longitudinal axis restrained for all the PC beam models as indicated on Figure 8-5 above. This boundary condition was chosen based on the connection type (fin plate) used in the experimental setup and the low minor axis stiffness of support beams, allowing thermal expansion. Due to the lateral restraint provided by the VP50-9 SD system to the channel and primary beams, eight lateral restraints were defined at the locations depicted above in Figure 8-5. The dimensions of the lateral restraints correspond to the hanger bolt connection points of the channel beams to the VP50-9 SD system.

Since the channel beams deflect in relation to the cellular beams (i.e. they move downward as the CBs deflect), the deflection results obtained from the single element cellular beam model analyses were saved as amplitudes and applied to the end boundary conditions of the parallel channel models in the second (thermal) analysis step. This eliminates the need to do post-processing, and means that outputs are directly comparable to the experimental results.

### ***Cellular beam structural loads and boundary conditions***

Figure 8-6 below depicts the structural loading and boundary conditions specified for the cellular beam models. The loads transferred from the parallel flanged channel beams to the cellular beams were applied as concentrated point loads at the connection points of the cellular beam model. The point loads, of 6.73 kN, were applied at the centre point of the line of action connecting the bolt hole centres of the fin plates as shown in Figure 8-6 below. However, no coupling constraints were used in these connections as in the PC beam model analyses, with the load applied to a single node only at this location. The self-weight of the beam was applied separately as a distributed line load by defining concentrated point loads along 37 nodes of the cellular beam. The end boundary conditions of the cellular beams were defined at the centre points of each of the angle bolt hole centres. This was achieved by using coupling constraints to constrain the circumference of the bolt holes to the centres of the bolt holes. The boundary conditions were then specified at the control points of the coupling constraint at each bolt hole centre. A pinned-roller connection type was assumed for the end boundary conditions of the cellular beams with the torsional rotation fixed as well. It was assumed in the single element model of the cellular beams that the parallel channels provide full lateral stability to the cellular beams at the points of connection. However, this is not a perfect representation as the parallel channel beams may also expand and contract due to thermal elongation or buckling, thus pushing the cellular beams laterally out or pulling it inwards. This behaviour is further investigated in the global structural model. Thus, lateral restraints were also defined at the fin plate connections of the cellular beams, with the lateral restraint points applied at the same node locations as the single concentrated point loads. However, in a real-world version of the CBS that is many bays wide the lateral support provided to cellular beams is likely to be ensured due to the global structural restraint provided.

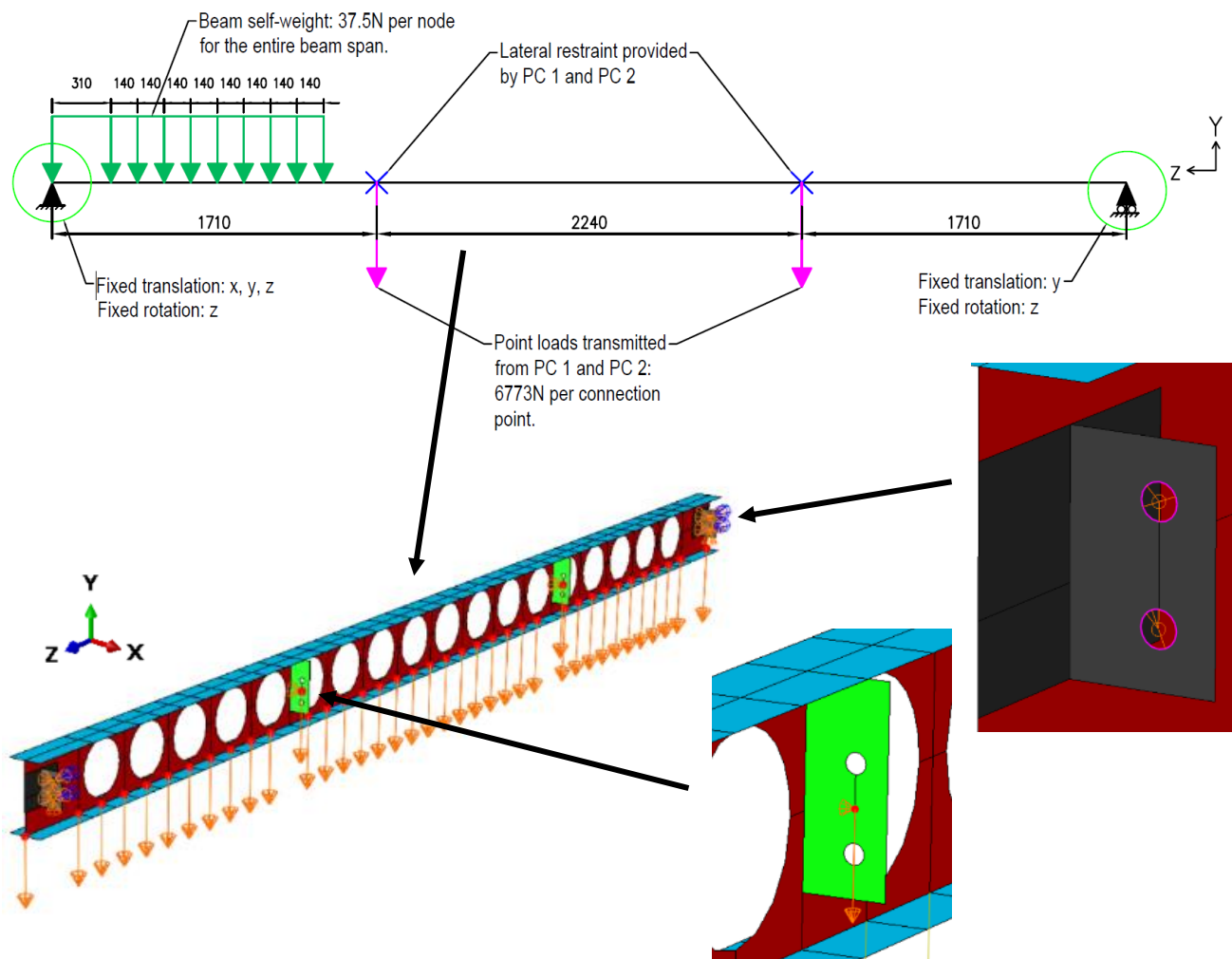
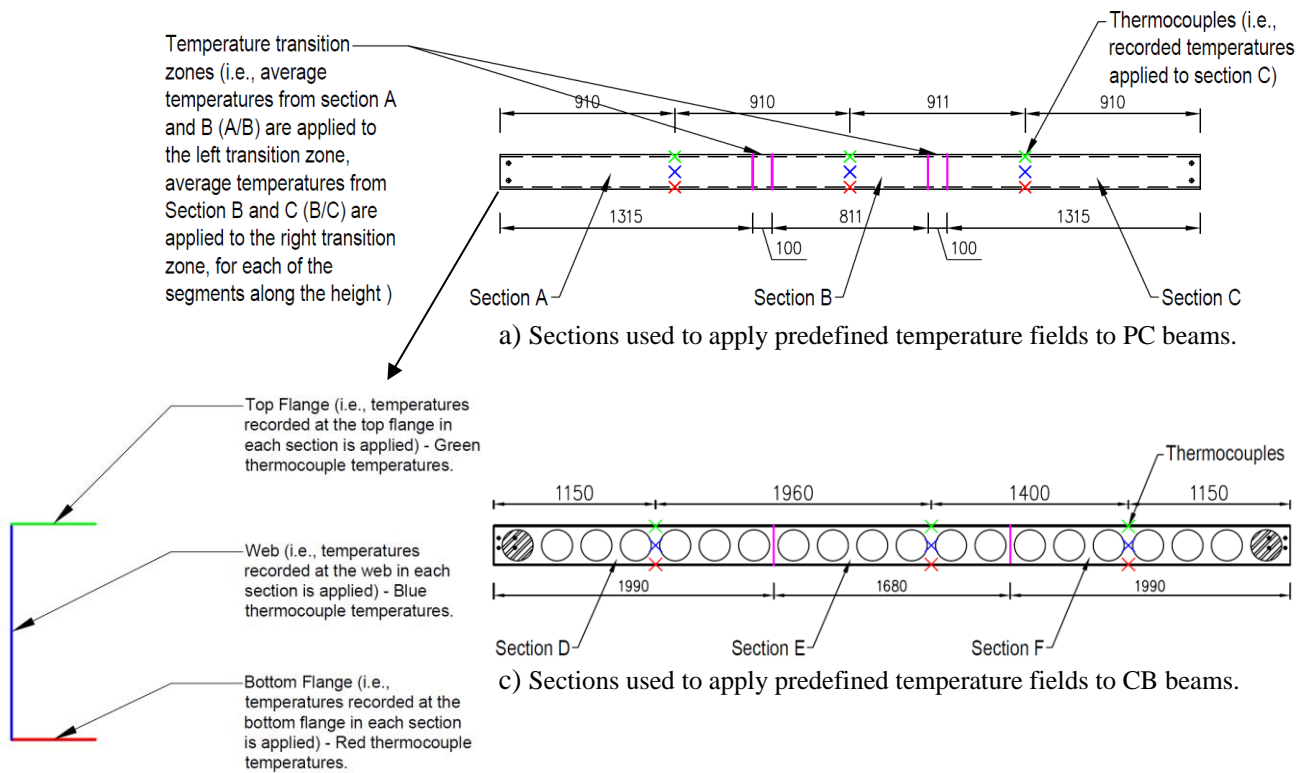


**Figure 8-6 Cellular beam model loads and boundary conditions.**

### 8.3.3 Thermal loading

The time-temperature curves recorded during LST-2 for the cellular and channel beams were saved as amplitudes for each respective model, which are provided in Figure 5-32 to Figure 5-34, for CB 1, PC 1, and PB 1, respectively. For the full set of time-temperature curves, the reader is referred to the online repository (Claasen *et al.*, 2021). The thermal loading was then applied to each model as a predefined field. Each model was split into three sections down the length of the beam based on the thermocouple locations as shown below in Figure 8-7 (a and b), for the PC (PC 1 and PC 2) and CB (CB 1 and CB 2) beams, respectively. Thus, the temperatures measured within each respective section could then be applied accordingly. Temperature measurements were also taken over the height of the beam sections in LST-2, thus, a total of three predefined fields were assigned to each of the sections along the beam height, which includes the bottom flange, the web, and the top flange of the beam section as shown by example in Figure 8-7 (b), for the PC beams.

During the preliminary stages of modelling, convergence issues were encountered in the PC beam models (but not the CB models) due to high temperature gradients between the defined sections down the length of the beam. Localised variations in thermal exposure during the experiment seem to have caused them. To overcome this issue, 100 mm temperature transition zones were implemented into the model as indicated on Figure 8-7 (a) below. The average temperatures between each of the sections were then applied in the transition zones between the two respective sections, for example, the average temperatures of section A and B were applied in the transition zone between section A and B. This allows for a more gradual temperature difference between the sections. Thus, a total of 15 predefined temperature fields were applied in the PC beam model analyses and a total of 9 predefined fields applied in the cellular beam model analyses. The thermal loads of the beams were applied in the third and final step (thermal step) of the analysis. Table 8-2 above contains a list of temperatures of the beams at 66 minutes, as a summary of typical values applied.



b) Segments of PC beams to apply the predefined temperatures along the height of the beam.

**Figure 8-7 Sections used to apply thermal loading to the parallel channel beam (Top) and cellular beam (Bottom-Right) models. Segments used to apply the temperatures along the beam height in each section as shown by example for the PC beams (Bottom-Left)**

## 8.4 Global structure model

The following section details the development of the global structural model. The sections are presented in a similar fashion as with the single element models. Firstly, the geometry and mesh of the model are discussed. Next, the assumed structural loading applied to the structure is detailed. Following that, a brief discussion on the use of coupling constraints to model the connections between the model parts is presented. The final section provides detail pertaining to the thermal loading applied to the structural elements.

### 8.4.1 Geometry and mesh

The geometry of the global structural model is based on the drawings supplied in the online repository (Claasen *et al.*, 2021) of the experimental frame tested in LST-2 and comprise the horizontal structural members and columns. To emulate the lateral rigidity provided by the VP50-9 SD system to the experimental frame, 30 mm × 30 mm steel links have also been included in the model. The size of the steel links approximates the area of the steel decking, FCB and CSB combined. Simulation results are not highly sensitive to the size of the link.

The geometry of the model is as depicted in Figure 8-9 below, along with the structural loading and boundary conditions. The parts created in the single element PC and CB beam models were imported and reused in the global model, whilst the remaining parts were created individually and used to assemble the global model in the assembly module. Three-dimensional wire elements were used to create the column and link parts, with their respective profile geometries assigned in the property module. The H-section 152 × 152 × 23 UB specifications were assigned to the column profile, while a square profile was assigned to the steel link profile. Three-dimensional shell elements were used to model the rest of the parts as in the single element models.

The connection parts used in the experimental setup have been included in the global structural model in an analogous manner as in the single element models. This was achieved by specifying the combined thicknesses of the connection part and beam section wherever the connection parts are parallel with the beam sections. This is illustrated below in Figure 8-8, where the double angle cleat connections have been defined in the model by combining the thicknesses of the parallel part of the connection to the cellular and primary beams, respectively. Implementation of the end-plate connections used to connect the primary beams to the columns are also depicted in Figure 8-8 below. Consequently, the fin plate connections are only defined in the channel beam parts.

Quadrilateral 4-node S4R shell elements were defined for the horizontal structural members as in the single element models, and 2-node linear beam elements defined for the column and link wire parts. A global seed size of 15 mm was defined for all the horizontal structural members and a seed size of 10 mm defined for the columns and links, resulting in a total of 44 282 elements used in the global model analysis.

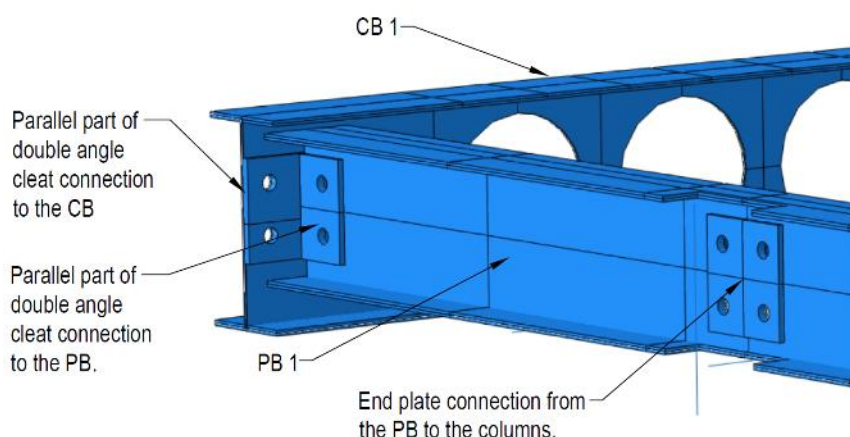


**Figure 8-8 Implementation of connection parts in global structural model.**

#### 8.4.2 Structural loading and boundary conditions

An approximate total load of 42 kN was applied to the global structural model. About 64% (13.5 kN per beam) of the total load was applied to the channel beams (PC 1 and PC 2) and 29.3% (6.17 kN per beam) of the total load was applied to the primary beams (PB 1 and PB 2). The loads were applied as uniformly distributed line loads and included the self-weight of the beams. The remaining 6.6% (1.39 kN per beam) of the total load was applied to the cellular beams and only accounted for the self-weight of the cellular beams. The loads applied to the channel and primary beams were done in the same manner as in the single element models, with the loads applied as concentrated point loads to the bottom flange nodes, along the entire lengths of the beams. Again, the concentrated loads were only applied to the interior nodes of the beam bottom flanges. The self-weight of the cellular beams was defined in the global model as in the single element models, with 37 concentrated point loads placed at uniform intervals along the beams. Finally, as seen in Figure 8-9 below, end boundary conditions were applied only to the columns. The columns connected to PB 1 were completely fixed (i.e., translation and rotation fixed in all directions), whilst the columns connected to PB 2 were fixed in all directions apart from the rotation degree of freedom (DOF) in the x-direction. This was to allow for the thermal expansion of the cellular beams in the longitudinal direction and is a more accurate representation of reality as the experimental frame was able to deflect laterally outwards as detailed in Section 5.3.3.

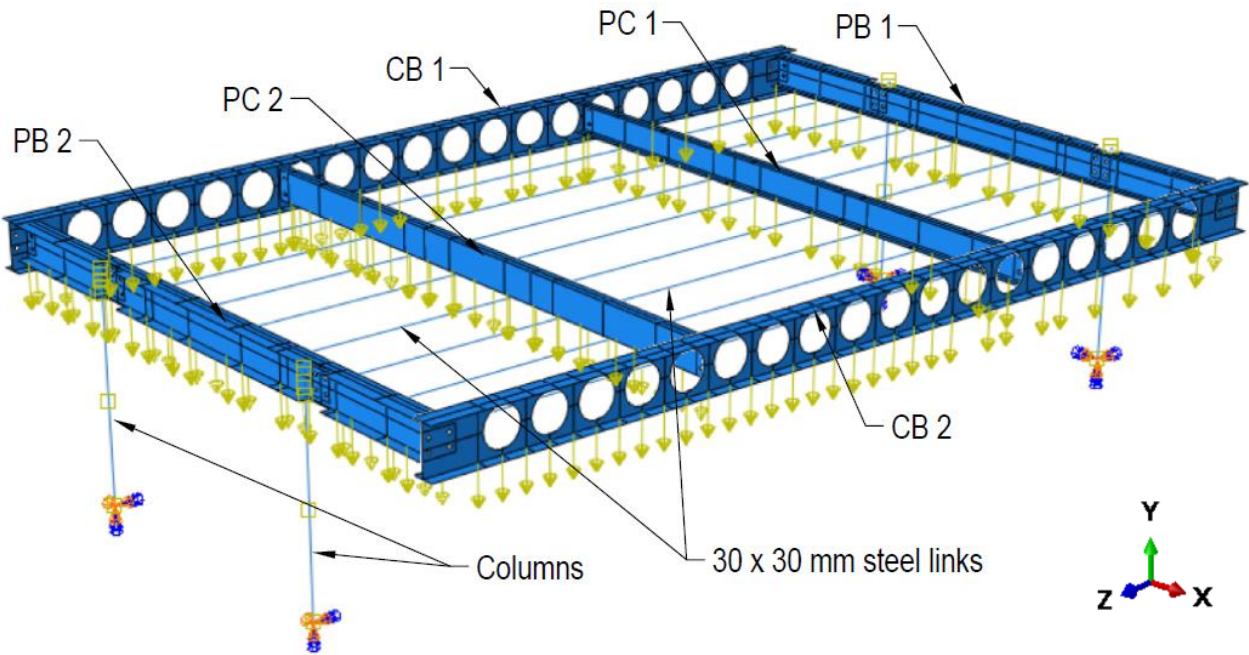


**Figure 8-9 Geometry, loading and boundary conditions of the global structural model.**

#### 8.4.3 Interactions

Numerous coupling constraints were utilized to connect the various parts in the global model. This technique was also adopted by Kloos (2017), and implemented in an identical manner in this work. The coupling constraints were applied to the structure such that no moment forces are transferred between the interconnected parts, thus assuming pinned connections between the structural members. The constraints were also defined such that torsional rotation is prevented for all the horizontal structural elements. Implementation of this method is detailed in the next section using the illustrated Figure 8-10 below.

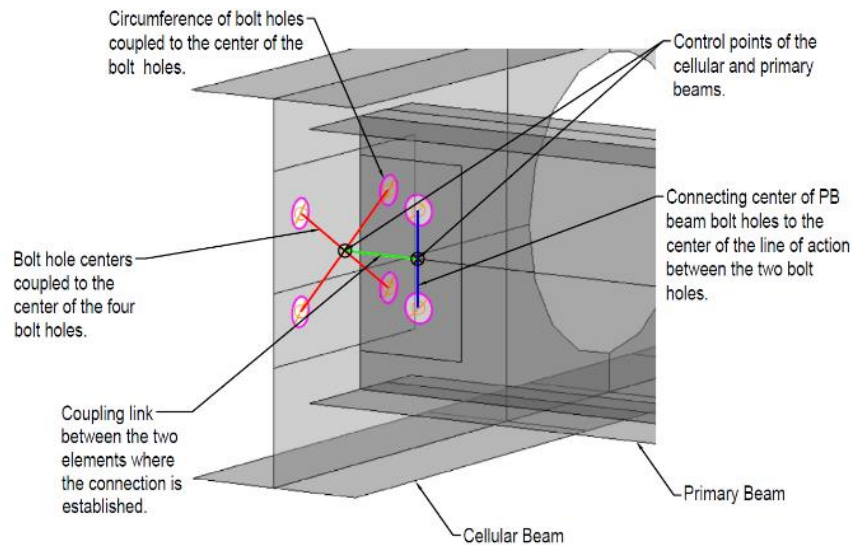


**Figure 8-10 Connection of interconnected structural elements in global model.**

Figure 8-10 above depicts the simulated double angle cleat connection between the primary and cellular beam parts. Firstly, the bolt hole circumferences were coupled to each of the bolt hole centres, as in the end boundary conditions of the cellular beam single element model. The four bolt holes of the cellular beam were then coupled to the centre of the collective bolt holes as indicated by the red lines, with the control reference point at the intersection of the red lines. Next, the bolt holes of the primary beam were coupled to the centre of the bolt holes line of action, as indicated by the blue line, with the reference control point at the middle of the line of action. Finally, the two control points are then linked to form the connection between the two beams as indicated by the green line, where the constrained DOF between the two respective beam sections are defined.

#### *8.4.4 Thermal loading*

The same approach was used to apply the thermal loads of the PC and CB parts in the global model as in the single element models. Each of the horizontal structural members were split into three sections, and each section split into three segments along the height of the beam as in the single element models. The temperatures recorded in LST-2 were then applied to each of the corresponding segments as predefined temperature fields. However, the convergence issue encountered for the PC beam model due to high temperature gradients between the respective sections along the beam length were not found in the global model. Hence, the transition zones implemented in the single element PC beam model was excluded from the global model, where the PC beams were split into three sections only, as for the cellular beam parts, without the transition zones. Thus, a total of 9 predefined temperature fields were assigned to each of the cellular and channel beam parts. However, the same time-temperature curves applied to the single element models (PC 1, PC 2, CB 1, and CB 2) was applied in the global model.

For the primary beam parts (PB 1 and PB 2) the temperatures measured along the length of these short beams for each of the respective segments along the height of the beams were averaged since the variation between them was limited, as shown in Figure 5-34 for PB 1. The average temperatures recorded for each segment along the height of the beams were saved as amplitudes and applied to the respective segments of the beams in the model as predefined temperature fields. Thus, a total of three predefined temperature fields were applied to each of the primary beam parts.

## **8.5 Results**

The following section presents the results from all the numerical scenarios of the single element models and the results from the global model in comparison to each other and the experimental data. Section 8.5.1 will present an overview of the data obtained from the global model in comparison to the experimental data in a single graph. The naming convention used to present the numerical and experimental data is also presented. Sections 8.5.2 and 8.5.3 will present the single element model and global model results of the parallel channel and cellular beams in comparison to the experimental results. Section 8.5.4 presents a discussion on the comparison of the single element and global structural models.

### 8.5.1 Data overview and naming convention

Figure 8-12 below depicts the final deformed shape and stress distribution of the global model. The locations at which the deflection data was obtained from the numerical models is also indicated on Figure 8-12 below and correspond to the same locations used to measure the deflections of the experimental frame in LST-2. The experimental data captured in LST-2 for CB 1 (LVDT-3 and LVDT-6) has been averaged into a single time-deflection curve and denoted as “Experimental-CB 1”. LVDT-1 malfunctioned during the LST-2 experiment as stated above in Chapter 5, hence, only the data captured by LVDT-4 has been included and denoted as “Experimental-CB 2”. The data captured for the parallel channel beams (i.e., LVDT-5 for PC 1, and LVDT-2 for PC 2), will be denoted as “Experimental-PC 1” and “Experimental-PC 2”, respectively. Similarly to the experimental data of CB 1, the numerical data obtained from the two locations of CB 1 and CB 2 have been averaged into single time-deflection curves and denoted as “FEM-Full Scale-CB 1” and “FEM-Full Scale-CB 2”, respectively. The numerical data captured for the PC beams are denoted as “FEM-Full Scale-PC 1” and “FEM-Full Scale-PC 2” for PC 1 and PC 2, respectively.

Furthermore, the same naming convention will be used to present the data in the sections to follow. However, as the data will be presented for each beam section separately, the numerical data for the single element models will only be denoted as “FEM-Single” and the global model data denoted as “FEM-Full”, while the experimental data will keep the same denotations. Where data is compared between different single element model results or to the global model element results, care will be taken such that clear distinctions can be made between the data sets.

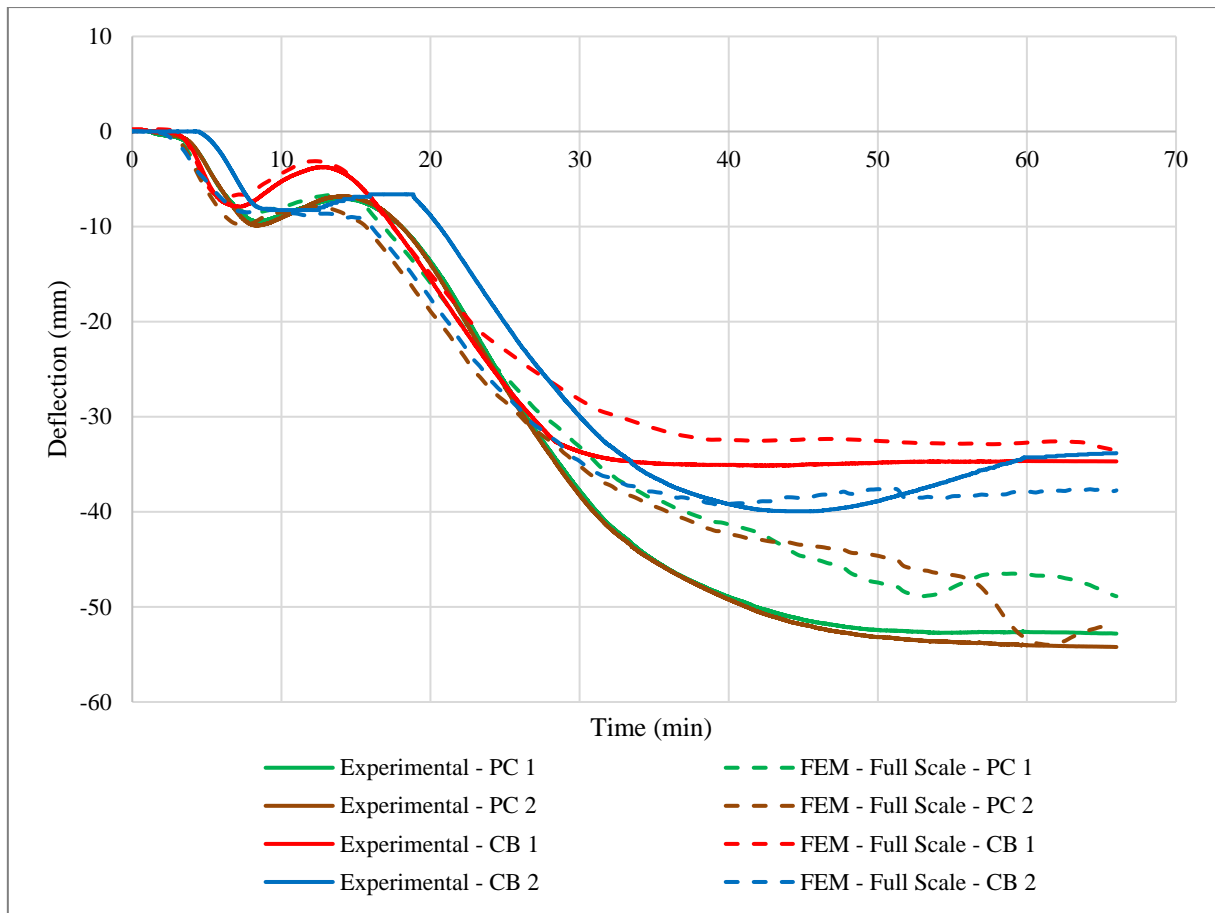


Figure 8-11 Comparison of the global structural model and experimental data.

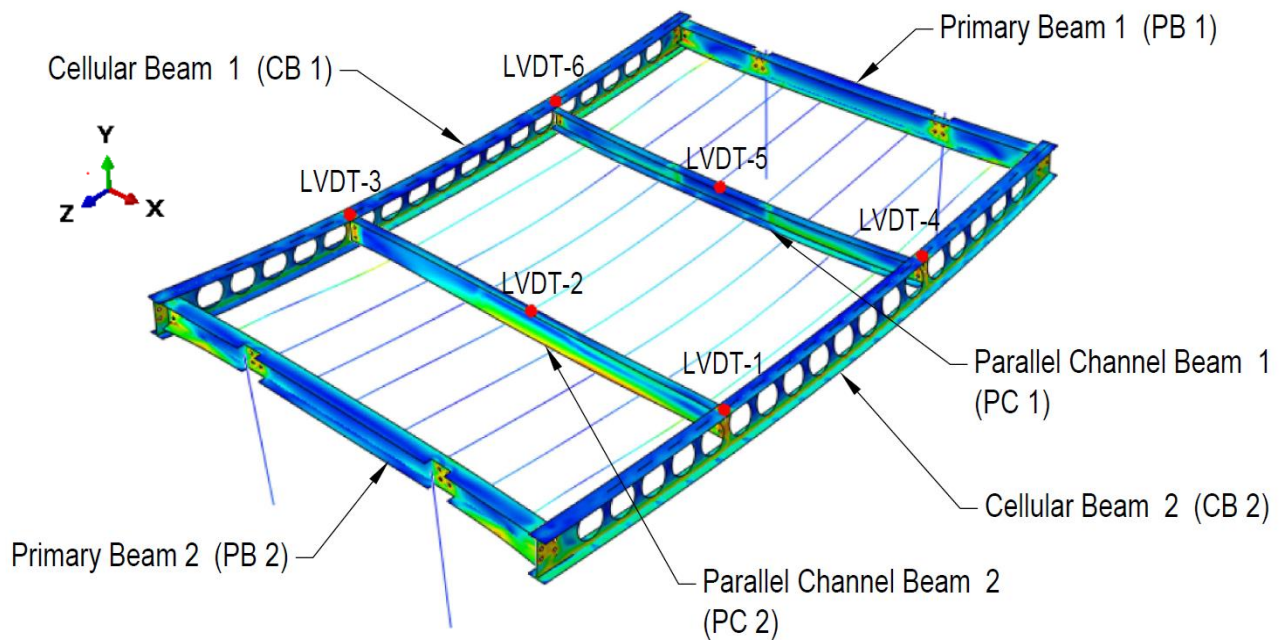
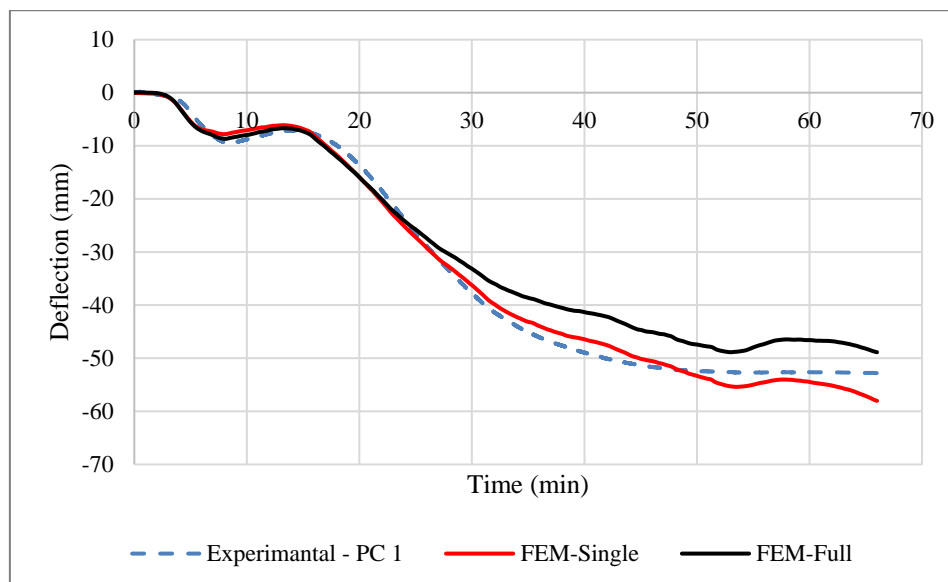


Figure 8-12 Final deformed shape and stress distribution of global structural model. (Deformation magnification factor = 3)

### 8.5.2 Parallel flange channel support beams (PC) results

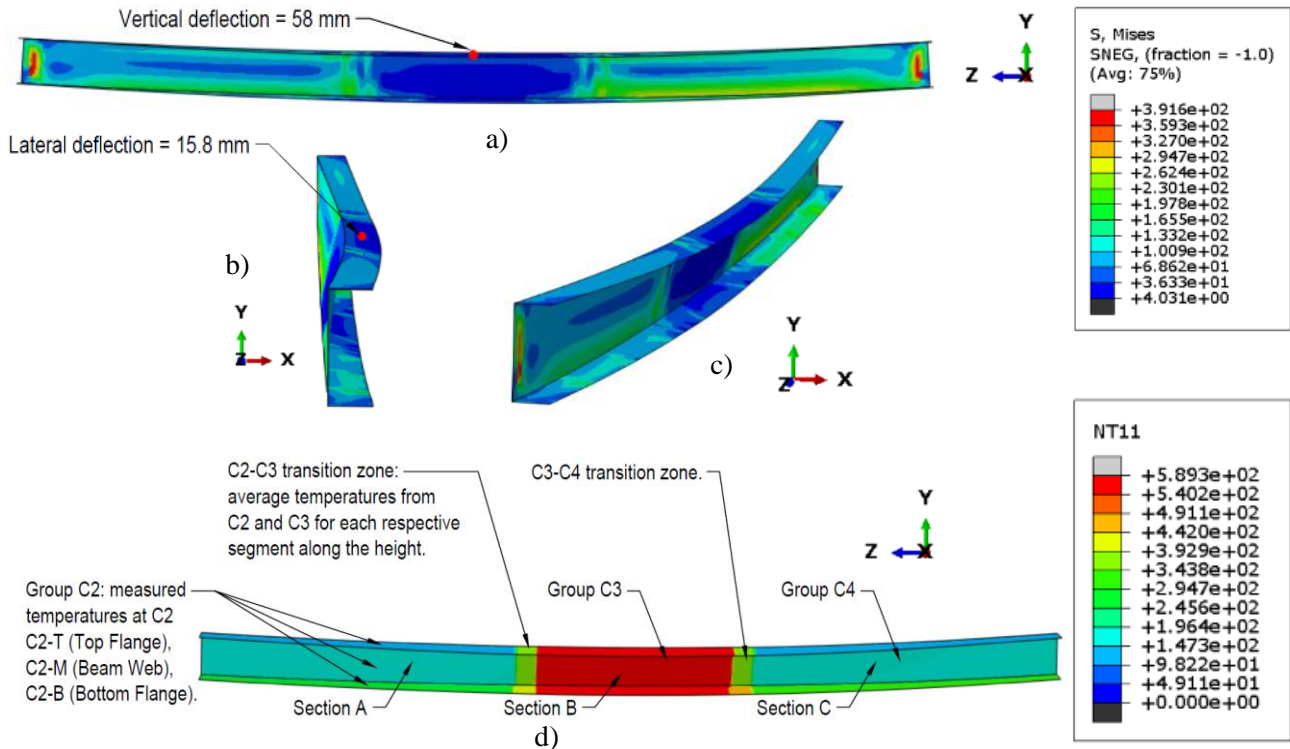
#### **Parallel flange channel beam 1 (PC1)**

Figure 8-13 below presents the single element and global structural model deflections of PC 1 in comparison to the experimental data.



**Figure 8-13 Numerical and experimental deflection data of PC 1.**

As seen in Figure 8-13 above, the predicted deflection behaviour of PC 1 in the single element and the global structural model correlate well with the experimental data. This indicates that global structural interactions have limited impact on behaviour, except for a 15.6% difference in deflections at 60 minutes between the single element and global model. Furthermore, there is a 3.6% and -11.4% error between the single element and global model results when compared to the experimental data at the 60-minute mark, respectively. However, the same lateral-torsional buckling behaviour is predicted by PC 1 in both the single element and global model analyses. This behaviour starts to occur at about 54 minutes into each of the analyses. Figure 8-14 (a, b, and c) below depict the PC 1 single element model deflected shape and stress distribution (MPa) from three different perspectives. The final temperature distribution of PC 1 is also depicted in Figure 8-14 (d), where the different sections (Section A, B and C) of the beam are indicated as detailed in Section 8.3.3 above, along with the specific temperature groups (i.e., C2-Series, C3-Series, and C4-Series) that were applied in each of the respective sections. The temperature groups for each of the structural members can be found in the online repository (Claasen *et al.*, 2021).



**Figure 8-14 Deflected shape, stress and temperature distribution of PC 1 at the end of the single element model analysis. (Deformation magnification factor = 3). NT11 provides the elemental temperature in °C at the end of the analysis.**

Figure 8-15 below depicts the lateral deflections of PC 1 from the single element and global structural model. To illustrate the influence of increasing temperature on lateral deflections the average recorded temperatures from Group C3 thermocouples is plotted, which is discussed below.

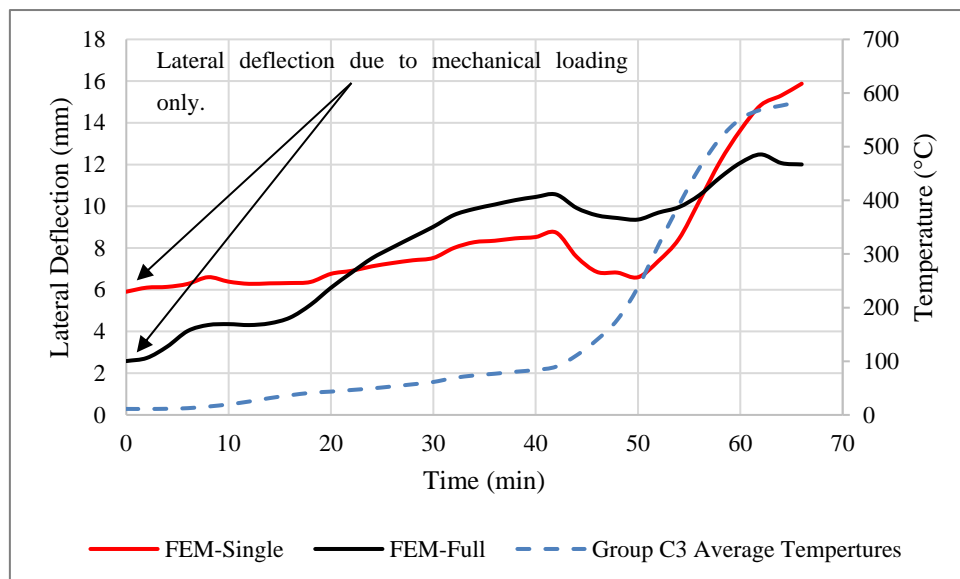


**Figure 8-15 Lateral deflections of PC 1 from the single element and global structural model in comparison to the average temperatures recorded at C3-Series.**

The behaviour of PC 1 in the single element model is as follows: (1) At the start of the analysis (mechanical step), due to the lateral restraints at the bottom flange of the beam as detailed in Section 8.3 above, the top flange of the beam deflects 5.9 mm laterally (measured at the same location as the vertical deflection) under the mechanical load only, as indicated on Figure 8-14 (b) above. (2) The beam maintains a similar deflected shape in the second (thermal) step of the analysis, where it primarily deflects vertically in relation to the cellular beams. During this period, the lateral deflection of the beam's top flange increases by 2.8 mm from the start of the analysis to the 42<sup>nd</sup> minute mark. (3) At about 42 minutes into the analysis, the top flange of the beam recovers some of the lateral deflection (2.1 mm) over a period of about 8 minutes until the 50<sup>th</sup> minute mark, where the beam starts to deflect laterally again. This lateral deflection continues until the end of the analysis as the beam experiences lateral-torsional buckling. However, load carrying capacity is still maintained.

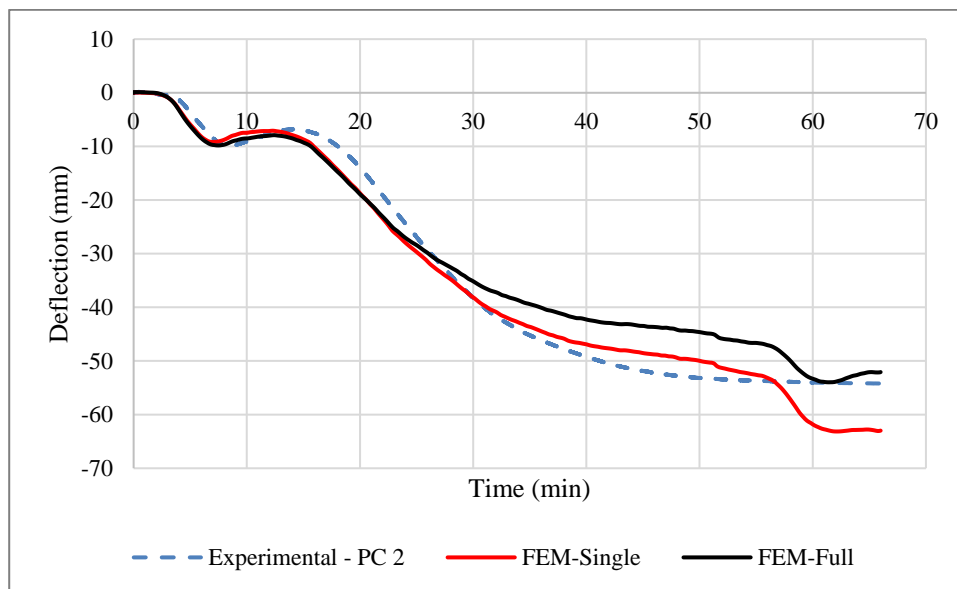
As seen above in Figure 8-15, there is a strong correlation between the rise in the average temperature at C3 (average temperatures of the three thermocouples along the beam height at Section B plotted in the figure) and the lateral deflection experienced at the top flange of the beam. Furthermore, as seen in Figure 8-14 (d) above, there is a large temperature gradient between the different beam sections along the beam length (Section A, B and C). The middle section experiences significantly higher temperatures on average compared to the two outer sections. It is likely that a localised failure of the ceiling must have occurred, allowing hot gases into the plenum, such as CSB ceiling joints widening caused by the deflection of the structure or a localized crack shown in Figure 5-30 above. As the beam heats up more at the centre in relation to the outer sections, the beam experiences different rates of thermal expansion within each of these sections. Moreover, as the average temperatures of the outer sections do not exceed 150°C, the middle section of the beam lost more strength and stiffness compared to the outer sections when passing the 55<sup>th</sup> minute into the analysis, where the middle section starts to experience temperatures in excess of 400°C (Bottom flange). Thus, as the beam sections start to heat up at different rates and experience different rates of thermal elongation, the hotter middle section of the beam tries to expand while the colder outer sections prevent it. When this is coupled with the loss of stiffness at temperatures exceeding 400°C, the beam starts to deflect laterally at the middle section and buckle outwards. Furthermore, due to the asymmetrical nature of the channel beams and the lateral restraint provided by the decking at the bottom flange, the beams will experience this lateral-torsional buckling behaviour under normal loading as well. However, the high temperatures exposed to the middle section of the beam expedites this process. This is especially evident as the buckling behaviour is experienced by the single element model, indicating that interactions from the other structural members as in the global model is not the cause of this behaviour.

Furthermore, when considering PC 1 in the global structural model, similar behaviour of the beam can be observed in the numerical data presented above in Figure 8-13, in terms of vertical deflections and initiation time of the buckling behaviour. However, when observing the lateral deflections in Figure 8-15 above, the initial lateral deflections induced in the PC beam in the global model are less than that of the single element model. There is a difference of 3.3 mm in the initial lateral deflections, where the single element model has an initial lateral deflection of 5.9 mm and the global model only 2.58 mm. This can be attributed to the attachment of the

steel links at the points of lateral restraint as indicated above in Figure 8-5, which provided additional lateral load paths for the load carried by the PC beams, as opposed to the single element model that was fixed in the lateral direction at these locations. However, the PC beam in the global model experiences a higher rate of increase in lateral deflection from the start of the analysis till the 42<sup>nd</sup> minute into the analysis when compared to the single element model. With a 7.9 mm increase in the lateral deflection from 2.58 mm to 10.56 mm. The global model PC beam undergoes the same lateral deflection recovery (1.2 mm) from the 42<sup>nd</sup> minute until about the 50<sup>th</sup>, after which the beam also experiences the same buckling behaviour as in the single element model. The overall buckling behaviour of the PC beam in the global model can be attributed to the same factors as discussed for the PC 1 single element model.

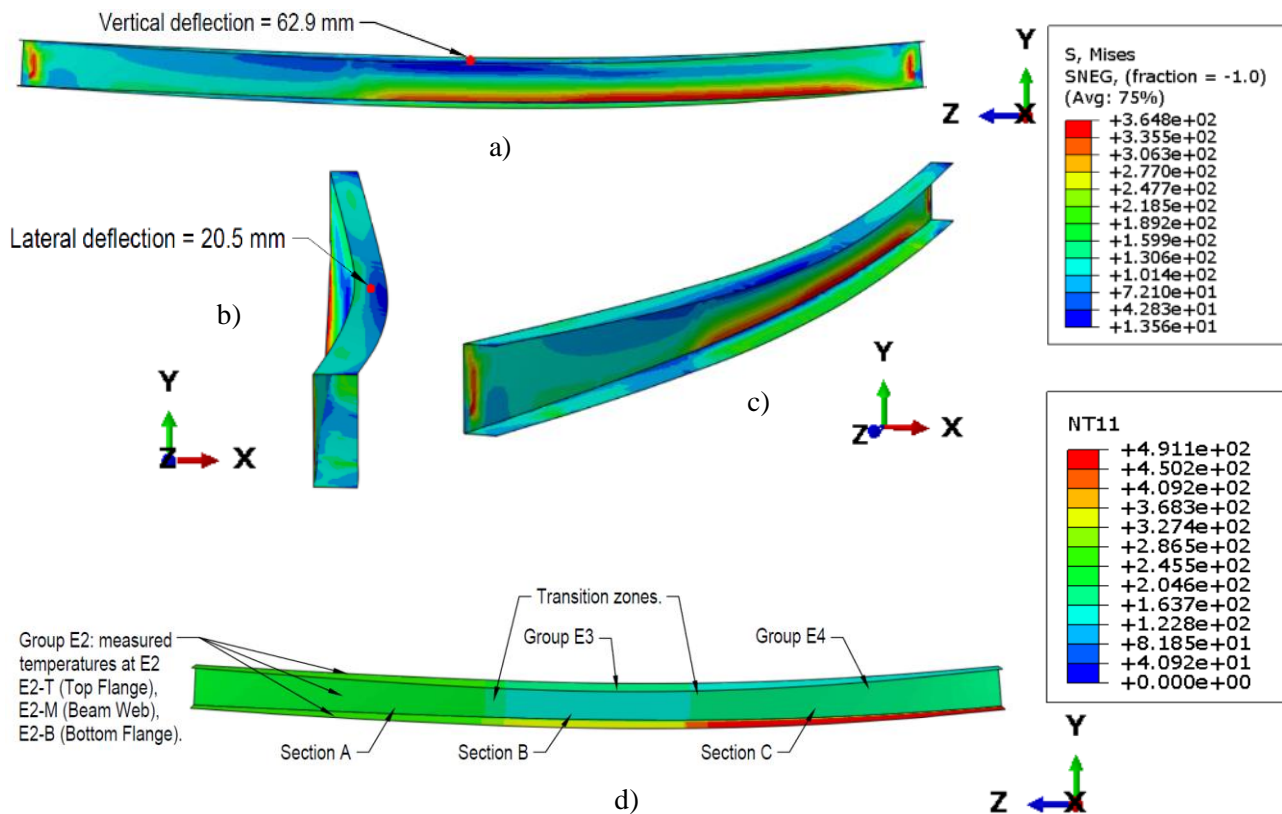
### ***Parallel flange channel beam 2 (PC2)***

Figure 8-16 below presents the single element and global structural model deflection results of PC 2 in comparison to the experimental data.



**Figure 8-16 Numerical and experimental deflection data of PC 2.**

As seen in Figure 8-16 above, the predicted deflections from both the single element and global model of PC 2 correlate well with the experimental data. However, similarly to that of PC 1, both the single element and global model experience a lateral-torsional buckling behaviour towards the end of the analysis. When comparing the data at the 60-minute mark, a difference of 15.1% is found between the single element and the global model for PC 2, and an error of 14.7% and -1.4% for the single element and global models when compared to the experimental results, respectively. The deflected shape, stress and temperature distribution of PC 2 at the end of the analysis is depicted below in Figure 8-17 (a, b, c, and d).



**Figure 8-17** Deflected shape, stress and temperature distribution of PC 2 at the end of the single element model analysis. (Deformation magnification factor=3). NT11 provides the elemental temperature in °C at the end of the analysis.

Figure 8-18 below presents the E4-B temperatures measured at the bottom flange of PC 2 (i.e., only the bottom flange temperature measured from the Group E4 thermocouples) in comparison to the lateral deflections measured in both the single element and global model. Again, the buckling behaviour of PC 2 in the numerical models can be primarily attributed to the temperature evolution in the beam, the bottom lateral restraints, and the unsymmetrical nature of the beam. A concentrated stress distribution can be seen along the bottom part of Section C (Figure 8-17 (a, c)) of the beam web where the beam is exposed to the highest temperatures along the bottom flange. The middle section of PC 2 is around 223°C cooler than PC1, when comparing the middle bottom flange temperatures, but the temperature difference between the top and bottom flange is higher (181°C vs 366°C at 66 minutes) which influences this behaviour.

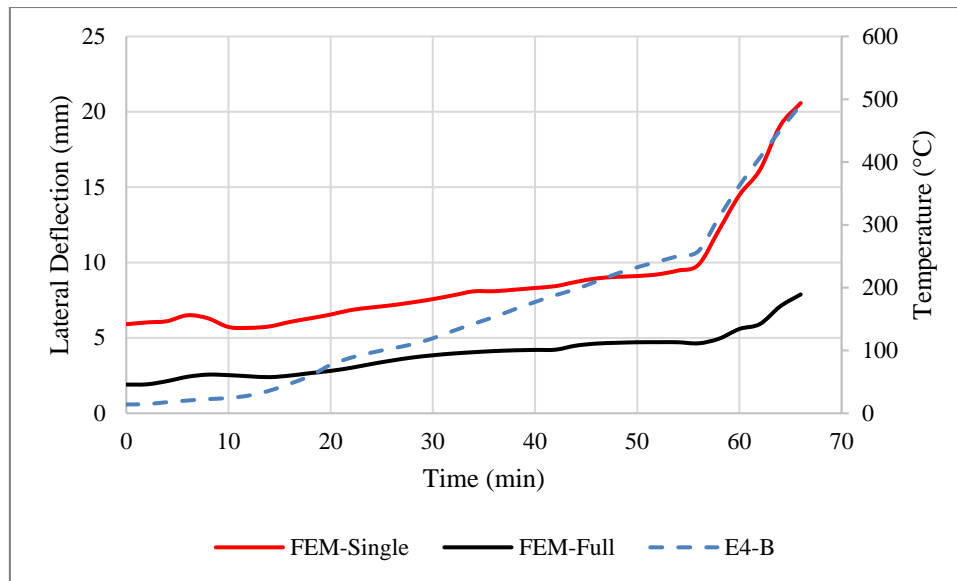


**Figure 8-18 Lateral deflections of PC 2 from the single element and global structural model in comparison to the average temperatures recorded along the bottom flange of PC 2.**

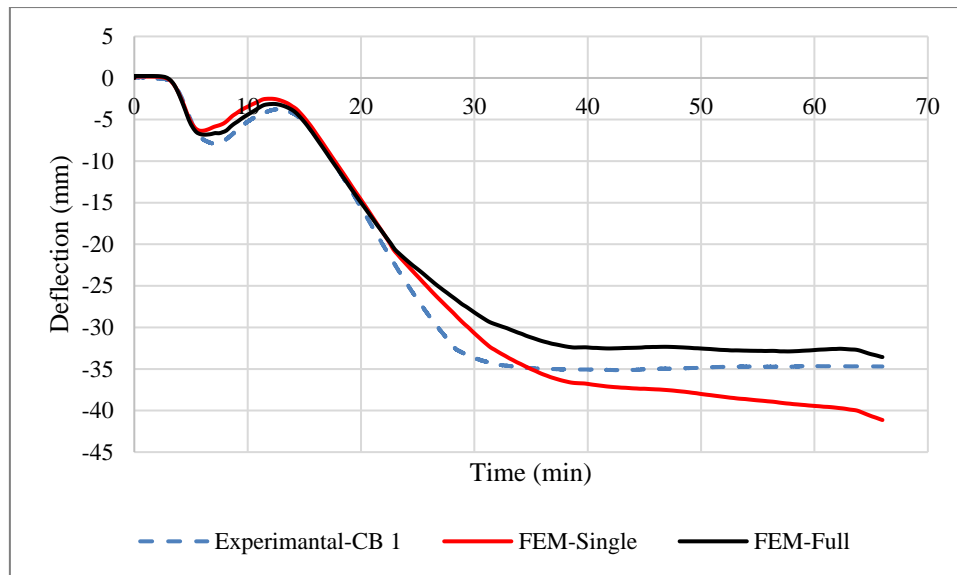
The deflection behaviour of PC 2 is similar to that of PC 1 and can be summarised as follows: (1) the top flange of the beam also deflects 5.9 mm laterally due to the applied mechanical loading; (2) at the 56<sup>th</sup> minute mark the lateral deflection of the beam's top flange increased from 5.9 mm to about 9.85 mm at an approximate linear rate; and (3) after the 56<sup>th</sup> minute mark, the beam starts to deflect at a significantly higher rate as the beam experiences lateral-torsional buckling until the end of the analysis, although load carrying capacity is still maintained.

Similar behaviour can be observed in the global model for PC 2, hence, as in the case of PC 1, the initial lateral deflection due to mechanical loading is lower than that of the single element model, and for the same reason. Conversely, the progression of the lateral deflections in the global model for PC 2 does not exceed that of the single element model at any point, as in the case of PC 1.

### 8.5.3 Main cellular support beam (CB) results

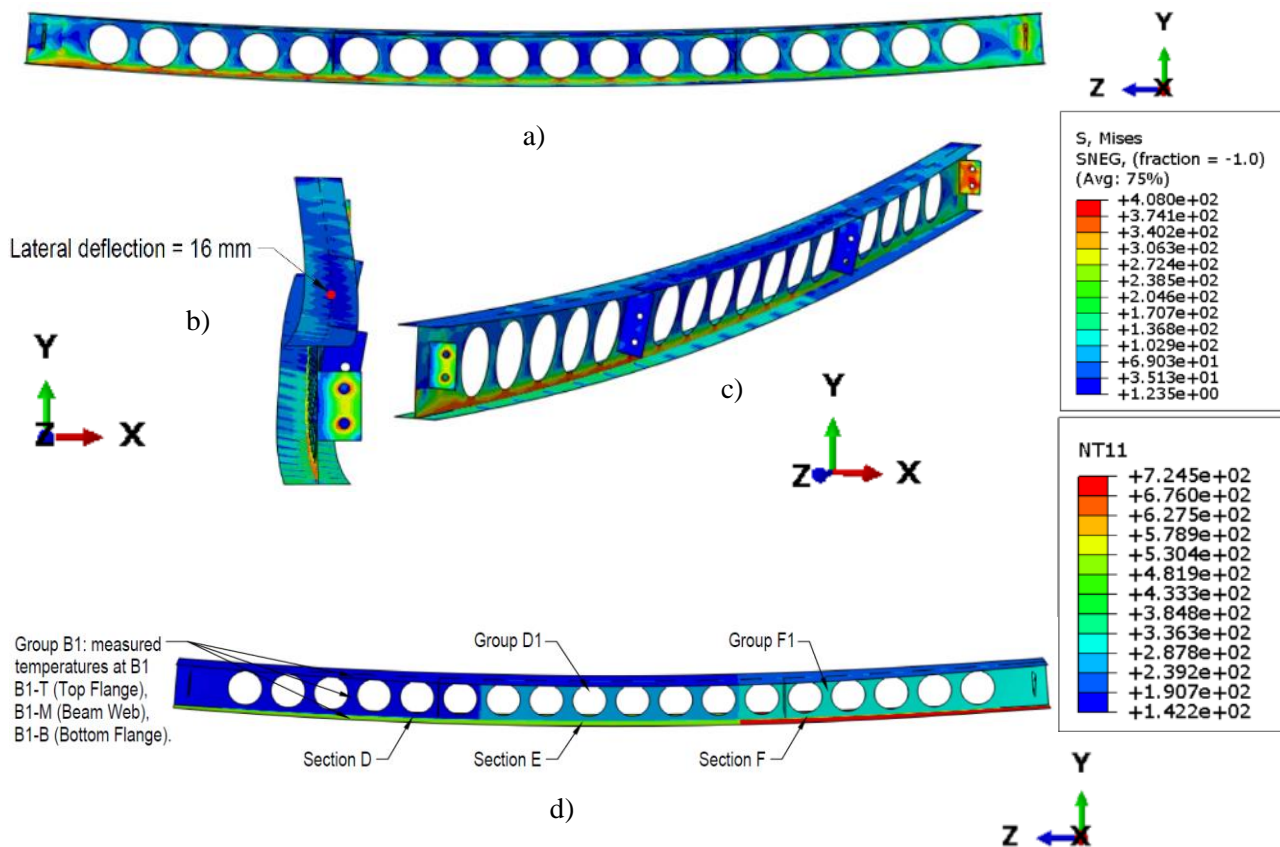
#### **Cellular support beam 1 (CB1)**

Figure 8-19 below presents the single element and global structural model deflection results of CB 1 in comparison to the experimental data.



**Figure 8-19 Numerical and experimental deflection data of CB 1.**

As seen from Figure 8-19, the single element and global structural model agrees well with the experimental data captured for CB 1. However, the single element model did not reach a constant deflection, as in the global model and experimental results. This behaviour is seen in Figure 8-19, as the beam continuously deflects vertically from about the 40<sup>th</sup> minute mark until the end of the analysis, whilst the deflection of CB 1 in the global model and experimental data reach a constant deflection. Again, this can be attributed to the additional load paths available in the global model and experimental frame. Furthermore, when comparing the data at the 60-minute mark, a difference of 18.6% is found between the single element and global models, and an error of 13.8% and -5.5% for the single element and the global models when compared to the experimental data. Figure 8-20 (a, b, c, and d) below depicts the deflected shape, stress and temperature distribution of CB 1 at the end of the single element model analysis. Load capacity is maintained throughout the analysis.



**Figure 8-20 Deflected shape, stress and temperature distribution of CB 1 at the end of the single element model analysis. (Deformation magnification factor = 2 ).**

The general deflection behaviour of the CB 1 single element model is as follows: (1) a torsional force is induced in the beam by the mechanical loading, causing the beam to deflect by 10.7 mm laterally to the right (i.e., in the direction of the side where the loading is applied to the fin plates). (2) At about 3 minutes into the second step of the analysis, the beam starts to rapidly deflect vertically until a deflection of about 6.3 mm at the 6<sup>th</sup> minute mark, where the beam stops deflecting downwards and starts to recover. This initial deflection is caused by the rapid heating of the beams bottom flange in relation to the web and top flange, causing the beam to deflect due to thermal bowing, as detailed in Chapter 5 (Section 5.3.3 ). (3) After the 6<sup>th</sup> minute mark, the beam starts to deflect upwards and recover about 3.85 mm of the vertical deflection over a time period of about 5.9 minutes until the 12<sup>th</sup> minute mark into the analysis. The recovery of the beam during this time period can be attributed to a reduced temperature gradient in the section, resulting in lower vertical deflection. (4) After this brief reduction in deformation, the beam starts to deflect vertically downwards again due to increased thermal bowing as the temperature gradient along the height of the beam increases again, along with decreasing material properties as the beam temperatures surpass the 400°C mark.

### ***Cellular support beam 2 (CB2)***

Figure 8-21 below presents the single element and global structural model deflection results of CB 2 in comparison to the experimental data. The predicted deflection behaviour of CB 2 correlates well with the experimental data, although with an approximate 5-minute offset which cannot be readily explained as this did not occur for any of the other beams and all experimental data was verified. When comparing all data at the 60-minute mark, a difference of 15% is found between the single element and global model, and an error of 28.6% and 10.5% is found for the single element and global model, when compared to the experimental data, respectively. Due to the similarities in the behaviour of CB 1 and CB 2, only a brief discussion will be presented on the numerical results of CB 2. Figure 8-22 (a, b, c, and d) below depicts the final deflected shape, stress and temperature distribution of CB 2 at the end of the single element model analysis.

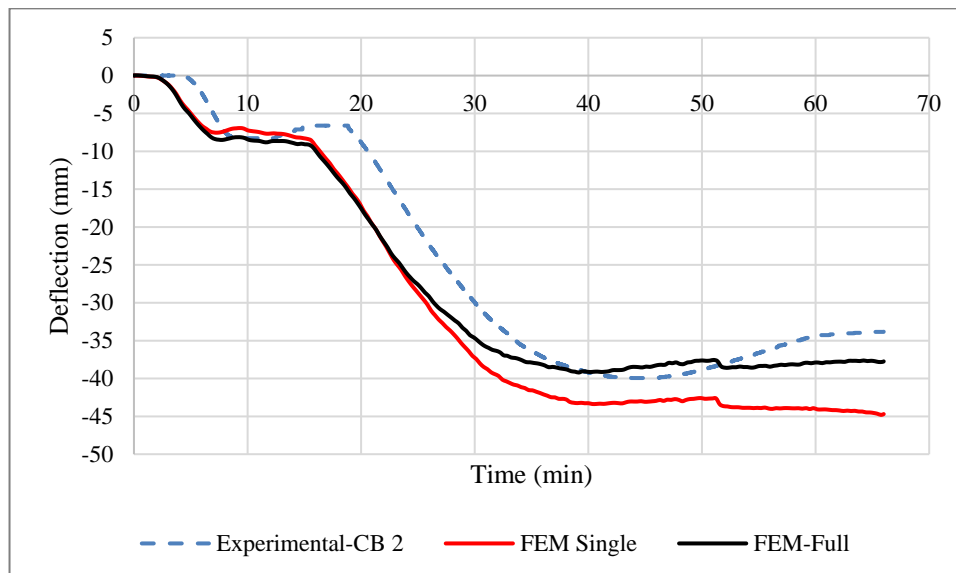


**Figure 8-21 Numerical and experimental deflection data of CB 2.**

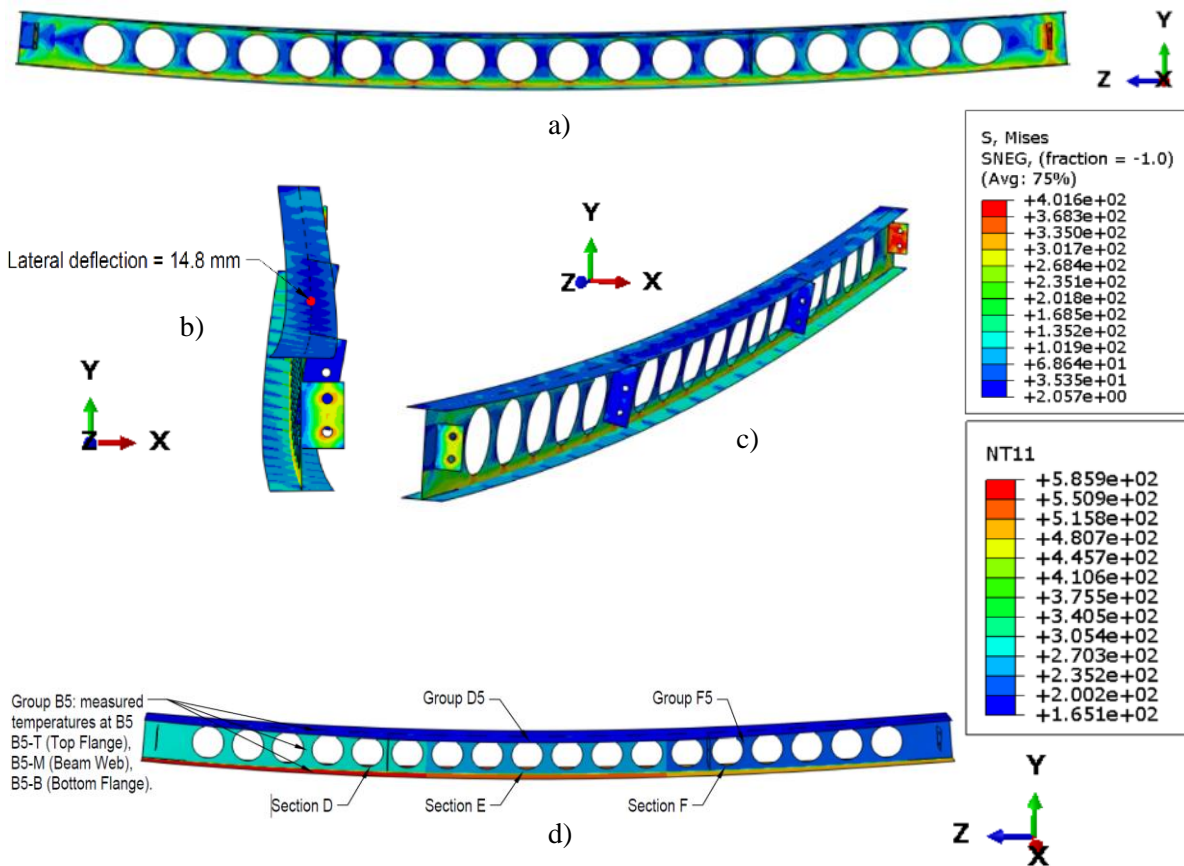


**Figure 8-22 Deflected shape, stress and temperature distribution of CB 2 at the end of the single element model analysis. (Deformation magnification factor = 2).** .

The deflection behaviour of CB 2 can be summarised as follows: (1) From mechanical loading a torsional force is induced in the beam, causing the top flange of the beam deflect laterally by 10.7 mm. (2) CB 2 experiences the same initial vertical deflection to CB 1 due to thermal bowing at the start of the second step until about the 7.3-minute mark into the analysis, where the beam starts to stabilize and deflect vertically at a slower rate. This slow rate of deflection continues for about 8.58 minutes until about the 16<sup>th</sup> minute mark, where the beam starts to deflect vertically downwards again at a higher rate. Similar to that of CB 1, this halt in deflection is caused by more uniform heating of the cellular beam along the section height. (3) The beam continues to deflect until the 40<sup>th</sup> minute into the analysis, where the rate of deflection slows down, and the beam reaches a constant deflection. (4) The final lateral deflection of the beam caused by the torsional forces induced by the point loading is 14.8 mm as shown above in Figure 8-22 (b).

#### 8.5.4 Comparison between single beam and full analysis models, and interconnectional behaviour

Figure 8-23 below depicts the final deflected shape and stress distribution of the global structural model.

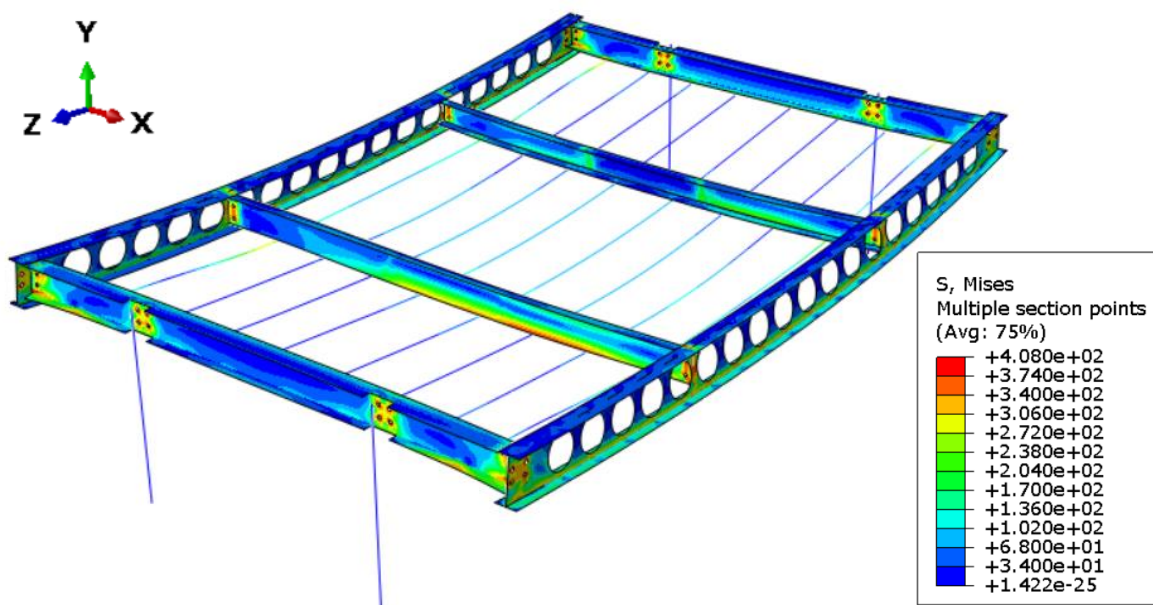


**Figure 8-23 Final deflected shape and stress distribution at the end of the global model analysis. (Deformation magnification factor = 3 )**

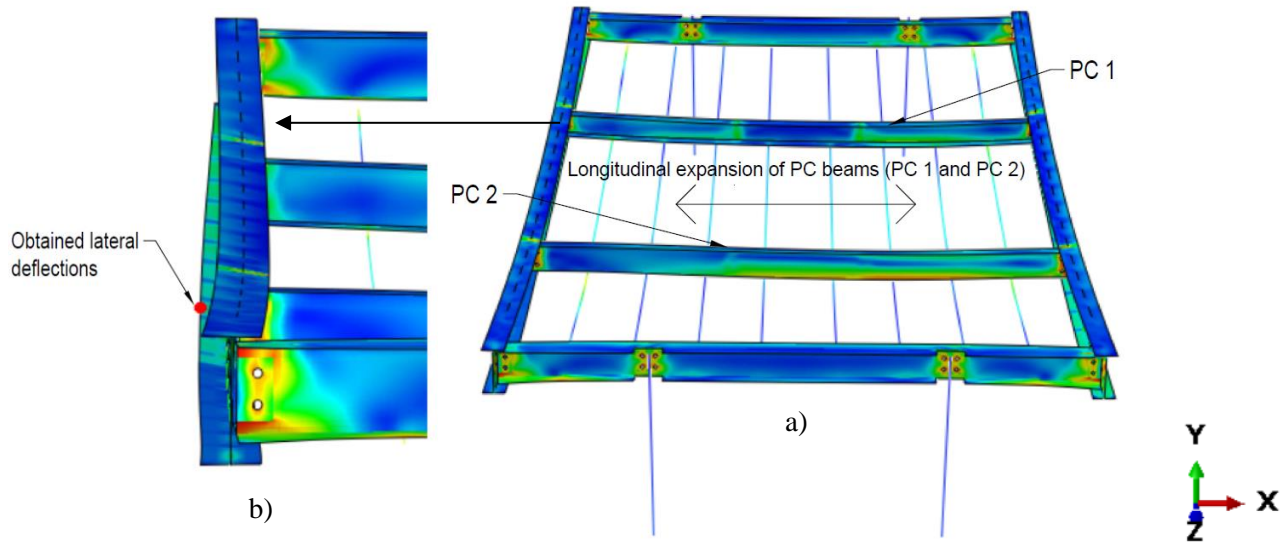
As seen above in the numerical results presented above for each of the structural elements that the behaviour of the global structural model is highly correlated with the behaviour of the single element models for each of the structural members considered, especially in the earlier parts of the experiment. As seen in Figure 8-13 and Figure 8-16, the single element model results start to deviate from the global structural model results from the 30<sup>th</sup> minute mark onwards for the parallel channel single element models. When comparing the numerical data at the 60-minute mark, the percentage differences between the single element and global model results are less than 16% for the PC 1 and PC 2 beam models, respectively. Furthermore, a similar deduction can be made for the numerical model analyses of CB 1 and CB 2, the general behaviour of the single element and global structural models are well correlated. The percentage differences between the single element and global structural model analyses for CB 1 and CB 2 are in the order of less than 20% for both beams. This is significant, as it may indicate that designers in the future will only need to consider single element models when analysing the structural behaviour of the system in fire. A similar conclusion was made by Kloos (2017) based on the FEM developed in his work. However, at the time experimental data and accurate steel temperatures were not available to validate this finding. Furthermore, it can also be observed that the single element models consistently over-predict the deflection behaviour of the structural elements when compared only to the global model results. This can be attributed to the presence of the steel links in the global structural model, and the different load paths that the load can be distributed to by the interconnected members as stated above as well. This is also evident when observing the global model data in comparison to the experimental data for all beams, where the error differences between the global model and the experimental data is less than 12% at the 60-minute mark. Which indicates that the global model is able to predict the experimental data more consistently.

Table 8-3 below summarises the percentage differences between the single element and global models, and the error differences between the single element models and the global model to that of the experimental data for all recorded vertical deflections at the 60-minute mark.

**Table 8-3 Percentage differences between the single element and global models, and the error differences between the single element models and the global model to that of the experimental data for all recorded vertical deflections at the 60-minute mark.**

Beam Section	Data compared	Difference in deflection (mm)	% Difference and % error (%)
PC 1	Single element numerical to full-scale numerical	7.9	15.6
	Single element numerical to experimental data	1.9	3.6
	Full scale numerical to experimental data	6	11.4
PC 2	Single element numerical to full-scale numerical	8.7	15.1
	Single element numerical to experimental data	7.9	14.7
	Full scale numerical to experimental data	0.7	1.4
CB 1	Single element numerical to full-scale numerical	6.7	18.6
	Single element numerical to experimental data	4.7	13.8
	Full scale numerical to experimental data	1.9	5.5
CB 2	Single element numerical to full-scale numerical	6.1	15
	Single element numerical to experimental data	9.8	28.6
	Full scale numerical to experimental data	3.6	10.5

Figure 8-24 below depicts the global structural model from the X-Y plane of view and Figure 8-25 presents the lateral deflections of CB 1 from the single element and global models, and the longitudinal thermal expansion of the PC beams from the single element and global models (as measured from the end connected to CB 1 in the global model).



**Figure 8-24 Longitudinal expansion of Parallel Channel beams (a). (Deformation magnification = 3), Close-up of induced torsional twisting in CB 1 beam by the PC beams (b). (Deformation magnification = 3).**

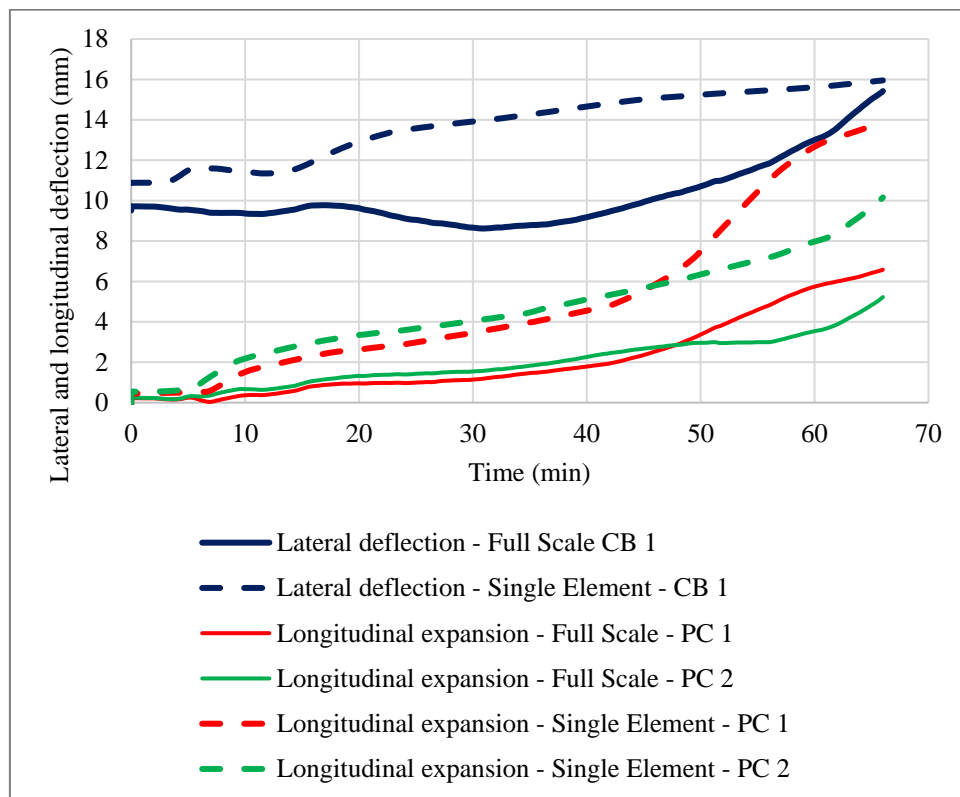


**Figure 8-25 Lateral deflections of CB 1 from the single element and global models, and the longitudinal thermal expansion of the PC beams from the single element and global models.**

As discussed above in Section 8.5.3 for the single element models, the main cellular beams have an induced twist caused by the mechanical loading applied to the beams, and is exacerbated as the strength and stiffness of the beam is reduced by the increase in applied temperatures over time. When considering the ends of the PC beams connected to CB 1 (as shown in Figure 8-24 (b)) in the global model, the total expansion of the PC beams are in the order of 5.7 mm and 3.6 mm for PC 1 and PC 2 at the 60-minute mark, respectively. Hence, it can be concluded that the twisting behaviour of the main cellular beams are due to the mechanical loading transferred and the longitudinal expansion experienced by the PC beams, in combination with the reduced mechanical properties of the cellular beams as the applied temperature increases. However, when observing the data presented in Figure 8-25, the lateral deflections of the bottom flange at the mid-point of the cellular beams (as indicated in Figure 8-24 (b)) are similar towards the end of the analyses. This signifies that the overall effect of the channels on the cellular beams are minimal, with regards to the thermal expansion of the channels. Furthermore, as stated in Chapter 3 (Section 3.4), the design of the experimental frame is based on the layout of a single module of the CBS system only, hence, the fly-bracing was excluded from the design. The fly-bracing only works as intended when they are connected on both sides of the beams (in this case, CB 1 and CB 2), which is only achieved when the entire sub-structure is assembled. Hence, this behaviour is not expected for the internal secondary cellular beams of the actual CBS system (i.e., the internal J-Beams of the actual CBS system). However, this behaviour should be kept in mind when considering the external secondary cellular beams of the CBS system (i.e., the outer J-Beams in the CBS design (Figure 3-1)), where the fly-bracing is only connected to one side of the cellular beams. Moreover, this behaviour was not exhibited in the numerical models developed by Kloos (2017) by the secondary cellular beams (J beams). Nonetheless, this represents a limitation in the design and model of the experimental frame tested in this work.

Figure 8-26 and Figure 8-28 below presents axial forces induced in the parallel channel and cellular beams at the end of the analyses for both the single element models and the global model, respectively. The axial forces were obtained at three intervals along the beam sections, which have been denoted as “Left” “Middle” and “Right”. The “Left” and “Right” axial force values were obtained near the connection points of the beam elements, where the axial forces tend to be the highest. The “Middle” axial forces were obtained from the geometrical centres of the beam elements. However, the axial force components in each of the beam elements, as shown in Figure 8-26 and Figure 8-28, for both the single element models and the global model, can vary significantly along the beam lengths. Hence, the axial forces were also obtained from each of the numerical models at 200 mm intervals along the beam lengths, and averaged. This was done such that the average axial forces induced in each of the elements can be quantified and visualized. However, as the axial forces change with time, the average axial forces were obtained through this manner (i.e., average axial force from axial force components obtained at 200 mm intervals) at four time-intervals, 0, 40, 60, and 66 minutes, as shown in Figure 8-27 and Figure 8-29 below, for the parallel channel and cellular beams, respectively.

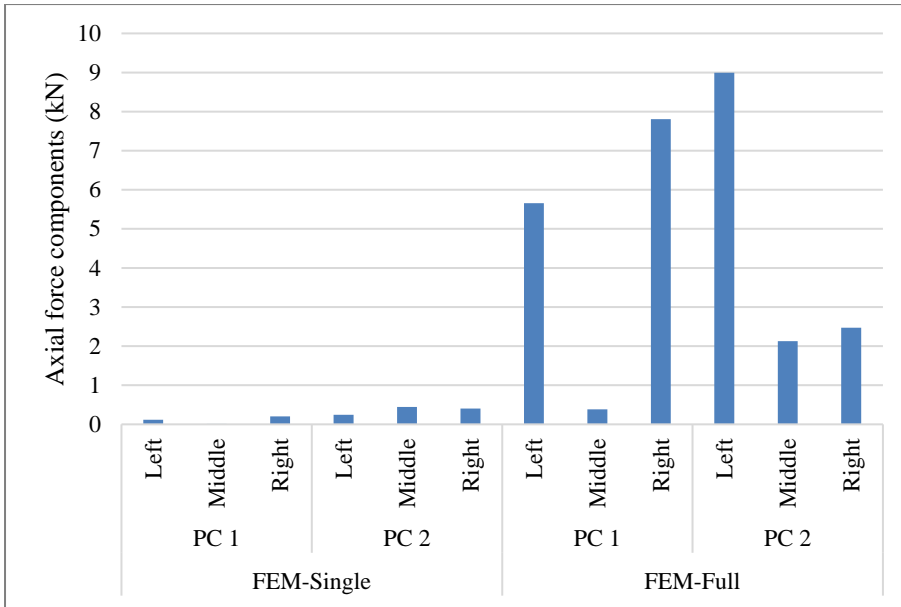


Figure 8-26 Axial force components as measured along three intervals along the PC beam lengths for both the single element and global models at 66 minutes.

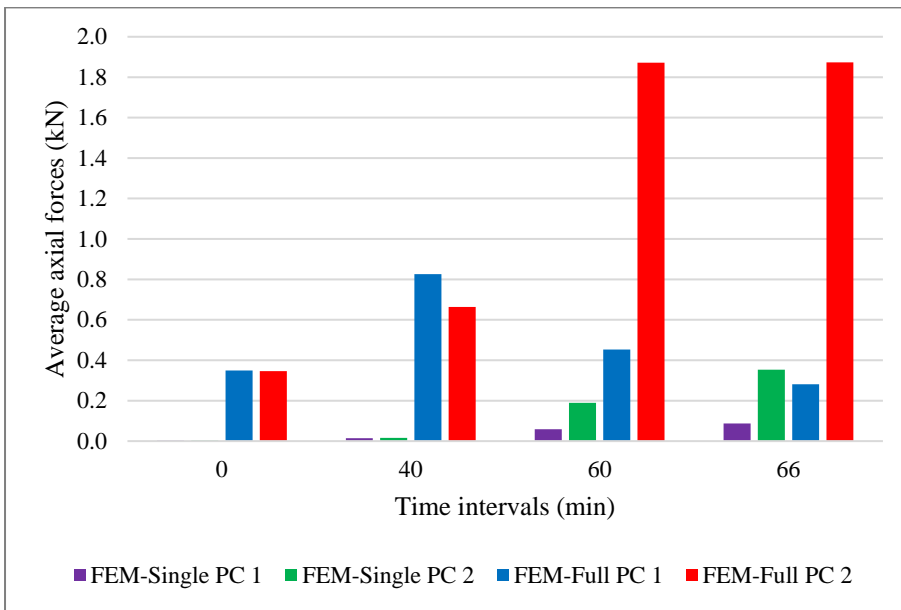


Figure 8-27 Average axial forces induced in the PC beams, for both the single element and global models.

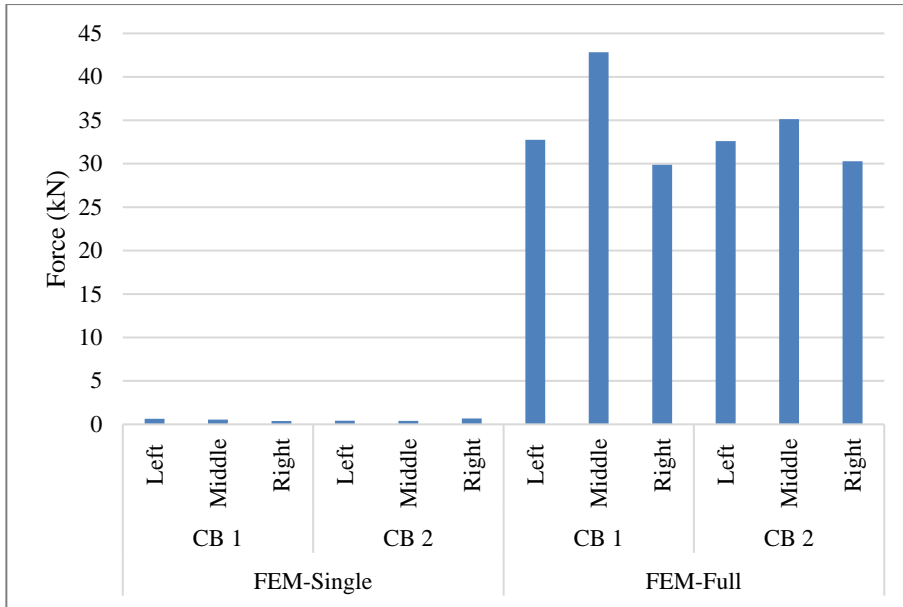


Figure 8-28 Axial force components as measured along three intervals along the CB beam lengths for both the single element and global models at 66 minutes.

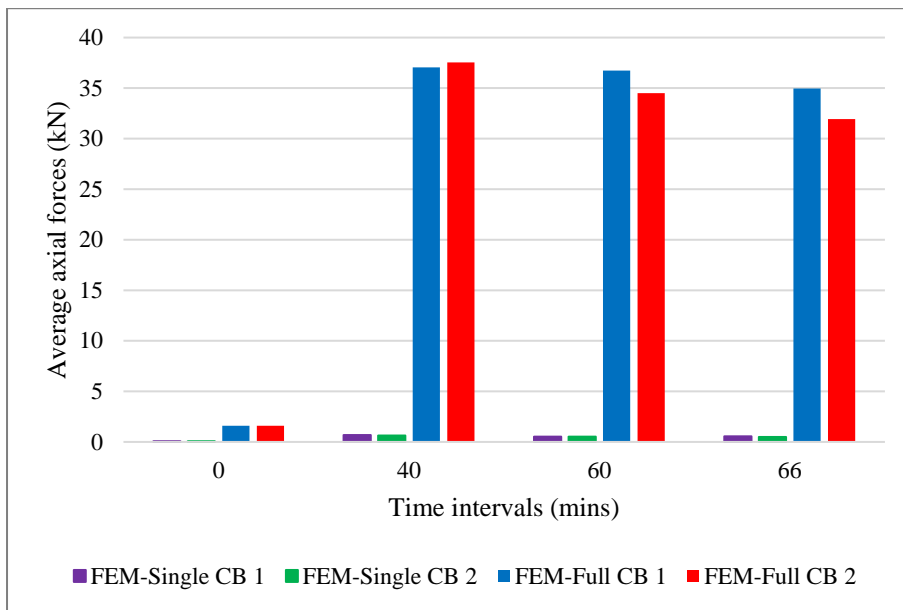
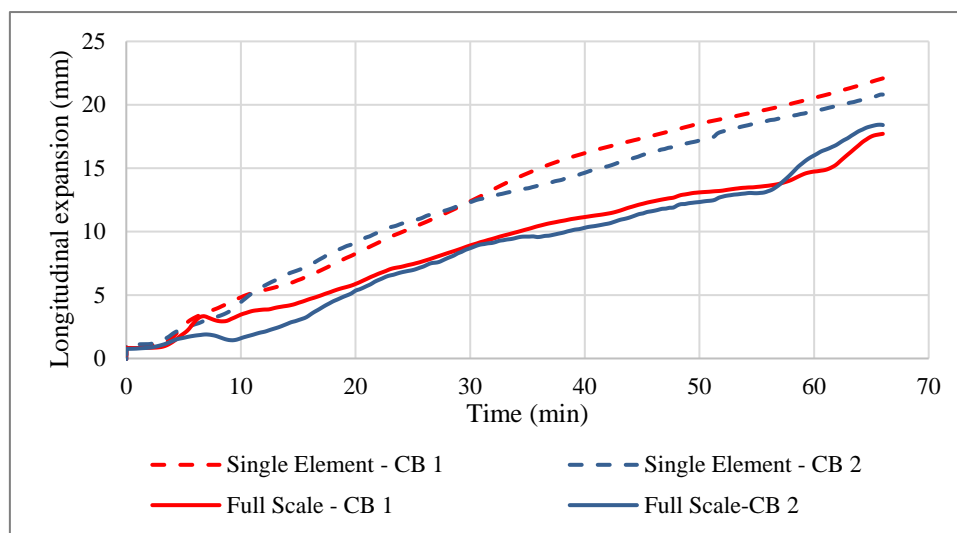


Figure 8-29 Average axial forces induced in the CB beams, for both the single element and global models.

When comparing the thermal expansions of the PC beams from both the single element models to that of the global model as presented in Figure 8-25 above. The beams exhibit similar deflection behaviour, however, there is an offset in deflections between the single element models and the global model, ranging from 1.5 mm at the 20<sup>th</sup> minute to 7 mm at the 60<sup>th</sup> minute. This indicates that the thermal expansion of the PC beams in the global model are slightly reduced by the main cellular beams. Furthermore, when examining the axial force data in Figure 8-26, it can be observed that the induced axial forces near the connection points of the PC beams in the global model, where the induced axial forces tend to be the highest, are higher for the PC beams in the global model. This further indicates that the thermal expansion of the PC beams in the global model were reduced by the main cellular beams. However, when observing the average axial forces induced in the global model PC beams, as presented in Figure 8-27 above, the induced axial forces are typically less than 2 kN, which signifies that the main cellular beams offer little resistance to the PC beams and bends about their weak axis, causing the torsional behaviour in the cellular beams.

Figure 8-30 below presents the longitudinal thermal expansion deflections of the cellular beams from both the global and single element models as measured from a single end of the elements.



**Figure 8-30 Longitudinal expansion of the cellular beams in both the global and single element models.**

As seen above in Figure 8-30, the thermal expansion of the main cellular beams in the global model and the single element models, have comparable deflection behaviour. However, similar to that of the PC beams, the cellular beams have a deflection offset, ranging from about 4 mm at the 20<sup>th</sup> minute mark to about 6 mm at the 50<sup>th</sup> minute mark. This also signifies that the thermal expansion of the cellular beams are reduced by the primary beams (PB 1 and PB 2) in the global model. Furthermore, when observing the axial force data presented in Figure 8-28 and Figure 8-29, the induced axial forces of the cellular beams in the global model are much higher than that of the single element models. This is in line with the reduced thermal expansion deflections observed for the cellular beams in the global model.

Furthermore, significant axial forces are induced in the global model cellular beams when observing the average force data presented in Figure 8-29 above. This indicates that the primary beams have a notable restraint on the cellular beams. Hence, these induced axial forces can be attributed to the relatively high stiffness of the primary beams due to them being so short. Nonetheless, this is significant as it indicates that the design of the CBS system should accommodate for the thermal expansion of the secondary cellular beams.

Finally, when observing Figure 8-23, it can be seen that the yield stress has been exceeded at localized areas around the experimental frame. This is especially evident around the connection areas of the horizontal structural members, the connections of the primary beams to the columns, and the bottom flange area of CB 1. However, as there are additional load paths, the structure was able to accommodate for these localized plastic strains and still able to maintain load bearing capacity.

## 8.6 Conclusion

This chapter presented the development of numerical models, including multiple single element models and a single global model, to predict the elevated temperature structural response of the steel members tested in large-scale test 2 (LST-2). The single element models detailed in this chapter are that of the cellular beams (CB 1 and CB 2), and the tertiary parallel channel beams (PC 1 and PC 2). No single element models were developed for the primary beams (PB 1 and PB 2). The global model developed included all the main horizontal structural elements, the columns, and steel links implemented in the global model to emulate the lateral rigidity provided by the SD system to the experimental frame.

Sections 8.2 to 8.4 gives a detailed description of the development of the single element and global models. The results from all the numerical models developed are then presented in Section 8.5. Section 8.5 was further divided into four sub-sections presenting (a) an overview of the data obtained from the global model in comparison to the experimental results, (b) the parallel channel (PC 1 and PC 2) numerical data from both the single element models and the global model in comparison to the experimental data, (c) the numerical data of the cellular beams (CB 1 and CB 2) from both the single element and global models in comparison to the experimental data, and (d) an overview of the single element models data in comparison to the global model data.

Predictions regarding structural behaviour correlate well with measured experimental deflections. Also, the single and global structural models provide comparable results, although with the single element models consistently predicting higher vertical deformations. All structural elements maintained their load bearing capacity up until the end of the experiment which is positive for the work. Vertical deflections for the channels and the cellular beams are around 20 mm (actual deflection of PC beams) and 34 mm at 60 minutes respectively. This translates to deflections of around  $\text{span}/283$  and  $\text{span}/166$  respectively. Hence, vertical deformations are well within the fire limit state requirements of  $\text{span}/20$  (BSI, 2009).

The lateral deformations of the beams should be carefully considered as they could potentially compromise the integrity of the SD system if deformations induce tension and cause cracks to develop. The lateral deflections of the channels and main cellular beams at the top flange are around 16-21mm and 15-16mm respectively, based on the numerical models. It is possible that localised crushing or bearing in the SD may occur near the connectors where the steel decking and FCB bear against the connectors that carry the support plate under the decking. In the experiment tensile cracking of the boards due to lateral deformations was not directly observed. However, this may have influenced the cracking and SD system at PC1 which led to the significantly increased localised temperatures.

Axial forces induced in channel sections are low, at less than 2kN, due to limited minor axis stiffness of the cellular beams. Axial forces induced in the cellular beams are significantly higher at around 37 kN. However, the beams were still able to maintain load bearing capacity, with localized yielding occurring only. Also, the primary end beams are relatively short, as are the columns, meaning that in real structures axial restraint is likely to be lower than encountered here for the cellular beams.

Given the success of the SD and CBS system as a whole when subjected to standard fire conditions, the work conducted in this research can serve as the foundation to a new perspective of structural fire performance designs for steel structures built using cellular beams. As described in Section 2.6.4 above, the main focus of the research on cellular beams in fire was aimed at predicting the failure mechanisms of the cellular beams exposed to fire and using the experimental data to formulate analytical solutions to quantify the performance and critical steel temperatures for design purposes. However, this research has shown that there is a potential that if sufficient evidence is provided that the protective flooring system will not fail during an unwanted fire, the steel temperatures will most likely not be an issue and can perhaps be designed at ambient temperature while the flooring system is ensured to have the appropriate standard fire rating. Unfortunately, no key failure mechanisms have been identified in this work for the CBS system such that comparisons to other studies can be performed. Furthermore, as this system is different from the typical cellular beam concrete composite structures, the data provided in this work will not advance the specific progress made by the researchers mentioned in Section 2.6.4 but rather provide a potential different approach to the design of cellular beams in fire. However, that does not limit the findings from being utilized to formulate simple analytical methods to predict the behaviour of cellular beams in fire.

## Chapter 9 Conclusions

### 9.1 Overview

The main goal of this dissertation was to evaluate experimentally numerically quantify the newly proposed Cellular Beam Structural (CBS) system under standard fire conditions, addressing both the structural steelwork members and the sandwich decking (SD) systems. This dissertation was founded on the work of previous researchers (Kloos, 2017; Marx, 2018), who performed a fully-decoupled thermal-stress numerical analysis on the CBS system based on experimental data obtained from small-scale standard fire testing conducted by Marx (2018). Significant insights into the performance of the CBS system at elevated temperatures were gained from this past work, but it pointed to areas requiring further investigation:

- 1 The CBS system's fire rating is primarily based on the SD system's thermal and structural performance. Hence, both the mechanical and elevated temperature performance of the SD system needed to be established.
- 2 The SD system has several advantages over traditional construction flooring systems, including the ability to function as a standalone trafficable fire-rated flooring system that can be incorporated into other structural designs. Hence, focus on the SD in isolation may result in a standalone system that can be used in a variety of scenarios.
- 3 Due to the size of past experimental tests conducted, and limitations inherent to numerical modelling, full-scale testing of the system was required.

To address the aspects above the following objectives have been achieved through this work:

1. To carry out large-scale tests fire have been carried out on the CBS and SD systems.
2. To develop and validate numerical models for the structural and thermal performance of the system.
3. To compare and contrast the numerical models with the experimental data, thereby providing insight into the behaviour observed.
4. Establishing the extent to which a fire rating can be assigned to the systems.
5. The flexural resistance of the SD flooring has been quantified such that its failure modes and capacities have been quantified.

These objectives have been achieved through the chapters provided in this work as listed below.

## 9.2 Overview of chapters

### 9.2.1 *Introductory chapters – Chapters 1 to 3*

The first chapter (Chapter 1) provides a brief overview of the CBS system as well as the motivation for the research project. The SD system used in the CBS system is also discussed in order to familiarize the reader with the two main components of the CBS design, namely the CBS structural members and the composite flooring system (i.e. SD system). The chapter concludes with a description of the study objectives, scope, and limitations.

The current literature relevant to structural fire engineering was laid out in Chapter 2. A brief introduction to the field's historical background was presented. Following that, the chapter delves into the various testing methodologies and design approaches used in structural fire engineering, including standard fire testing and performance-based testing. After that, a brief overview of fire behaviour and heat transfer mechanisms was presented. The chapter continues with a discussion of steel structures in fire, including mechanical and thermal properties of steel at high temperatures, as well as a brief overview of the status quo of cellular beam testing in fire. After that, the chapter concludes with a summary of the various advanced calculation methods and software used to analyse structures at high temperatures.

Chapter 3 presents an overview of the CBS system investigated in this research, giving insight to the structural layouts and terminology used to describe the originally proposed CBS system and the originally proposed composite flooring system to be implemented in the CBS design. The chapter goes on to give a detailed description of previous research conducted on the CBS and SD systems, as well as the conclusions drawn about their performance in fires. Following that, a brief description on the design methodology, terminology and layout of the experimental frame tested in this work is presented. The chapter ends with a brief description of the SD system's evolution to the final proposed version tested in this study.

### 9.2.2 *Experimental programme – Chapter 4 to 5*

Chapter 4 details the small-scale materials tests conducted on the material components used in the SD system and of the structural steel utilized in the experimental frame and the medium-scale four-point bending tests conducted on the SD systems. A total of 12 samples built to the design aspects of the SD system were tested as part of this work. Five different combinations of the VP50 profiled steel decking were tested: two samples with 12 mm FCB, two samples with 9 mm FCB, and one isolated sample with only the VP50 profiled steel decking. The remaining samples included VP115 profiled steel decking, four of which were tested with a 20 mm FCB and two of which had different connector spacing. Only the VP115 profiled steel decking was included in the final sample. Using the effective width method, theoretical values of the moment of resistance were calculated for the isolated VP50 and VP115 samples tested, which showed good agreement. In addition, a simple elastic analysis was performed using the transformed area method to determine the maximum load capacities of the tested SD samples tested. Finally, the chapter concludes by comparing the experimental data obtained from the

four-point bending tests to the results of a full-interaction elastic analysis performed on the SD system as in the experimental setup.

Chapter 5 describes the two large-scale standard fire tests (LST-1 and LST-2) that were conducted as part of this research. Details on the testing methodology, experimental setup, and the results of both tests are described in detail. A final discussion on the results obtained from each of the experimental tests are then summarised at the end of each respective section.

### 9.3 Main findings

The main findings obtained throughout this dissertation will be presented in the next section. Only a brief summary of the results obtained will be presented, and for a more in-depth discussion, the reader is referred to the respective chapters mentioned above.

#### *9.3.1 Medium-scale four point bending tests*

##### ***VP50 SD system findings***

Two different failure modes were experienced by the various VP50 SD samples when comparing the VP50-9 and VP50-12 SD samples (9mm and 12mm FCB respectively): both the VP50-9 samples both failed via local buckling of the top flute steel at the points of load applications, while the VP50-12 sample failed via cracking of the CSB at the bottom. The isolated VP50 sample failed via local buckling of the top flute steel along the point of load application, similar to the VP50-9 samples tested. Furthermore, the experimental data shows that the presence of the FCB increased the load capacity of the VP50 profiled steel decking by 70.4% and 85.3% when compared to the VP50-9-T1 and VP50-12-T2 sample results, respectively. The theoretical moment capacity calculated for the isolated VP50 sample compared well with the experimental data, with only a 12.8% variation between the theoretically calculated moment capacity and the actual moment capacity as obtained from the experiments. The theoretically calculated moment capacities calculated using the transformed area method for the composite SD samples also correlated well with the experimental data obtained from the VP50-9/12 SD samples tested. Maximum variations in predicted results differ with experimental values by 11.6% for the VP50-9-T1 and 15% for the VP50-12-T2 samples, respectively. Hence, both identification of potential failure mechanisms and simple analytical methods for predicting failure capacities are provided through this work. Simple calculation models are suitable for quantifying failure. Lastly, the data obtained from all the VP50 SD sample tests indicate that the SLS governs the design capacity of the system. The maximum span lengths calculated at the SLS is 2.43 m and 2.42 m for the VP50-9-T1 and the VP50-12-T1 samples, respectively.

### ***VP115 SD system findings***

A variety of failure modes were observed for the VP115 SD samples tested: (1) the VP115-12-T1 sample experienced shear failure of the CSB in the longitudinal direction along the line of fixities. (2) The VP115-12-T2 sample failed via cracking of the Calcium Silicate board in the transverse direction between the points of load application. (3) The VP115-20-T1 sample experienced two different failure modes, firstly, local buckling of the steel at the bottom trough and crushing of the CSB at the supports, which was followed closely by local buckling failure at the steel top flute area between the points of load application. (4) The VP115-20-T2 sample failed via local buckling of steel decking trough sections at the supports and followed shortly by local buckling at the steel top flute area between the points of load application. (5) Sample VP115-20-T3 experienced failure via local buckling of the steel decking flute between the points of load application and fixities through pull-out failure as the test continued. (6) Sample VP115-20-T4 experienced failure via warping/local buckling of the steel top flute area between the points of fixities located between the points of load application. The experimental data shows that the presence of the FCB increased the load capacity of the VP115 profiled steel decking by 290% when compared to the VP115-20-T1 sample, where the latter yielded the highest load capacity of the VP115 SD samples tested.

Next, the theoretically calculated moment capacity of the isolated VP115 profiled steel decking using (a) the effective width method and the (b) theoretically calculated moment capacities of the VP115 SD samples using the transformed area method did not correlate well with the experimental data. The maximum error difference between the experimental data of the SD samples and the theoretically calculated moment capacities is 173% and 129.5% for the VP115-12-T1 and the VP115-20-T4 samples, respectively. Similar to that of the VP50 SD system, the design capacity of the VP115 SD system is governed by the SLS, with a maximum span length of 2.65 m calculated for the VP115-20-T1 sample.

The analytical results provide a good indication that the VP115 SD samples (a) do not exhibit full composite behaviour, and (b) a variety of failure mechanism may need to be considered. Hence, a more comprehensive method of analysis was required to calculate the load capacities of the VP115 SD samples, where partial interaction is also considered.

#### *9.3.2 Large-scale standard fire tests*

Two large-scale fire tests on 4x6m specimens were conducted. The first test served primarily as a dry-run for the work, but has also provided interesting insight regarding potential failure mechanisms and practical aspects. The second test provides the primary source of data for understanding the SD and CBS systems at elevated temperature.

### ***Large-scale standard fire test 1 (LST-1)***

Failure of the VP50-9 SD system tested in LST-1 was experienced at the South-West corner of the experimental setup. The failure was primarily caused by a piece of fibre ceramic blanket that detached from the supporting beams and covered the nozzle of one of the diesel burners. This caused the temperatures to spike at this location and cause the subsequent failure of the VP50-9 SD flooring. Additionally, in part due to this failure, the initial setup of the diesel burners caused a temperature gradient within the furnace and was not able to produce the desired time-temperature curve required for standard fire testing. When comparing with the average unexposed surface temperatures, both the average and single point Fire Limit State (FLS) temperatures of 160°C and 200°C was exceeded.

### ***Large-scale standard fire test 2 (LST-2)***

No structural failure of the decking system or the structural components of the experimental frame occurred during the second large-scale test conducted. Time-temperature data was obtained from a total of 90 thermocouples placed at various points of interest on the attached VP50-9 SD system and the horizontal structural components of the experimental frame. Additionally, vertical deflection data was also obtained from a total of 6 (two of which malfunctioned during testing) locations along the horizontal structural components.

When considering the time-temperature data acquired from the SD system the following observations were made: (1) The data clearly indicates the dehydration period that the CSB undergo when a temperature of 100°C is reached, where the temperature rise of the unexposed side of the Calcium Silicate board is halted for an average duration of 4.4 minutes. (2) When comparing the time-temperature data obtained from the steel decking flute area (FD) to the steel decking trough area (TD), it can be observed that the measured temperatures of the FD locations are higher than that of the TD locations. Hence, the main mechanism of heat transfer through the layers of the SD system is cavity radiation via the flute area of the SD system, when compared to the conduction of heat at the trough sections of the SD system.

(3) The highest temperature was recorded at the location referred to as Group 2 (G2) for the thermocouple groups placed along the SD system (BT location, which refers to the top for the calcium silicate board) with a temperature of 695°C at the end of the experiment. (4) With regards to the FLS insulation criteria, the experimental data showed that the SD system performed relatively well. When comparing the unexposed average temperatures, the SD system was able to keep the average temperature rise within the specified FLS average temperature of 149.8°C, with the average unexposed top of the FCB at the flute area (F-FCT) temperatures only surpassing this limit at about 59 minutes into the experiment. The final total average temperatures captured on the unexposed side (i.e., F-FCT and T-FCT) is 146.8°C at the end of the test (66-minutes), which is well within the specified FLS average temperature. However, the FLS temperature for a single location was exceeded at the Group 1 and Group 5 locations for the F-FCT thermocouple at about the 57<sup>th</sup> and 61<sup>st</sup> minutes into the experiment.

(5) The CBS and SD systems were able to meet the requirements of the FLS load bearing and integrity criteria. (6) The highest temperature recorded for the horizontal structural components was at the bottom flange area of main cellular beam (CB 1), with a temperature of 724°C at the end of the experiment. If the steelwork forms part of the trafficable area it will result in insulation failure occurring for the plenum. This has also led to the recommendations provided below. (7) The deflection of the structure comprised three deflection mechanisms, namely, thermal bowing, thermal elongation, and mechanical deflection. As the parallel channel beams deflected in relation to the cellular beams, the highest recorded deflection of 54 mm was obtained at the mid-point of the PC 2, which is within the FLS requirements.

### ***Prediction of deflection behaviour of the VP115 SD system***

The numerical model developed for the VP115-20 SD system was compared and validated against two sets of experimental data, namely the VP115-20-T1 and VP115-20-T3 experimental data. The structural finite element model with connectors at 200mm spacing with spring stiffnesses of 3695 N/mm (FEM-200-3695 N/mm model) was able to accurately predict the linear elastic phase deflection of the VP115-20-T1 sample tested. However, as bearing failure and material yielding starts to occur, the model under-predicts the experimental data. The maximum error difference between the numerical model and the experimental data is about 24%, which occurs at the end of the analysis. When considering the VP115-20-T3 sample and FEM-300-3695 N/mm model, the model was able to predict the deflection behaviour of the tested sample with greater accuracy, with an error difference of less than 10%. Even though these models have different numbers of connectors it appears the total connector capacity in the two models are in agreement. A third case was also modelled where full interaction was assumed (i.e., the connectors were modelled as beam elements), with the results showing that the stiffness of the full interaction model being higher than that of the experimental data, as expected. However, the full interaction numerical model analysis also starts to under-predict the experimental data when deflections beyond the linear elastic limit is reached. Factors accounting for this discrepancy are detailed in Chapter 6.

### ***Thermal response model of the VP50-9 SD system***

In general, the numerical model developed to predict the temperature evolution of the VP50-9 SD system compared well with the experimental data. The model was able to predict the temperature evolution on the unexposed side of the CSB with reasonable accuracy, with an error difference of less than 10.5% from 20<sup>th</sup> minute into the analysis and an error difference of 2.1% at the end of the analysis. Furthermore, implementation of the modified specific heat values proved to be successful in predicting the dehydration occurring in the CSB when a temperature of 100 °C is reached. When considering the temperature evolution within the cavities of the SD system (i.e., top of decking (DT) and top of flute (FD) locations), there is a noticeable difference in the behaviour of the model and the experimental data for the first 15 minutes of the analysis. However, when compared to the experimental data, the model temperatures at these two locations converge to similar final temperatures, with an error difference of 6.2 % and 2.8 % for the FD and TD locations, respectively.

When considering the unexposed surface temperatures at the top of the FCB (above the trough (T-FCT) and flute (F-FCT)), the model was able to predict the recorded temperatures well up until the 40<sup>th</sup> and 50<sup>th</sup> minute mark for the F-FCT and T-FCT locations respectively, where the predicted temperatures start to increase at a more rapid rate and diverge from the experimental data. The error difference in the final temperatures predicted at the F-FCT location is 52% and 71% at the T-FCT location. Reasons for lack of agreement are provided. Finally, when comparing the numerical data to the FLS average and single point limit temperatures, the FEM-T-FCT and FEM-F-FCT temperatures surpassed both the average and single point temperatures at the 56<sup>th</sup> and 63<sup>rd</sup> minute mark, and at the 42<sup>nd</sup> and 48<sup>th</sup> minute mark, respectively. Thus, the estimated fire resistance rating for the VP50-9 SD system calculated by the model is 42 minutes.

### ***Thermal-stress models of the experimental frame***

The single element and global models developed in this work were able to simulate the thermal-stress behaviour of the experimental frame tested in LST-2 well, and in general had good correlations with the experimental data. Furthermore, good agreement was also found when comparing the respective elements from the single element models to that of the global model. The percentage differences between the single element and global models, and the error differences between the single element models and the global model to that of the experimental data for all recorded vertical deflections at the 60-minute mark are listed in Table 8-3 above. No significant failure mechanisms were predicted in the models for both the single element and global model, however, some of the models did exhibit some localized plastic behaviour. However, they were still able to maintain load bearing capacity. Furthermore, the PC 1 and PC 2 beams in both the single element and global models exhibited lateral-torsional buckling behaviour towards the end of the analyses. This behaviour was caused by the asymmetric nature, the lateral restraints provided at the bottom flange, and the temperature evolutions of the PC beams. The thermal expansions and axial forces induced in the single element and global model PC and CB beams are presented in Figure 8-24 to Figure 8-30 above. The data shows that the CB beams have little restraint to offer and bend about the weak axis when pushed up against by the PC beams due to thermal expansion, however, this behaviour does not have a significant overall effect on the behaviour of the CB beams. Conversely, due to the relatively short PB beams tested in the experimental frame, which have a much higher stiffness as a result, induced significant axial forces within the CB beams. However, only localized plastic yielding occurred and the beams were still able to maintain load bearing capacity as mentioned above. Finally, the final deflections of the CB and PC beams were around 34 mm and 54 mm at the 60<sup>th</sup> minute mark, which is still within the recommended limit of span/20.

## 9.4 Recommendations and future research

### *9.4.1 Proposed details for the CBS and SD for the future*

Based on the research conducted by Kloos (2017); Marx (2018), and the findings of this dissertation, the following design recommendations are given for the construction of the CBS system: (1) No major design modifications are required for the structural elements of the CBS system, if the SD system is able to uphold the requirements of the FLS criteria, the structural elements of the CBS system should be able to maintain load bearing capacity during an unwanted fire for the required amount of time. However, to further limit the exposure of the structural elements to high temperatures from unwanted fires, a single design recommendation is further provided below. (2) Based on the four-point bending tests conducted in this work, and consultation with practitioners, the VP115-20 SD system (which includes the VP115 profiled steel decking, the 20 mm FCB and the 9 mm CSB ceiling) should be implemented in the design of the CBS system. This system has shown to provide the highest load bearing capacity and limits the possibility of shear punching and cracking occurring from point loads. Depending on the construction details, the FCB boards may be design based on the capacity of the profiled decking only, as this provides a more practical and conservative approach. However, if continuity is provided between the FCB's, such as using strips to join adjacent boards, the capacity of the SD system may also be based on the composite strength of the system. (3) As the VP50-9 system has shown to have the capability of achieving a required fire rating of over 57 minutes, the design of the SD system variation will most likely be governed by the SLS and ULS requirements, as the FLS requirements will be satisfied.

When LST-2 was conducted, the bottom flange of the experimental frame's horizontal structural components (Primary and parallel channel beams) was directly in contact with the VP profiled steel. To further reduce the heat conducted into the bottom flange of the CBS systems horizontal structural components, the vertical spacing of the steel plates used to attach the SD system could be increased such that the FCB can be slid under the steel to provide extra protection to the primary and tertiary structural components, as shown by example of the PC beams in Figure 9-1 below, where the FCB is shown in blue. Slots will need to be cut into FCB during installation to make this possible. However, boards are already cut significantly to fit between beams, meaning that the amount of labour required is not significantly increased.

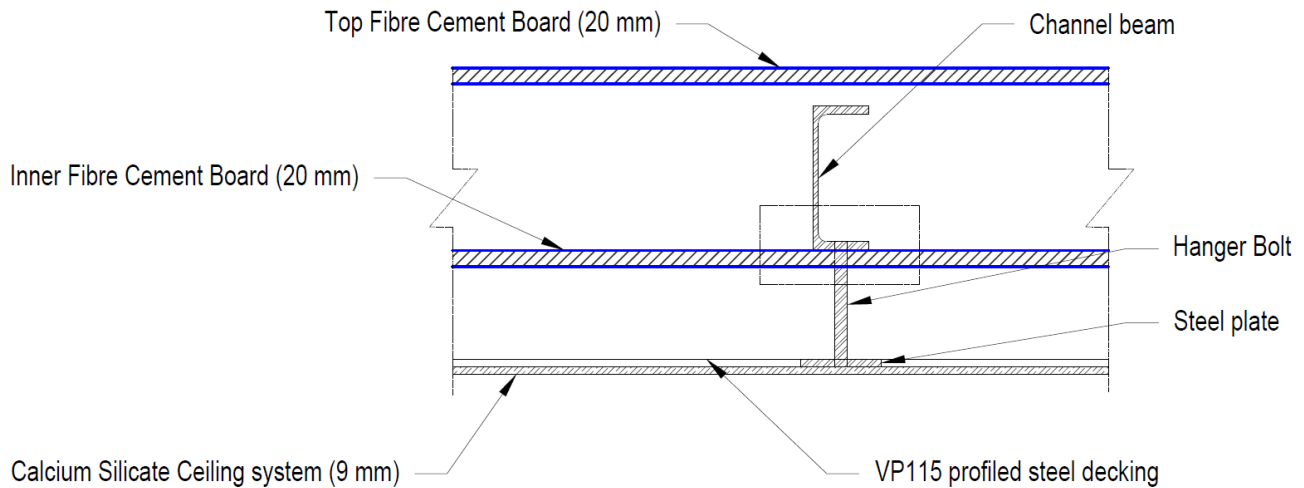


**Figure 9-1 Design implementation to further reduce thermal exposure of primary and tertiary beams by making the FCB continuous under the beams.**

Furthermore, as the secondary cellular beams are comprised of the deepest sections and run parallel with the SD system, this element would be the most exposed to the high temperatures during an unwanted fire. To limit this exposure, extra strips of CSB can be slid under the beams on top of the CBS ceiling as with the CSB strips that are used to join adjacent CSB's. This technique was also implemented in the numerical models developed by Marx (2018), as shown in Figure 3-5 above for the configuration of the J-Beams, where 10 mm FCB strips were implemented.

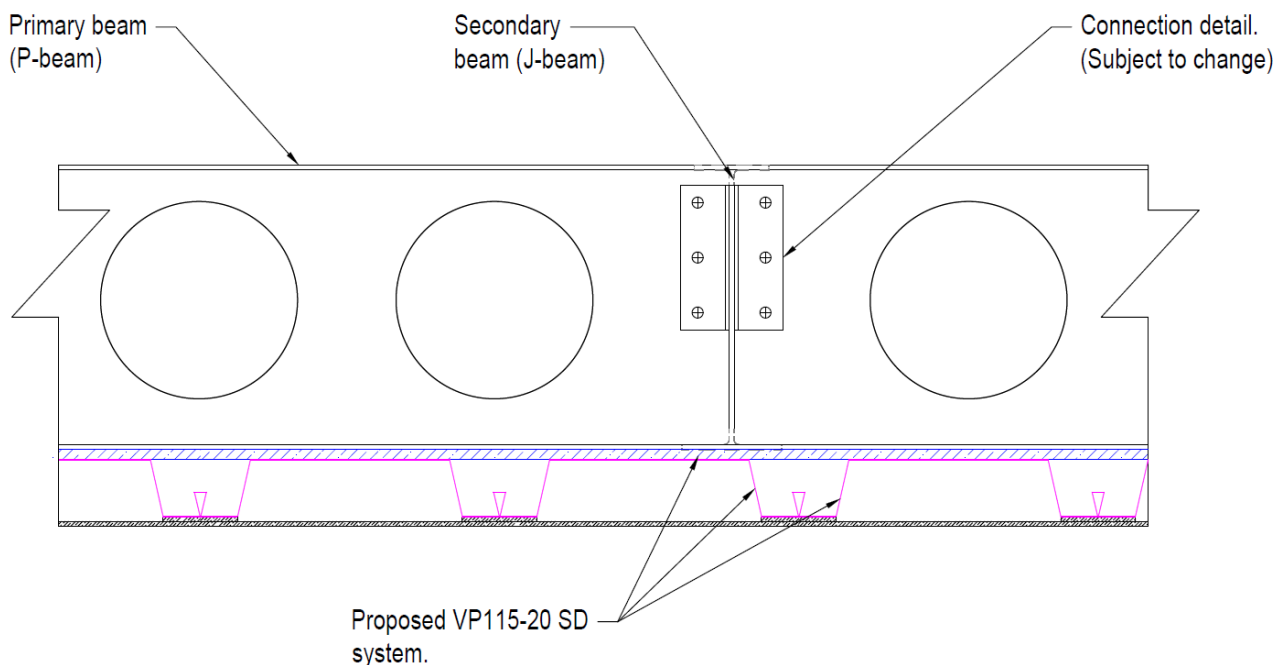


**Figure 9-2 Design implementation to allow for the SD system to be situated underneath all the horizontal structural elements.**

Alternatively, the design of the CBS system can be modified such that the SD system is attached to the bottom of the beams in a manner which will allow for all the horizontal structural elements to be situated on top of the inner FCB. Figure 9-2 above depicts a simplified example of this modification, where the secondary cellular beam (J-Beam), which runs parallel with the SD system, is situated on top of the inner FCB. However, this design implementation will change the depth of the secondary cellular beams to accommodate the SD system underneath. Furthermore, as the size of the primary and secondary beams will become similar, the secondary beams will have to be notched at the top and bottom to allow for the connections to be made between the beams. Further studies will have to be conducted to establish the influence this change in size to the secondary beams will have with regards to capacity and structural behaviour.

The importance of flexibility in the structure has been demonstrated by Kloos (2017) in his research and in this work. As a result, it is further recommended that the secondary cellular beam connections to the primary beams be designed as double angle cleat connections with slotted holes to allow for free expansion of the secondary beams at high temperatures.

#### *9.4.2 Recommendations for future research*

When the CBS system is exposed to high temperatures, a number of factors influence its performance. However, as previously stated, the CBS system's fire performance is largely determined by the SD system's thermal performance. According to the FLS criteria, the VP50-9 SD system tested in LST-2 was able to produce a 57-minute fire rating. Furthermore, the CSB remained intact throughout the experiment, with no detachments from the VP profiled decking observed during testing. As a result, sufficient evidence has been presented in this dissertation that the SD system has the necessary attributes to serve as the CBS system's horizontal components' built-in fire protection. However, many factors that may influence the SD system's thermal performance have not been investigated in this study. First and foremost, because the VP115 SD system is the most likely candidate for integration into the CBS system, its thermal performance must be investigated. However, based on the results obtained from the VP50-9 SD system tested in LST-2, the VP115 SD system is expected to yield more favourable results, given the deeper deck and thicker FCB used.

The impact of holes in the CSB for services such as lighting and electrical wiring needs to be investigated. This is especially important because the experimental results showed that any cracks in the Calcium Silicate board had a significant impact on the SD system's ability to protect the CBS components from fire.

Furthermore, when considering the SD system's flexural performance. The mechanical model developed in this study was based on simplified assumptions such as perfect elastic-plastic mechanical properties of the SD system material components and assumed stiffnesses of the model's connector elements. As a result, fixity pull-out tests should be conducted in the future so that specific stiffness values for the fixities used with the FCB and CSB in combination with the VP profiled steel decking can be obtained and incorporated into future models.

Furthermore, the scope of this thesis was limited to determining the SD system's flexural capacity at ambient temperature. Research on the load-bearing FLS capacity of the decking is required, although experimental testing showed that capacity was maintained. Aspects not considered in this research are likely to be enhanced or affected by the system configurations proposed. More research into the damping the system may provide is required, as this is critical for the system's serviceability limit state when dynamic loads are considered. Moreover, the acoustics provided by the system are unknown and need to be investigated as well. Furthermore, the system has only been experimentally tested in single span simply supported experimental setups, hence, experimental testing needs to be carried out on the SD system in multi-span experimental setups.

Lastly, the experimental testing conducted in this research has shown that the flexural rigidity of the VP115-20 SD has a limit on the distance it can span, based on its capacity. This may limit its application in some environments (e.g. a trafficable floor above offices). However, the updated versions of the VP decking provided by the suppliers will soon be released into the market with enhanced mechanical properties when compared to the version tested in this work. The newly released versions of the VP decking has a higher yield strength of 550 MPa, although the stiffness remains the same.

Throughout this study, it was assumed that the CBS system's columns would be protected using standard protective boarding materials. However, no investigations into the behaviour of the CBS system when the columns are exposed to high temperatures has been conducted. Furthermore, Kloos (2017) only considered a single floor of the CSB system in his research, as did this study. As a result, future models can be expanded to include multiple floors, cross-bracing, columns, and other such factors that may affect the system's behaviour. The influence of global interactions at both ambient and elevated temperature may provide insight on forces that could be induced.

## Chapter 10 References

- Ahmed, E., Wan Badaruzzaman, W.H. and Rashid, K. (1996), “A simplified elastic composite floor section analysis with incomplete interaction”, *Jurnal Kejuruteraan*, Vol. 8, pp. 67–78.
- Ahmed, E., Wan Badaruzzaman, W.H. and Wright, H.D. (2000), “Experimental and finite element study of profiled steel sheet dry board folded plate structures”, *Thin-Walled Structures*, Vol. 38 No. 2, pp. 125–143.
- Al-Shaikhli, M.S., Wan Badaruzzaman, W.H., Baharom, S. and Hilo, S.J. (2017), “Theoretical and finite element analysis of the two-way PSSDB floor system”, *Journal of Constructional Steel Research*, Elsevier, Vol. 135 No. April, pp. 49–55.
- Al-Shaikhli, M.S., Wan Badaruzzaman, W.H., Shahrizan, B. and Ahmed, W.A. (2017), “The two-way flexural performance of the PSSDB floor system with infill material”, *Journal of Constructional Steel Research*, Vol. 138, pp. 79–92.
- Ariyanayagam, A.D. and Mahendran, M. (2017), “Fire tests of non-load bearing light gauge steel frame walls lined with calcium silicate boards and gypsum plasterboards”, *Thin-Walled Structures*, Elsevier Ltd, Vol. 115 No. February, pp. 86–99.
- ASFP. (2014), *The Yellow Book - Fire Protection for Structural Steel in Buildings 5th Edition*, 5th ed., Association for Specialist Fire Protection, Hampshire, UK.
- Awang, H. and Badaruzzaman, W. (2011), “Development of profiled steel sheeting dry board roof panel system in school classroom modules”, *Journal of Civil Engineering and Construction Technology*, Vol. 2 No. 4, pp. 72–81.
- Awang, H., Nordin, N. and Wan Badaruzzaman, W.H. (2009), “the Application of Profiled Steel Sheeting Dry Board (Pssdb) Industrialised Building System”, Vol. 1.
- Awang, H. and Wan Badaruzzaman, W.H. (2010), “Structural performance and applications of a reversed profiled steel sheeting dry board roof panel system”, *Asian Journal of Civil Engineering*, Vol. 11 No. 3, pp. 371–384.
- Badaruzzaman, W., Ahmed, E. and Rashid, A. (1996), “Behaviour of Profiled Steel Sheet Dry Board System”, *Beijing International Conference*, pp. 21–24.
- Bisby, L., Gales, J. and Maluk, C. (2013), “A contemporary review of large-scale non-standard structural fire testing”, *Fire Science Reviews*, Vol. 2 No. 1, p. 1.
- BSI. (1996), *BS EN 310 Wood-Based Panels - Determination of Modulus of Elasticity in Bending and of*

*Bending Strength*, London, British Standards Institute.

BSI. (2002), *Eurocode 1: Actions on Structures - Part 1-2: General Actions - Actions on Structures Exposed to Fire*, *Eurocode 1: Actions on Structures*, Vol. 1, London, British Standards Institute.

BSI. (2005), *Eurocode 3: Design of Steel Structures - Part 1-2: General Rules - Structural Fire Design*, London, British Standards Institute, available at: <http://hdl.handle.net/10019.1/102683>.

BSI. (2009), *BS 476: Fire Tests on Building Materials and Structures.*, London, British Standards Institute.

Buchanan, A.H. and Abu, A.K. (2017), *Structural Design for Fire Safety*, 2nd Ed., Wiley, New York.

CAL FIRE. (2019a), *Top 20 Deadliest California Wildfires*, California, available at: [https://www.fire.ca.gov/media/lbfd0m2f/top20\\_deadliest.pdf](https://www.fire.ca.gov/media/lbfd0m2f/top20_deadliest.pdf).

CAL FIRE. (2019b), *Top 20 Most Destructive California Wildfires.*, California, available at: [https://www.fire.ca.gov/media/t1rdhizr/top20\\_destruction.pdf](https://www.fire.ca.gov/media/t1rdhizr/top20_destruction.pdf).

Claasen, J., Walls, R.S. and Cicione, A. (2021), “figshare - My data”, *Stellenbosch University*, available at: <https://doi.org/https://doi.org/10.6084/m9.figshare.16940824>.

de Clercq, H. (2016), *Southern African Steel Construction Handbook*, Eighth., the Southern African Institute of Steel Construction.

Dassault Systemes. (2016), “Abaqus 2016 Documentation. Dassault Systemes Simulia Corporation”, *Dassault Systemes*, available at: <http://130.149.89.49:2080/v2016/index.html> (accessed 18 October 2021).

Degler, J. (2016), *Determination of the Conductivity of Insulation Boards Made of Calcium Silicate by Test in the Cone Calorimeter.*, Luleå University of Technology, available at: <http://www.diva-portal.org/smash/get/diva2:1026626/FULLTEXT02>.

Dilworth, R. (2011), *Cities in American Political History*, edited by Richardson Dilworth, CQ Press, United States of America.

Drennan, M.B. (2017), *Comparative Construction Costs of Typical Low-Rise Office Buildings in South Africa.*, Stellenbosch University., available at: <https://scholar.sun.ac.za/handle/10019.1/101015>.

ETEX Group. (2020), *Kalsi Partition Technical Data Sheet*, available at: <https://etexasassets.azureedge.net/-/dam/tds-kalsipartition-technical-datasheet-en-2020-12.pdf/pi34813/original/tds-kalsipartition-technical-datasheet-en-2020-12.pdf?v=617231435>.

Feng, M., Wang, Y.C. and Davies, J.M. (2003), “Thermal performance of cold-formed thin-walled steel panel systems in fire”, *Fire Safety Journal*, Vol. 38, pp. 365–394.

- Gales, J., Maluk, C. and Bisby, L. (2012), “Large- scale structural fire testing- How did we get here, Where are we, and where are we going?”, *15th International Conference on Experimental Mechanics: Fire Symposium*, pp. 1–22.
- Gebremeskel, A. (2013), *MODULAR ACCESS FLOOR OFFICE BUILDING SYSTEM*, *Steel Future Conference*.
- Govindan, S.K. and Madhavan, M. (2019), “Experimental and analytical study of lightweight floor system built-up with cold-formed profile steel sheet and hot-rolled steel plate (CFPSS-HRSP)”, *Structures*, Elsevier, Vol. 22 No. April, pp. 291–309.
- Grossman, R. (2016), “Which Chicago mayor reformed the police and quit?”, *CHICAGO TRIBUNE*, available at: <https://www.chicagotribune.com/opinion/commentary/ct-medill-rahm-emanuel-police-reform-per-flash-0124-jm-20160120-story.html> (accessed 31 October 2021).
- History.com Editors. (2010), “Chicago Fire of 1871”, *A&E Television Networks*, available at: <https://www.history.com/topics/19th-century/great-chicago-fire> (accessed 31 October 2021).
- Holman, J.P. (2009), *Heat Transfer*, 10th ed., McGraw-Hill, New York.
- Hurley, M.J., Gottuk, D., Hall, J.R., Harada, K. and Kuligowski, E. (2015), *SFPE Handbook of Fire Protection Engineering*, 5th Ed., Springer, New York, available at: <https://doi.org/10.1007/978-1-4939-2565-0>.
- Ignis Testing. (2021), “Ignis Testing - Fire Resistance Testing Laboratory - Cape Town”, available at: <https://ignistesting.co.za/direction-and-related-issues-for-fire-door-testing/> (accessed 14 October 2021).
- Jacquotte, O.P., Oden, J.T. and Becker, E.B. (1986), “NUMERICAL CONTROL OF THE HOURGLASS INSTABILITY”, *International Journal for Numerical Methods in Engineering*, Vol. 22, pp. 219–228.
- Jaffar, M.I., Kamarulzaman, K. and Lias, M.R. (2018), “21system between Geopolymer Concrete and Normal Concrete Infill : Experimental and Finite-Element Modeling”, *Asian Journal of Technical Vocational Education And Training*, Vol. 5 No. September 2018, pp. 15–33.
- Jahan, A. (2018), *Axial and Shear Behavior of Profiled Steel Sheet Dry Borad (Pssdb) Composite Walling System*, *Abu Dhabi University*.
- Jeffers, A., Wickstrom, U. and McGrattan, K. (2012), *Documentation of the Solutions to the SFPE Heat Transfer Verification Cases*, available at: <http://www.sfpe.org/>.
- KALSI. (2020), “kalsifloor - Kalsi”, *Kasli-Buidling-Solutions*, available at: <https://www.kalsi-building-solutions.com/en/products/all-products/boards/kalsifloor/>.
- Khan, M.A. (2019), *Analysis of Perforated Beams in Fire Using a Virtual Hybrid Simulation Approach*, Brunel

University London.

Kloos, M. (2017), *An Investigation into the Structural Behaviour of a Novel Cellular Beam Structure in Fire*, Stellenbosch University, available at: <http://hdl.handle.net/10019.1/102683>.

Kloos, M. and Walls, R.S. (2019), “Finite Element Modelling of the Structural Behaviour of a Novel Cellular Beam Non-composite Steel Structure in Fire”, *International Journal of Steel Structures*, Korean Society of Steel Construction, Vol. 19 No. 5, pp. 1367–1380.

Law, A. and Bisby, L. (2020), “The rise and rise of fire resistance”, *Fire Safety Journal*, Elsevier Ltd, Vol. 116, p. 103188.

Lennon, T. (2011), *Structural Fire Engineering*, ICE Publishing, London.

Malhotra, H.L. (1982), *Design of Fire-Resisting Structures*, Surrey University Press, Glasgow.

Marx, H. (2018), *Thermal Behaviour of a Novel Cellular Beam Structural System in Fire*, Stellenbosch University, available at: <http://hdl.handle.net/10019.1/103350>.

Marx, H. and Walls, R. (2019), “Thermal behaviour of a novel non-composite cellular beam floor system in fire”, *Journal of Structural Fire Engineering*, article, , Vol. 10 No. 3, pp. 354–372.

Nadjai, A., Bailey, C., Vassart, O., Han, S., Zhao, B., Hawes, M., Franssen, J.M., *et al.* (2011), “Full-scale fire test on a composite floor slab incorporating long span cellular steel beams”, *The Structural Engineer*, Vol. 89 No. November, pp. 18–25.

Nadjai, A., Goodfellow, N., Vassart, O., Ali, F. and Choi, S. (2008), “Simple calculation method of composite cellular beams at elevated temperatures.”, *Proceedings of the Fifth International Conference on Structures in Fire (SiF'08)*, No. May, pp. 551–559.

Nadjai, A., Petrou, K., Han, S. and Ali, F. (2016), “Performance of unprotected and protected cellular beams in fire conditions”, *Construction and Building Materials*, Elsevier Ltd, Vol. 105, pp. 579–588.

Nadjai, A., Vassart, O., Ali, F., Talamona, D., Allam, A. and Hawes, M. (2007), “Performance of cellular composite floor beams at elevated temperatures”, *Fire Safety Journal*, Vol. 42 No. 6–7, pp. 489–497.

Nadjai, A., Vassart, O. and Zhao, B. (2012), *Membrane Action of Composite Structures in Case of Fire.*, University of Ulster.

Naili, E., Nadjai, A., Han, S., Ali, F. and Choi, S. (2011a), “Experimental and Numerical Modelling of Cellular Beams with Circular and Elongated Web Openings at Elevated Temperatures”, *Journal of Structural Fire Engineering*, Vol. 2 No. 4, pp. 289–300.

- Naili, E.H., Nadjai, A., Han, S., Ali, F. and Choi, S. (2011b), “Experimental and numerical modelling of cellular beams with circular and elongated web openings at elevated temperatures”, *Journal of Structural Fire Engineering*, Vol. 2 No. 4, pp. 289–300.
- Najafi, M. and Wang, Y.C. (2017), “Axially restrained steel beams with web openings at elevated temperatures, part 1: Behaviour and numerical simulation results”, *Journal of Constructional Steel Research*, Vol. 128, pp. 745–761.
- Newmark, N.M., Siess, C.P. and Viest, I.M. (1952), “TESTS AND ANALYSIS OF COMPOSITE BEAMS WITH INCOMPLETE INTERACTION.”, *Proceedings of the Society of Experimental Stress Analysis*, pp. 75–92.
- Nordin, N., Wan Badaruzzaman, W.H. and Awang, H. (2009), “Connector Stiffness of ‘Peva-Cemboard’ Screwed Connection in Profiled Steel Sheet Dry Board (PSSDB) Panel”, *Collaboration and Integration in Engineering, Management and Technology*, pp. 1476–1482.
- Oliveira, T.B. De, Alves, T.A. and Mesquita, L.M.R. (2018), “Thermal Conductivity of Calcium Silicate Boards at High Temperatures: An Experimental Approach”, *Proceedings of the 1st Iberic Conference on Theoretical and Experimental Mechanics and Materials / 11th National Congress on Experimental Mechanics*, No. November, pp. 171–182.
- Oven, V.A., Burgess, I.W., Plank, R.J. and Abdul Wali, A.A. (1997), “An analytical model for the analysis of composite beams with partial interaction”, *Computers and Structures*, Vol. 62 No. 3, pp. 493–504.
- Pettersson, O., Magnusson, S.E. and Thor, J. (1976), *Fire Engineering Design of Steel Structures*, Swedish Institute of Steel Construction., Vol. 50, available at: <https://lucris.lub.lu.se/ws/portalfiles/portal/5989339/1245743.pdf>.
- PROMAT. (2020), “Promatec-H”, available at: <https://www.promat.com/en-au/construction/products-systems/products/boards/promatec-h-fire-board/>.
- Purkiss, J.A. (2007), “Fire safety engineering: design of structures”, *Fire Safety Engineering Design of Structures*, Second., 2007 Elsevier Ltd., Great Britain, p. 389.
- Quintiere, J.G. (2016), *Principles of Fire Behavior*, 2nd Ed., CRC Press.
- Rafiei, S. (2011), *Behaviour of Double Skin Profiled Composite Shear Wall System under In-Plane Monotonic, Cyclic and Impact Loadings*, Ryerson University, available at: [https://rshare.library.ryerson.ca/articles/thesis/Behaviour\\_of\\_double\\_skin\\_profiled\\_composite\\_shear\\_wall\\_system\\_under\\_in-plane\\_monotonic\\_cyclic\\_and\\_impact\\_loadings/14663553](https://rshare.library.ryerson.ca/articles/thesis/Behaviour_of_double_skin_profiled_composite_shear_wall_system_under_in-plane_monotonic_cyclic_and_impact_loadings/14663553).
- Rahmadi, A.P., Wan Badaruzzaman, W.H. and Arifin, A.K. (2013), “Prediction of deflection of the composite

profiled steel sheet MDF-board (PSSMDFB) floor system”, *Procedia Engineering*, Elsevier B.V., Vol. 54, pp. 457–464.

Rahmanian, I. (2011), “Thermal and Mechanical Properties of Gypsum Boards and Their Influences on Fire Resistance of Gypsum Board Based Systems”, *School of Civil Engineering*, Vol. Doctor of, p. 252.

Ranzi, G., Bradford, M.A. and Uy, B. (2004), “A direct stiffness analysis of a composite beam with partial interaction”, *International Journal for Numerical Methods in Engineering*, Vol. 61 No. 5, pp. 657–672.

SABS. (2005), *SANS 10177-2:2005 - Fire Testing of Materials, Components and Elements Used in Buildings Part 2: Fire Resistance Test for Building Elements*, SABS Standards Division.

SABS. (2010), *SANS 6892-1 : 2010 ISO 6892-1 : 2009 SOUTH AFRICAN NATIONAL STANDARD Metallic Materials — Tensile Testing Part 1 : Method of Test at Room Temperature*, SABS Standards Division.

SABS. (2011a), *SANS 10400 Part T*, SABS Standards Division.

SABS. (2011b), *SANS 10162-1 : 2011 SOUTH AFRICAN NATIONAL STANDARD The Structural Use of Steel Part 1: Limit-States Design of Hot-Rolled Steelwork*, SABS Standards Division.

SABS. (2011c), *SANS 10162-2 : 2011 SOUTH AFRICAN NATIONAL STANDARD The Structural Use of Steel Part 2 : Cold-Formed Steel Structures*, SABS Standards Division.

SABS. (2011d), *SANS 10160-1 : 2011 SOUTH AFRICAN NATIONAL STANDARD Basis of Structural Design and Actions for Buildings and Industrial Structures Part 1 : Basis of Structural Design*, SABS Standards Division.

Schaumann, P. and Hothan, S. (2002), “Fire Design of a New Slim Floor Beam System Using Fem-Analysis”, *2nd International Workshop “Structures in Fire”*, pp. 291–302.

Seraji, M., Wan Badaruzzaman, W.H. and Osman, S.A. (2014), “Non-linear analysis of membrane action effect in profiled steel sheeting dry board flooring system”, *International Journal of Steel Structures*, Vol. 14 No. 2, pp. 305–314.

Shahbazian, A. and Wang, Y.C. (2013), “A simplified approach for calculating temperatures in axially loaded cold-formed thin-walled steel studs in wall panel assemblies exposed to fire from one side”, *Thin-Walled Structures*, Elsevier, Vol. 64, pp. 60–72.

Steau, E. and Mahendran, M. (2021), “Elevated temperature thermal properties of fire protective boards and insulation materials for light steel frame systems”, *Journal of Building Engineering*, Elsevier Ltd, Vol. 43 No. April, p. 102571.

Steau, E., Mahendran, M. and Poologanathan, K. (2020), “Experimental study of fire resistant board

configurations under standard fire conditions”, *Fire Safety Journal*, Elsevier Ltd, Vol. 116 No. May, p. 103153.

Vassart, O. (2009), *Analytical Model for Cellular Beams Made of Hot Rolled Sections in Case of Fire*, available at:

[https://www.researchgate.net/publication/279263512\\_Analytical\\_model\\_for\\_cellular\\_beams\\_made\\_of\\_hot\\_rolled\\_sections\\_in\\_case\\_of\\_fire](https://www.researchgate.net/publication/279263512_Analytical_model_for_cellular_beams_made_of_hot_rolled_sections_in_case_of_fire).

Vassart, O., Bailey, C.G., Bihina, G., Hawes, M. and Nadjai, A. (2010), “Parametrical Study on the Behaviour of Steel and Composite Cellular Beams Under Fire Conditions”, *Structures in Fire - Proceedings of the Sixth International Conference, SiF'10*, pp. 349–357.

Vassart, O., Bouchaïr, A., Muzeau, J. and Nadja, A. (2008), “Analytical Model for the Web Post Buckling in Cellular Beams Under Fire”, *Proceedings of the Fifth International Conference on Structures in Fire (SiF'08)*, pp. 3–11.

Vassart, O., Brasseur, M., Hawes, M., Simms, I., Bin, Z., Franssen, J.M. and Nadjai, A. (2011), *Fire Resistance of Long Span Cellular Beam Made of Rolled Profiles ( FICEB )*.

Vassart, O., Hawes, M., Simms, I., Zhao, B., Franssen, J.M. and Nadjai, A. (2011), *Fire Resistance of Long Span Cellular Beam Made of Rolled Profiles - Design Guide, Research Programme of the Research Fund for Coal and Steel Steel RTD*, available at: [https://orbi.uliege.be/bitstream/2268/95913/1/FICEB\\_Design\\_Guide.pdf](https://orbi.uliege.be/bitstream/2268/95913/1/FICEB_Design_Guide.pdf).

VOIDCON. (2020), “Voidcon – Innovative Permanent Formwork”, available at: <https://voidcon.com/>.

Walls, R.S. (2016), *A Beam Finite Element for the Analysis of Structures in Fire*, Stellenbosch University, available at: <http://hdl.handle.net/10019.1/100331>.

Wan Badaruzzaman, W.H., Zain, M.F.M., Akhand, A.M. and Ahmed, E. (2003), “Dry boards as load bearing element in the profiled steel sheet dry board floor panel system - Structural performance and applications”, *Construction and Building Materials*, Vol. 17 No. 4, pp. 289–297.

Wang, H.-B. (1995), *Heat Transfer Analysis of Components of Construction Exposed to Fire*, University of Salford, available at: <http://usir.salford.ac.uk/id/eprint/14780/>.

Wang, P., Ma, N. and Wang, X. (2014), “Numerical studies on large deflection behaviors of restrained castellated steel beams in a fire”, *Journal of Constructional Steel Research*, Elsevier Ltd, Vol. 100, pp. 136–145.

Wang, Y., Burgess, I.W., Wald, F. and Gillie, M. (2012), *Performance-Based Fire Engineering of Structures*, 1st ed., CRC Press, London.

- Wang, Y., Chuang, Y.J., Lin, C.Y. and Zhang, H. (2018), “The Standard Fire Testing and Numerical Modelling of the Behavior of Calcium Silicate Board Metallic-Framework Drywall Assembly with Junction Box”, *Advances in Materials Science and Engineering*, Vol. 2018, available at:<https://doi.org/10.1155/2018/8130647>.
- Wickstrom, U. (2016), *Temperature Calculation in Fire Safety Engineering, Journal of Fire Sciences*, Vol. 34, Springer International Publishing Switzerland, available at:<https://doi.org/10.1007/978-3-319-30172-3>.
- Wickström, U. and Palsson, J. (1999), “A Scheme for verification of Computer Codes for Calculating Temperature in Fire Exposed Structures”, *Fire Technology, SP Report*, Vol. 36.
- Woody, R.H. (1947), “A Description of the Chicago Fire of 1871”, *The Mississippi Valley Historical Review*, Vol. 33 No. 4, pp. 607–616.
- World Steel Association. (2020), *2020 World Steel in Figures, 2020 World Steel in Figures*, Beijing, available at: <http://www.worldsteel.org/wsif.php>.
- Wright, H.D., Evans, H.R. and Burt, C.A. (1989), “Profiled steel sheet/dry boarding composite floors”, Vol. 67, pp. 114–120.